Structural studies on heme containing proteins

Chiara Bruckmann

Thesis presented for the degree of Doctor of Philosophy

University of Edinburgh

2008

A Davide

Declaration

The work presented in this thesis is the original work of the author, except where specific reference is made to other sources. It has not been submitted in part, or in whole, for any other degree. Some of the results have already been published.

Chiara Bruckmann

Acknowledgements

I'd like to thank my supervisor Prof Steve Chapman, for giving me the opportunity to work in his group and for support and help during my PhD formation. I'm grateful to Prof Graeme Reid, Dr Simon Daff, and Prof Malcolm Walkinshaw for advice during these years. Special thanks to Dr Chris Mowat for teaching me x-ray crystallography from the very beginning, for travelling together at the various synchrotrons and for always having time for my questions. Thanks you Chris, also for sharing the office and for your good music over the past three years.

I wish to acknowledge Dr Ross Anderson and Miss Sarah Thackray for kinetic and electrochemical studies on tryptophan 2,3-dioxygenase and for providing huge amounts of pure proteins for my crystallographic experiments (Chapters 3 and 4), Dr Katy Drewette for the characterization of flavocytochrome b_2 double mutant (Chapter 5), Mr Davide Papale for his work on nitric oxide synthase G586S mutant (Chapter 6), and Dr Caroline Miles for providing the constructs used in the these two last projects. Furthermore I'd like to thank Miss Laura Campbell for continuing most of the above mentioned projects after me. I wish to thank also the co-authors of the original publications at the Columbia University, Prof Liang Tong and Dr Farhad Forouhar.

Many thanks to all the past and present members of the Chapman, Daff, and Reid groups, who have made the lab a stimulating place to work. I also owe my gratitude to all the people of "Swann 3" for the friendly atmosphere, advice in the lab and with computers.

I'd like to thank Dr Martin Walsh, Dr Hassan Belrhali and Dr Heinz Gut at BM14, ESRF (Grenoble) for beam time allocation and invaluable support during data collection.

I am deeply grateful to Dr Juan-Carlos Fontecilla–Camps, the head of the Laboratory of Crystallography and Crystallogenisis of Proteins (LCCP) in Grenoble for giving me the opportunity to work in his lab during last autumn. I really had great time with people at LCCP. In particular I'd like to thank Mr Xavier Vernede for his help with the diatomic ligand experiments and for teaching me the propane flash-freezing technique. I would like to remember Dr Lilian Jaquamet who has recently died, and to whom is dedicated Chapter 6, because without his encouragement the structure of nitric oxide synthase G586S mutant wouldn't have been solved.

Ringrazio i miei genitori per essermi sempre e comunque vicini in ogni circostanza, nonostante le migliaia di chilometri che ormai ci separano da qualche anno, mia nonna, e la persona a cui voglio piu' bene, mia sorella Sara, con l'augurio che anche se forse non vivremo mai piu' nello stesso Paese, saremo sempre vicine. Un ringraziamento particolare alle mie amiche di sempre, Angela, Roberta e Francesca.

Infine Davide. Senza di te il mondo sarebbe semplicemente troppo grande. Ti dedico la mia tesi, e tu (e solo tu) sai davvero cosa rappresenta per me.

Abstract

This thesis reports the high-resolution structures of four different heme-containing enzymes: two dioxygenases (tryptophan 2,3-dioxygenase and a indoleamine 2,3-dioxygenase), and mutant forms of flavocytochrome b_2 and nitric oxide synthase.

Tryptophan 2,3-dioxygenase (TDO) and indoleamine 2,3-dioxygenase (IDO) belong to an important, but relatively poorly understood, family of dioxygenases. TDO catalyzes the dioxygenation of L-tryptophan to N-formyl kynurenine. This reaction is the first step in tryptophan catabolism. IDO catalyzes the same reaction except with a broader substrate tolerance.

We have solved the x-ray crystal structure of TDO from *Xanthomonas campestris* in the apo-form (at 2.7 Å resolution) and with ferric heme at the active site (at 2.6 Å resolution). Two 1.6 Å and 1.8 Å resolution structures of the catalytically active, ferrous form of the enzyme in binary complex (respectively with the substrate L-tryprophan and with the substrate analogue 6-fluoro-tryptophan) have also been determined. These data allow important insights into substrate recognition, defining the substrate specificity. The structure shows that the enzyme is a tetramer with a heme cofactor and a substrate molecule bound at each active site. A second, possibly allosteric, L-Trp-binding site is also identified at the tetramer interface. The active site is fully formed only in the binary complex, showing that TDO is an induced-fit enzyme with significant structural changes on the binding of substrate.

The structure of TDO in complex with L-Trp revealed that histidine 55 hydrogen bonds to substrate, helping to correctly position it in the active site and possibly being implicated as a catalytic base during the reaction. Histidine 55 was replaced by alanine (H55A) by site-direct mutagenesis. The crystal structure of TDO H55A has been solved to 2.15 Å resolution in a new crystal form, in the presence of the substrate L-Trp. In this different crystal form, the N-terminal region is better defined than in the wild-type TDO. Structural and functional studies on the H55A mutant provide insights into the molecular mechanism established by TDO to control substrate binding to the active site. A structural comparison with wild-type TDO reveals that the point mutation causes only small overall structural changes. Biochemical data suggest that histidine 55 is not essential for turnover but controls the binding of

substrate to the active site. Histidine 55 greatly disfavours the mechanistically unproductive binding of L-Trp to the oxidized enzyme, promoting the productive binding of L-Trp to the reduced enzyme, regulating the binding of dioxygen and allowing precise control of catalysis.

SO4414 from *Shewanella oneidensis,* is a homolog of human IDO, but its natural substrate has not yet been identified. The crystal structure of the reduced form of this putative IDO from *Shewanella oneidensis* was obtained at 2.4 Å resolution. Despite differing in their sequences (they share only 12% sequence identity), a comparison between human IDO and the *Shewanella* homolog reveals great structural similarities, both in terms of the overall protein folding and of the active site design, suggesting that these two enzymes are likely to share a common mechanism.

Flavocytochrome b_2 is an oxidoreductase that catalyzes the oxidation of L-lactate. The flavin-binding and cytochrome domains of flavocytochrome b_2 are connected by a hinge sequence. In order to study the role of inter-domain mobility during catalysis, site-directed mutagenesis was used to engineer a double mutation, asparagine 42 to cysteine and lysine 324 to cysteine (N42C:K324C). Limited domain mobility caused by disulfide-bridge formation affects electron transfer processes in the enzyme. The crystal structure of the N42C:K324C mutant obtained at 3.0 Å resolution confirms the formation of the disulfide bond and validates the kinetics assays.

Nitric oxide synthase (NOS) is a cytochrome P450-like oxygenase that catalyzes the oxidation of L-arginine to form L-citrulline and NO. Characterization of a functional mutant of rat neuronal NOS truncated heme domain ($nNOS_{oxy}$), where glycine 586 was replaced by a serine residue (G586S), led to the detection of a novel reaction intermediate, whose UV spectrum resembles that of the ultimate reactive species of P450 (compound I). The crystal structure of the $nNOS_{oxy}$ G586S mutant determined at 2.6 Å resolution in binary complex with L-Arg confirms the presence of the engineered mutation and suggests a new capability of L-Arg for formation of a supplementary hydrogen bond with the introduced serine 586, thereby stabilising the reaction intermediate,

Abbreviations and units

A. Amino Acids

Both the single and three letter notations are used.

Amino acid	Three letter code	Symbol
Alanine	Ala	A
Arginine	Arg	R
Asparagine	Asn	N
Aspartic acid	Asp	D
Cysteine	Cys	C
Glutamic acid	Glu	E
Glutamine	Gln	Q
Glycine	Gly	G
Histidine	His	H
Isoleucine	Ile	I
Leucine	Leu	L
Lysine	Lys	K
Methionine	Met	M
Phenylalanine	Phe	F
Proline	Pro	P
Serine	Ser	S
Threonine	Thr	T
Tryptophan	Trp	W
Tyrosine	Tyr	Y
Valine	Val	V

B. Kinetic parameters

K_m	Michaelis constant
k_{cat}	Rate constant at saturation
K_d	Dissociation constant
K_{obs}	Observed rate constant

C. Standard units

m	meter	**°C**	degree Celsius	**Hz**	hertz
g	gram	**K**	degree Kelvin	**Ω**	ohm
s	second	**l**	litre		
V	volt	**M**	molar		
Å	Ångstrom	**Da**	Daltons		

D. Other unit abbreviations

s^{-1}	first order rate constant	**ppm**	part per million
$M^{-1}s^{-1}$	second order rate constant	**rpm**	revolution per minute
$M^{-1}\ cm^{-1}$	molar extinction coefficient	**mw**	molecular weight
v	volume	**w**	weight

E. Abbreviations referred to proteins

IDO	indoleamine 2,3-dioxygenase
NOS	nitric oxide synthase
nNOS	neuronal NOS
$nNOS_{oxy}$	oxygenase domain of nNOS
sIDO	*Shewanella Oneidensis* putative IDO
TDO	tryptophan 2,3-dioxygenas

F. Buffers and chemical

4-PI	4-phenil imidazole
5-F-Trp	5-fluoro-D/L-tryptophan
6-F-Trp	6-fluoro-D/L-tryptophan
EDTA	2-[2-(bis (carboxymethyl) amino)ethyl-(carboxymethyl)amino]acetic acid

DMSO	dimethyl sulfoxide
DTT	dithiothreitol
GSH	glutathione
HEPES	4-(2-hydroxyethyl) piperazine-1-ethanesulfonic acid
IPTG	isopropyl-β-D-thiogalactopyranoside
L-Trp	L-tryptophan
L-Arg	L-arginine
MES	2-[N-morpholino] ethanesulfonic acid
NOHA	N^{ω}-hydroxy-L-arginine
PEG	polyethylene glycol
PMSF	phenylmethylsulphonyl fluoride
SDS	sodium dodecyl sulphate
TCEP	Tris(2-carboxyethyl) phosphine hydrochloride
Tris	2-amino-2-hydroxymethyl-propane-1,3-diol

G. Other abbreviations

ESRF	European Synchrotron Radiation facility
FAD	flavin adenine dinucleotide
FMN	flavin mononucleotide
H_4B	(6R)-tetrahydro-biopterin
I	ionic strength
NADH	β-nicotinammide adenine dinocleotide
NMR	nuclear magnetic resonance spectroscopy
OTTLE	optically transparent thin layer electrochemistry
PAGE	poly acrylamide gel electrophoresis
PDB	protein data bank
rms	root-mean-square
SAD	single-wavelength anomalous dispersion
SHE	standard hydrogen electrode
SRS	synchrotron radiation source
WT	wild-type
Vis	visible
UV	ultraviolet

Contents

Chapter 1: Introduction

Chapter 2: Materials and methods

Chapter 3: Structural studies on tryptophan 2,3-dioxygenase (TDO) and indoleamine 2,3-dioxygenase (IDO)

Chapter 4: Crystallographic studies on histidine 55 mutant of tryptophan 2,3-dioxygenase from *Xanthomonas campestris*

Chapter 5: Structural characterisation of the N42C:K324C mutant of flavocytochrome b_2

Chapter 6: Crystallographic studies on rat neuronal nitric oxide synthase heme domain mutant G586S

Chapter 1

Introduction

Introduction

1.1 Bioenergetic pathways

Every living organism on Earth faces the problem of energy transformation and storage. All life processes, including growth, reproduction and locomotion require energy. Energy in nature can be found as light, ion gradients, chemical energy or mechanical energy, but to be utilized by living organisms such forms of raw potential energy require to be converted into a biologically relevant form.

Adenosine triphosphate (ATP) is an immediate source of energy for many cellular functions. Energy can be stored in the high-energy phosphoester bond of ATP and then released in an efficient manner when and where needed.

Under physiological conditions the hydrolysis of ATP to ADP (adenosine diphosphate) + P_i produces about 30.5 $kJmol^{-1}$. ATP hydrolysis is only one of many reactions the cell could have selected to store and generate energy. The hydrolysis of [ATP] is coupled to the dislocation of [ADP] away from [ATP]. Indeed, ATP hydrolysis generates energy through spatial separation of metabolic reactants, because the situation where [ATP] >> [ADP] is far from equilibrium [150].

Respiration, fermentation and photosynthesis form the basis of bioenergetic pathways in all organisms. Through these processes the potential energy generated by ion-gradients, the chemical energy stored in organic molecules and the power of solar energy can be converted to ATP pools. The formation of ATP during fermentation involves the direct transfer to ADP of a phosphate group from a phosphorylated high-energy metabolic intermediate. In respiration and photosynthesis, the potential energy of an electrochemical gradient is converted into ATP. In the two latter pathways the ion-gradient is generated *via* electron-transfer reactions [1]. Electrons are sequentially transferred from an initial donor to a final acceptor over a large difference of potential, via a cascade of oxidation-reduction (redox) reactions.

Such electron-transfer reactions are extraordinary examples of chemical evolution by natural selection to convert energy into a biologically valuable form.

Electron-transfer reactions may involve complex chains of redox species (proteins and cofactors) closely associated with cellular membranes (periplasmic membranes in prokaryotes and membranes of organelles such as mitochondria and chloroplasts in eukaryotes). All electron-transfer processes are mediated by enzymes and coenzymes, many of which are organized in large complexes and consist of several subunits. Such subunits include electron carriers which individually are catalytically active proteins and participate in the overall transfer process because they are closely associated with other proteins.

The electron-transfer process in chloroplasts during photosynthesis shows striking similarities with mitochondrial respiration, both in terms of structural organization and redox partners. While respiration and photosynthesis are perhaps the most complex and important biological redox systems, many other redox proteins are involved in metabolizing and catabolizing organic molecules through oxidation/reduction reactions. Prokaryotic organisms exhibit a great diversity in composition of electron-transfer chains and can utilize a great variety of donor/acceptor couples.

Due to their biological importance, the last decades have seen a growing interest in studying the mechanism and architecture of proteins involved in electron-transfer pathways.

To understand the details of electron-transfer reactions in proteins it is necessary to know their structural arrangement in great detail. The structure of proteins cannot be simply predicted from the amino-acid sequence. Polypeptide chains are organized into a three-dimensional structure and folded into a specific functional shape. The final shape depends on the molecular interactions that each amino acid has with its neighbours, with surrounding water molecules and with other amino acids which are distant in terms of sequence, but that become close as a result of folding. X-ray crystallographic studies of energy transduction proteins and protein complexes can provide information about possible geometries of electron-transfer centres and to determine in a precise and systematic manner the factors that regulate the electron-transfer reactions. Furthermore, three-dimensional X-ray structures of catalytically active proteins are often the starting point for investigating their function.

1.2 Electron-transfer reactions

Electron transfer reactions might be classically described as adiabatic processes: the electrons, considered as particles, need to cross an energetic activation barrier before the formation of the transition state, which subsequently decays into products.

In the quantum mechanical view, the electron is described as a wave function that has a small but real probability of penetrating the energy barrier [2]. In other words, if during a reaction the wave penetrates far enough through the energy barrier to reach the acceptor, the electron that was localized in the donor, will now be localized at the acceptor. Such an event corresponds to the displacement of electrons from the narrow potential energy well of the donor, to the well of the acceptor, moving *through* the energetic barrier rather than *over* it. In quantum mechanics this is defined as "electron tunnelling". Such a view contrasts with the classical transition state theory, where thermal energy (generated by the collision of the reactants) is required to surmount the energetic barrier.

Indeed, the equation which describes the electron transfer between weakly coupled donor and acceptor is not dependent upon temperature, but only on the distance between the redox centres:

$$\mathbf{H^2_{AB} \sim e^{-R}} \qquad \text{(eq. 1.1)}$$

where H_{AB} represents the electronic coupling between the reactants (A and B) and R the distance between them.

When the wave of the donor penetrates the energy barrier of the reaction, the electronic orbitals of the redox centres form an "encounter complex" [3]. In this state the electron is potentially able to oscillate between the two reactants in a resonant process. The resonance vibration depends on the distance (R) and on the relative energy of the wells of the donor/acceptor couple.

In a biological system, donor and acceptor will have a different energy state, enough to break the resonance state and allow the electron transfer to progress to completion.

The system has to satisfy both the Franck-Condon and energy conservation principles. The Franck-Condon principle states that electronic motions occur rapidly compared with the time scale of nuclear transitions [4, 5] . During the transition, if electrons are moving to a new vibration level this new energy level must be instantaneously equal to the nuclear energy configuration.

1.2.1 Marcus theory

The conditions for electron transfer, taking the Franck-Condon and energy conservation principles into consideration, have been described by Marcus both in classical and quantum mechanistic terms [6, 7].

The energy configurations (U) of both reactants and products can be represented by a parabola plotted against the reaction coordinate (fig 1.1). Both the profiles (reactants in blue and products in black) display an energy minimum. Given that reactants and products have different minimum energy configurations, the transfer must occur at the intersection represented in fig 1,1, where the nuclear configurations are isoenergetic (Ur=Up). The potential energy minimum of the products (black parabola) is shifted to a more negative level (ΔG), than that of the reactants and the difference between these is the free energy of the reaction. The variation between the energy state before and after the electron transfer described by the ΔG represents also the driving force of the reaction and corresponds to the total Gibbs free energy change for the electron-transfer reaction.

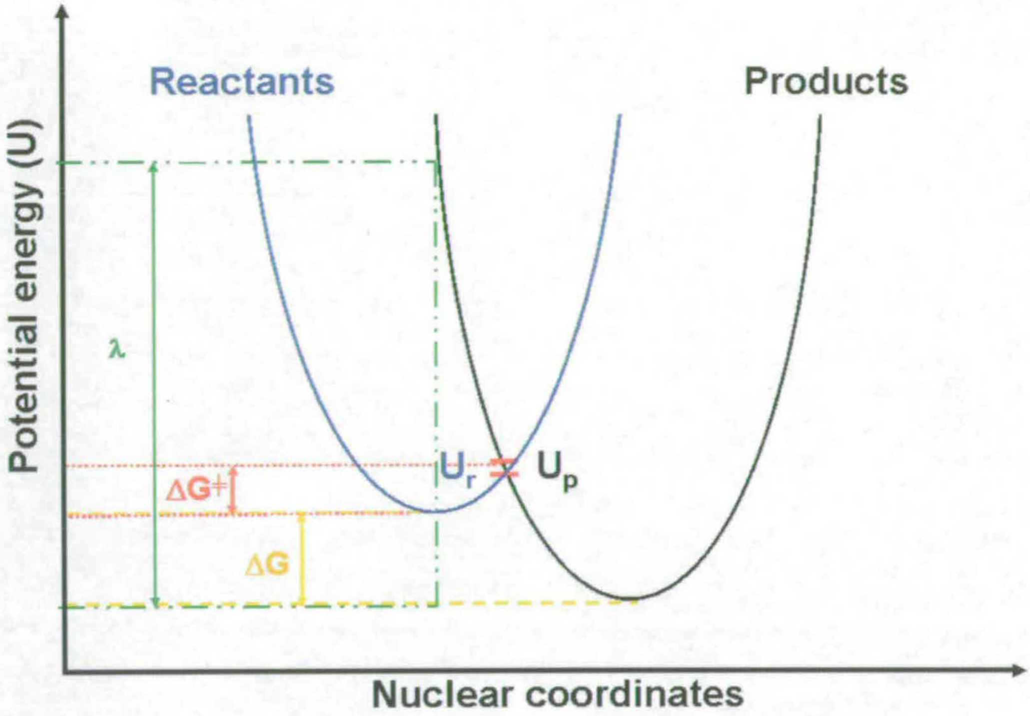

Fig 1.1: Potential energy diagrams during electron transfer: energy surfaces for the Reactants and Products state along the reaction. The parabola represents a many-dimensional potential surface of the reactants plus surrounding medium (Reactants) and that of products plus medium (Products). (λ: reorganization energy $\Delta G^{\ddagger}$: activation energy ΔG: free energy).

To satisfy the Franck-Condon principle, the transfer will only occur at fixed positions and momenta of the atoms, and because the potential energy of the reactants (Ur) equals the potential energy of the products (Up) at the intersection of the reactants and products surfaces, energy is also conserved.

The energy required for all geometrical adjustments, which are needed in order that reactant and product assume the configuration required for the transfer of the electron, is the reorganization energy λ. Reorganization energy can be illustrated as the energy gap between the bottom of the energy profile of the product up to the interception with the energy profile of the product in the same nuclear configuration as the energy minimum of the reactant (fig 1.1).

Marcus theory provides a relationship between the free energy of activation $\Delta G^{\ddagger}$ and the standard free energy change ΔG of a chemical reaction. In electron-transfer reactions $\Delta G^{\ddagger}$ is the activation energy required to bring the electrons to the energy level at the intersection of the two potential energy surfaces. Upon activation, the reaction can occur and then the reactants return to a lower energy state. The activation energy $\Delta G^{\ddagger}$ is related to the driving force ΔG and to the reorganization energy λ by the equation:

$$\Delta G^{\ddagger} = (\Delta G + \lambda)^2 / 4\lambda \qquad \text{(eq. 1.2)}$$

In quantum theory interpretation of electron transfer, the energy potential curves are simple harmonic oscillators, where only some energy levels are permitted: these levels correspond to the frequency of the oscillator ($h\omega$). In this case the transfer depends upon the overlap of the harmonic oscillator wave functions of the two reactants.

1.2.2 Electron-transfer rate

In the adiabatic case, the electron-transfer rate depends on the activation energy according to the equation:

$$k_{ET} = \kappa \exp -(\Delta G + \lambda)^2 / 4\lambda\, k_B T \qquad \text{(eq. 1.3)}$$

where k_{ET} represents the observed electron-transfer rate, κ is the electron-transfer rate when ΔG^0 is zero (maximum rate electron transfer) and k_B the Boltzmann constant and T is the absolute temperature.

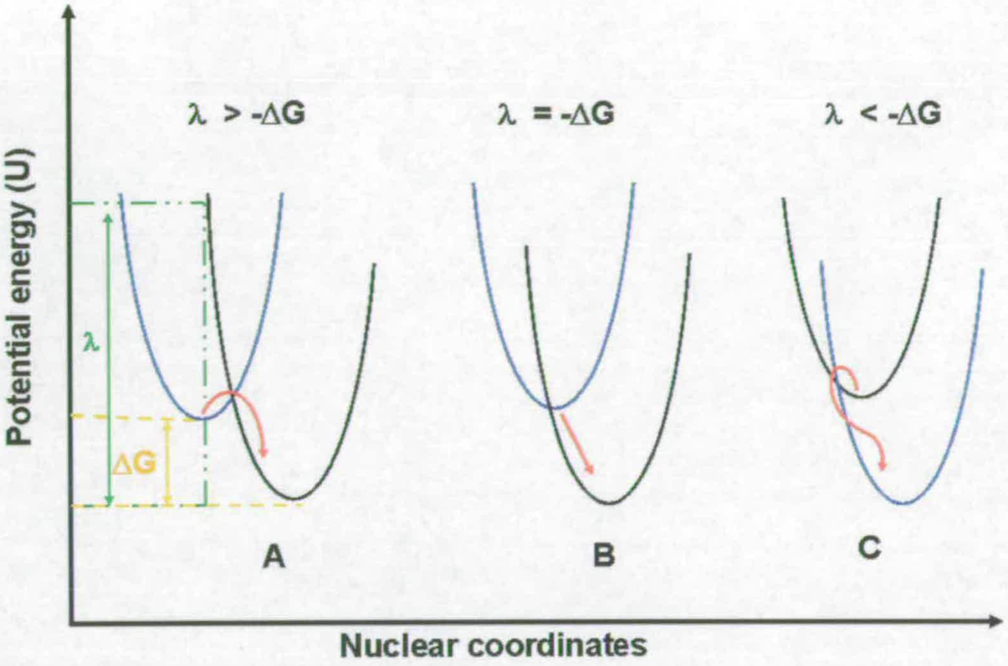

Fig 1.2: A diagram of the nuclear potential energy (free energy) vs nuclear coordinates. The potential well of the reactants is shown in black and that of the products is shown in blue. Case (a) is the 'normal' region for electron transfer, (b) is 'activationless' electron transfer and (c) electron transfer in the 'inverted' region.

(λ: reorganization energy ΔG_0: activation energy ΔG: free energy)

Three possible cases can be observed:

1) *Normal region* (fig 1.2a): when $\lambda > -\Delta G$, which means $\Delta G + \lambda > 0$
2) *Activationless* region (fig 1.2b): when $\lambda = -\Delta G$, which means $\Delta G + \lambda = 0$

   the barrier for electron transfer is zero and $k_{ET} = \kappa$
3) *Inverted region* (fig 1.2c): when $\lambda < -\Delta G$, which means $\Delta G + \lambda < 0$

   When the driving force ΔG increases, the activation energy increases and leads to slowing the electron-transfer rate. The electron-transfer rate variation is illustrated in fig 1.3.

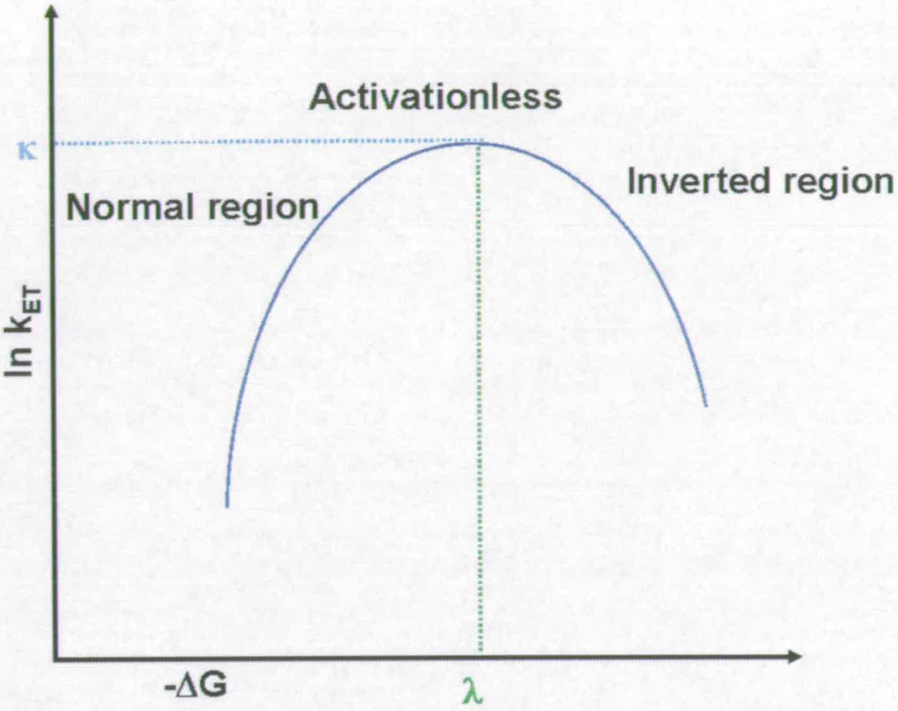

Fig 1.3: Parabolic dependence of ln k_{ET} *on energy variation* ΔG. *ln* k_{ET} *reaches a maximum where* $-\Delta G = \lambda$, *and decreases where* $-\Delta G > \lambda$ *(inverted region).*

In the quantized view the dependence upon temperature (T) of the electron-transfer rate in equation (1.3) is not allowed and T is replaced by the quantum energy of the oscillator, $h\omega$.

The factors that control electron movement are influenced by the space separating the donor and the acceptor, not only in terms of the distance between the reactants, but also in terms of the medium which contribute to propagating the transfer. The decay of the electron-transfer rate due to the medium is related to the distance by the equation:

$$\kappa \propto e^{-1/2\beta R} \qquad \text{(eq. 1.4)}$$

where β (expressed in Å^{-1}) is the coefficient which describes the decay through the medium and R is the travelling distance of the electron.

To summarize, electron-transfer theory states that electron-transfer rates are determined by two factors: the thermal oscillation necessary to take reactants and products to isoenergetic states and the probability of electron tunnelling between these isoenergetic states. The thermal oscillation depends on the contribution of the environment to the electron charge. The electron tunnelling probability is determined by the chemical nature and by the structure of the electron-transfer elements. Theoretical and experimental investigations over the last 20 years have confirmed the dependency of electron tunnelling reactions on both the distance between the electron donor and acceptor and the nature of the molecular bridge separating the reactants [8-11].

1.3 Biological electron transfers

In biological systems some electron-transfer reactions can move electrons 10 Å and more between redox cofactors [12]. The composition of the propagating medium between donor and acceptor, and the primary, secondary, and tertiary structures of the insulating protein, all together contribute to determining the rate of electron transfer [10]. Two major theories predict the most likely routes that electrons take through electron-transfer proteins:

1) The through-bond electron-transfer theory considers that the interactions between the donor and acceptor sites are mediated by covalent bonds or hydrogen bonds interconnecting these sites. The electron transfer is then happening between cofactors through insulating protein [13].
2) The through-space electron-transfer theory describes the electronic transfers as depending on direct orbital overlap between the donor and acceptor sites.

In biological systems the value of the decay coefficient (β) is much higher *in vacuo* ($\beta = 2.9 - 4.0$ Å^{-1}) [14, 15] than in a protein matrix ($\beta = 1.2 \pm 0.2$ Å^{-1}). The polypeptide chain surrounding the redox centre clearly facilitates electron transfer, which is occurring faster than *in vacuo* and at comparable values to synthetic bridges (like homogeneous organic glass) [16].

There has been much debate surrounding the routes that electrons follow through electron-transfer proteins. Indeed, both theories of through-bond and the through-space electron transfers are supported by experimental evidence, although they both agree on the contribution of the polypeptide chain on facilitating electron-transfer rates [10, 17, 18].

In fact, electrons move much slower if they tunnel through empty space. However the through-space path can actually be optimal if it enables electrons to take shortcuts. That means that electrons may sometimes "jump" through space, because this alternative route can be shorter (fig 1.4).

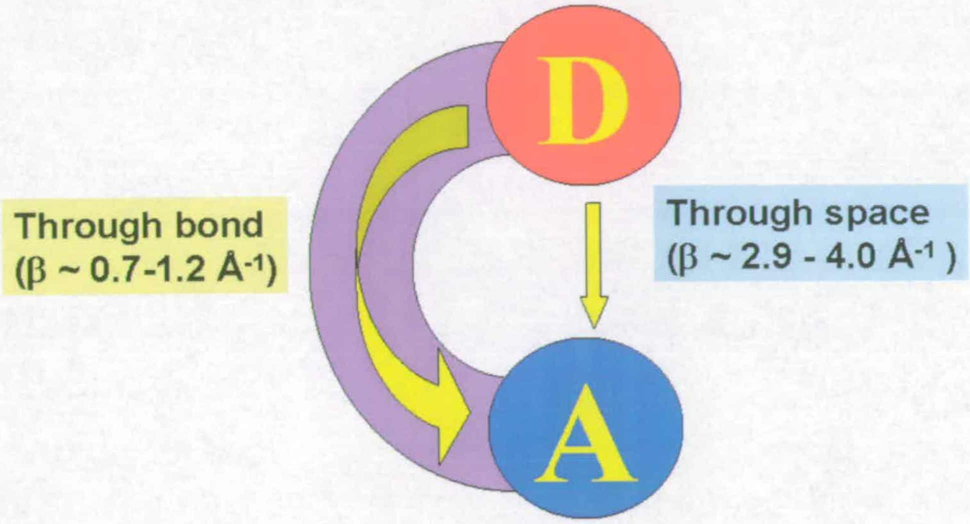

Fig 1.4: Through bond and through space electron transfer. D: electron donor A: electron acceptor

Moser and Dutton [14] suggested that natural selection has favoured electron-transfer in proteins where the distance between redox centres is within 14 Å. According to equation 1.4, the electron-transfer rate decreases exponentially with distance. Furthermore they suggested that the polypeptide structure acts as a low-energy route through bonds and atoms for productive electron tunnelling, while *vacuum* space is shown to be effectively a barrier. They assign a general value for λ (reorganization energy) and β (decay coefficient), both calculated on the average of the whole electron-transfer centre and protein.

Metal-labelling techniques [8] have introduced another tool for experimentally investigating electron transfer within biological systems. Through this technique it is possible to measure the electron-transfer rates of Ru-labelled proteins, such as cytochrome *c*, cytochrome b_{562}, myoglobins and iron proteins [19]. Shining laser light on these Ru-modified proteins allows monitoring the movement of electrons in great detail. Using such a technique, together with combined quantum mechanical and classical calculations, Beratan and co-workers [19] were able to capture electron pathway fluctuations. For Beratan and co-workers, in the three-dimensional arrangement of electron-transfer protein, several diverse and discontinuous tunnelling pathways between donor and acceptor can be identified. This means in other words that electron-transfer proteins actually evolved their shapes to allow electrons the alternative of using quantum rules, to pass through molecular folds and gaps.

The effect of distance on productive electron tunneling is clear and dominant in all the theories describing electron transfer. Indeed, the distance ranging from van der Waals contact to 14Å accommodates over 95% of distances between cofactors performing efficient electron transfer through protein. However, new studies on electron-transfer rates between heme centres within cytochrome bo_3 and in a heme-copper oxidase [20] demonstrate that tunneling medium might be heterogeneous and this can also influence the rate of the transfer.

A multi-pathway view, governed by quantum mechanistic rules, seems at the moment the most realistic interpretation of electron-transfer reactions [21]. Although how often and where nature has evolved specific or multiple pathways routes for electrons remains to be established, all the latest studies agree that atomic resolution structural details of electron-transfer proteins will be essential to fully understand electron-transfer mechanisms [22].

1.4 Electron-transfer proteins

All biological macromolecules have evolved through a selective pressure to perform their specific function. Although electron tunnelling can productively occur through peptide bonds, nature has selected much more efficient redox elements. Redox centres are often built around metal ions or aromatic groups (e.g. nicotinamide, flavins) which can exploit a wide range of reduction potentials. Electron-transfer proteins are characterized by redox centres that facilitate rapid and efficient electron transfer with the minimum structural change for the protein.

Biological electron-transfer systems are normally classified on the basis of the chemical structure of the prosthetic group and the manner of its attachments to the protein. Redox proteins include heme-binding proteins, metalloproteins (such as iron [23], copper [24], molybdenum [25] , and nickel proteins [26]) and flavoproteins [27].

1.4.1 Metal centres

Modulated by the protein environment, the redox properties of metals are used to catalyze a great variety of biological reactions. Electron-transfer proteins generally have metal coordination sites which serve to tune the reduction potential of the metal. Furthermore, the reorganization energy (λ) (see section 1.2.1) and structural changes resulting from oxidation/reduction reactions are minimized. Two representative examples of redox metallo-proteins are iron-sulfur proteins and blue copper proteins.

Iron-sulfur [Fe-S] clusters play a crucial role in many biochemical pathways, including respiration, photosynthesis, and amino acid biosynthesis.

Iron-sulfur clusters mediate a single electron transfer oscillating between ferric (Fe (III)) and ferrous (Fe (II)) oxidation states and are classified according to the number of iron ions in the prosthetic centre. Examples of these include rubredoxin [1Fe-1S] [28], ferredoxins [2Fe-2S] that contain two iron atoms and two inorganic sulfides coordinated to four cysteine residues [29], feredoxins [4Fe-4S] that contain four iron atoms, four inorganic sulfides, coordinated to the protein in a distorted tetrahedral geometry through four cysteines [30]. High-redox potential 4Fe-4S ferredoxins (HiPIPs) form a family of iron-sulfur proteins that function in anaerobic electron transport chains. Fig 1.5 shows examples of these three different types of Fe-S clusters.

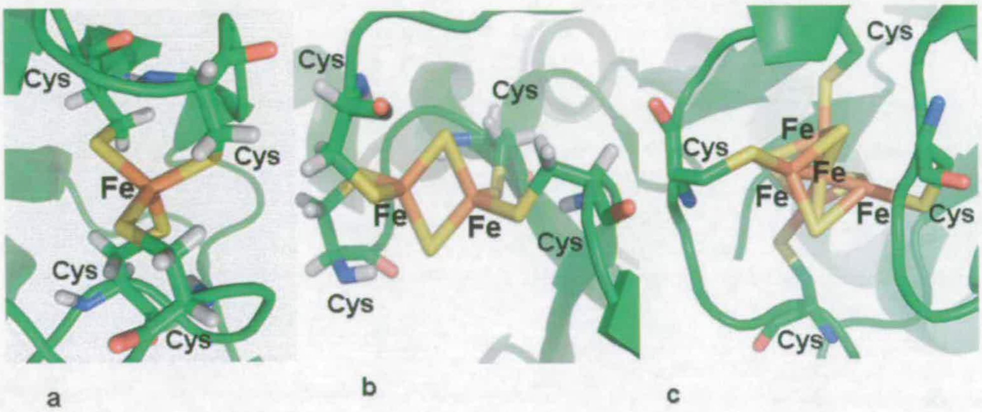

Fig 1.5: Iron-sulfur cluster centres. Iron is bound to the protein by the sulfur atoms of cysteine residues.
a) Crystal structure of rubredoxin from Clostridium pasteurianum showing a [1Fe-1S] cluster (PDB entry 4RXN) b)[2Fe-2S] ferredoxin-like cluster from Halobacterium salinarium (PDB entry 1E0Z) c) [3FE-4S] cluster ferredoxin from Azotobacter vinelandii (PDB entry 1FDD)

In the case of copper-binding proteins the metal is often held by the protein matrix in a pseudo tetrahedral arrangement, which in this case represents a compromise between the copper geometries for Cu^{2+} (Cu (II)) (which prefers square planar geometry) and Cu^{1+} (Cu (I)) (which prefers tetrahedral geometry).

Azurin belong to the class of blue copper proteins, so called because of their remarkable blue colour ($\lambda_{max} \sim 600$ nm). A single copper atom is bound in their active sites. Common to all mononuclear type sites of copper binding proteins is the presence of three firmly binding residues, two histidines and a cysteine. The strong colour originates from the charge transfer between the Cu atom and the S of the cysteine ligand.

The crystal structure of azurin [24] (fig 1.6) shows a very irregular tetrahedral coordination sphere comprising two sulfurs from methionine and cysteine, and two nitrogens from the histidines. Such an irregular and high energy arrangement at the Cu centre in azurin corresponds to the entatic state between the tetrahedral and square planar geometries configurations of the two oxidation states of Cu and allows enhanced rates of electron transfer.

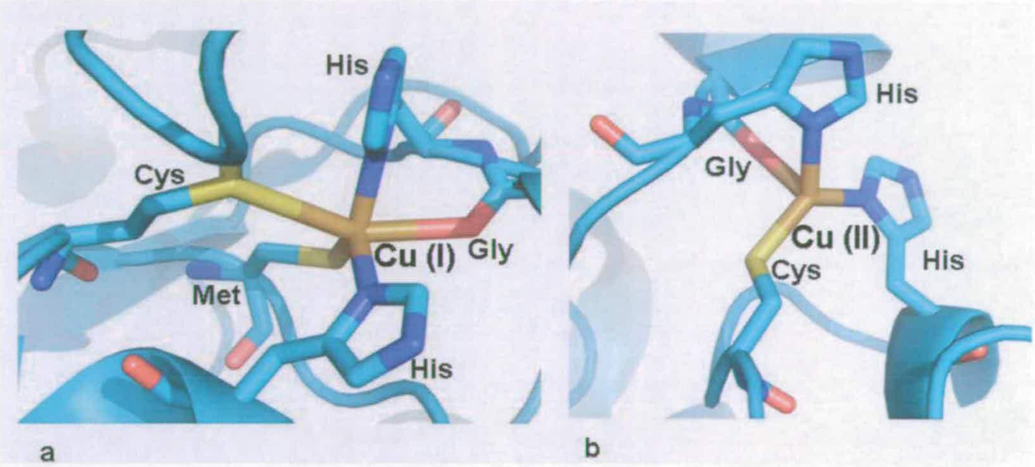

Fig 1.6: Azurin copper centre a) Pseudomonas aeruginosa reduced azurin (Cu (I)) (PDB entry 1JZG) b) Pseudomonas aeruginosa oxidized azurin (Cu (II)) (PDB entry 1JZF)

1.4.2 Flavin

Flavins are compounds containing the 6,7-dimethylisoalloxazine ring. In nature they occur as flavin adenine dinucleotide (FAD) or flavin mononucleotide (FMN) where the isoalloxazine ring is attached to a phosphorylated ribityl chain (fig 1.7).

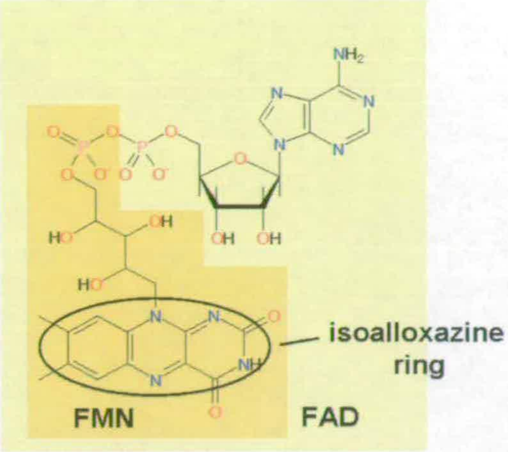

Fig 1.7: The structures of the oxidized forms of the coenzymes FAD (whole figure) and FMN (orange background).

The isoalloxazine ring functions as a redox cofactor, and can exist in three different redox states. These are flavoquinone (fully oxidized), flavosemiquinone (one electron reduced, half-reduced) and flavohydroquinone (two electrons reduced, fully reduced) (fig 1.8).

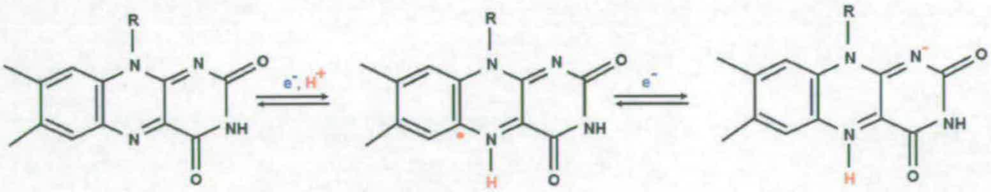

Fig 1.8: The electronic structures of the reduced and semiquinone flavin. The three different redox states of FMN; fully oxidized (quinone), one-electron reduced (semiquinone), and two-electron reduced (hydroquinone).

Flavins are therefore able to take part in mechanisms involving single electron-transfer reactions (flavoquinone is converted to flavosemiquinone or the flavosemiquinone to flavohydroquinone), but also in two-electron-transfer reactions (the flavin oscillates back and forth between flavoquinone and flavohydroquinone). Although free flavosemiquinone is chemically unstable and the addition of two electrons would be preferred, the semiquinone species is stabilized by the properties of the surrounding protein.

1.4.3 Hemes

Heme-proteins are metalloproteins containing one or more heme prosthetic groups, which may or may not be covalently bound to the polypeptide chain. The heme group is a porphyrin and consists of an iron atom coordinated in the centre of four pyrrol rings; these four rings are linked by bridging groups in a planar geometry.

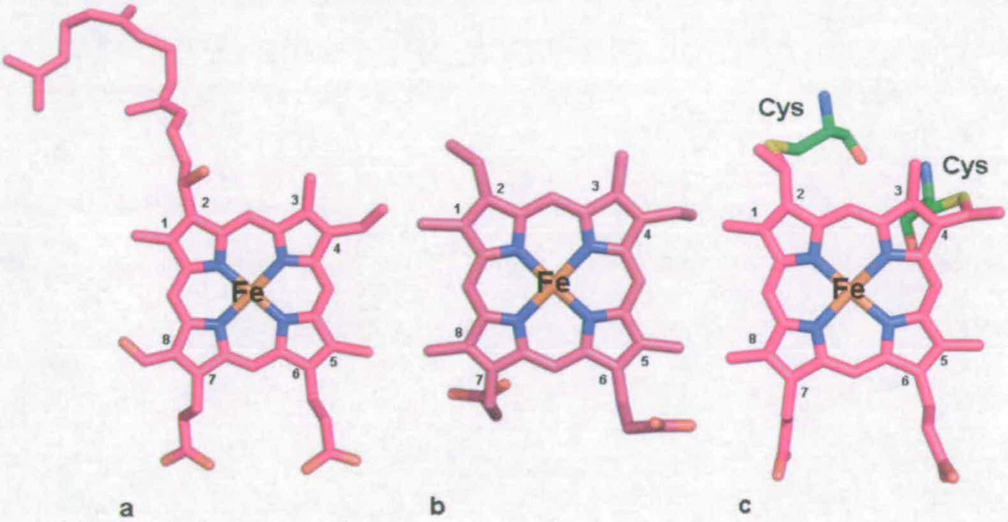

Fig 9: Hemes commonly found in biological systems. Heme a (a); heme b (b); heme c (c)

The most common hemes found in proteins are: heme *b*, heme *c* and heme *a* (fig 1.9):

1) Heme *b* (also termed protoheme IX or iron-protoporphyrin IX) shows four methyl groups in positions 1, 3, 5 and 8; at position 2 and 4 are two vinyl groups, while in position 6 and 7 two propionates (fig 1.9b).

2) Heme *c* is covalently bound to the protein matrix via thioether linkages of the vinyl groups in position 2 and 4 with the sulfhydryl portion of cysteine residues (fig 1.9c).

3) Heme *a* has a hydroxyethylfarnesyl side chain in position 2 of the protoporphyrin ring and a formyl group at position 8 (fig 1.9a).

Heme-proteins can perform an impressive variety of biological functions including electron transfer, redox reactions catalysis and diatomic gas transportation and storage. The heme iron can normally adopt two oxidation states, Fe (II) and Fe (III), but the Fe (IV) oxidation state has been found in some systems as a reaction intermediate [31].

Indeed, the oxidation state of the iron plays an essential part in the roles of the heme proteins, but such proteins display great functional diversity due to variation of the protein environment around the heme. The heme iron atom has two coordination sites not occupied by the porphyrin macrocycle, and the reactivity of the cytochrome and the heme iron reduction potential is strongly related to the number and the nature of the ligands that ligate iron axial sites.

Penta-coordination is generally found in enzymes and globins (fig 1.16) [32]. For catalytically-active enzymes the heme requires an available coordination site for substrate binding, and in globins the sixth position remains free for diatomic gas coordination.

In contrast, electron-transfer proteins need to minimize the reorganization energy at the heme centre during electron transfer so the coordination sphere of the iron centres is invariably saturated and hexa-coordinated. The axial ligands can be two histidines [33, 34] (fig 1.10 and fig1.15), histidine and methionine (fig 1.12) [35], and rarely two methionines [36], or histidine and asparagine (fig 1.11) [37].

The nature of the axial ligands also affects the spin state of the heme iron: the iron will generally be high-spin when penta-coordinated or hexa-coordinated with a water molecule, while coordination of CO, NO, O_2 or CN^- as a sixth ligand will lead to a change to low spin.

1.5 Redox proteins

Two main categories of redox centres can be distinguished. These are, 1) electron-transfer sites, and 2) sites that catalyze oxidation-reduction reactions upon substrate molecules.

The first group mainly consists of cytochromes (section 1.3.2.1).

The second group comprises several different protein types. These include globins, which are heme-proteins, mainly implicated in diatomic gas binding and transportation (section 1.3.2.3), and also oxidoreductases. Oxidoreductases such as cytochrome P450 (section 1.3.2.4.1), nitric oxide synthase (section 1.3.2.4.2), heme oxygenases, indoleamine 2,3-dioxygenase, and tryptophan 2,3-dioxygenase (section 1.3.2.4.3) are involved in the enzymatic transformation of markedly different substrates. Flavocytochrome b_2 (section 1.3.2.5) is an oxidoreductase involved in aerobic respiration in yeast.

1.5.1 Cytochromes

Cytochromes are broadly called proteins that contain one or several heme groups and carry out electron transport or catalyze reductive/oxidative reactions [38]. Cytochromes have been localized in eukaryotes (in the mitochondrial inner membrane [33] and in the endoplasmic reticulum [39]), in plants (in the chloroplasts [40]), in photosynthetic microorganisms [41], and in bacteria [37, 42-46]. Indeed, proteins of obviously different functions are found in this family. A structural classification can be followed for cytochromes, after the type of the porphyrin bound or enclosed by the protein and further by sequence similarity [38].

1.5.1.1 Cytochromes *b*

Cytochromes *b* contain a *b*-type heme group and are mainly involved in enzymatic processes or as components in electron-transfer systems. The best known examples of cytochromes *b* are cytochromes b_5, which are electron transport proteins found ubiquitously in nature. The microsomal and mitochondrial cytochromes b_5 are membrane associated, while those from prokaryotes or from other animal tissues are soluble.

Flavocytochrome b_2 is a tetrameric L-lactate dehydrogenase found in backer's yeast (*Saccaromyces cerevisiae*) which is localized in the intermembrane space of mitochondria. Flavocytochrome b_2 shows a bis-His coordinated heme. Flavocytochrome b_2 will be described in more detail in section 1.5.5 and chapter 5.

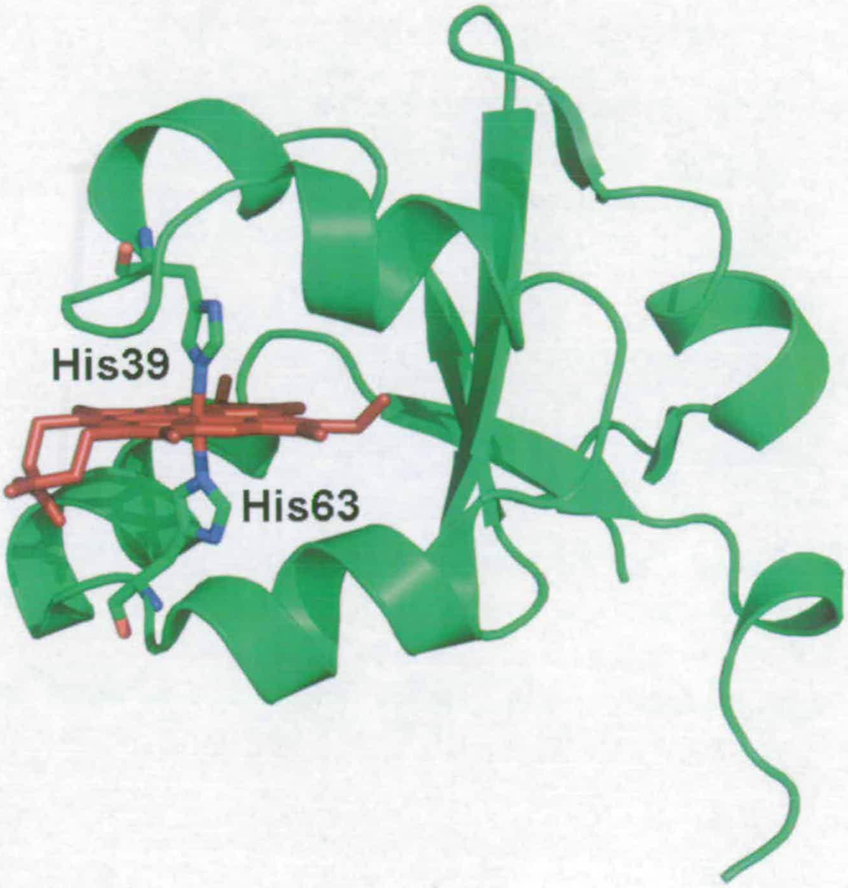

Fig 1.10: Rat outer mitochondrial membrane cytochrome b_5 (PDB entry 1ICC). The heme group is represented using sticks and coloured dark red. The two histidines (His39 and His63) ligating the heme are also represented as sticks coloured by element (colour code: green = carbon, red = oxygen, blue = nitrogen) [33].

Cytochromes P450 and nitric oxide synthases represent two special classes of cytochromes *b*, which will be described respectively in section 1.5.4.1 and section 1.5.4.2 of this chapter.

1.5.1.2 Cytochromes *c*

Cytochromes *c* contain a heme which has at least one thioether bridge between the vinyl group(s) of the porphyrin and the cysteine(s) of the protein. The cysteines (Cys) are provided by the characteristic sequence motif Cys-X-X-Cys-His, where the histidine (His) represents the fifth ligand to the iron [47].

This class of cytochromes has been reported in all living organisms, but prokaryotes show the highest degree of diversity [48].

Cytochromes *c* can be classified into six groups, based on their three-dimensional arrangement [49]:

1) Class I cytochromes *c* have an entirely alpha helical fold, with three conserved helices enclosing the heme group. In such fold, one edge of the heme remains exposed to the solvent. This class comprises the soluble cytochromes *c* of mitochondria and cytochrome c_2 from *Rhodobacter sphaeroides.* The covalent attachment sites to the heme are localized close to the N-terminus of the protein, while the sixth axial ligand is localized in the C-terminus portion and is generally a methionine. An exception to this rule has been reported in s*phaeroide*s heme protein (SHP), where the sixth ligand is an asparagine [50] (fig 1.11).

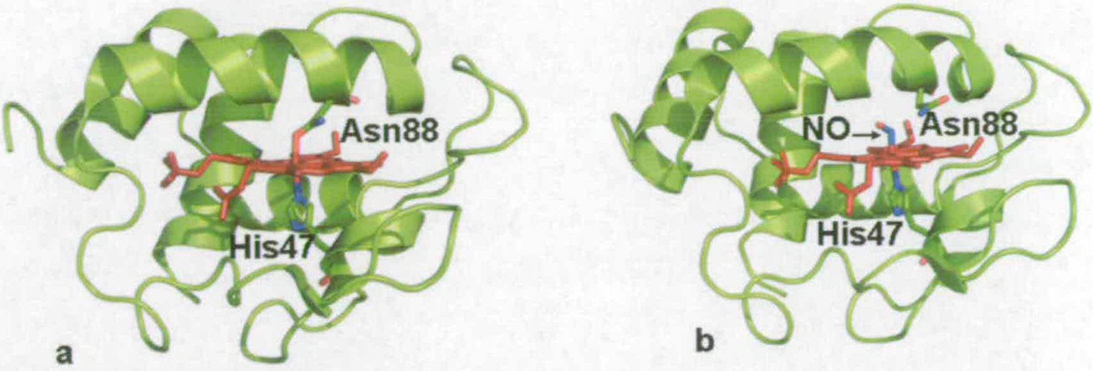

Fig 1.11: Crystal structures of the oxygen-binding cytochrome c from Rhodobacter sphaeroides heme protein (SHP). a) Oxidized SHP (PDB entry 1DW0), b) Reduced SHP in complex with nitric oxide (PDB entry1DW2). The hemes are displayed as sticks and coloured dark red. Residues of interest are shown in stick models and coloured by element element (colour code: green = carbon, red = oxygen, blue = nitrogen)[51].

2) Class II cytochromes *c* have a four alpha helical bundle fold, with the heme attachment site near to the C-terminus [52]. This class includes the high-spin histidine-ligated cytochromes *c′* (which are electron transport proteins broadly distributed in photosynthetic and aerobic bacteria) and the low-spin methionine ligated cytochromes, such as cytochrome c_{556} (fig 1.12).

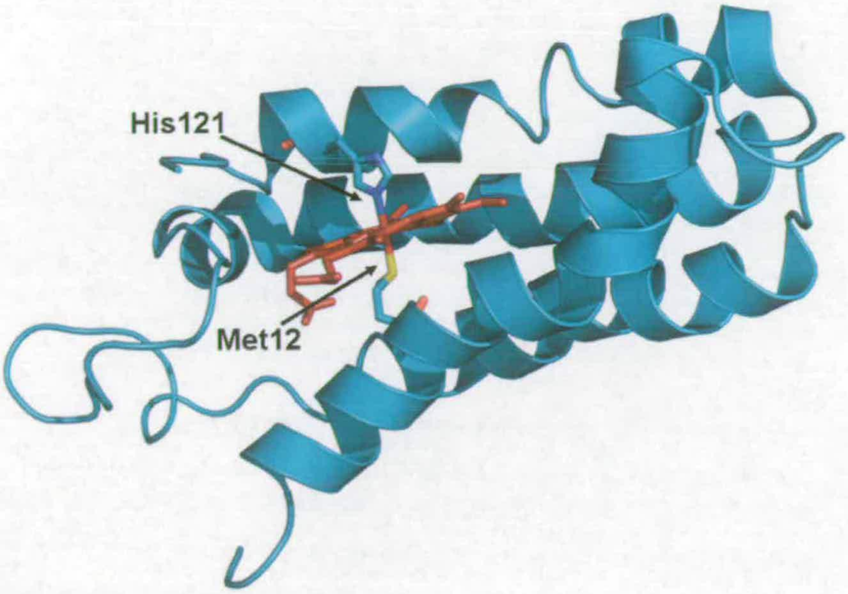

Fig 1.12: NMR model of oxidized R. palustris cytochrome c_{556}*. The heme is displayed as sticks and coloured dark red. Met12 and His121, ligating the heme, are shown in sticks and coloured by element (colour code: blue-green = carbon, red = oxygen, blue = nitrogen)*[35] *(PDB entry 1SO5).*

3) Class III cytochromes *c* display a low amino acid:heme composition, with only 25-40 amino acids per heme. This class includes the low reduction potential (0 to -400 mV), bis-histidine ligated multiheme cytochromes *c*. Multiheme cytochromes (fig 1.13) have been found in several bacteria, but in particular in the *Desulfovibrio*, *Geobacter*, and *Shewanella* genera where, they play important roles in bioenergetic pathways [44, 53-55].

Fig 1.13: Crystal structure at 2.2 Å resolution of octaheme cytochrome c from Shewanella oneidensis. The *eight heme groups are displayed in the stick representation and coloured dark red (PDB entry 1SP3)*[55].

4) Class IV initially comprised all the proteins containing other prosthetic groups together with the heme *c*, such as flavocytochrome *c* and cytochromes *cd*. Now this class includes only tetraheme proteins, which contains both bis-histidine and histidine-methionine coordinated hemes [56].

5) Class V includes several recently characterized cytochromes *c*, which have no structural homology but share similarities in the distribution of clusters of paired hemes. Such an arrangement is thought to be relevant for the type of electron-transfer processes, in which all of the proteins belonging to this group are involved. This class includes cytochrome c_1 and cytochrome *f*, which function as electron carriers in photosynthetic process, hydroxylamine oxidoreductase ((HAO) which

contains eight covalently bound hemes [57]), and the tetraheme c_{554} from *Nitrosomonas europaea*, pentaheme cytochrome c_{552} from *Sulfurospirillum deleyianum*; and the flavocytochrome c_3 fumarate reductase from *Shewanella* species (fig 1.14) [58].

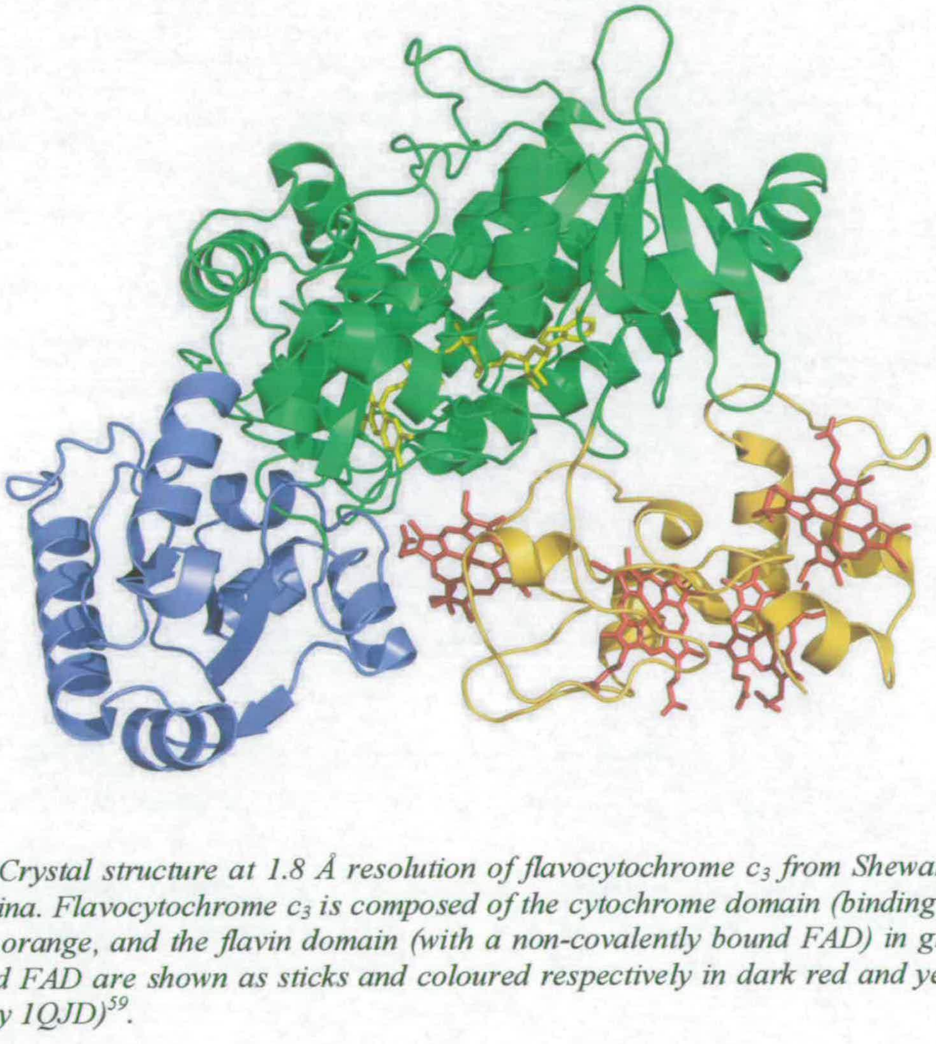

Fig 1.14: Crystal structure at 1.8 Å resolution of flavocytochrome c_3 from Shewanella frigidimarina. Flavocytochrome c_3 is composed of the cytochrome domain (binding four hemes) in orange, and the flavin domain (with a non-covalently bound FAD) in green. Hemes and FAD are shown as sticks and coloured respectively in dark red and yellow (PDB entry 1QJD)[59].

6) In addition to the above classes, there are several cytochromes *c* that cannot be assigned to any of the above groups. Examples includes the decaheme cytochromes *c* from *Shewanella oneidensis* [61], and the diheme cytochromes *c* from *Pseudomonas*

aeruginosa [60] *Rhodobacter sphaeroides* (fig 1.15) and *Rhodobacter adriaticum* [62].

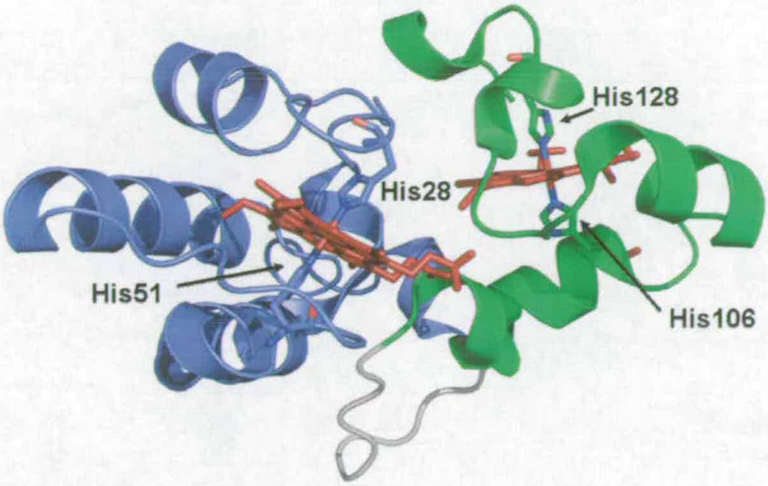

Fig 1.15: Crystal structure of the diheme cytochrome c (DHC) from Rhodobacter sphaeroides at 2.0 Å resolution. DHC is arranged into two domains each containing one heme. The N-terminal domain (in blue) is a class I cytochrome c, while the C-terminal domain (in green) constitutes a novel cytochrome c structural motif. The hemes (both bis-His coordinated) are displayed as sticks and coloured dark red (PDB entry 2FW5) [63].

1.5.2 Flavocytochromes

Electron-transfer proteins can contain more than one redox-active prosthetic group. Flavocytochromes contain both flavin and heme. The association of these two cofactors results in enzymes with great catalytic versatility. This class of proteins can be involved in a wide range of redox processes, from simple electron transfer to oxidation and reduction of organic molecules, or activation of molecular oxygen.

This is the case for P450s (section 1.5.4.1 in this chapter), NOSs (section 1.5.4.2 in this chapter) and yeast L-lactate dehydrogenase, also called flavocytochrome b_2 (section 1.5.5 in this chapter). Flavocytochromes can be very different in reactivity, but nevertheless share some recurrent features in their structural arrangement. Typically, the reductase and oxidase domains are organized in two distinct regions connected via a linker peptide (the larger of these subunits contains the FMN and the smaller the heme(s)). This common architecture does not necessarily correlate with a common function, but the modulation of substrate and cofactor reactivity and the exact positioning of the substrate are key elements in the mode of action of these enzymes.

1.5.3 Globins

Globins are heme proteins involved in diatomic gas binding and transportation. This large protein family embraces vertebrate hemoglobin and myoglobin, but also invertebrate globins and fungal and bacterial flavohemoglobins. Almost all globins contain *b*-type heme, axially coordinated by a histidine side chain. The globin three-dimensional structure is all alpha-helical (fig 1.16a). Their characteristic and evolutionarily-conserved six α-helical fold also contributes to preventing rapid oxidation of the heme iron. However, globins are capable of reversibly binding O_2 to the Fe (II) heme (fig 1.16b) and such binding results in a transition from high-spin to low-spin state of the heme iron. All the globins originate from a common protoglobin ancestor, which held a globin-type fold but functioned as redox protein [64, 65] . When dioxygen became available in the atmosphere, globins evolved their dioxygen binding properties to finally reach their present function.

Bacterial flavohemoglobins [66] contain a heme binding region enclosed in the classical globin fold, associated with a FAD-containing NADH dependent reductase extension. Like most the eukaryotic globins, the heme in flavohemoglobins is five-coordinated through a histidine.

Interestingly myoglobin and hemoglobin were the first two proteins to have their structures determined by x-ray crystallography [67, 68].

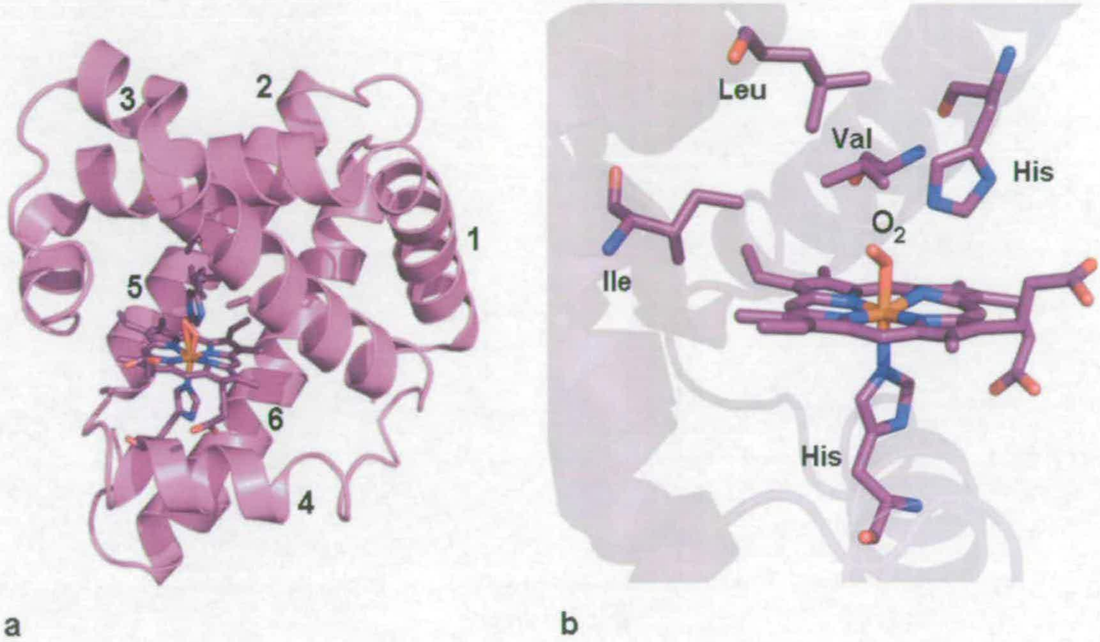

Fig 1.16: Crystal structure of sperm whale oxymyoglobin at 1.6 Å resolution (PDB entry 1MBO[32]*). The heme is displayed as sticks. Residues of interest are also shown in stick models and coloured by element (colour code: nitrogen blue, oxygen red and carbon purple)*

a) Characteristic six helical fold of myoglobins (helixes numbered 1 to 6)

b) Detail of the active site, showing oxygen bound to the heme

1.5.4 Oxygenases

Oxygenases are heme containing enzymes that catalyze the incorporation of one or both atoms of molecular oxygen (O_2) into their substrate. They can be distinguished as two types, dependent on their reaction mechanism. Monooxygenases (such as P450s and nitric oxide synthases) incorporate a single atom from O_2 and dioxygenases (such as tryptophan 2,3-dioxygenase and indoleamine 2,3-dioxygenase) incorporate both atoms of dioxygen.

The activation of molecular oxygen is a crucial process for every aerobic organism. Molecular oxygen has a low reactivity with organic substrates because it exists as a triplet in its ground state. Thus, oxygenases are able to activate oxygen and catalyze oxygen incorporation into various substrates, and their importance has been recognized in the biosynthesis and transformation of steroids, prostglandins and amino acids, and also in the metabolism of drugs and xenobiotics.

1.5.4.1 Cytochromes P450

Cytochromes P450 (P450s) are a diverse superfamily of enzymes, so called after the peak at 450nm in the visible spectrum when CO is bound to the ferrous form of the enzyme [69]. They all contain a *b*-type heme, axially coordinated through the thiolate side chain of a conserved cysteine residue, and are present in a wide range of organisms including mammals, insects, molluscs, plants, fungi and bacteria [70].

P450s catalyze the mono-oxygenation of a broad variety of organic molecules. Although it has been more than 50 years since the identification of the first cytochrome P450 [71] the interest in this family of proteins is still increasing. This is due to their involvement in a number of reactions of great biological significance, including oxidation of drugs, steroid transformation, pro-carcinogen activation, detoxification processes and fatty acid metabolism [72].

Electron transfer represents a crucial step in P450 function. In fact, P450s can be classified into two main groups based on the redox partners that donate electrons during their catalytic cycle (fig 1.17):

1) Class I P450s (found in the mitochondrial membrane of eukaryotes and in most bacteria) receive electrons from ferrodoxin (an iron-sulfur protein) which is, in turn, reduced by a ferrodoxin reductase (which binds NADPH and FAD). In bacteria these complexes are soluble (P450 cam) [73], while in mitochondria they are usually associated with membranes (e.g. P450 scc) [74].
2) Class II P450s (found exclusively in eukaryotes and associated with the endoplasmatic reticulum) require an FAD/FMN-containing P450 called NAPH-cytochrome P450 oxidoreductase (CPR) for transfer of electrons [75].

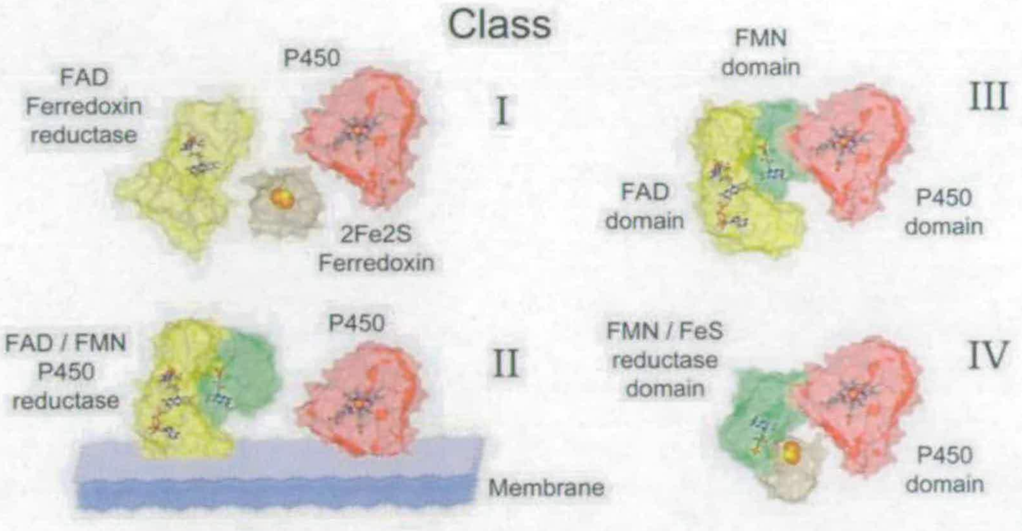

Fig 1.17: Representation of the diverse classes of cytochromes P450. P450 domains are represented in red and redox partner components in yellow (FAD domain), green (FMN domain) and blue (iron-sulfur cluster). Class I system comprised of FAD, iron sulfur and P450 subunits. Class II system comprised of FAD/FMN reductase and P450 subunits. Class III system formed by fused FAD/FMN reductase and P450 domains. Class IV P450s, recently discovered such as P450 Rhf and P450 cin carring other unique combinations of redox cofactors. Picture from [151].

3) In NADPH-cytochrome P450 reductase the FAD group serves as an electron acceptor from NADPH, whereas the FMN moiety interacts directly with the P450 and reduces it. When a homologue of cytochrome P450 reductase and a P450 are fused together in a unique enzyme they belong to a minor group, defined as class III P450; this is exemplified by the bacterial flavocytochrome P450 BM3 [76].

It should be noted that in addition to these there are P450 systems with other unique combinations of redox cofactors, such as P450 Rhf and P450 cin [77] which do not belong to any of the above described classes (fig 1.17e).

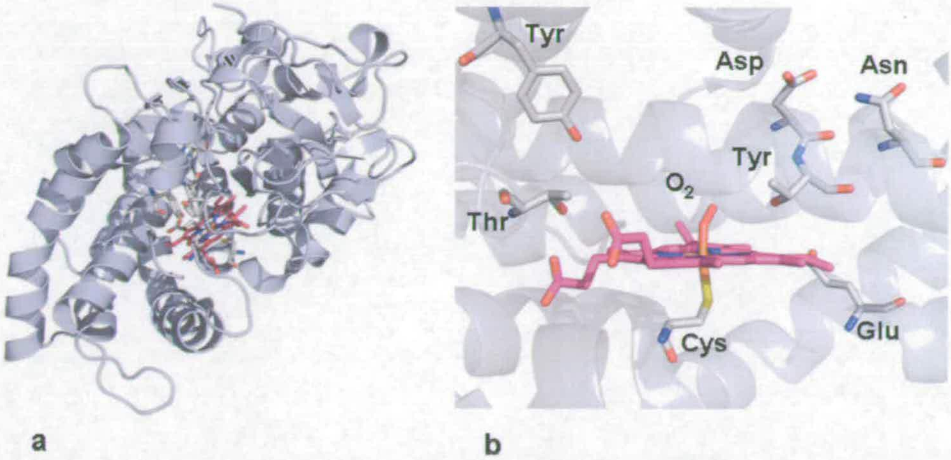

Fig 1.18: Crystal structure of ferrous P450cam from Pseudomonas putida. The heme is displayed as sticks and coloured magenta. Relevant residues are shown in sticks and coloured by element (colour code: nitrogen blue, oxygen red and carbon grey). a) Protein folding shown in cartoon representation b) Oxygen bound complex of P450cam from Pseudomonas putida (PDB entry 1DZ8)

Throughout the superfamily there is conservation of the fold of the cytochromes domain subunit. The heme is enclosed by four helices, which also provide the important catalytically residues, including the cysteine which coordinates the iron atom as the fifth ligand. When the iron is reduced, the strong electron donating nature of the thiolate from the cysteine activates molecular oxygen bound to the heme (Fig1.18b).

The reaction catalyzed by cytochrome P450 (fig 1.19) comprises an initial phase in which molecular oxygen is activated, and a final phase where the substrate is attacked and the transients rearranged.

$$\mathbf{RH + O_2 + 2H^+ + 2e^- \xrightarrow{P450} ROH + H_2O}$$

Fig 1.19: General reaction scheme for P450 hydroxylation

The reaction mechanism of cytochromes P450 will be discussed in more detail in chapter

6 in comparison with the reaction of nitric oxide synthase.

1.5.4.2 Nitric oxide synthases

Nitric oxide synthases (NOSs) are flavocytochromes that have some similarities with the cytochromes P450. They have been found in many organisms, including vertebrates and invertebrates, fungi and bacteria. NOSs are oxygenases, containing a *b*-type heme which is axially coordinated via a thiolate ligand derived from a cysteine residue of the polypeptide chain. Bacterial NOSs consist exclusively of the heme oxygenase domain and therefore require an external source of electrons [78, 79]. Like some P450s, the heme-containing domain of NOSs can be covalently coupled to an NADPH-dependent domain which includes FAD and FMN cofactors.

NOSs catalyze the two-steps sequential monooxygenation of the guanidino nitrogen of L-arginine (L-Arg), producing N-hydroxy-L-arginine in the first step and NO and L-citrulline as final products (fig 1.20) [80]. By controlling NO distribution and concentration in eukaryotes, NOSs take part in a great number of physiological functions, ranging from neurotransmission, the immune response and cardiovascular homeostasis [81, 82].

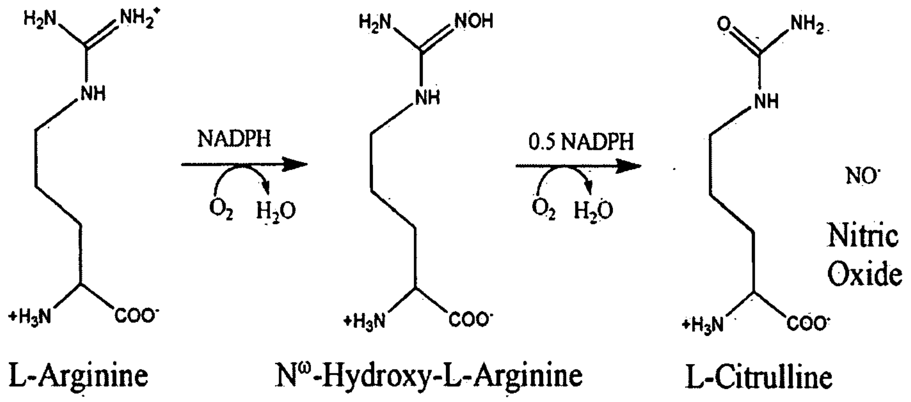

Fig 1.20: Reaction catalyzed by nitric oxide synthases

Mammalians produce three isoforms of NOS, all encoded by different genes: inducible (iNOS) and neuronal (nNOS) which are soluble and mainly localized in the cytoplasm, and endothelial (eNOS) which is associated with endothelial cell membranes. The sequences of each isoform of the three NOSs are highly conserved among different species, but the sequence identity between any two isoenzymes is only 50-60%.

All three NOSs are homodimers and each monomer shares a common architecture:

1) The N-terminal catalytic oxygenase domain that hosts the single *b*-type heme catalytic centre, the redox cofactor (6R)-5,6,7,8-tetrahydrobiopterin (H_4B) and the substrate (L-Arg) binding site
2) The C-terminal reductase domain, containing flavin mononucleotide (FMN), flavin adenine dinucleotide (FAD) and NADPH [83]. This domain is structurally and functionally related to the soluble portion of mammalian microsomal P450 reductase.
3) The link between the N-terminal and C-terminal domains, consisting of a calmodulin-binding domain that also regulates the electron transfer from the reductase to the oxygenase domains [84, 85].

Compared to P450s, NOSs are more complex from a structural point of view. The active form is a homodimer, complexed with two molecules of H_4B and a zinc atom at the dimer interface. Binding to calmodulin is also required for catalytic activity. Furthermore, the reductase domain appears to supply electrons to the heme domain of the alternate subunit (fig 1.21) [86]. The NOS catalytic reaction and the structural details of the enzyme will be described in chapter 6.

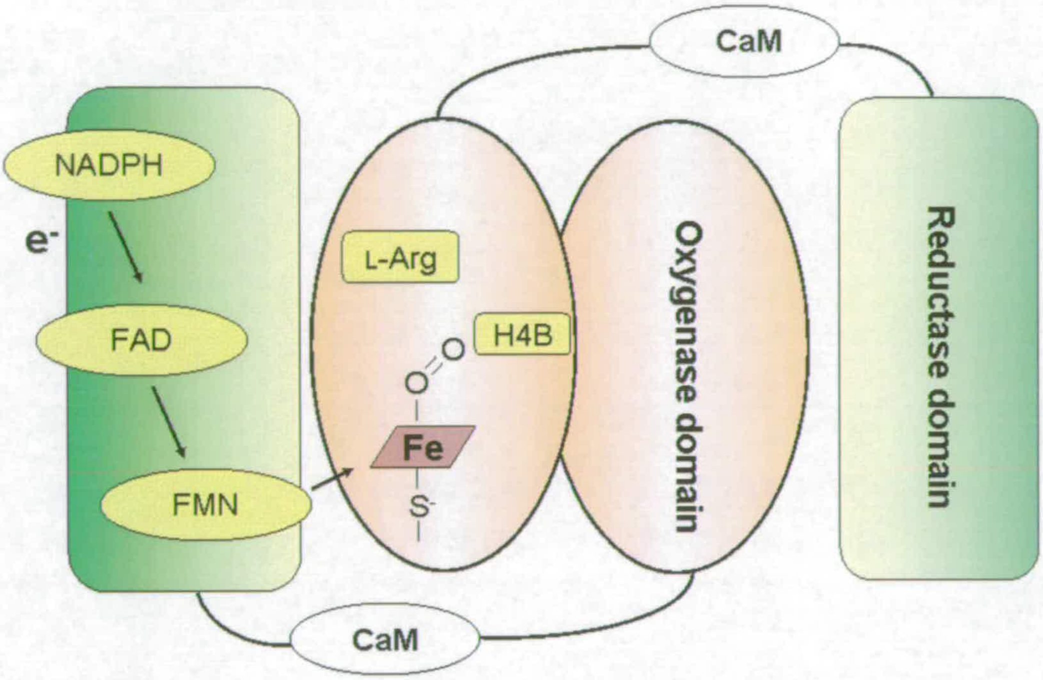

Fig 1.21: Illustration of the electron (e^-) flow through the NOS domains during the reaction. Electrons pass to the heme domain of the other subunit. The reductase domain is represented in green, the calmodulin binding domain in white, and the oxygenase domain in salmon. Cofactors (NADPH, FAD, FMN, and H_4B) and substrate (L-Arg) are all represented in yellow, while the heme is in dark red.

1.5.4.3 Indoleamine 2,3-dioxygenase and tryptophan 2,3-dioxygenase

Indoleamine 2,3-dioxygenase (IDO) and tryptophan 2,3-dioxygenase (TDO) are examples of heme dioxygenases. IDO and TDO have been both isolated from mammals [87, 88]. Currently no functional prokaryotic IDO has been identified, whilst TDO has been found in many bacteria [89, 90].

Both enzymes catalyze the oxidative cleavage of the tryptophan pyrrole ring, between its 2- and 3-positions, incorporating two atoms of oxygen (fig 1.22).

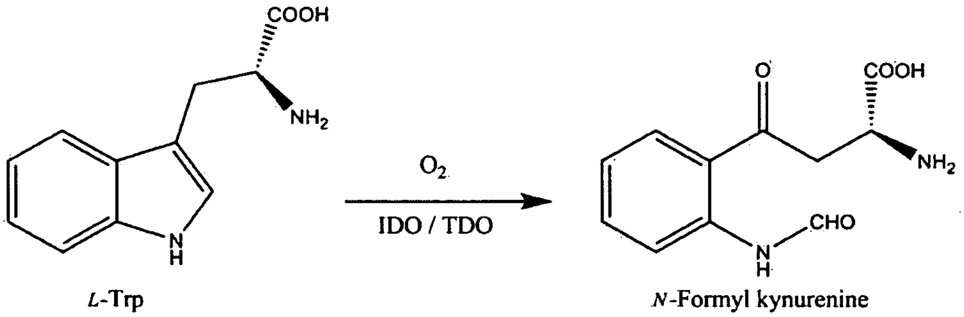

Fig 1.22: Reaction catalyzed by IDO and TDO

In mammals, this reaction is part of the tryptophan hepatic catabolism and kynurenine formation pathway. IDO and TDO have a fundamental importance in human physiology. Several neurological or psychiatric diseases have been associated with an excess of kynurenine metabolites [91, 92]. L-tryptophan is also a precursor in the synthesis of the neurotransmitter serotonin and the hormone melatonin. Nevertheless the chemistry of TDO and IDO is still poorly understood, primarily due to the lack and incompleteness of structural information.

Although IDO and TDO catalyze the same reaction, the sequence similarity between the enzymes is low. Alignment of sequences across this family of enzymes is only possible based on their three-dimensional architecture. TDO and IDO carry a *b*-type heme, which shows a positive reduction potential both in presence of tryptophan (up to +150 mV) and when the substrate is not bound (+20 mV) [89, 90]. The positive potential of the heme, together with a histidine as the fifth ligand of the heme iron, contribute to keep the iron reduced. Physiologically these enzymes are most probably always present with the iron in its reduced state. It is generally reported that the ferrous enzyme is the active form, although some catalytic activity by ferric IDO and TDO has been shown, possibly due to trace amounts of Fe(II) [93].

IDO and TDO will be described in more detail in chapters 3 and 4.

1.5.5 Flavocytochrome b_2

Flavocytochrome b_2 is a tetrameric enzyme (Fig 1.23) found in baker's yeast (*Saccaromyces cerevisiae*) and localized in the intermembrane space of mitochondria. This enzyme is involved in the oxidation of L-lactate to pyruvate during aerobic respiration. Each subunit contains one heme *b* and one flavin (FMN) [27].

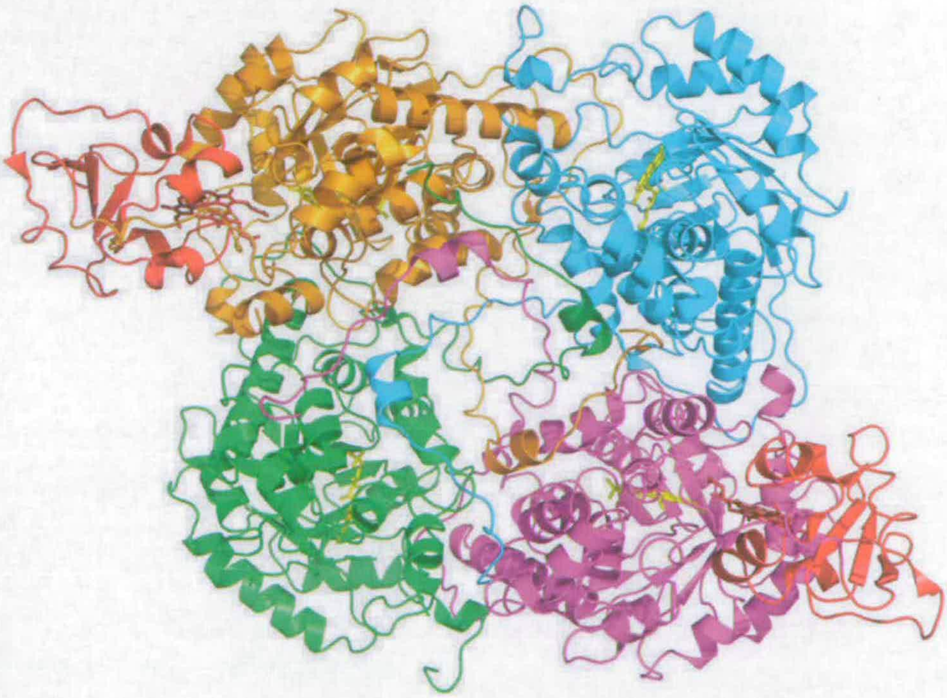

Fig 1.23: Crystal structure of flavocytochrome b_2 (PDB entry 1FCB)[27]. Each of the four monomers is represented with a different colour. Heme domains (only defined in two monomers) are coloured in red. FMN and heme are represented as sticks and coloured in yellow.

The enzyme catalyzes the two-electron oxidation of L-lactate to form pyruvate, with subsequent electron transfer to cytochrome *c* through the flavin and heme groups. The reaction proceeds in steps. First, two electrons are passed from the lactate to the flavin, which becomes fully reduced as the flavinohydroquinone species. Then the electrons are transferred to the heme moiety one at a time with the formation of a flavin semiquinone intermediate and consequent reduction of the heme. The last step is the only inter-protein electron transfer event involving flavocytochrome b_2. The electron is passed from the heme moiety to a molecule of cytochrome *c*, leaving the heme able to receive the second electron. The oxidised heme is then reduced again by the flavin semiquinone carrying the other electron. After the removal of this second electron by cytochrome *c*, the cycle is complete (fig 1.24).

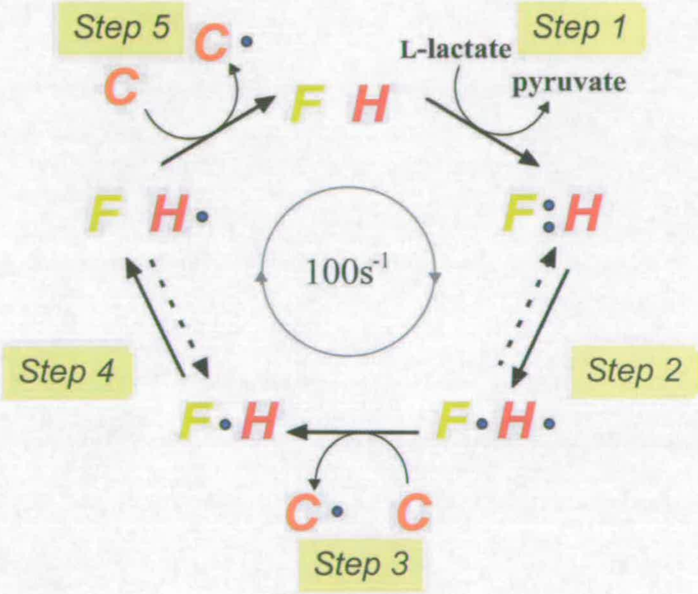

Fig 1.24: The electron transfer steps in the catalytic cycle of a single subunit of flavocytochrome b_2. (Flavin (F); b-heme (H); cytochrome c (C). Electrons are represented by blue dots).

The cytochrome domain is located at the N-terminus of the protein and it is oriented with the heme pocket facing the flavin domain. The distance from the heme iron to the centre of the flavin is 16 Å, but only 10Å from the edge of the heme pyrrole ring to the edge of the flavin [27].

There is certainly mobility between the two domains of the enzyme [94], which suggests a conformational influence on inter-domain electron transfer. The flavin domain and cytochrome domains are separated by a hinge region, whose integrity and length are important for optimal flavin hydroquinone to heme electron transfer. The flavocytochrome b_2 structure will be treated in more detail in chapter 5.

1.6 X-ray crystallography

In many cases the specific role of the redox cofactors, ligands and protein matrix in controlling the biological functions of proteins have been elucidated thanks to our knowledge of high-resolution structures of redox proteins.

Over the last 70 years three techniques have been developed to experimentally determine the three-dimensional structures of macromolecules: cryo-electron microscopy (cryo-EM), nuclear magnetic resonance (NMR spectroscopy) and x-ray crystallography.

Through cryo-EM it is possible to work on complete macromolecular complexes (macromolecular weight over 150 kDa), visualize them in their physiological environment and in different functional states. The electron density maps obtained from a cryo-EM structural study are generally at low resolution and insufficient for atomic structure details.

Only using NMR and macromolecular crystallography is it possible to characterize macromolecules at near atomic resolution and these two techniques have provided three-dimensional structures of many important biological molecules and their complexes. Structure-function studies have provided important insights into the mechanisms by which cellular functions are regulated.

The structure of small proteins can be solved using NMR spectroscopy. Using NMR spectroscopy it is possible to investigate structure and dynamics simultaneously, because the macromolecules are studied in aqueous solution. The main limitation of NMR spectroscopy is a limit on protein size of about 40 kDa, a boundary which excludes the application of this method to study of a large portion of macromolecules.

Due to this limitation x-ray crystallography is in fact the most powerful method to determine, the three-dimensional structure of small and large macromolecules, as well as macromolecular assemblies (viruses, ion channels, ribosomes and proteasomes) with atomic precision. The current status and future perspectives of macromolecular crystallography have been recently described by Dauter, 2006[95].

1.6.1 Diffraction conditions

Crystals are geometrical three-dimensional objects and they often appear as beautiful regular solids with sharp edges and plane faces. This is the reason why crystalline solids have been considered since early times as the archetype of perfection and purity.

Internally, a crystal consists of millions of molecules, atoms or ions which are stacked together systematically in all three spatial directions. The regularity of a crystal can be described with a translation lattice of a repeating unit. The basic unit of the lattice is defined as the unit cell. Unit cells are arranged within the crystal in sets of parallel and equivalent layers (fig 1.25).

When electromagnetic radiation (i.e.: x-rays) with a wavelength of the same order of magnitude as the distance between atoms strikes against a collection of atoms, diffracted scattered waves will interfere and result in a pattern of stronger and weaker waves.

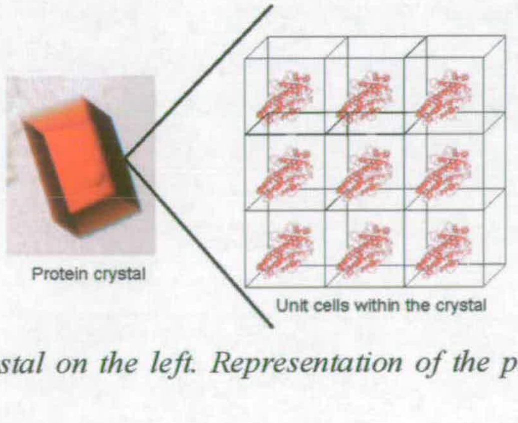

Fig 1.25: Protein crystal on the left. Representation of the protein (in red) within the unit cell

If atoms are neatly arranged in a three-dimensional crystal lattice, then the scattering will occur only in specific directions. These directions are determined by the geometry of the crystal lattice, by the orientation of the crystal lattice, by the wavelength of the incident beam but not by the position of the atoms within the unit cell. To explain why crystals appear to reflect x-ray beams only at certain angles of incidence θ (theta), physicists William Henry Bragg and his son Sir William Lawrence Bragg in 1913 derived the equation:

$$n\lambda = 2d\sin\theta \qquad \text{(Bragg's law)}$$

where d is the distance between atomic planes in the crystal lattice, λ is the wavelength of the incident x-ray beam and n is an integer.

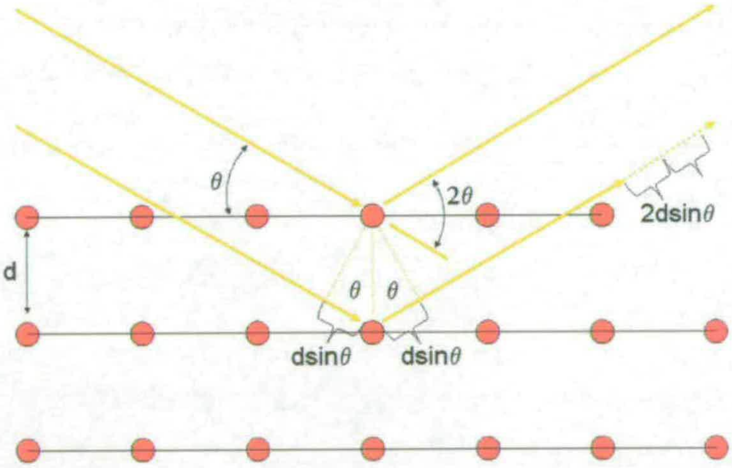

Fig 1.26: Bragg's law. Electromagnetic radiation scattering from objects in the crystal lattice. Picture adapted from [96]. (θ: incidence angle λ: wavelength d: distance between lattice planes)

Each lattice point represents the same arrangement of atoms, and the electrons within these atoms scatter the x-ray radiation (fig 1.26). Therefore all lattice points will generate a reflected wave at the same angle as the incident wave with the plane, and with the same amplitude.

Constructive interference of reflected waves will occur only if the path difference of the reflected x-rays is a whole number. Furthermore, diffracted waves not satisfying Bragg's law will extinguish each other, resulting in a total intensity of zero [97, 98].

1.6.2 Protein crystals

A great number of substances can adopt a crystalline form: some of these crystallize readily (salts, sugar), some require great pressure (diamond) while others, such as proteins, require special physico-chemical conditions.

Inorganic crystals can grow up to several centimetres in length, while protein crystals generally do not grow over 1-2 millimetres in any dimension (Fig 1.27).

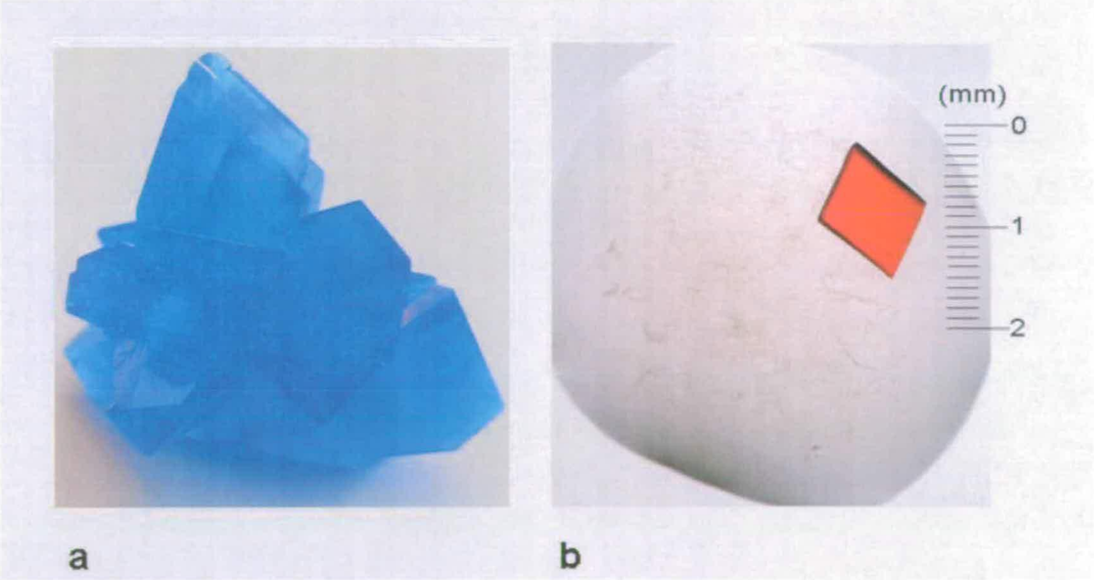

Fig 1.27: a) Salt (copper sulphate) crystal compared to a b) protein crystal

Although protein crystals appear externally similar to crystals from inorganic material, from a chemical point of view there are major differences. Inorganic crystals are composed by rigid and small molecules, held together by strong electrostatic attractions of charged ions [96]; in a protein crystal, the nature of the interaction between molecules is mainly hydrogen bonds between hydrated molecules, and only a few direct contacts between the molecules exist. Another important difference between protein and chemical crystallography is that protein crystals differ from most organic, inorganic or organometallic crystals because they contain large volumes of solvent, which normally occupy around 50% of the unit cell. The large solvent volume is not ordered and causes poor diffraction behaviour compared to most inorganic crystals. The presence of solvent in protein crystals also has the benefit of ensuring that protein molecules are in a more or less natural environment. The natural state of the protein in the crystal is confirmed by the observation that if different crystalline forms of a protein exist, the main difference between these crystal forms comes from the packing of the molecules; no essential differences are found in the conformation of the protein molecules themselves. Another indication of the biological relevance of protein crystal structures is that some crystallized proteins are still capable of binding substrates and performing their biological tasks [99-102].

1.6.3 Protein crystallization

The essential prerequisite in order to determine protein structure using diffraction techniques is to obtain at least one single crystal of the target protein. Protein crystallization is a physical-chemical process in which a protein is slowly precipitated from its solution [103]. A protein remains stable in solution up to a certain limiting concentration. Above this limit the solution is supersaturated and the protein is no longer soluble. At this stage small crystal nuclei are formed and crystal growth can begin. The crystallization process can be illustrated using a two-dimensional phase diagram (fig 1.28) [104].

The presence of impurities in the protein sample, but also the homogeneity of the solution, can interfere with the crystallization process [105]: purity of the preparation, both in terms of homogeneity and conformation of the molecules, is required for protein crystal growth.

During the crystallization process the solvent is slowly displaced from the protein solution using controlled conditions [106]. Common additives to achieve precipitating conditions are salts and polyethyleneglycols (PEG). The attraction exerted by electrostatic forces of opposite charges upon different protein molecules causes the protein to precipitate: the hydrated ions of salts and PEG not only remove the water from the solution, but also decrease the solubility of the protein. Electrostatic attraction or repulsion between protein molecules can also be controlled by varying the pH of the solution, or through the addition of organic solvents. On the other hand, hydrophobic interactions can be influenced by varying the temperature [96].

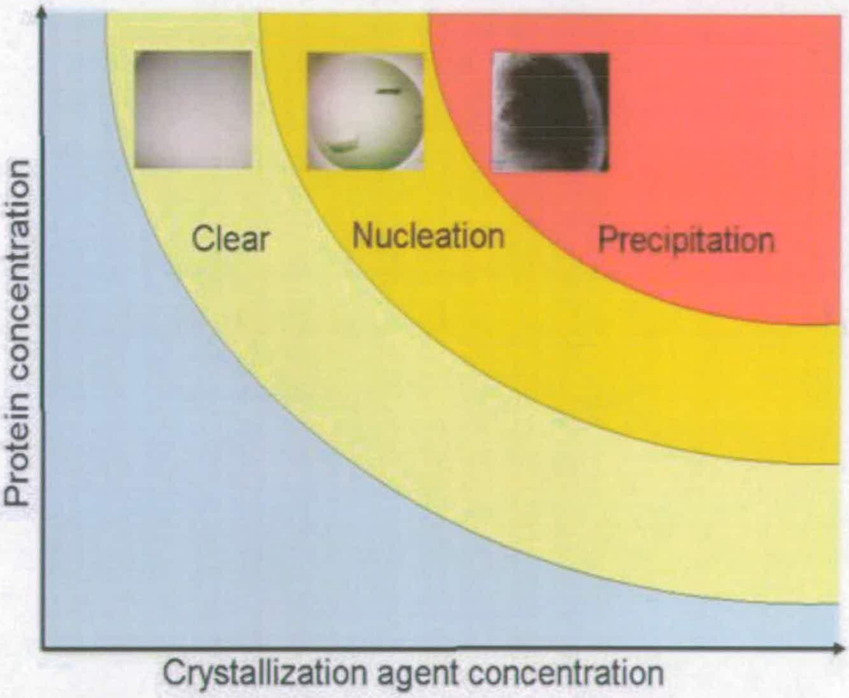

Fig 1.28: Phase diagram of protein crystallization. The blue area represents a non-saturated solution. Crystal nucleation depends directly upon protein and crystallization agent(s) concentrations.

A common technique to carry out protein crystallization experiments is the vapour diffusion method, through hanging drop or sitting drop approaches (fig 1.29) [106-108].

A small drop (2-4 μl) of protein solution is mixed with the precipitant(s) solution. The drop is sealed in a small well (2-3 cm^3) and allowed to equilibrate with a reservoir of approximately 1 ml. The reservoir contains the same buffer and precipitants as the drop but at higher solute concentration.

The initial concentration of precipitants in the protein drop may be not enough to precipitate or crystallize the protein, but in the closed system of the well, there is transfer of water through the vapour phase from the protein drop to the reservoir.

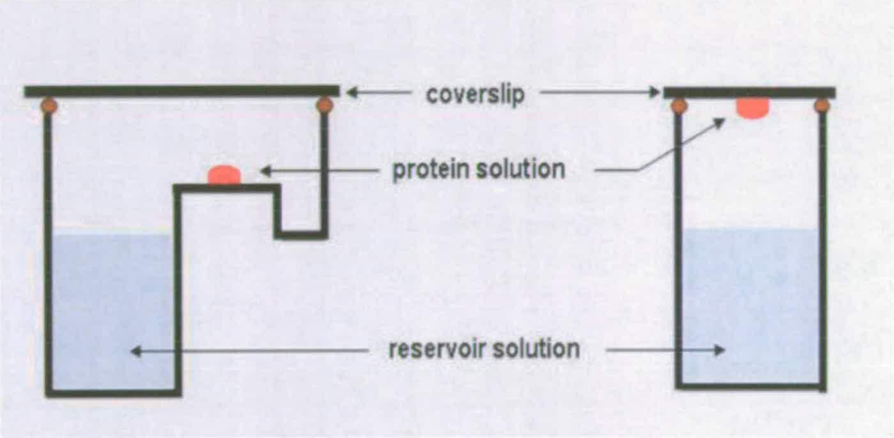

Fig 1.29: Sitting drop (left) and hanging drop (right) crystallization methods

At equilibrium the concentration of precipitants in the drop is increased and can reach the optimal level for precipitation and crystallization [109, 110].

1.6.4 Intermolecular interactions

An interesting application of x-ray crystallography is the investigation of structure-function relationship of a target protein. X-ray crystallography has also been successfully applied to study protein-protein and protein-ligand interactions and to elucidate mechanisms of protein-ligand binding [89, 102].

Protein-ligand complex formation can be achieved during the stages of expression and purification of the protein: this method is particularly useful if the protein is structurally unstable without the ligand. Most commonly, the target ligand can be either co-crystallized with the protein or added by soaking to pre-grown crystals [111]. In the soaking method, crystals of the protein are grown in the absence of the ligand. Crystals are then transferred in a solution containing the appropriate concentration of the ligand, which has to be higher than the K_d/K_m values [112]. The ligand can diffuse into the crystal through channels within the protein crystal which are filled with solvent. The soaking method often leads to crystal cracking or significant loss of the diffraction properties of the crystals: this can be due to conformational adjustments induced by ligand binding to the protein that result in changes of the unit-cell dimensions [111].

1.7 X-rays

X-rays are electromagnetic radiations with a wavelength range of 0.02-100Å, while covalent bonds are typically around 1.5 Å in length. Therefore, x-ray diffraction provides an experimental method of determining the position of individual atoms in molecules. When x-rays meet with electrons they are quickly absorbed by the electron cloud, causing the electron to vibrate at the same frequency as the incoming x-ray.

X-ray diffraction is not useful for observing the positions of light and mobile atoms with few electrons. Beyond x-rays lie γ-rays, with wavelengths of 0.01 Å or smaller. Neutron diffraction technique allows the direct location of small parts of the protein structure, such as hydrogen atoms and bound solvent [113]. Neutron diffraction would be an excellent method for the study of protein structure and hydration, but an important limitation to the success of this technology is the lack of intense, single-wavelength beams of neutrons in sufficient quantities. X-ray crystallography is the most widely-used method for macromolecular structure determination: at the moment about 83% of the three-dimensional molecular structures empirically determined have been solved through x-ray diffraction crystallography (PDB, 2008) [145].

1.7.1 X-ray sources

The production of x-rays can result from two different methods. The first method is to accelerate electrons, using an electrical field, against a metal target (x-ray tube, rotating anode). The energy generated by the collision of electrons with the metal target (usually copper or chromium) [114] is emitted as x-rays.

The second method is to use synchrotrons, in which the particles are accelerated in a ring of constant radius (fig 1.30 and fig 1.31a).

Fig 1.30: European Synchrotron Radiation Facility (ESRF) Grenoble, France. Picture from [146]

These are the most efficient and powerful sources of monochromatic x-ray beams at high intensity and short wavelength [115]. Synchrotron radiation was originally considered as an undesired by-product of high energy particle accelerators [116]. Electrons (or positrons) are injected into the synchrotron ring and accelerated at speeds approaching the speed of light [117]. Electromagnetic radiation is emitted when the charged particles travelling at near the speed of light are forced into a circular orbit by bending magnets. The particles are losing energy while emitting electromagnetic radiation; the energy of the charged particles is maintained each cycle by radio-frequency inputs. Special insertion device magnets called "wigglers" are made of poles of alternating polarity, where the electrons are forced to perform a sinusoidal type trajectory. In this way a field more intense than that of the bending magnets can be employed and the intensity of the radiation, emitted by from the electron trajectory inside the wiggler is higher (fig 1.31b).

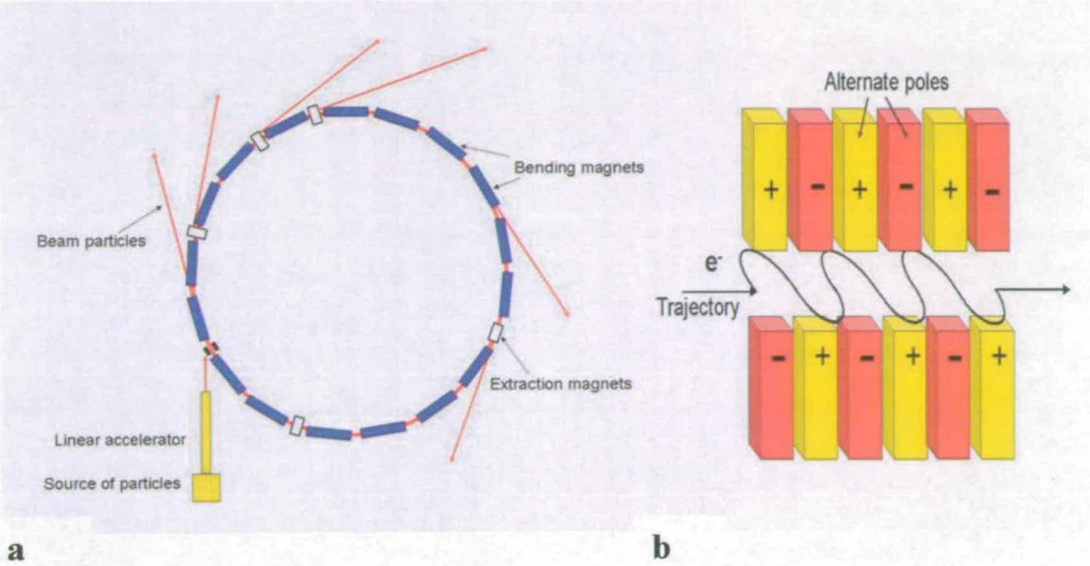

Fig 1.31: a) synchrotron ring, where the main components making up the particles accelerator are illustrated: the source of particles, the linear accelerator, the storage ring, and the insertion devices (bending magnets and extraction magnets) b) magnetic wigglers, where the magnetic field between the alternate poles causes the beam to oscillate back and forth while it traverses the wiggler. The arrow shows the direction of the beam passing through the wiggler.

Third generation synchrotrons provide high amplitude x-rays, generated by bending magnets and/or by wigglers. This high intensity radiation enables crystallographers to obtain data from very small or weakly diffracting crystals [118]. The spectrum of radiation emitted is focussed by mirror systems and monochromators to provide a sharp beam of intense and tuneable single-wavelength x-ray radiation [119].

1.7.2 X-ray radiation damage

Crystals exposed to intense synchrotron radiation are susceptible to specific structural and chemical damages [120]. The quality of the model resulting from structure determination might be compromised after an excessive radiation dose [121]. Radiation damage can induce irreversible modifications in the crystal, including breakage of covalent bonds, loss of definition of the carboxyl group of acidic residues, generation of free radicals, charge alteration and ionization [122]. Active sites of enzymes have been reported to be highly sensitive to radiation damage [123-125]. Damage can also occur to metal centres within proteins [126] causing reduction. Data collection at cryogenic temperatures (around 100 K) can minimize some of these problems, reducing the diffusion of free radicals, decreasing molecular motion and disorder and increasing the resolution limit of the data collected [127]. Furthermore, at cryogenic temperatures ligand-protein complexes and reaction intermediates can be trapped [99-101].

In order to expose the protein crystal to cryogenic temperatures, a suitable cryoprotectant agent has to be used to prevent ice formation during the data collection which can disrupt the internal order of the crystal and interfere with the diffraction pattern of the protein crystal. A complete overview of cryotechniques has been recently written by Garman & Owen, 2006 [128].

Over the last 10 years, the use of brighter synchrotron sources (third generation synchrotrons) has massively increased the dose of radiation to which crystals are exposed during the data collection, resulting in damage to protein samples even at 100K. The use of tuned x-ray sources at synchrotron radiation facilities, implemented with cryogenic techniques, allow crystals to tolerate x-ray without influencing the diffraction quality [129]. Although a clear understanding of radiation damage is still in its infancy, the modifications induced by the x-rays to specific sites in the crystal can be now used to determine the crystal structures of biological macromolecules (radiation-damage-induced phasing)[130].

1.7.3 Data collection

In a diffraction experiment the crystal is placed on a diffractometer goniostat under a continuous stream of nitrogen vapour at 100 K [131].

The intensities resulting from the diffracted beam are visualized using a detection system (usually an image plate or charged camera detector (CCD)). The detector records a pattern of scattered and regularly spaced spots, known as reflections, where diffracted waves have collided (fig 1.32).

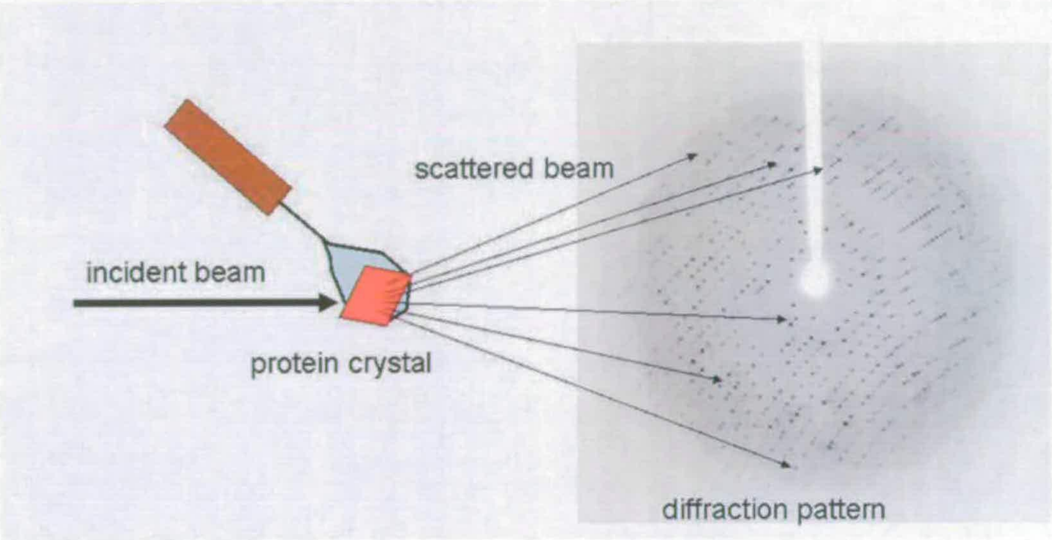

Fig 1.32: Diffraction pattern (on the right) generated by the incident beam passing through a protein crystal (represented in red) mounted in a loop

During data collection using monochromatic x-rays of fixed wavelength, the crystal is rotated with respect to the incident beam, in order to record a set of two dimensional images of reflections. Each degree of rotation causes a change in the diffraction pattern. The range required to be covered by rotation depends upon the crystal symmetry [132].

Data collection strategies are determined by several parameters [133]: crystal symmetry and quality, x-ray source, radiation damage, detector type and computer software available. Each dataset is composed of a series of indexed reflections and their associated intensities. The most important parameters to consider during data collection are completeness of measured intensities of all possible reflections within the resolution limit [127].

Strategy software systems have been recently developed for collecting complete datasets in efficient and successful ways. These software systems are based on analysis (space group and cell parameters determination, mosaicity calculation, integration and refinement) of a few diffraction patterns collected at different orientations, providing the information necessary to set a data collection run (detector distance, time of exposure, rotation range, oscillation etc.) in order to obtain a complete dataset [134-136].

1.8 Data processing

Two dimensional images of reflections recorded during data collection are used to obtain the three dimensional atomic coordinates and their corresponding electron density maps. Reflections have to be indexed for an initial interpretation and their individual intensity pixels integrated with the total pixel intensity. Same or symmetrically equivalent reflections from different images are then merged together. Subsequently all the images have to be placed on a common relative scale, in order to remove systematic error introduced into the data for example by a non-ordered crystal (high mosaicity) or variation of the incident beam.

In particular, crystal imperfections such as mosaicity can causes difficulties in processing data, because the diffraction spots can appear smeared or in higher number than expected. In a highly mosaic crystal (fig 1.33b), each mosaic block diffracts independently of each other.

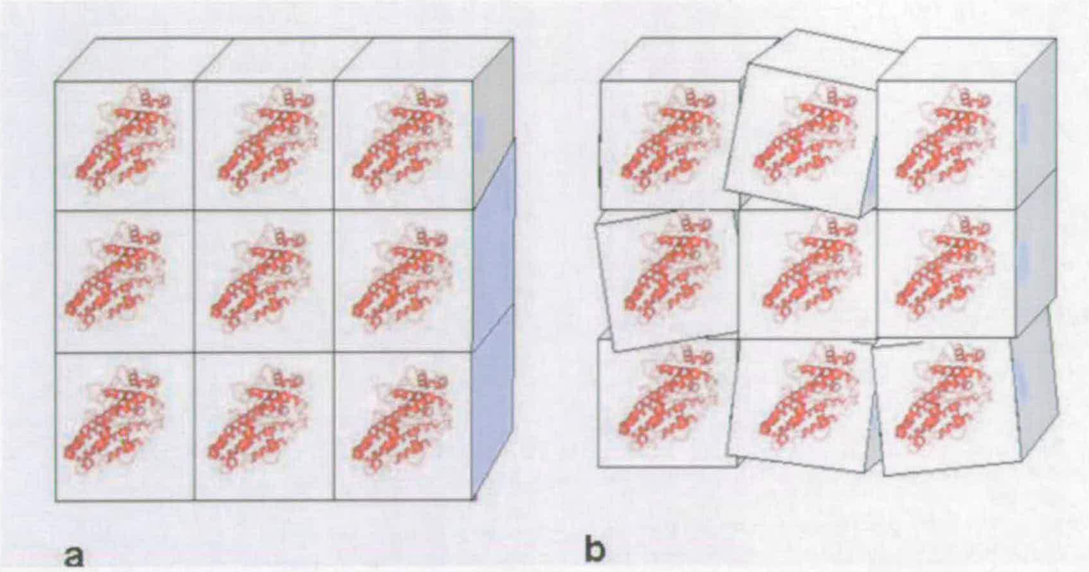

Fig 1.33: Crystal mosaicity: a) low-mosaic crystal, b) highly mosaic crystal

During the data collection, any rotation of the whole crystal corresponds to a different range of rotation angles for the single mosaic blocks. Spots from highly mosaic crystals are likely to be in diffraction conditions for longer and will then overlap with other spots.

The most common software systems used for data processing are MOSFLM [135], HKL2000 [137], XDS [138] and, recently, PHENIX [139].

1.8.1 The phase problem

A wave is characterized by the amplitude (related to the intensity) and by the phase (related to the frequency).

A diffraction experiment measures the intensities and angles of diffraction of the x-rays. The information about the phase of the wave is systematically lost in a data collection experiment. Together with the amplitudes, the phase information of the diffracted x-rays is essential for the solution of crystal structures: reflections with the same amplitude but different phases correspond to different structures.

The phase can not be directly measured, but needs to be obtained in order to solve a structure: this missing information is known as "the phase problem" [140].

The phase problem can be expressed by the following equation:

$$\rho_{(x,y,z)} = \frac{1}{V} \sum\sum\sum |F_{(h,k,l)}| \exp[-2\pi i (hx + ky + lz - \alpha_{(h,k,l)})]$$

where ρ (xyz) is the electron density, V is the cell volume and α the phase angle. From the position of the reflections it is possible to determine their triple indexes (h,k,l) and assign the appropriate intensity to them. These intensities are proportional to the structure factor amplitudes, |F(hkl)| and correspond to scalar values.

Initial phase estimates can be recovered in a variety of ways:

1) Direct methods (DM), which are common in small molecule crystallography (≤1000 non-hydrogen atoms) and require high resolution data (≤1.4 Å resolution) to derive the model by using known phase relationships between diverse groups of reflections[141].

2) Molecular replacement (MR) method was first developed by Rossmann [147]. In MR the phase is calculated using as a search model a previously solved structure, homologous (>25%) to the target model and fitted in the experimental electron density obtained from data collection (fig 1.34). This procedure is based on the observation that proteins, homologous in sequence, share a similar folding. In order to place the molecule in the target unit cell two steps are required: these are rotation and translation. In the rotation step the spatial orientation of the known and the unknown molecules with respect to each other is calculated. In the translation step the two molecules, already correctly oriented, are superimposed.

   Molecular replacement methods are based on the properties of the Patterson function [96, 119]. The Patterson function is the Fourier transform of the intensities rather than the Fourier transform structure factors. Patterson function gives a map of the vectors between atoms. The peaks in the Patterson function are proportional to the interatomic vectors distances of the peaks of the two atoms in the electron density map. The Patterson function is important because it can be obtained without phase information. The superposition of the interatomic vectors of the search and the target models in the rotation and translation functions gives a maximum value when the search model is optimally rotated onto the observed data. When the model is oriented correctly and placed in the correct position in the unit cell, the two Pattersons should be similar. Once the correct orientation and position are found, phases are calculated from the model and combined with the observed structure factor amplitudes. The electron density map is then calculated using observed structure factor amplitude and theoretical phases calculated from molecular replacement solution.

The structure factors thus obtained and the corresponding electron density map might contain a bias towards the starting model, especially in low resolution structures. In this case, the resulting electron-density map will have the same characteristics of the model even if some features are not actually present in the structure [42]. Indeed, model bias can make the electron-density maps difficult to interpret. Refinement of a model, where incorrectly placed atoms are omitted, can reduce the bias. However, structure factor bias can be effectively minimized by using information contained in the first electron density map to bring out structure factor information. A small fraction of the model, (i.e. ~3-5%), is systematically omitted for phasing: in this way the model bias is reduced by a small percentage of the atoms in the model. The recovered densities in the omitted region are then combined with the initial phases to form the composite omit map. Then, omit maps (and simulated annealing omit maps) allow to test for bias. The density in the omit region of such composite maps is not biased by the model within that omit region. The result is that the phase information obtained by using these maps have lowered model bias compared with that obtained directly from a model [148]. Even when a wrong part of the structure is removed, since all of the other atomic coordinates have already been refined to reinforce the positions of those parts that are now absent, the resultant biased phases may create electron density that again reinforces the wrong parts even if their atoms are not used to calculate phases. Thus, it is necessary to re-refine the model in the absence of the omitted part so that a new model can be generated without any bias.

3) Single and multiple isomorphous replacements (SIR and MIR), based on the effect on the diffraction pattern of electron-dense metal atom(s) (i.e. heavy atoms) bound to the protein. The changes in the scattering amplitudes in comparison to the "native" diffraction pattern can be interpreted to calculate the phases. Heavy atoms are introduced into the protein by co-crystallization or by soaking the crystal in a heavy atom-containing solution. The heavy atom method is the original approach by which protein crystal structures were solved. The mains difficulties associated with isomorphous replacement are in the positioning of heavy atom(s) and issues related to their occupancy at these positions. Collecting data at different wavelengths can facilitate the location of heavy atoms: this method is known as the multi-wavelength anomalous diffraction (MAD). At the moment the atom most commonly used for phase determination by MAD is selenium, because it is possible to replace the natural sulfur-containing methionine with selenomethionine [140]. Atoms naturally present in proteins which are also suitable for this purpose are metal ions in metallo-proteins.

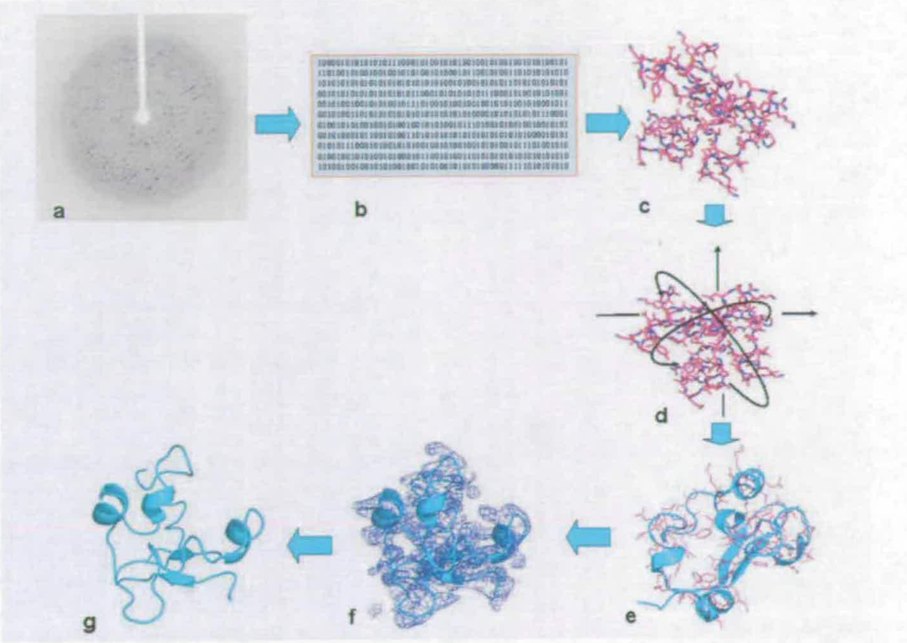

Fig 1.34: Representation of the molecular replacement phasing method. a) data collection b) experimental data c) model search >25% homology d) rotation translation operations of the model search in the experimental data e) and f) phasing fitting in the search model g) model (re)building and refinement using the target molecule

1.8.2 Model building, refinement and structure validation

The model building process depends directly upon the phase information and the resolution of the data. With phase data, an initial model can be generated using automated programs such as *ARP/wARP* [142] and RESOLVE [143]. This initial model can then be used to improve the phase calculations and build a more accurate model. The new model generated is then fitted to the new electron density map and rounds of refinement are performed. Refinement is the process in which the model is adjusted to find the closer agreement between the calculated and the observed structure factors. Indeed initially, calculated structure factors are generally in poor agreement with the observed structure factors.

Statistical parameters are used as measure of the global quality of the refinement and rebuilding processes, and they express the correlation of the final model with the experimental data. The most important parameter is the “residual” (R) factor, which is defined as:

$$R = \frac{\Sigma_{all}\ \text{reflections}\ \mid F_0 - F_c \mid}{\Sigma_{all}\ \text{reflections}\ \mid F_0 \mid}$$

where F is the structure factor and the sum extends over all the observed reflections (F_O) and their calculated counterparts (F_c).

In addition the free R parameter (R_{free}) corresponds to a fraction of ~5% of the total measurements not processed through refinement [144]; R_{free} is used to monitor the progress of refinement as well as reliably estimate the error in the final model.

R factor values generally increase proportionally to the size of the molecule and directly correlate with the resolution of the data. R_{free} should be approximately the resolution in Ångstroms divided by 10: a data-set with 2 Å resolution should give a final R_{free} of roughly 0.2 [55].

Another important parameter is the B-factor (temperature factor or "Debye-Waller factor). This factor describes the degree to which the electron density is smeared. B-factor indicates the dynamic mobility of an atom, but it can also indicate where there are errors in model building. The B-factor is given by:

$$B_i=8\pi^2U_i^2$$

where U_i^2 is the mean square displacement of the *i*th atom. As U increases, B increases. If atoms are incorrectly built, their B-factors will tend to be higher than correctly built atoms.

Each atom in a structure can be described by its position (x,y,z) and by its atomic displacement parameter (B-factor). During the refinement process, the adjustment of the model consists of changing these positional parameters and the temperature factors for the atoms, to obtain a better agreement with the measured data.

However, refinement process has generally to deal with the poor observation (number of independent reflections) to parameter ratio which affects macromolecular structure determination and is directly dependent on the resolution of the data. For example, considering as only parameters the position of the atoms and their temperature factors, at a resolution of about 2.8Å, there is only one observation for each parameter. That means that it is easy to over fit the data to get a deceptive level of agreement between model and experiment.

When the ratio of observation:parameters to be refined is poor, additional "observations" are incorporated in the refinement process. These are stereochemical data (bond length and angles), solvent information (solvent flattering) [149] and non-crystallographic symmetry [119]. This last observation, if it exists, makes important contribution to the refinement of the protein structure.

Stereochemical information (bonds length, bonds angles, etc) can be applied in two ways:

♦ as constrained, when they are taken as rigid and only dihedral angles are varied. This can reduce the number of parameters to be refined

♦ as restrained, when the stereochemical parameters are allowed to vary around a theoretical value. Typical restraints include bond lengths, bond angles and van der Waals contact distances.

In high-resolution and well-refined structures the electron density might show that multiple conformations of certain residues exist. In this case multiple sets of coordinates are reported for the same atom. Alternate conformations can be observed where it looks that part of the structure lies in two or more different places. However, in the high-resolution structure (1.6 Å) reported in this work (Chapter 3) we did not observe any alternate conformation. If we had seen any they would have been refined with partial occupancy until the balance would had looked right.

Many other parameters have to assets the data quality and used to validate every crystallographic model before deposition to the Protein Data Bank: these have been recently reviewed by Kleywegt, G. J, 2000 [42].

1.9 References

1. Mitchell, P. Coupling of phosphorylation to electron and hydrogen transfer by a chemi-osmotic type of mechanism. Nature 191, 144-148 (1961).

2. Bendall, D. S. (ed.) (Kluwer Academic Publishers, New York, 1996).

3. Bard, A. J. & Faulkner, L. R. (eds.) (Wiley, New York, 1980).

4. Franck, J. Elementary processes of photochemical reactions. Transactions of the Faraday Society 21, 536-542 (1926).

5. Condon, E. Nuclear motions associated with electron transitions in diatomic molecules. Physical Review 32, 858-872 (1928).

6. Marcus, R. A. On the theory of oxidation-reduction reactions involving electron transfer. J. Chem. Phys 24, 966-978 (1956).

7. Marcus, R. A. & Sutin, N. Electron transfers in chemistry and biology. Biochim. Biophys. Acta 811, 256-322 (1985).

8. Gray, H. B. & Winkler, J. R. Electron tunnelling through proteins. Q. Rev. Biophys. 36, 341-372 (2003).

9. Winkler, J. R., Nocera, D. G., Yocom, K. M., Bordignon, E. & Gray, H. B. Electron-transfer kinetics of pentaammineruthenium(III)(histidine-33)-ferricytochrome *c*. Measurement of the rate of intramolecular electron transfer between redox centers separated by 15.ANG. in a protein. J Am Chem Soc 104, 5798-5800 (1982).

10. Beratan, D. N., Betts, J. N. & Onuchic, J. N. Protein electron transfer rates set by the bridging secondary and tertiary structure. Science 252, 1285-1288 (1991).

11. Lewis F.D., Liu J., Weigel W., Retting W., Kurnikov I.V. & Beratan D.N. Donor-bridge-acceptor energetics determine the distance dependence of electron tunneling in DNA. proc. Natl. Acad. Sci. U S A 99, 12536-12541 (2002).

12. Bertini, I., Gray, H. B., Stiefel, E. I. & Valentine, J. S. (eds.) Biological Inorganic Chemistry (Sausalito, CA, 2007).

13. Page, C. C., Moser, C. C., Chen, X. & Dutton, L. P. Natural engineering principles of electron tunnelling in biological oxidation-reduction. Nature 402, 47-52 (1999).

14. Moser, C. C., Keske, J. M., Farid, R. S. & Dutton, P. L. Nature of biological electron transfer. Nature 355, 796-802 (1992).

15. Beratan, D., Onuchic, J., Winkler, J. & Gray, H. Electron-tunneling pathways in proteins. Science 258 1740-1741 (1991).

16. Gray, H. B. & Winkler, J. R. Long-Range Electron Transfer Special Feature: Long-range electron transfer. Proc. Natl. Acad. Sci. USA 102, 3534-3539 (2005).

17. Langen, R., Chang J., Germanas J.P., Richards J.H., Winkler J.R. & Gray H.B. Electron tunneling in proteins: coupling through a beta strand. Science 268, 1733-1735 (1995).

18. Mei, H., Wang, K., Peffer, N., Weatherly, G., Cohen, D. S., Miller, M., Pielak, G. J., Durham, B. & Millett, F. Role of configurational gating in intracomplex electron transfer from cytochrome c to the radical cation in cytochrome c peroxidase. Biochemistry 38, 6846-6854 (1999).

19. Prytkova, T. R., Kurnikov, I. V. & Beratan, D. N. Coupling coherence distinguishes structure sensitivity in protein electron transfer. Science 351, 622-625 (2007).

20. Jasaitis, A., Johansson, M. P., Wikstrom, M., Vos, M. H. & Verkhovsky, M. I. Nanosecond electron tunneling between the hemes in cytochrome bo3. Proc. Natl. Acad. Sci. USA 104, 20811-20814 (2007).

21. Baratan, D. N. & Balabin, I. A. Heme-copper oxidases use tunneling pathways. Proc. Natl. Acad. Sci. USA 105, 403-404 (2008).

22. Baratan, D. & Balabin, I. Heme-copper oxidases use tunneling pathways. Proc. Natl. Acad. Sci. USA 105, 403-404 (2008).

23. Nicolet, Y., Piras, C., Legrand, P., Hatchikian, C. & Fontecilla-Camps, J. Desulfovibrio desulfuricans iron hydrogenase: the structure shows unusual coordination to an active site Fe binuclear center. Structure Fold.Des 7, 13-23 (1999).

24. Crane, B. R., Bilio, A. J. D., Winkler, J. R. & Gray, H. B. Electron tunnelling in single crystals of Pseudomonas aeruginosa azurins. J.Am.Chem.Soc. 123, 11623-11631 (2001).

25. Liu, M., Wuebbens, M., Rajagopalan, K. & Schindelin, H. Crystal structure of the gephyrin-related molybdenum cofactor biosynthesis protein MogA from Escherichia coli. J.Biol.Chem. 275, 1814-1822 (2000).

26. Darnault C., Volbeda A., Kim E.J., Legrand P., Vernade X., Lindahl P.A., Fontecilla-Camps J.C. Ni-Zn-[Fe4-S4] and Ni-Ni-[Fe4-S4] clusters in closed and open subunits of acetyl-CoA synthase/carbon monoxide dehydrogenase. Nat.Struct.Biol. 10, 271-279 (2003).

27. Xia, Z.-X., Shamala N., Bethge P.H., Lim L.W., bellamy H.D., Xuong N.H., Lederer F. & Mathews F.S. Three.Dimensional strcture of flavocytochrome b2 from baker's yeast at 3.0 Å resolution Proc. Natl. Acad. Sci. USA 84, 2629-2633 (1987).

28. Watenpaugh, K. D., Sieker, L. C. & Jensen, L. H. Crystallographic refinement of rubredoxin at 1 x 2 A degrees resolution. J.Mol.Biol. 138, 615-633 (1980).

29. Marg, B. L., Schweimer, K., Sticht, H. & Oesterhelt, D. A two-alpha-helix extra domain mediates the halophilic character of a plant-type ferredoxin from halophilic archaea. Biochemistry 44, 29-39 (2005).

30. Shen B., Martin L.L., Butt J.N., Armstrong F.A., Stout C.D., Jensen G.M., Stephens P.J., La Mar G.N., Gorst C.M. & Burgess B.K. Azotobacter vinelandii ferredoxin I. Aspartate 15 facilitates proton transfer to the reduced [3Fe-4S] cluster. J.Biol.Chem. 268, 25928-25939 (1993).

31. Varotsis, C., Zhang, Y., Appelman, E. H. & Babcock, G. T. Resolution of the Reaction Sequence During the Reduction of O_2 by Cytochrome Oxidase. Proc. Natl Acad. Sci. USA 90, 237-241 (1993).

32. Phillips, S. E. V. Structure and refinement of oxymyoglobin at 1.6 Å resolution. Journal of Molecular Biology 142, 531-554 (1980).

33. Altuve A., Silchenko S.,.Lee K.H, Kuczera K., Terzyan S., Zhang X., Benson D.R. & Rivera M. Probing the differences between rat liver outer mitochondrial membrane cytochrome b_5 and microsomal cytochromes b_5. Biochemistry 40, 9469-9483 (2001).

34. Gibson, H. R., Mowat, C. G., Miles, C. S., Li, B.-R., Leys, D., Reid, G. A. & Chapman, S.K. Structural and Functional Studies on DHC, the Diheme Cytochrome *c* from *Rhodobacter sphaeroides*, and its Interaction with SHP, the sphaeroides Heme Protein. Biochemistry 45, 6363-6371 (2006).

35. Bertini, I., Faraone-Mennella, J., Gray, B. H., Luchinat, C., Parigi, G. & Winkler, J. R., NMR-validated structural model for oxidized *Rhodopseudomonas palustris* cytochrome c_{556}. J. Biol. Inorg. Chem 9, 224-230 (2004).

36. Devreese, B., Brige′ A., Backers K., Van Driessche G., Meyer T. E., Cusanovich M. A.., & Van Beeumen J. J. Primary Structure Characterization of a Rhodocyclus tenuis Diheme Cytochrome *c* Reveals the Existence of Two Different Classes of Low-Potential Diheme Cytochromes c in Purple Phototropic Bacteria. Archives of Biochemistry and Biophysics 381, 53-60 (2000).

37. Leys, D., Backers K., Meyer T. E., Hagen W. R., Cusanovich M. A. & Van Beeumen J. J. Crystal structures of an oxygen-binding cytochrome *c* from Rhodobacter sphaeroides. J.Biol.Chem. 275, 16050-16056 (2000).

38. Nomenclature Committee of the International Union of Biochemistry. Nomenclature of electron-transfer proteins. Eur. J. Biochem 200, 599-611 (1991).

39. Guillou, H., D'Andrea S., Rioux V., Barnouin R., Dalaine S., Pedrono F., Jan S. & Legrand P. Distinct roles of endoplasmic reticulum cytochrome b5 and fused cytochrome b5-like domain for rat {Delta}6-desaturase activity. J. Lipid Res. 45, 32-40 (2004).

40. Rao, L. V. M., Usharani, P., Butler, W. L. & Tokuyasu, K. T. Localization of Cytochrome b_{559} in the Chloroplast Thylakoid Membranes in Spinach. Plant Physiol. 80, 138-141 (1986).

41. Kirilovsky, D., Roncel M., Boussac A., Wilson A., Zurita J. L., Ducruet J.-M., Bottin H., Sugiura M., Ortega J. M. & Rutherford A. W. Cytochrome c_{550} in the Cyanobacterium Thermosynechococcus elongatus: STUDY OF REDOX MUTANTS. J. Biol. Chem. 279, 52869-52880 (2004).

42. Kleywegt, G. J. Validation of protein crystal structures. Acta Cryst. D56, 249-265 (2000).

43. Moore, G. Bacterial four alpha-helical bundle cytochromes. Biochim. Biophys. Acta 1058, 38-41 (1991).

44. Mowat, C. & Chapman, S. Multi-heme cytochrome: new structures, new chemistry. Dalton Trans. 21, 3381-3389 (2005).

45. Pessanha M.,. Louro R.O, Correia I.J., Rothery E.L., Pankhurst K.L., Reid G.A., Chapman S.K., Turner D.L. & Salgueiro C.A. Thermodynamic characterization of a tetrahaem cytochrome isolated from a facultative aerobic bacterium, *Shewanella frigidimarina*: a putative redox model for flavocytochrome c_3. Biochem. J. 370, 489-495 (2003).

46. Pessanha M., Rothery E.L., Louro R.O., Turner D.L., Miles C.S., Reid G.A., Chapman S.K., Xavier A.V.& Salgueiro C.A. Redox behaviour of the haem domain of flavocytochrome c_3 from *Shewanella frigidimarina* probed by NMR. FEBS Lett 578, 185-190 (2004).

47. Allen, J. W. A., Leach, N. & Ferguson, S. J. The histidine of the c-type cytochrome CXXCH haem-binding motif is essential for haem attachment by the *Escherichia coli* cytochrome *c* maturation (Ccm) apparatus. Biochem. J. 15, 389:587 (2005).

48. Zannoni, D. (ed.) Respiration in Archaea and Bacteria: Diversity of Prokaryotic Electron Transport Carriers (Springer-Verlag New York, LLC, 2004).

49. Ambler, R. P. Sequence variability in bacterial cytochromes *c* Biochim. Biophys. Acta 1058, 42-47 (1991).

50. Klarskov, K., Leys, D., Backers, K., Costa, H. S., Santos, H., Guisez, H. & Van Beeumen J.J. Ligand binding and covalent structure of an oxygen-binding heme protein from *Rhodobacter shaeroides*, a representative of a new structural family of c-type cytochromes. Biochemistry 37, 5995-6002 (1998).

51. Leys, D. Backers K., Meyer T. E., Hagen W. R., Cusanovich M. A. & Van Beeumen J. J. Crystal structures of an oxygen-binding cytochrome c from *Rhodobacter sphaeroides*. J.Biol.Chem. 275, 16050-16056 (2000).

52. Moore, G. R. Bacterial four alpha-helical bundle cytochromes. Biochim. Biophys. Acta 1058, 38-41 (1991).

53. Pessanha M., Rothery E.L., Louro R.O., Turner D.L., Miles C.S., Reid G.A., Chapman S.K., Xavier A.V. & Salgueiro C.A. Redox behaviour of the haem domain of flavocytochrome c_3 from *Shewanella frigidimarina* probed by NMR. FEBS Lett 578, 185-190 (2004).

54. Pessanha M., Rothery E.L., Louro R.O., Turner D.L., Miles C.S., Reid G.A., Chapman S.K., Xavier A.V.& Salgueiro C.A. Redox behaviour of the haem domain of flavocytochrome c_3 from *Shewanella frigidimarina* probed by NMR. FEBS Lett 578, 185-190 (2004).

55. Mowat, C., Rothery E., Miles C. S., McIver L., Doherty M. K., Drewette K., Taylor P., Walkinshaw M. D., Chapman S. K. & Reid G. A.Octaheme tetrathionate reductase is a respiratory enzyme with novel heme ligation. Nat Struct Mol Biol. 10, 1023-1024.

56. Deisenhofer, J., Epp, O., Sinning, I. & Michel, H. Crystallographic refinement at 2.3 Å resolution and refined model of the photosynthetic reaction centre from *Rhodopseudomonas viridis*. J. Mol. Biol. 246, 429-457 (1995).

57. Prince, R. C. & George, G. N. The remarkable complexity of hydroxylamine oxidoreductase. Nature Struct. Biol. 4, 247-250 (1997).

58. Pealing, S. L., Lysek, D. A., Taylor, P., Alexeev, D., Reid, G. A., Chapman, S. K. & Walkinshaw, M. D. Crystallization and preliminary X-ray analysis of flavocytochrome c_3, the fumarate reductase from *Shewanella frigidimarina*. J Struct Biol. 1, 76-78 (1999).

59. Taylor, P., Pealing, S. L., Reid, G. A., Chapman, S. K. & Walkinshaw, M. D. Structural and mechanistic mapping of a unique fumarate reductase. Nat.Struct.Biol. 6, 1108-1112 (1999).

60. Fülöp, V., Ridout, C. J., Greenwood, C. & Hajdu, J. Crystal structure of the di-haem cytochrome *c* peroxidase from *Pseudomonas aeruginosa*. Structure 3, 1225-1233 (1995).

61. Myers, C. R. & Myers, J. M. Outer membrane cytochomes of *Shewanella putrefaciens* MR-1: spectral analysis and purification of the 83 kDa *c*-type cytochrome. Biochim. Biophys. Acta 1326 307-318 (1997).

62. Vandenberghe, I., Leys, D., Demol, H., Van Driessche, G., Meyer, T. E., Cusanovich, M.A. & Van Beeumen, J. J. The primary structures of the low-redox potential diheme cytochromes *c* from the phototrophic bacteria *Rhodobacter sphaeroides* and *Rhodobacter adriaticum* reveal a new structutal family of c-type cytochromes. Biochemistry 37, 13075-13081 (1998).

63. Gibson, H. R., Mowat, C. G., Miles, C. S., Li, B.-R., Leys, D., Reid, G. A. & Chapman, S.K. Structural and Functional Studies on DHC, the Diheme Cytochrome *c* from *Rhodobacter sphaeroides*, and its Interaction with SHP, the sphaeroides Heme Protein. Biochemistry 45, 6363-6371 (2006)

64. Freitas T. A. K., Hou S., Dioum E. M., Saito J. A., Newhouse J., Gonzalez G., Gilles-Gonzalez M.-A., & Alam M. Ancestral hemoglobins in Archaea. Proc. Natl. Acad. Sci. USA 101, 6675-6680 (2004).

65. Hardison, R. Hemoglobins from bacteria to man: evolution of different patterns of gene expression The Journal of Experimental Biology 201, 1099-1117 (1998).

66. Ilari, A., Bonamore, A., Farina, A., Johnson, K. A. & Boffi, A. The X-ray structure of ferric *Escherichia coli* flavohemoglobin reveals an unexpected geometry of the distal heme pocket. J. Biol Chem 277, 23725-23732 (2002).

67. Kendrew, J. C., Bodo, G., Dintzis, H. M., Parrish, R. G. & Wyckoff, H. A three-dimensional model of the myoglobin molecule obtained by X-ray analysis. Nature 181, 662-666 (1958).

68. Perutz, M. F. X-ray analysis of haemoglobin. Nature 149, 491-496 (1942).

69. Omura, T., Ishimura, Y. & Fujii-Kuriyama, Y. (eds.) Cytochrome P-450 (Tokyo, Japan, 1993).

70. Nelson D.R., Kamataki T., Waxman D.J., Guengerich F.P., Estabrook R.W., Feyereisen R., Gonzalez F.J., Coon M.J., Gunsalus I.C., Gotoh O., Okuda K., Nebert D.W. The P450 superfamily -update on new sequences, gene-mapping, accession numbers, early trivial names of enzymes, and nomenclature DNA Cell. Biol. 12, 1-51 (1993).

71. Brodie B. B., Axelrod J., Cooper J. R., Gaudette L., La Du B. N., Mitoma C. & Udenfriend S. Detoxication of drugs and other foreign compounds by liver microsomes. Science 121, 603-604 (1955).

72. Sevrioukova, I. F., Li, H., Zhang, H., Peterson, J. A. & Poulos, T. L. Structure of a cytochrome P450-redox partner electron-transfer complex. Proc. Natl. Acad. Sci. USA 96, 1863-1868 (1999).

73. Gunsalus, I. C., Pederson, T. C. & Sligar, S. G. Oxygenase-catalyzed biological hydroxylations. Ann. Rev. Biochem. 44, 377-407 (1975).

74. Lambeth, J. & Kamin, H. Adrenodoxin reductase.adrenodoxin complex. Flavin to iron-sulfur electron transfer as the rate-limiting step in the NADPH-cytochrome *c* reductase reaction. J. Biol. Chem. 8, 2766-2774 (1979).

75. Munro A.W., Noble M.A., Ost T.W., Green A.J., McLean K.J., Robledo L., Miles C.S., Murdoch J. & Chapman S.K. (2000) Flavocytochrome P450 BM3 substrate selectivity and electron transfer in a model cytochrome P450. Subcell Biochem 35:297–315

76. Modi, S., Sutcliffe, M. J., Primrose, W. U., Lian, L. Y. & Roberts, G. C. The catalytic mechanism of cytochrome P450 BM3 involves a 6 Å movement of the bound substrate on reduction. Nat. struct. Biol. 5, 414-417 (1996).

77. Hawkes, B., Adams, G. W., Burlingame, A. L., Ortiz de Montellano, P. R. & de Voss, J. J. Cytochrome P450cin (CYP176A), isolation, expression, and characterization. J. Biol. Chem. 31, 27725-27732 (2002).

78. Adak S., Bilwes A. M., Panda K., Hosfield D., Aulak K. S., McDonald J. F., Tainer J. A., Getzoff E. D., Crane B. R. & Stuehr D. J. Cloning, expression, and characterization of a nitric oxide synthase protein from Deinococcus radiodurans. Proc. Natl. Acad. Sci. U. S. A. 99, 107-112 (2002).

79. Pant, K., Bilwes, A. M., Adak, S., Stuehr, D. J. & Crane, B. R. Structure of a nitric oxide synthase heme protein from *Bacillus subtilis*. Biochemistry 41, 11071-11079 (2002).

80. Griffith, O. W. & Stuehr, D. J. Nitric oxide synthases: properties and catalytic mechanism. Annu Rev Physiol 57, 707-736 (1995).

81. Taylor B. S., de Vera M. E., Ganster R. W., Wang Q., Shapiro R. A., Morris Jr. S. M., Billiar T. R. & Geller D. A. Multiple NF- B Enhancer Elements Regulate Cytokine Induction of the Human Inducible Nitric Oxide Synthase. Gene J. Biol. Chem 273 15148-15156 (1998).

82. JR Lancaster, J. Simulation of the Diffusion and Reaction of Endogeneously Produced Nitric Oxide Proc. Natl. Acad. Sci. USA 91 8137-8141 (1994).

83. Kadish, K., Smith, K. & Guilard, R. (eds.) The porphyrin handbook (Academic, San Diego, 2000).

84. Cho H.J., Xie Q.W., Calaycay J., Mumford R.A., Swiderek K.M., Lee T.D. & Nathan C. Calmodulin is a subunit of nitric oxide synthase from macrophages. J Exp Med 176, 599-604 (1992).

85. Abu-Soud, H. M., Yoho, L. L. & Stuehr, D. J. Calmodulin controls neuronal nitric-oxide synthase by a dual mechanism. Activation of intra- and interdomain electron transfer. J Biol Chem 269, 32047-32050 (1994).

86. Daff S., Noble M. A., Craig D. H., Rivers S. L., Chapman S. K., Munro A. W., Fujiwara S., Rozhkova E., Sagami I., Shimizu T.Control of electron transfer in neuronal NO synthase. Biochemical Society Transactions 29, 147-152 (2001).

87. Littlejohn, T., Takikawa, O., Truscott, R. & Walker, M. Production of Truncated Enzymically-Active Human Indoleamine 2,3-Dioxygenase (IDO) Using Site-Directed Mutagenesis. J. Biol. Chem. 278, 29525-29531 (2003).

88. Batabyal, D. & Yeh, S.-R. Human Tryptophan Dioxygenase: A Comparison to Indoleamine 2,3-Dioxygenase. J. Am. Chem. Soc. 129, 15690-15701 (2007).

89. Forouhar F., Anderson J.L., Mowat C.G., Vorobiev S.M., Hussain A., Abashidze M., Bruckmann C., Thackray S.J., Seetharaman J., Tucker T., Xiao R., Ma L.C., Zhao L., Acton T.B., Montelione G.T., Chapman S.K. & Tong L. Molecular insights into substrate recognition and catalysis by tryptophan 2,3-dioxygenase. Proc. Natl. Acad. Sci. USA 104, 473-8 (2007).

90. Zhang Y., Kang S., Mukherjee T., Bale S., Crane B., Begley T. & Ealick S. Crystal Structure and Mechanism of Tryptophan 2,3-Dioxygenase, a Heme Enzyme Involved in Tryptophan Catabolism and in Quinolinate Biosynthesis. Biochemistry 46, 145-155 (2007).

91. Takikawa, O. Biochemical and medical aspects of the indoleamine 2,3-dioxygenase-initiated l-tryptophan metabolism. Biochem. Biophys. Res. Commun 338, 12-19 (2005).

92. Khan, J., Forouhar, F., Tao, X. & Tong, L. Nicotinamide adenine dinucleotide metabolism as an attractive target for drug discovery. Expert Opin. Thera. Targets 11, 695-705 (2007).

93. Li, J. S., Han Q., Fang J., Rizzi M., James A. A. & Li J. Biochemical Mechanisms Leading to Tryptophan 2,3-Dioxygenase Activation. Archives of Insect Biochemistry and Physiology 64, 74-87 (2006).

94. Labeyrie, F., Beloeil, J. & Thomas, M. Evidence by NMR for mobility of the cytochrome domain within flavocytochrome b_2. Biochim. Biophys. Acta 2, 134-141 (1988).

95. Dauter, Z. Current state and prospects of macromolecular crystallography. Acta Cryst. D62, 1-11 (2006).

96. Rhodes, G. (ed.) Crystallography made crystal clear (Elsevier Inc, 2006).

97. Blow, D. (ed.) Outline of Crystallography for biologists (Oxford University press Inc., New York, 2004).

98. Bragg, W. L. The structure of some crystals as indicated by their diffraction of X-rays. Proceedings of the royal society of London 89, 248-277 (1913).

99. Kovaleva, E. G. & Lipscomb, J. D. Crystal structures of Fe^{2+} dioxygenase superoxo, alkylperoxo, and bound product intermediates 316, 453-7 (2007).

100. Li, H., Igarashi, J., Jamal, J., Yang, W. & Poulos, T. L. Structural studies of constitutive nitric oxide synthases with diatomic ligands bound. J Biol Inorg Chem. 11, 753-68 (2006).

101. Schlichting, I., Berendzen J., Chu K., Stock A. M., Maves S. A., Benson D. E., Sweet R. M., Ringe D., Petsko G. A. & Sligar S. G. The catalytic pathway of cytochrome p450cam at atomic resolution. Science 5458, 1615-1622 (2000).

102. Cavazza, C., Contreras-Martel, C., Pieulle L. , C., E , Hatchikian, E. & Fontecilla-Camps, J. C. Flexibility of Thiamine Diphosphate Revealed by Kinetic Crystallographic Studies of the Reaction of Pyruvate-Ferredoxin Oxidoreductase with Pyruvate. Structure 14, 217-224 (2006).

103. Weber, P. C. Physical principles of protein crystallization. Advances in protein chemistry 41, 1-36 (1991).

104. Asherie, N. Protein crystallization and phase diagrams. Methods 34, 266-272 (2004).

105. Hirschler, J. & Fontecilla-Camps, J. C. Contaminant Effects on Protein Crystal Morphology in Different Growth Environments. Acta Cryst. D52, 806-812 (1996).

106. McPherson, A. (ed.) Crystallization of Biological Macromolecules (Cold Spring Harbor Laboratory Press, New York, 1999).

107. Davies, D. R. & Segal, D. M. Protein crystallization. Micro techniques involving vapour diffusion. Methods Enzymol. 22, 266-269 (1971).

108. McPherson, A. (ed.) Preparation and Analysis of Protein Crystals (John Wiley & Sons., New York, 1982).

109. Chernov, A. A. Crystal growth and crystallography. Acta Cryst. A54, 859-872 (1998).

110. Chayen, N. E. Methods for separating nucleation and growth in protein crystallisation. Prog Biophys Mol Biol 88, 329-37 (2005).

111. Skarzynski, T. & Thorpe, J. Industrial perspective on X-ray data collection and analysis. Acta Cryst. D62, 102-107 (2006).

112. McNae, I. W., Kan, D., Kontopidis, G., Patterson, A., Taylor, P., Worrall, L. & Walkinshaw, M. D. Study of protein-ligand interactions using protein crystallography. Crystallography Reviews 11, 61-71 (2005).

113. Niimura, N. & Bau, R. Neutron protein crystallography: beyond the folding structure of biological macromolecules. Acta Cryst. A64, 12-2 (2008).

114. Yang, C., Pflugrath, J. W., Courville, D. A., Stence, C. N. & Ferrara, J. D. Away from the edge: SAD phasing from the sulfur anomalous signal measured in-house with chromium radiation Acta Cryst. D59, 1943-1957 (2003).

115. Abad-Zapatero, C. Notes of a Protein Crystallographer Our Unsung Heroes Structure 12, 523-527 (2004).

116. Blundell, T. L., Jhoti, H. & Abell, C. High-throughput crystallography for lead discovery in drug design. . Nat Rev Drug Discov. 1, 45-54 (2002).

117. Helliwell, J. R. (ed.) Macromolecular crystallography with synchrotron radiation (1992).

118. Sorensen, T. L., McAuley, K. E., Flaig, R. & Duke, E. M. New light for science: synchrotron radiation in structural medicine. Trends in Biotechnology 24, 500-508 (2006).

119. Drent, J. (ed.) Principles of protein X-Ray crystallography (1993).

120. Weik, M., Ravelli, R. B. G., Kryger, G., McSweeney, S., Raves, M., Harel, M., Gros, P., Silman, I., Kroon, J. & Sussman, J. L.Synchotron X-ray radiation produces specific chemical and structural damage to protein structures. Proc. Natl. Acad. Sci. USA 97, 623-628 (2000).

121. Ravelli, R. B. G. & McSweeney, S. M. The "fingerprint" that X-rays can leave on structures Structure 8, 315-328 (2000).

122. Burmeister, W. P. Structural changes in a cryo-cooled protein crystal owing to radiation damage. Acta Cryst. D56, 328-341 (2000).

123. Matsui, Y., Sakai K., Murakami M., Shiro Y., Adachi S., Okumura H. & Kouyama T. Specific Damage Induced by X-ray Radiation and Structural Changes in the Primary Photoreaction of Bacteriorhodopsin. J. Mol. Biol. 324, 469-481 (2002).

124. Adam, V., Royant, A., Niviere, V., Molina-Heredia, F. P. & Bourgeois, D. Structure of Superoxide Reductase Bound to Ferrocyanide and Active Site Expansion upon X-Ray-Induced Photo-Reduction. Structure 12, 1729-1740 (2004).

125. Baxter, R. H., Seagle, B. L., Ponomarenko, N. & Norris, J. R. Specific radiation damage illustrates light-induced structural changes in the photosynthetic reaction center. J. Am. Chem. Soc. 126, 16728-16729 (2004).

126. Carugo, O. & Carugo, K. D. When X-rays modify the protein structure: radiation damage at work. Trends Biochem Sci. 30, 213-219 (2005).

127. Garman, E. Cool data: quantity AND quality. Acta Cryst. D55, 1641-1653 (1999).

128. Garman, E. F. & Owen, R. L. Cryocooling and radiation damage in macromolecular crystallography. Acta Cryst. D62, 32-47 (2006).

129. Walsh, M. A., Dementieva, I., Evans, G., Sanishvili, R. & Joachimiak, A. Taking MAD to the extreme: ultrafast protein structure determination. Acta Cryst. D55, 1168-1173 (1999).

130. Ravelli, R. B. G., Leiros, H.-K. S., Pan, B., Caffrey, M. & McSweeney, S. Specific radiation damage can be used to solve macromolecular crystal structures. Structure 11, 217-224 (2003).

131. Teng, T.-Y. Mounting of crystals for macromolecular crystallography in a free-standing thin film. J. Appl. Cryst. 23, 387-391 (1990).

132. Arndt, U. W. & Wonacott, A. J. (eds.) The Rotation Method in Crystallography (Amsterdam: North Holland, 1977).

133. Dauter, Z. Data-collection strategies. Acta Cryst. D55, 1703-1717 (1999).

134. Ravelli, R. G. B., Sweet, R. M., Skinner, J. M., Duisenberg, A. J. M. & Kroon, J. STRATEGY: a program to optimize the starting spindle angle and scan range for X-ray data collection. J. Appl. Cryst. 30, 551-554 (1997).

135. Leslie, A. G. W. CCP4 Newslett. Protein Crystallogr. 32, 7-8 (1996).

136. Noble, M. E. M. PREDICT Package (1996) http://biop.ox.ac.uk

137. Otwinowski, Z. & Minor, W. Processing of x-ray diffraction data collected in oscillation model. Methods Enzymol. 276, 307-326 (1997).

138. Kabsch, W. Evaluation of Single-Crystal X-ray Diffraction Data from Position Sensitive Detectors. J. Appl. Crystallography. 21, 916-924 (1988).

139.. Adams, P. D., Grosse-Kunstleve R. W., Hung L.-W., Ioerger T. R., McCoy A. J., Moriarty N. W., Read R. J., Sacchettini J. C., Sauter N. K. & Terwilliger T. C. PHENIX: building new software for automated crystallographic structure determination. Acta Cryst. D58, 1948-1954 (2002).

140. Taylor, G. The phase problem. Acta Cryst. D59, 1881-1890 (2003).

141. Us6n, I. & Sheldrick, G. M. Advances in direct methods for protein crystallography. Curr. Opin. Struct. Biol. 9 (5), 643-648 (1999).

142. Perrakis, A., Morris, R. & Lamzin, V. S. Automated protein model building combined with iterative structure refinement. Nature Struct. Biol. 6, 458-463 (1999).

143. Terwilliger, T. C. Maximum-likelihood density modification using pattern recognition of structural motifs Acta Cryst. D57, 1755-1762 (2001).

144. Brunger, A. T. Free R value: a novel statistical quantity for assessing the accuracy of crystal structures. Nature 355, 472-475 (1992).

145. PDB, 2008 http://www.rcsb.org

146. ESRF, http://www.esrf.eu

147. Rossmann, M. G., E. Arnold Patterson and molecular-replacement techniques. International Tables for Crystallography, Vol. B. 230-263 (1993)

148. Terwilliger T.C., Grosse-Kunstleve R.W., Afonine P.V., Moriarty N.W., Adams P.D., Read R.J., Zwart P.H., and Hunga L.-W. Iterative-build OMIT maps: map improvement by iterative model building and refinement without model bias Acta Crystallogr D Biol Crystallogr. 64(Pt 5), 515–524 (2008)

149. Wang, B. C. Resolution of phase ambiguity in macromolecular crystallography. Methods In Enzymology 115, 90-112 (1985)

150. Nicholls D. G. & Ferguson S. J. (eds). Bioenergetics 3 (Academic Press, 2002)

151. http://www.chem.ed.ac.uk/chapman/p450.html

Aims of the project

In nature a large number of proteins are oxidoreductases. They participate in a wide spectrum of biological functions, including energy conversion (in photosynthesis and respiration), long-range electron transfer, drug detoxification, and catalyse a diverse range of biological reactions.

Investigating electron transfer reactions is fundamental in understanding how biological redox reactions are linked to the events of charge exchange, protein conformational change, chemical catalysis and energy conversion. Structural information at atomic resolution on electron-transfer proteins and enzymes is essential for gaining such understanding.

The redox proteins studied in this thesis are two dioxygenases (tryptophan 2,3-dioxygenase and indoleamine 2,3-dioxygenase), and mutant forms of nitric oxide synthase and flavocytochrome b_2. The main goal of the project has been to elucidate the architecture of these enzymes using x-ray crystallography techniques. In parallel with the structural investigations, functional studies have been carried out with the aim of elucidating all aspects of catalysis in the target enzymes.

Chapter 2

Materials and methods

Materials and methods

2.1 Growth and maintenance of bacterial strains

2.1.1 Bacterial strain

Escherichia coli BL21 (DE3) cells

2.1.2 Bacterial Plasmids

pXcR13-21.3: contains the *X. campestris* TDO coding sequences
pSoR52-21.1: contains the *S. oneidensis* SO4414 coding sequence
pCRNNR: contains the G586S rat NOS heme domain coding sequence
pKD209: contains the N42C *S. cerevisiae* flavocytochrome b_2 coding sequence
pKD212: contains the K324C *S. cerevisiae* flavocytochrome b_2 coding sequence
pKD213: contains the N42C:K324C *S. cerevisiae* flavocytochrome b_2 coding sequence

2.1.3 Site direct mutagenesis

All TDO and IDO constructs were created at Northeast Structural Genomics Consortium (NY, USA).

Neuronal NOS heme domain G586S mutant and flavocytochrome b_2 constructs were created by Dr. Caroline S. Miles, Institute of Molecular and Structural Biology, University of Edinburgh, UK.

2.1.4 Cell transformation

30 μl of competent cells BL21 *E. coli* were gently defrosted on ice before 5 to 10 ng of plasmid DNA in a volume of 1 to 5 μl were added and mixed. The mixture was incubated for 20 minutes on ice and then heat shocked at 42°C for exactly 45 seconds in a water bath before being quickly placed on ice again for 2 minutes. Pre-warmed SOC

medium (see table 2.1) (250 μl) was added before transferring the vial to 37°C for 1 hour in a shaker at 225 rpm. Susequently, different aliquots (10 to 100 μl) of the transformation mix were plated onto two LB plates containing the appropriate antibiotic concentration. A flame-sterilised loop was dragged across the surface of the culture and used to streak out the agar plate. The plates were incubated overnight at 37 °C in order to promote the growth of bacterial colonies.

2.1.5 Growth media

Luria-Bertani (LB) broth, Terrific Broth (TB), LB plates, SOC media (table 2.1).

2.1.6 DMSO stocks

From starter cultures small stocks for future use were prepared by adding 77 μl DMSO to 1 ml of cells dispersion (7% DMSO by volume). DMSO stocks were then stored at - 80°C until required and kept on ice while in use. The DMSO stocks were replaced periodically using colonies from freshly prepared LB agar plates.

2.1.7 Antibiotics

Stock solutions of antibiotics were prepared in Millipore water, passed through a 0.22 μm filter and stored at -20° C.

2.1.8 Growth of bacterial cultures

Liquid cultures of bacteria were grown in the appropriate broth by inoculating with a single colony using a sterile inoculating loop. Cultures of the bacterial strains were grown at the appropriate temperature.

Luria Bertani broth (LB)	For 1 litre: 10 g bacto tryptone 5 g yeast extract 5 g NaCl
Terrific broth (TB)	For 1 litre: 20 g bacto tryptone 10 g yeast extract 4 ml glycerol 2.6 g KH_2PO_4 4.3 g K_2HPO_4
Prepared using MilliQ ultrapure water (of resistivity 18 Ω cm^{-1}) and autoclaved sterilized	
LB Agar plates	15 gl^{-1} agar dissolved in LB Autoclaved agar was allowed to cool to room temperature. Prior to setting, agar was augmented with the appropriate antibiotic and poured into Petri dishes.
SOC medium	For 1 litre: 5 g bacto tryptone 5 g yeast extract 0.58 g NaCl 0.19 g KCl 1.2 g $MgSO_4$ 2.0 g $MgCl_2$ 3.6 g glucose

Table 2.1: Growth media and agar

2.2 Protein purification and storage

2.2.1 Cell extraction

Cells stocks were defrosted and suspended in the appropriate resuspension/lysis buffer allowing approximately 40 ml buffer for 25 g of cell pellet. Lysis of the *E. coli* cells was obtained by ultrasonication using a Sanyo Soniprep 150. Typically 8 sonication periods of 20 second each at 15 microns applied to a 40 ml cell suspension were required to distrupt cells. The cell suspension was kept on ice to prevent overheating. Eventually the lysate was pooled and cell debris separated by centrifugation at 20000 rpm for 1 hour at 4°C (Sorvall RC-5B centrifuge with a SS34 head). The clear supernatants containing the over-expressed target protein were collected and kept on ice prior to the chromatographic steps of purification.

2.2.2 Concentration and storage

Concentration of the purified proteins was obtained via centrifugation using a FALCON 6-300 centrifuge at 2000 rpm and Amicon Centriprep concentrators with a membrane size of 10-50 kDa. Protein concentration was spectrophotometrically measured. Pure and concentrated protein was divided into aliquots, flash frozen in liquid nitrogen and stored at -80°C until required.

2.2.3 Purity determination

The purity of the protein was measured at several stages by both analysis of UV/vis peak ratios and by SDS-PAGE (Sodium Dodecyl Sulfate-Poly Acrylamide Gel Electrophoresis).

2.2.4 Gel electrophoresis

SDS-PAGE was performed using NuPAGE® Novex 4-12 % Bis-Tris pre-cast polyacrylamide gels in combination with SeeBlue Plus 2® molecular weight markers. Assessment of the purity and integrity of the proteins was carried out through gel electrophoresis at various stages of the expression/purification. The protein samples were diluted using buffer as described in table 2.2 and boiled for 3 minutes to denature the protein and allow SDS binding. SDS bind with a constant ratio to the proteins as a function of their mass (1.4 g SDS: 1g protein) and shields their charges, the different distance to which each protein migrate depending only on its mass.

Sample buffer	25 µl NuPAGE® LDS 4x sample preparation buffer pH 8.4 25 µl diluted protein sample (>1 µM) or 50 µl dH_2O
Running buffer	NuPAGE® MES SDS 20x running buffer pH 7.0
Coomassie stain	50 ml dH_2O 40 ml methanol 10 ml acetic acid 1 ml Coomassie brilliant blue
Destain	50 ml dH_2O 40 ml methanol 10 ml acetic acid
All prepared using MilliQ ultrapure water (of resistivity 18 Ω cm^{-1}).	

Table 2.2: SDS PAGE buffers and stains

The central reservoir was filled with running buffer ensuring that the buffer level was beyond the sample loading wells. Aliquot of each sample (ranging from 5 to 15 µl) were loaded into the wells, reserving one well for SeeBlue Plus 2® molecular weight markers (5 µl). A potential difference (150 V, 120 mA and 60 W) was applied to the gel for the time necessary for the dye front to reach the bottom of the gel (approximately 1 hour). The voltage was then removed and the polyacrylamide gel was stained in Coomassie blue (Table 2.2) approximately for 15 minutes and destained for at least 1 hour to remove excess of stain. Coomassie blue binds to the protein, making a band visible, and the comparison between the positions of the blots with the markers give an indication about the presence of proteins and their size.

2.3 Buffer preparation

Buffer solutions were required for protein purification steps and crystallographic experiments. Buffers frequently used in this work are summarized in table 2.3.

Buffers composed of an acid and its salt were prepared by dissolving the acid form of the buffer in about ~ 60% of the water required for the final solution volume. The pH was adjusted using a strong base (i.e. NaOH). Preparation of buffers composed of a base and its salt, started with the base form and the pH was adjusted with strong acid (i.e. HCl). After correction to the desired pH, the volume was adjusted by addition of Millipore water. Buffer solutions were typically filtered using sterilizing-grade membrane filters (0.22 μm).

2.3.1 Sodium phosphate buffer

0.5 M sodium phosphate buffer was prepared by titrating 1 M NaH_2PO_4 with 1 M Na_2HPO_4 (both Sigma, prepared in Millipore water) to the desired pH and then the volume doubled by addition of Millipore water.

2.3.2 TrisHCl buffer

Ionic strength (μ or I) is a measure of the total concentration of ions in a solution, defined by:

$$\mu \text{ (or } I) = \tfrac{1}{2} \sum c_i z_i^2$$

where z_i is the charge of ionic species i and c_i is its concentration.

10 mM TrisHCl buffer was prepared by titrating 10 mM HCl (1 N standard solution, Sigma) to pH 7.5 with a saturated solution of Trizma® base, Sigma). Ionic strength was calculated and adjusted to I 0.10 by addition of NaCl (Fischer Scientific). All solutions were prepared in Millipore water.

Buffering system (all from Sigma)	**Buffering range**
Sodium citrate	3.0 - 6.2
Sodium acetate	3.7 - 5.6
2-(*N*-morpholino)ethanesulfonic acid (MES)	5.5-6.7
2-(bis(2-hydroxyethyl)amino)-2-(hydroxymethyl)propane-1,3-diol (Bis-Tris)	5.8-7.2
Piperazine-1,4-bis(2-ethanesulfonic acid) (PIPES)	6.1-7.5
4-(2-hydroxyethyl)piperazine-1-ethanesulfonic acid (HEPES)	6.8 – 8.2
Trizma®	7.0 - 9.00
N-(2-Hydroxyethyl)piperazine-N'-(3-propanesulfonic Acid) (HEPPS)	7.3-8.7
N,N-Bis(2-hydroxyethyl) Glycine (Bicine)	7.6-9.0
(N-Cyclohexylamino)ethane Sulfonic Acid (CHES)	8.6-10.0
3-(Cyclohexylamino)propanesulfonic Acid (CAPS)	9.7-11.1

Table 2.3: Commonly used buffers for protein purification and crystallization. Buffering ranges are referred at 25°C

2.3.3 Buffer degassing

The buffers used in anaerobic glove boxes were prepared as required and then degassed by nitrogen bubbling for at least 1 hour before introducing them into the anaerobic box. Protein samples degassed were kept in the box at least 1 day prior to use.

2.4 Protein crystallization

Crystals were growth by either hanging drops or sitting drops vapour diffusion methods [1-3], using 24 wells Linbro® Plate and Cryschem™ plates, respectively (both from Hampton Research).

Initial crystallization screenings were carried out using Hampton crystal screen Crystal Screen™, Crystal Screen 2™ and PEG/Ion Screen. In such screens, a number of different conditions for crystallization were tested.

When crystal nucleation was achieved, optimization of the condition was carried out varying protein concentration, pH, buffers and precipitants concentration.

2.4.1 Crystal mounting and flash-cooling

Mounted cryo-loop (Hampton Research or Molecular Dimensions ltd) assembly consists of three parts: the support, the pin and the base. The support is the interface between the loop to hold the crystal and the pin. The pin is attached to the base and the base is held on the goniometer head.

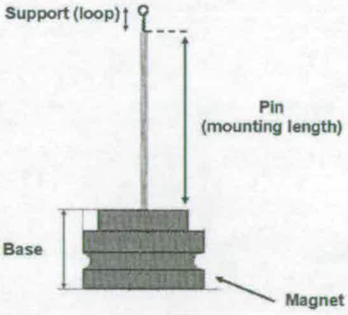

Fig 2.1: Mounted cryo-loop. The set involves a magnetic base (which attaches to goniometer head on the x-ray beam), a thin metal pin and a thin fiber loop of variable size (0.05-1.0 mm) where the crystal is mounted.

The choice of cryoprotectant was influenced by the mother liquor composition. In general the best choice of cryoprotectant was one that most closely resembles the composition of the mother liquor. The original mother liquor was generally supplemented with 23-30% glycerol.

Crystals of different proteins were sensitive to different protectants. Some cryo-protectants which were routinely tested are indicated in the following list:

- glycerol
- ethylene glycol
- 2-methyl-2,4-pentanediol (MPD)
- dimethyl sulfoxide (DMSO)
- polyethylene glycol (PEG) 400
- glucose, sucrose
- mineral oil

Crystals were washed in a solution containing the appropriate cryoprotectant. Some crystals needed to go through stepwise exposure to a cryoprotectant solution in order to prevent damage due to solvent change.

The freezing process was carried out rapidly in order to ensure the amorphous solidification of the solvent in and around the crystal and to allow isotropic freezing of the entire loop contents.

Two methods of flash-cooling were used:

1. Plunging the crystal into liquid nitrogen prior to transfer to the cold gaseous nitrogen stream or storage in liquid nitrogen.
2. Plunging the crystal into liquid propane prior to transfer to the cold gaseous nitrogen stream or storage in liquid nitrogen.

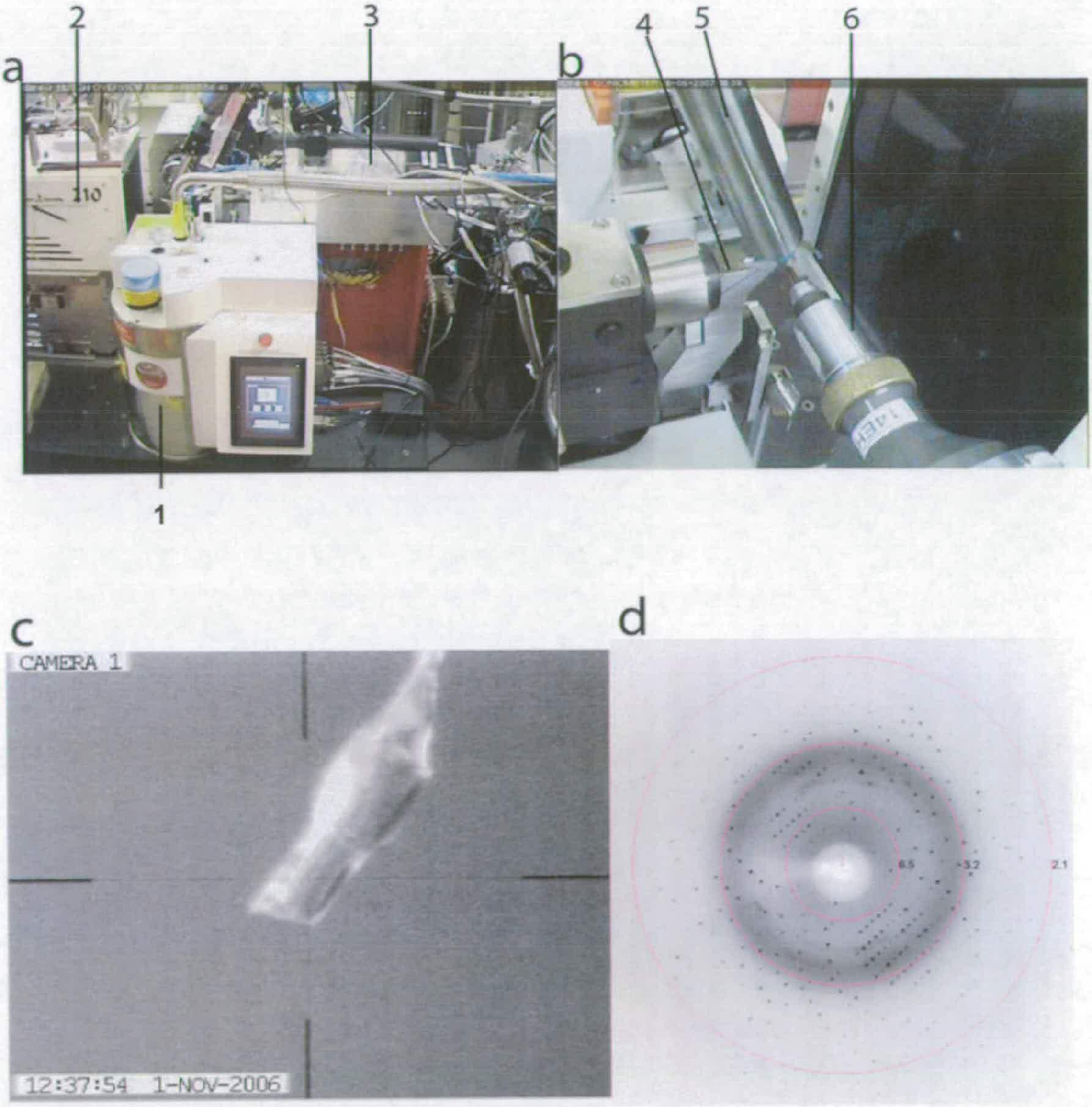

Fig 2.2: Data collection process at a synchrotron work station (pictures from Morgan, H. P. [4]*, with permission of the author).*

(a) Hutch view; (b) Crystal mounting area; (c) Crystal in a nylon loop; (d) Diffraction image. Labels; (1) Sample changing robot; (2) CCD x-ray detector; (3) Synchrotron beam source; (4) Pin-hole camera; (5) Nitrogen source(cryostream); (6) Goniometer head.

2.5 Data collection

All data were collected at Brookhaven National Laboratory at the X4A beam line, at the European synchrotron radiation facility (ERSF) in Grenoble, France on beam line BM14 UK MAD beam line) and BM30 and at SRS, Daresbury station 10.1. The data collection process is illustrated in figure 2.2. Data were typically collected as 1° (degree) oscillation images with the crystal maintained at 100 K in a nitrogen gas stream.

All the data collected were mainly processed through the CCP4 suite [5] XDS [6], or DENZO [7].

Diffraction images were indexed and integrated with MOSFLM [8], XDS [6], PHENIX [9]. MOSFLM was used to visualise the frames (fig 2.3).

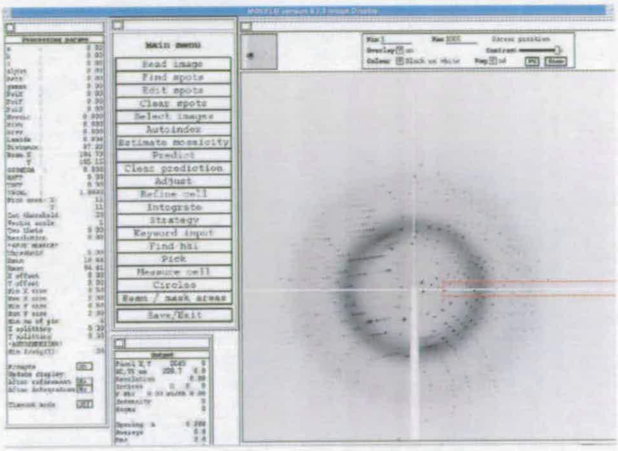

Fig. 2.3: Snapshot of the program MOSFLM.

Reflection data were scaled with CCP4 [8] or SCALEPACK [7] and all the reflections were merged into an average intensity scale. 5% of the collected reflections were assigned with an R_{free} flag [10]. Resolution settings were adjusted so that the I/σ for each resolution shell was greater then 1. The refinement was carried out using REFMAC5 [11] and PHENIX [9] was used for the rigid body refinement and the restrained refinement for the atomic anisotropic and positional B-factors for the models.

2.6 Visualization and manipulation of structures

All the molecular graphic figures displayed in this work were made using Pymol [12]. In chapter 3 and chapter 5 some figures were produced with Molscript [13] and rendered with Raster3D [14].

2.7 References

1. McPherson, A. (ed.) Preparation and Analysis of Protein Crystals (John Wiley & Sons., New York, 1982).

2. McPherson, A. (ed.) Crystallization of Biological Macromolecules (Cold Spring Harbor Laboratory Press, New York, 1999).

3. Segal, D. R. D. D. M. Protein crystallization. Micro techniques involving vapor diffusion. Methods Enzymol. 22, 266-269 (1971).

4. Morgan, H. P. in Institute of Structural and Molecular Biology (PhD thesis, University of Edinburgh, Edinburgh, 2008).

5. Potterton, E., McNicholas, S., Krissinel, E., Cowtan, K. & Noble, M. The CCP4 molecular-graphics project. Acta Cryst. D58, 1955-1957 (2002).

6. Kabsch, W. Evaluation of Single-Crystal X-ray Diffraction Data from Position Sensitive Detectors. J. Appl. Crystallography. 21, 916-924 (1988).

7. Otwinowski, Z. & Minor, W. Processing of x-ray diffraction data collected in oscillation model. Methods Enzymol. 276, 307-326 (1997).

8. Leslie, A. G. W. CCP4 Newslett. Protein Crystallogr. 32, 7-8 (1996).

9. Adams, P. D. et al. PHENIX: building new software for automated crystallographic structure determination. Acta Cryst. D58, 1948-1954 (2002).

10. Brunger, A. T. Free R value: a novel statistical quantity for assessing the accuracy of crystal structures. Nature 355, 472-475 (1992).

11. Murshudov, G., Vagin, A. A. & Dodson, E. Refinement of macromolecular structures by the maximum-likelihood method. Acta Cryst. D53, 240-255 (1997).

12. DeLano, W.The PyMOL molecular graphics system. DeLano Scientific LLC, San Carlos, CA, USA. http://www.pymol.org

13. Kraulis, P. MOLSCRIPT: a program to produce both detailed and schematic plots of protein structures. J Appl Crystallogr 24, 946-950 (1991).

14. Merritt, E. & Bacon, D. Raster3D: Photorealistic molecular graphics. Methods Enzymol 277, 505-524 (1997).

Chapter 3

Structural studies on tryptophan 2,3-dioxygenase and indoleamine 2,3-dioxygenase

Structural studies on tryptophan 2,3-dioxygenase (TDO) and indoleamine 2,3-dioxygenase (IDO)

3.1 Introduction

Tryptophan 2,3-dioxygenase (TDO) and indoleamine 2,3-dioxygenase (IDO) catalyze the oxidative cleavage of the L-tryptophan (L-Trp) pyrrole ring to form N-formyl-L-kynurenine (fig 3.1). In mammals, this reaction represents the first and rate-limiting step in L-Trp catabolism through the kynurenine pathway [1-3].

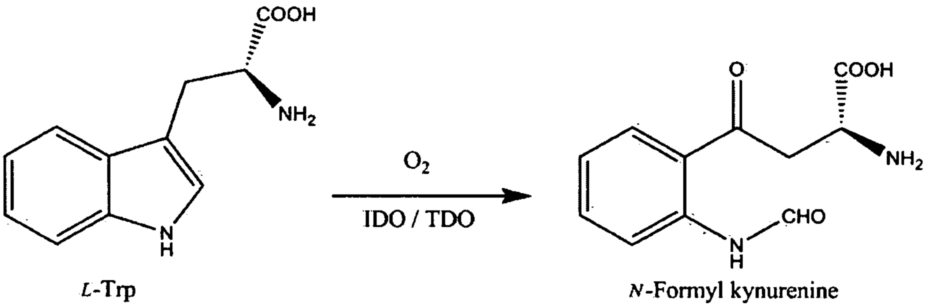

Fig 3.1: The reaction catalyzed by IDO and TDO

The kynurenine pathway accounts for the processing of over 90% of L-Trp utilised by humans [4]. It is important not only as a source of metabolites, but also due to the effect of IDO / TDO on the local tryptophan concentration. The build up of pathway metabolites due to IDO / TDO induction, or poor metabolism further along the pathway, can lead to numerous physiological conditions [5]. High levels of quinolinic acid and L-kynurenine in cerebrospinal fluid [6] may be involved in various neurological disorders (e.g. cerebral malaria, ischemic brain injury, multiple sclerosis and AIDS-related dementia [6-8]). Concentrations of these metabolites increase with the severity of neurological dysfunction or brain injury under a wide range of inflammatory conditions. For example, the kynurenine pathway metabolites 3-hydroxyanthranillic acid and 3-hydroxykynurenine are UV filters that can bind to lens proteins in the eye, and they have been implicated in cataract formation when present at high concentrations [9] (fig 3.2).

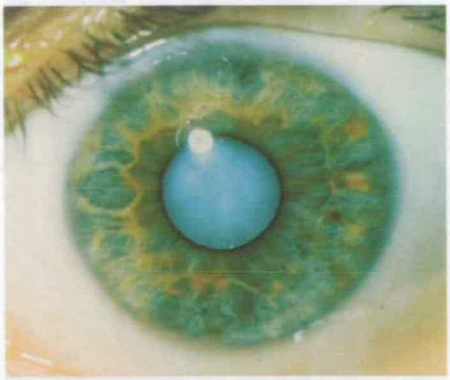

Fig 3.2: Kynurenilation of lens proteins is involved in age-related cataract formation. Picture from [10].

In addition, IDO has been implicated in a diverse range of physiological and pathological conditions, including suppression of T cell proliferation [11], maternal tolerance to allogenic fetus [12, 13], and immune escape of cancers [14], and is an attractive target for drug discovery against cancer and autoimmune and other diseases [2, 15-17]. IDO and TDO play a role in the physiological regulation of tryptophan distribution in the human body, also influencing serotogenic regulation [18]. The local depletion of tryptophan by enzymatic action is mainly associated with an antimicrobial response involving IDO or TDO, or immune regulation by IDO [19]. Some pathogens are sensitive to tryptophan degradation including viruses (Herpes viruses), intracellular bacteria (*Chlamydia* and *Rickettsia*) and extracellular bacteria (*Staphylococci)*, and this may be an effective mechanism for controlling their ability to proliferate.

3.2 Discovery of IDO and TDO

TDO was initially discovered in the 1930s [20]. It has been reported in both eukaryotes (human [21], rat [4] and rabbit [22]), and prokaryotes (*Xanthomonas campestris* [23], *Ralstonia metallidurans, Pseudomonas fluorescens* [24, 25]). Expression of TDO in mammals is normally restricted to the liver, but it has been identified in the brain and epididymis of some species, and in some tissues its production can be induced in response to stimuli.

IDO was first isolated from rabbit intestine in 1967 [26] and it has been isolated in many eukaryotes. In animals IDO is expressed throughout the body, except for in the liver [27-29]. Its production can be induced in many tissues in response to various stimuli and this specific expression in different cellular locations suggests that IDO has a distinct role from TDO [13].

3.3 Bacterial IDO and TDO

IDO and TDO are members of a family of enzymes that also includes sIDO from *Shewanella oneidensis* [23] and the second enzyme in the pyrrolnitrin biosynthetic pathway PrnB from *Pseudomonas fluorescens* [30], although dioxygenase activity has not been yet demonstrated for either of these. Homology between members of this family is apparent from their three-dimensional structures and from the conservation of certain amino acids in their active sites, but sequence alignment based on their structures often gives an identity of approximately 10 % [23].

Bacteria are also believed to use members of this family for the aerobic metabolism of L-Trp via the kynurenine pathway, however prokaryotic IDO-like proteins bear little sequence similarity to eukaryotic IDO proteins and very little is yet known about them.

3.4 Amino acid sequence information and substrate specificity of IDO and TDO

IDOs and TDOs from a number of eukaryotic species have been sequenced and can be found in protein databases.

Despite catalyzing identical biochemical reactions, the sequence similarity between TDO and IDO is extremely low. IDO is monomeric and contains approximately 400 amino acids, displaying high sequence similarity between eukaryotic species. TDO is homotetrameric, and eukaryotic TDOs contain approximately 400 amino acids per monomer, while prokaryotic TDOs contain approximately 300 amino acids. Sequence identities between prokaryotic and eukaryotic TDOs are around 20-30% demonstrating the remarkable evolutionary conservation of this enzyme [23, 31].

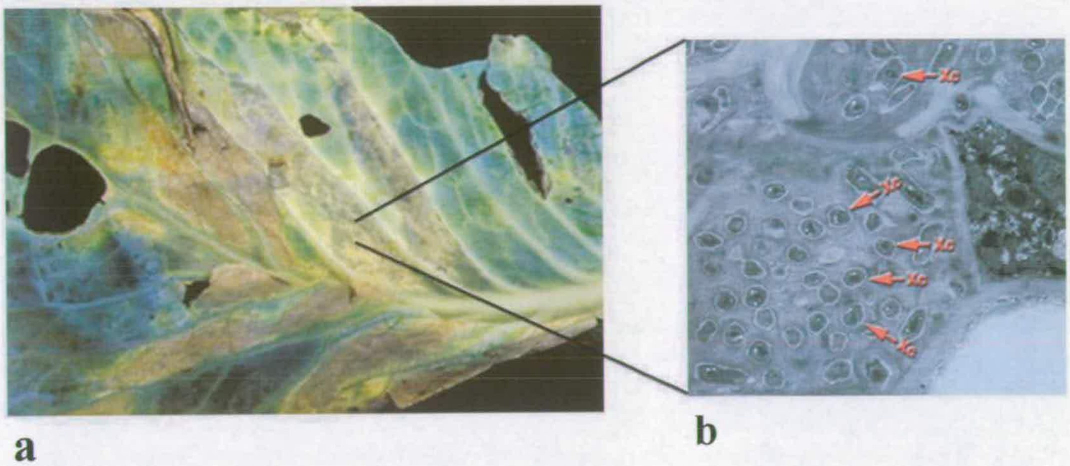

Fig 3.3: a) Bacterial spots on green leaf crucifer caused by Xanthomonas campestris, picture from [32], b) Xanthomonas campestris (Xc), picture from [33]

Xanthomonas campestris (Xc) is a plant pathogen gram-negative aerobic bacterium (fig 3.3). It infects crucifers such as Brassica and Arabidopsis, causing lesions that extend toward the base of the leaf resulting in extensive wilting and necrosis as the infection advances [34] . *Xanthomonas campestris* TDO shares 34% sequence identity with human TDO (fig 3.4).

```
Xc_TDO -----------------MPVDKNLRDL-EPGIHTDLEGRLTYGGYLRLDQLLSAQQPLSE
Hs_TDO MSGCPFLGNNFGYTFKKLPVEGSEEDKSQTGVNRASKGGLIYGNYLHLE-VLNAQELQSE

Xc_TDO PAH---HDE-MFIIQHQTSELWLKLLAHELRAAIVHLQRDEVWQCR---KVLARSKQV--
Hs_TDO TKGNKIHDEHLFIITHQAYELWFKQILWELDSVREIFQNGHVRDERNMLKVVSRMHRVSV

Xc_TDO -LRQLTEQWSVLETLTPSEYMGFRDVLGPSSGFQSLQYRYIEFLLGNKNPQML-------
Hs_TDO ILKLLVQQFSILETMTALDFNDFREYLSPASGFQSLQFRLLENKIGVLQNMRVPYNRHYR

Xc_TDO -------QVFAYDPAGQARLREVLEA-----PSL------------------YEEFLRYL
Hs_TDO DNFKGEENELLLKSEQEKTLLELVEAWLERTPGLEPHGFNFWGKLEKNITRGLEEFIRIQ

Xc_TDO ARFGHAIPQ----QYQARDWTAAHVADD-----------------TLRPVFERIYENTDR
Hs_TDO AKEESEEKEEQVAEFQKQKEVLLSLFDEKRHEHLLSKGERRLSYRALQGALMIYYREEPR

Xc_TDO YWREYSLCEDLVDVETQFQLWRFRHMRTVMRVIGFKRGTGGSSGVGFLQQALALTF-FP-
Hs_TDO FQVPFQLLTSLMDIDSLMTKWRYNHVCMVHRMLGSKAGTGGSSGYHYLRSTVSDRYKVFV

Xc_TDO ELFDVRTSVGVDNRPPQGSADAGK------------------R
Hs_TDO DLFNLSTYLIPRHWIPKMNPTIHKFLYTAEYCDSSYFSSDESD
```

Fig 3.4: Amino acids sequence alignment of Xanthomonas campetris (Xc) (in blue) and human (Hs) TDO (in black). Xc TDO shares 34% sequence identity with Hs TDO. In *magenta are highlighted the conserved residues.*

TDO is highly specific for L-Trp and related derivatives such as 5- and 6-fluoro-Trp as the substrate (fig 3.5, yellow background). In comparison, IDO shows activity toward a larger collection of substrates, including L-Trp, D-tryptophan (D-Trp), serotonin, and tryptamine [3] (fig 3.5), although the K_m for D-Trp is ~100-fold higher than that for L-Trp [29].

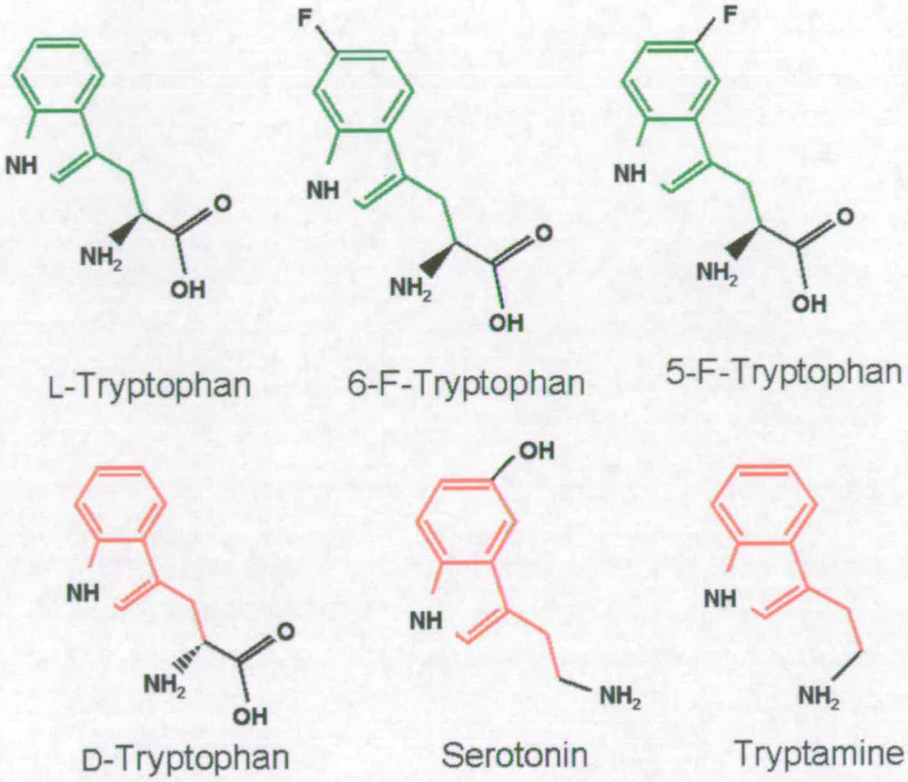

Fig 3.5: TDO can use substrates coloured in green, but not those coloured in red. IDO can use all substrates (red and green).

3.5 Indoleamine 2,3-dioxygenase

The structure of human IDO in the catalytically inactive ferric state in complex with the inhibitor 4-phenylimidazole (4-PI) has recently been reported [35, 36]. Although this structure provides information about potentially important active site residues, the inhibitor is coordinated to the heme iron and does not provide any information regarding Trp or oxygen binding (fig 3.6b).

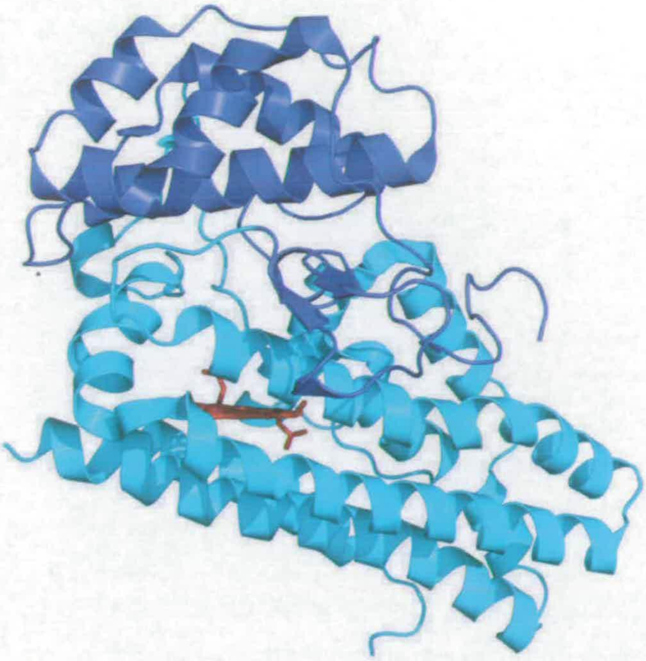

Fig 3.6: Human indoleamine dioxygenase (IDO) crystal structure at 2.3 Å resolution (PDB entry 2D0T). The smaller N-terminal domain is shown in blue, and the larger domain in cyan. The heme is shown in sticks, colored in red.

The structure of human IDO revealed that the enzyme is folded into two distinct domains (fig 3.6). The larger (and C-terminal) of these is completely helical (fig 3.6 in blue), with thirteen α-helices and two 3_{10}-helices, and belongs to the family of IDO-like protein folds [37]. The smaller N-terminal domain (fig 3.6 in blue) consists of six α-helices, two short β-strands, and three 3_{10}-helices. The heme is bound within the larger domain, but is close to the domain interface. The loop region connecting the two domains (residues 250-267) lies above the distal face of the heme, close to the active site.

The inter-domain contact is extensive, with a buried surface area of 3100 $Å^2$.

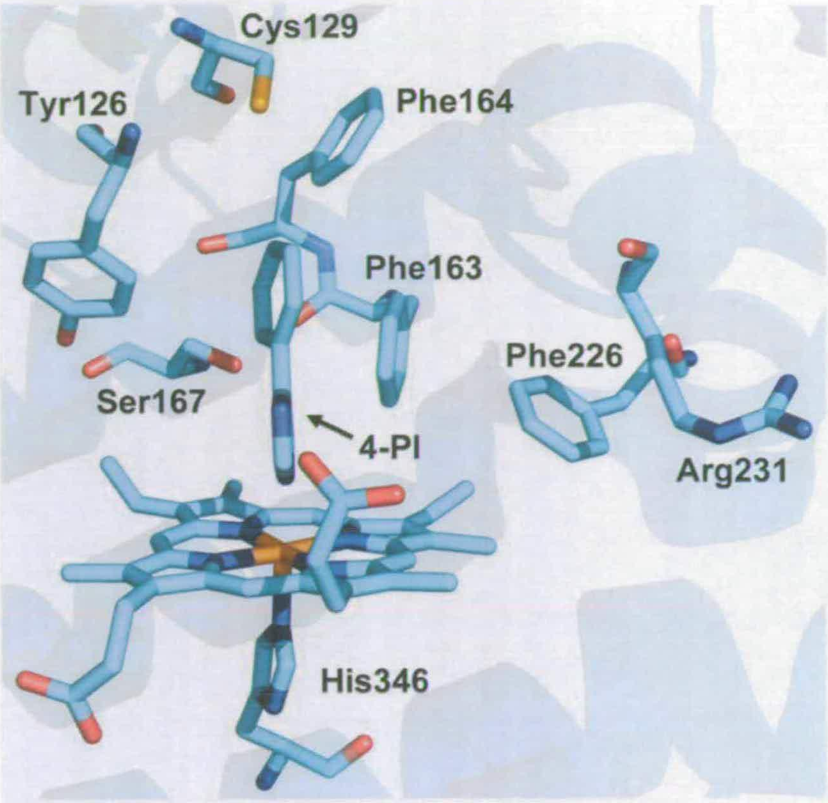

Fig 3.7: The active site of human IDO. Potentially important active site residues are shown, along with the bound inhibitor 4-PI.

The heme pocket (fig 3.7) is formed by residues from the small domain (Tyr126, Cys129) and from the large domain (Phe163, Phe164, Phe226, Arg231, Ser263, Gly261 and Gly262). Phe163 interacts with 4-PI. Ser167 is one of the closest residues to the inhibitor. Phe164 and Cys129 contribute to the hydrophobic wall of the active site pocket, but are too distant to interact with the inhibitor. Due to the nature of the inhibitor bound to the active site, the structure provides little information on the binding mode of L-Trp (or any substrate).

To provide direct insight into substrate recognition and catalysis by IDO and TDO, we sought to obtain the crystal structures of the oxidised and reduced forms of TDO from *X. campestris* in binary complex with the substrate L-Trp or 6-fluoro-D/L-tryptophan (6-F-Trp). Furthermore, we obtained the structure of the active reduced form of a putative IDO from *Shewanella oneidensis*. The description of the above mentioned structures will be the subject of this chapter.

3.6 Results

3.6.1 Expression of *Xanthomonas campestris* TDO

Full-length *X. campestris* TDO construct was created at the centre for Advanced Biotechnology and Medicine (Northeast Structural Genomics Consortium), Rutgers University, Piscataway, NJ 08854._The expression plasmid was produced by cloning the the full-length *Xanthomonas campestris* TDO (Q8PDA8_XANCP, NESG ID XcR13) into a pET21d (Novagen) derivative, generating the plasmid pXcR13-21.3, with a C-terminal hexa-histidine tag, as described in Acton, *et al.* (2004)[38]. The resulting XcR13 contains 8 (LEHHHHHH) nonnative residues at its C terminus. The construct sequence was verified by standard DNA sequence analysis. *Escherichia coli* BL21 (DE3) pMGK cells, a rare codon-enhanced strain, were transformed with pXcR13-21.3. Two single isolates were cultured individually in either LB containing hemin (7 μM final concentration) for the holoenzyme [39], or MJ9 minimal media [40], containing selenomethionine, lysine, phenylalanine, threonine, isoleucine, leucine, and valine for selenomethionyl XcR13 [41]. Initial growth was carried out at 37 °C until the OD_{600} of the culture reached 1.0 units. The incubation temperature was then decreased to 17°C, and protein expression was induced by the addition of IPTG at a final concentration of 1 mM. After overnight incubation at 17 °C, the cells were harvested by centrifugation.

3.6.2 Purification of *Xanthomonas campestris* TDO

Native heme-containing and selenomethionyl XcR13 protein was purified by standard methods. The cell pellet was resuspended in lysis buffer (Tris / HCl pH 7.5, 500 mM NaCl, 40 mM imidazole, and 1 mM TCEP) and disrupted by sonication. Cell debris was removed by centrifugation at 26,000 × g for 45 min at 4 °C. The XcR13 protein, in its separate supernatant, was then purified using an AKTA-Express (GE Heathcare) two-step purification strategy. Briefly, the His-tagged protein in the supernatant was loaded onto a HisTrap HP column (GE Heathcare), washed with lysis buffer, and eluted with the same buffer, containing 250 mM imidazole, into a 10-ml sample loop. The loop content was then injected onto a gel-filtration column (Sephadex G75; GE Heathcare), and eluted in buffer 2 (10 mM Tris / HCl (pH 7.5), 5 mM DTT, 100 mM NaCl, 0.2% (w/v) NaN_3). The purified XcR13 protein resulting from gel filtration was concentrated to 5-10 mg/ml, while sample purity (~ 97 %) and molecular weight were verified by SDS-PAGE (fig 3.8) and MALDI-TOF mass spectrometry (data not shown). All steps in the preparation of heme-containing proteins used buffers without the DTT reducing agent.

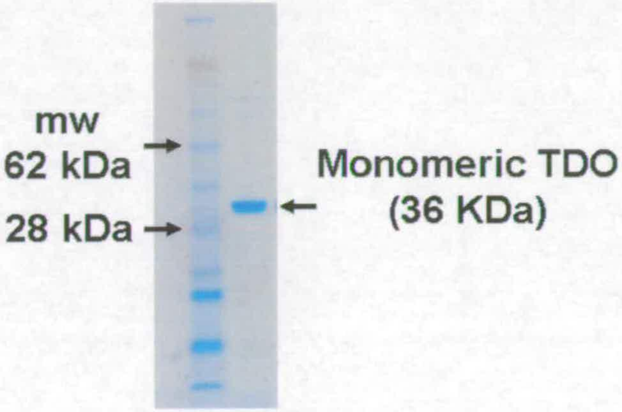

Fig 3.8: Purified Xc TDO. Samples are analyzed by 4-12% SDS-PAGE and visualized by Coomassie staining.

Protein and heme concentrations were determined by the Bradford [42] and pyridine hemochrome methods [43], respectively. An extinction coefficient of $\varepsilon_{404} = 180500\ M^{-1}\ cm^{-1}$ per protomer was calculated for ferric of *X. campestris* TDO.

3.6.3 Protein crystallization

Crystals of TDO were produced by the hanging-drop vapor-diffusion method [44] at 18°C, for the apoenzyme the reservoir solution comprised 50 mM Tris / HCl pH 7.0, 13% (w/v) PEG 3350, 100 mM magnesium chloride, and 5 mM DTT. In the case of the holoenzyme the well solution was 50 mM MES pH 6.15, 12% (w/v) PEG 1000, and 60 mM manganese chloride.

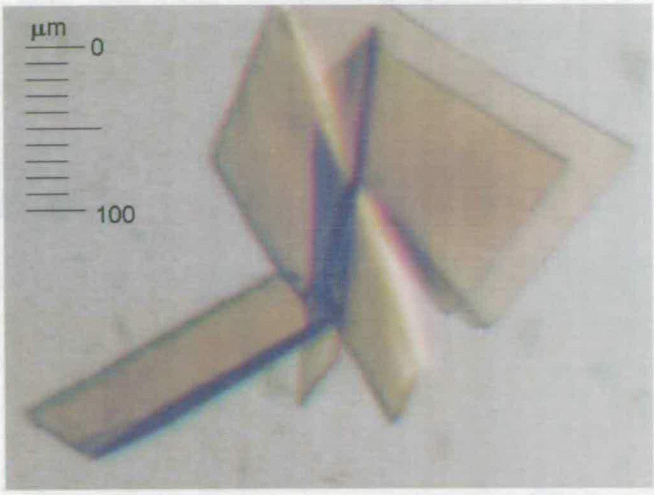

Fig 3.9: Crystals of the holoenzyme TDO grown using a reservoir comprising 50 mM MES pH 6.15, 12% (wt/vol) PEG 1000, and 60 mM manganese chloride

The enzyme was at 20 mg/ml concentration. Crystals of the apoenzyme (without heme) were cryoprotected in paratone, and those of the holoenzyme (fig 3.9) in mother liquor supplemented with 25% (v/v) glycerol, before being flash-cooled for data collection at 100 K.

In order to obtain the structure of TDO in the ferrous state, the crystallization process was conducted in a Belle Technology (Belle Technology, Dorset, U.K.) anaerobic glove box (fig 3.10) with the O_2 concentration maintained < 2 ppm.

Prior to crystallization, the protein was chemically reduced by the addition of sodium dithionite. Excess sodium dithionite was removed by gel filtration (Sephadex G25 column) before crystallization (fig 3.11). The gel filtration buffer contained 50 mM Tris / HCl pH 8.0, 1 mM EDTA, and 2 mM L-tryptophan or 8 mM 6-fluoro-D/L-tryptophan (6-F-Trp).

Crystals of TDO were grown by the sitting-drop vapour-diffusion method [44] with a well solution comprising 100 mM pH 6.3 MES, 10-12% (w/v) PEG 4000, 60 mM $MnCl_2$, 10 mM sodium dithionite and 2 mM L-tryptophan or 8 mM 6-F-Trp. All crystallization solutions were prepared outside the anaerobic box and degassed to exclude oxygen from solutions before the crystallization experiment as described in materials and methods in the section 2.3.3. Furthermore, all solutions were allowed to equilibrate inside the anaerobic box for at least 1 day to make sure they were oxygen-free.

Crystals appeared after 4 days and slowly reached maximum size in four weeks Before mounting in cryo-loops (Molecular Dimensions ltd) and flash-cooling in liquid nitrogen, crystals were immersed in a cryoprotectant solution composed of mother liquor (with L-Trp concentration increased to 50 mM) supplemented with 23% (v/v) glycerol.

Fig 3.10: Belle technology anaerobic glove box. One side of the anaerobic box is adapted for the setting up of the crystallization experiments, while the other is fitted with a microscope for the observation and the manipulation of crystals

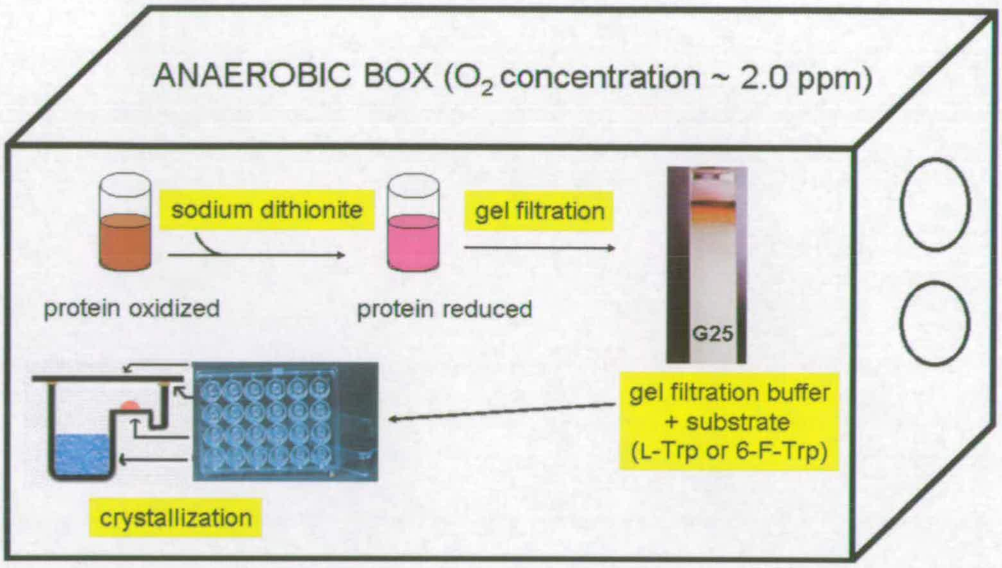

Fig 3.11: Oxidised pure protein was chemically reduced inside the glove box with sodium dithionite. Before crystallization, sodium dithionite was removed using a gel filtration column (Sephadex G-25) and eluted with a buffer containing L-*Trp or 6-F-Trp.*

3.6.4 Data collection and processing

X-ray diffraction data were collected on an ADSC CCD at the X4A beam line of the NSLC at Brookhaven National Laboratory (NY) for the holoenzyme of TDO, on a Mar225 detector at the 21BM beam line at the Advanced Photon Source (Argonne, IL) for the apo enzyme of TDO, and on a Mar225 detector at the BM14 beamline at ESRF (Grenoble, France) for the binary complexes. The diffraction images were processed and scaled with the HKL package [45]. The data processing statistics are summarized in Table 3.1.

3.6.5 Structure determination and refinement

Crystals of the apoenzyme of TDO belong to space group $P2_12_12_1$, with cell dimensions *a* = 89.7 Å, *b* = 110.2 Å, and *c* = 149.4 Å. There is a single tetramer of TDO in the asymmetric unit.

Crystals of the holoenzyme of TDO (fig 3.9) belong to space group $P2_12_12_1$, with cell dimensions *a* = 88.9 Å, *b* = 109.4 Å, and *c* = 125.5 Å. Again there is a single tetramer of TDO in the asymmetric unit.

Crystals of the binary complex of TDO (with L-Trp or 6-F-Trp) belong to space group $P3_121$, with cell dimensions $a = b = 114.1$ Å, and $c = 96.2$ Å. In this case, the asymmetric unit contains two TDO monomers.

The structure of the apoenzyme of TDO was determined by the selenomethionyl single-wavelength anomalous dispersion method (SAD) (PDB entry 1YW0) [46]. The selenium sites were located with SnB [47], and the reflection phases were calculated with Solve/Resolve [48]. The structures of the holoenzymes and the binary complexes were determined by the molecular replacement method, with the programs COMO [49] and AMoRe [50]. The atomic models were built with the programs O [51] and TURBO-FRODO [52], and the structure refinement was carried out with CNS [53].

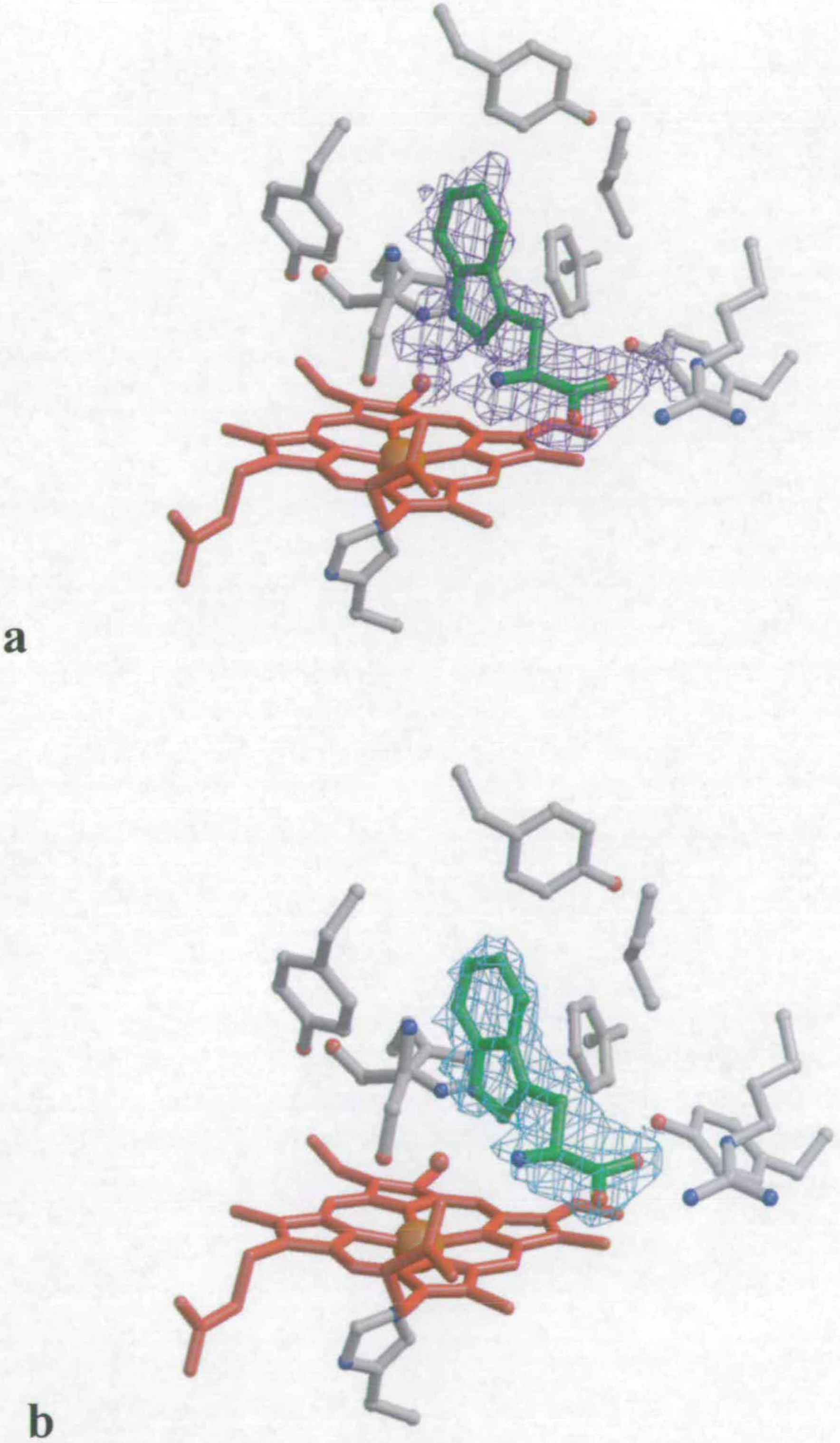

Fig 3.12: Active site: F_o –F_c prior to ligand fitting (a) and 2 F_o –F_c TDO L-Trp complex (b) Figure produced with Molscript [54] *and rendered with Raster3D* [55].

Protein	TDO (holoenzyme)	TDO (holoenzyme)	TDO (holoenzyme)	TDO (apoenzyme)
Beam line	ESRF BM14	ESRF BM14	NSLS X4A	APS 21BM
Ligand	L-Trp	6-F-Trp	None	None
PDB entry	2NW8	2NW9	2NW7	1YW0
Space group	$P3_121$	$P3_121$	$P2_12_12_1$	$P2_12_12_1$
Cell dimensions (Å)	$a = b = 114.1$ $c = 96.2$ Å	$a = b = 114.1$ $c = 96.2$ Å	$a = 88.9$, $b = 109.4$, $c = 125.5$	$a = 89.7$, $b = 110.2$, $c = 149.4$
Resolution (Å)	24.5-1.6 (1.66-1.60)*	26.3-1.8 (1.86-1.80)*	46.4-2.6 (2.69-2.60)*	30.0-2.7 (2.8-2.7)*
no. of unique reflections	94048	67279	37833	71669
completeness (%)	87 (65)*	87 (61)*	72 (54)*	82 (68)*
$I/[\sigma(I)]$	23.8 (2.93)*	19.97 (2.5)*	10.4 (2.74)*	n/a
R_{merge} (%)[a]	6.9 (52.7)*	8.6 (60.9)*	13.0 (32.3)*	16.6 (74.0)*
R_{work} (%)[b]	17.1 (18.9)*	16.6 (17.9)*	25.7 (25.7)*	25.0 (32.1)*
R_{free} (%)[c]	18.9 (22.0)*	18.4 (21.1)*	26.3 (26.2)*	29.4 (35.1)*
rmsd from ideal values				
bond lengths (Å)	0.005	0.005	0.008	0.011
bond angles (deg)	1.0	1.0	1.2	1.6
Ramachandran analysis				
most favoured (%)	92.4	91.2	88.9	86.9
additionally allowed (%)	7.6	8.8	11.1	13.1
no. of waters included in refinement	708	596	142	105

Table 3.1: Summary of crystallographic information; * *Values in parentheses represent statistics for the highest resolution shell* [a] $R_{merge} = \Sigma_h\Sigma_i|I(h) - I_i(h)|/\Sigma_h\Sigma_i I_i(h)$, *where* $I_i(h)$ *and* $I(h)$ *are the ith and mean measurement of reflection h, respectively.* [b] $R_{work} = \Sigma_h|F_o - F_c|/\Sigma_h F_o$, *where* F_o *and* F_c *are the observed and calculated structure factor amplitudes of reflection h, respectively.* [c] R_{free} *is the test reflection data set, 5 % selected randomly for cross validation during crystallographic refinement.*

3.7 Structure of TDO

The structure of *X. campestris* TDO monomer contains 12 helices (named αA through αL) and no β-strands (fig 3.13).

TDO is an intimately associated tetramer and ~ 4500 Å^2 of the surface area of each monomer is buried in the tetramer. Helices αB and αC are located in the extensive, mostly hydrophobic interface between two of the monomers.

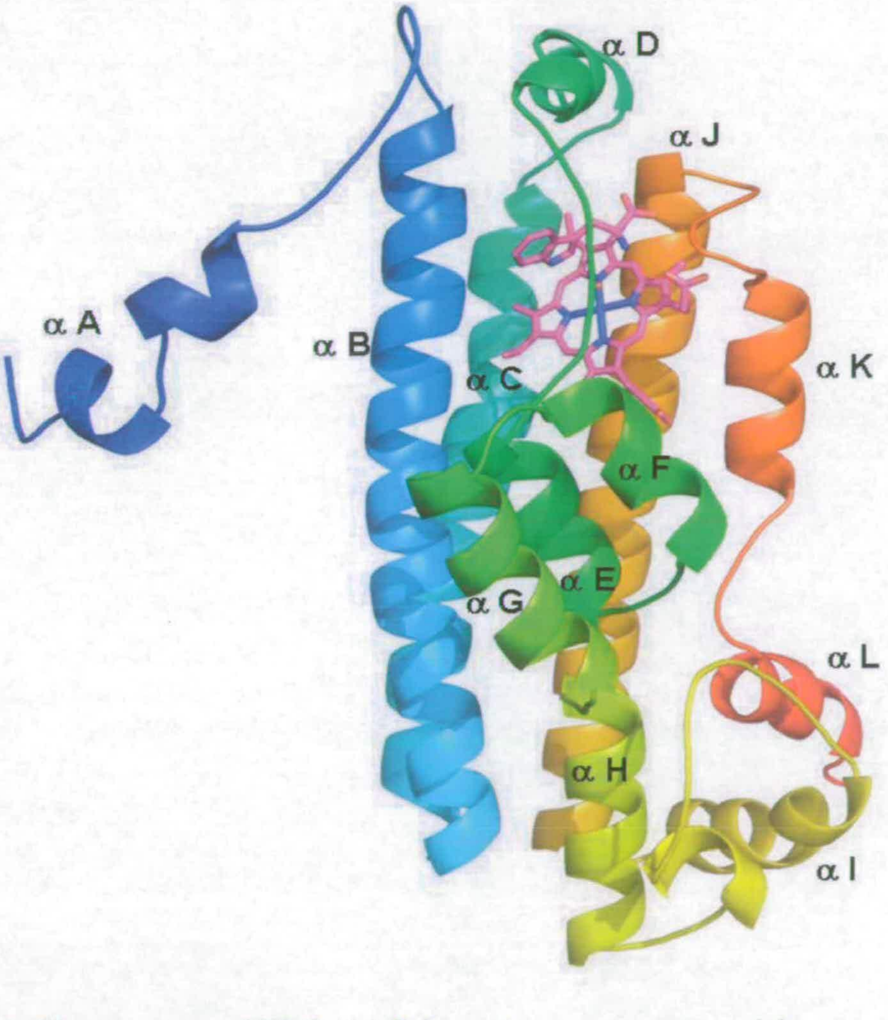

Fig 3.13: The structure of TDO. (a) Schematic representation of the structure of the monomer of X. campestris TDO. The α-helices are labelled. Heme and L-Trp are represented with sticks and shown in magenta. Gradient colour scheme: N-terminus to C-terminus, blue to red

The N-terminal segments (residues 21–40, including helix αA) of the two monomers are intimately associated with the adjacent monomer, which is important for catalysis by TDO because several residues in this segment are part of the binding site for the tryptophan substrate in the active site.

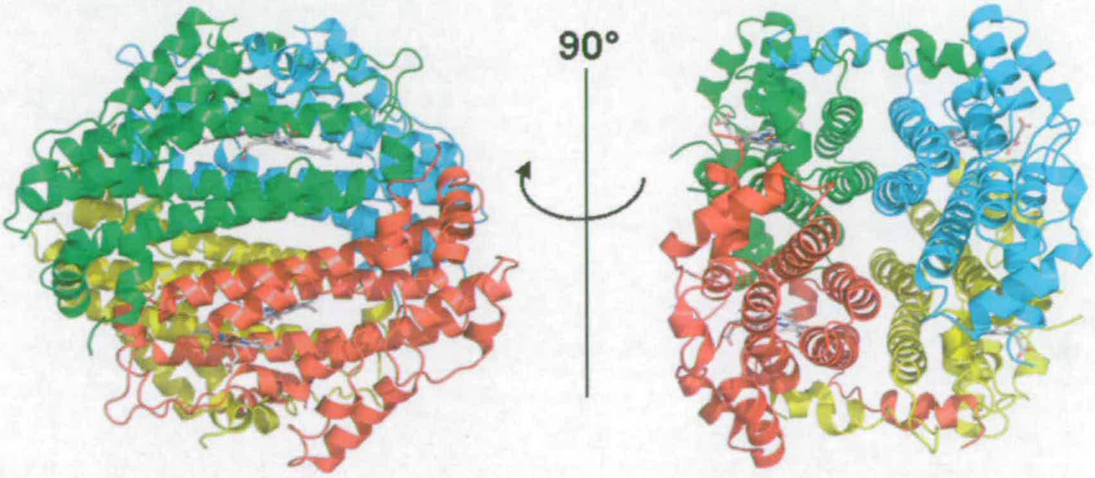

Fig 3.14: Representation of the tetramer of X. campestris TDO. The four monomers are coloured in yellow, cyan, red, and green) (PDB entry 2NW7).

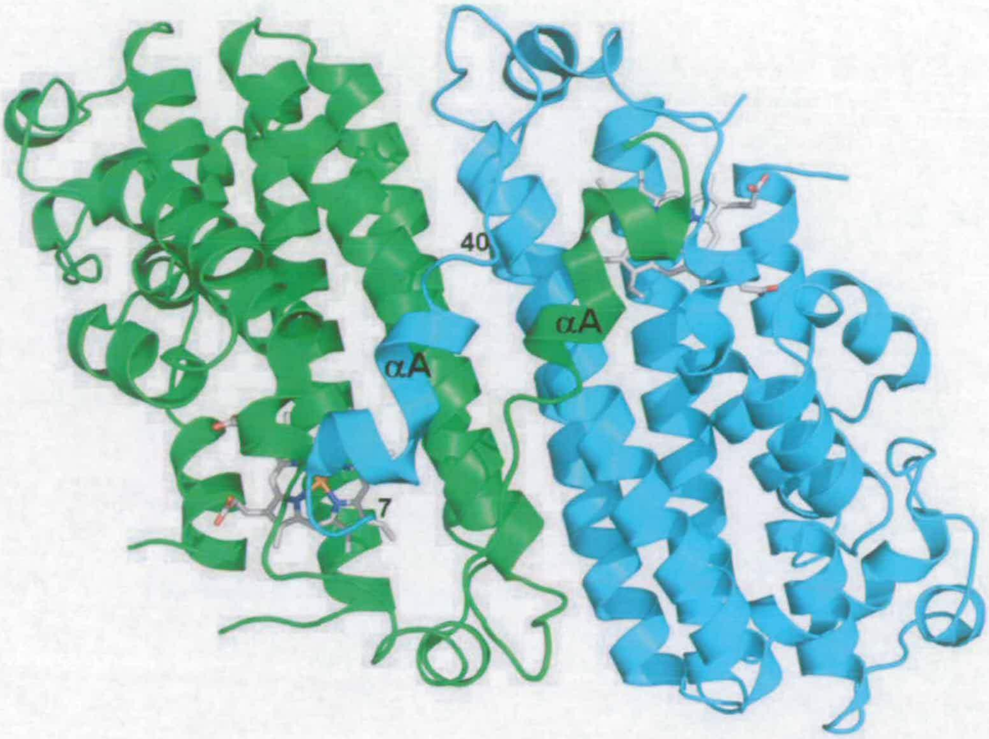

Fig 3.15: The structure of ferric X. campestris TDO. The 'dimer of dimers' arrangement can be seen, with one monomer coloured green and the other cyan. Residues 7-40 of the αA helix from one monomer interact intimately with the other monomer. Heme groups are shown in grey. This is the substrate free structure (PDB entry 2NW7*).*

3.7.1 Binding Mode of the L-Trp Substrate to TDO

The structure of the binary complex defines the molecular mechanism for the recognition of the L-Trp substrate by TDO. Clear electron density was observed for heme and L-Trp in the active site based on the crystallographic analysis at 1.6 Å resolution (fig 3.12 and fig 3.16).

The L-Trp substrate is located in a pocket over the distal face of the heme and has interactions with residues in helices αB and αD, and the αD–αE and αJ–αK loops.

The carboxylate group of L-Trp is recognized by bidentate ion-pair interactions with the side chain of Arg117 (in helix αD).

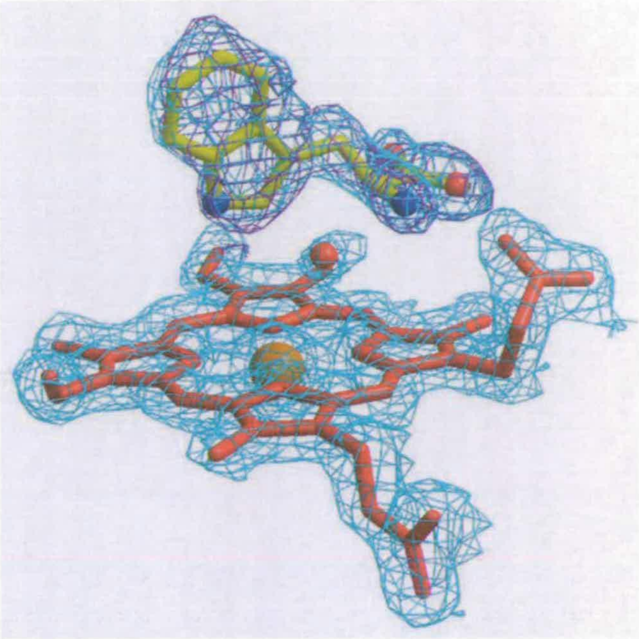

Fig 3.16: In cyan is the final $2F_o$–F_c electron density at 1.6 Å resolution for heme, L-Trp, and water in the active site contoured at 1σ.. In purple is the F_o–F_c omit map contoured at 3σ. Figure produced with Molscript [54] and rendered with Raster3D [55].

The carboxylate group is also hydrogen-bonded to the side chain hydroxyl of Tyr113 (helix αD) and the main-chain amide of Thr254 (αJ-αK loop). The ammonium moiety of L-Trp is recognized by the 7-propionate side chain of the heme group, and is also hydrogen-bonded to the side chain hydroxyl of Thr254. The indole ring is located ~3.5 Å above and perpendicular to the heme and is held in place by van der Waals interactions with the side chains of Phe51 (helix αB) and several other hydrophobic residues, including Tyr24, Tyr27, and Leu28 from the N-terminal segment of another monomer of the tetramer (fig 3.17, Leu28, Tyr24, and Tyr27, all in blue). In addition, the N1 nitrogen of the indole ring is hydrogen-bonded to the side chain of His55 (helix αB). The hydrophobic characteristics of the active site pocket surrounding the indole ring of L-Trp in comparison with the hydrophilic residues forming the hydrogen bond network around carboxylate group and ammonium moiety of the substrate are highlighted in fig 3.18 and fig 3.19, with the electrostatic surface representation.

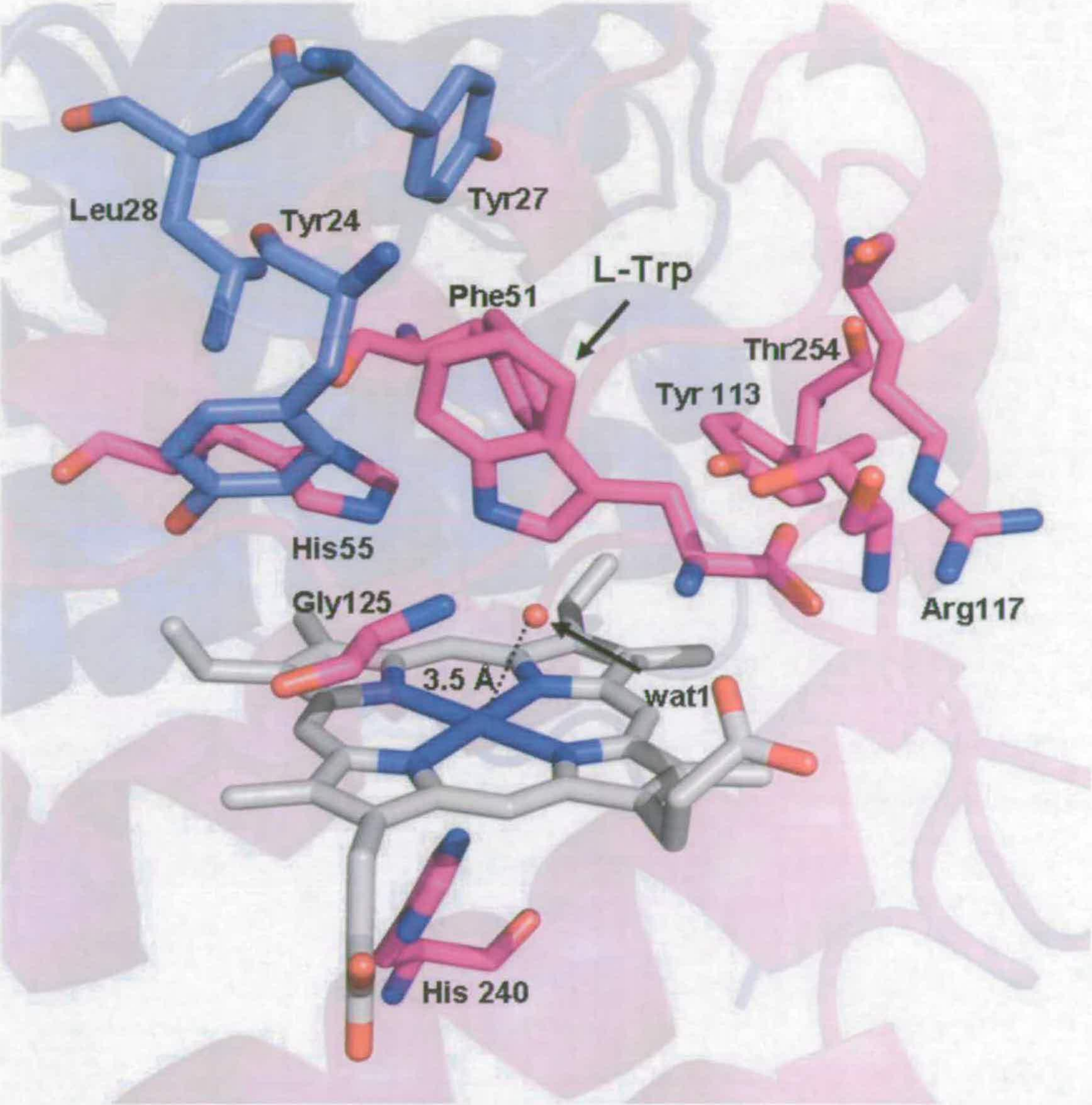

Fig 3.17: The active site of X. campestris TDO. Some of the residues involved in interactions between the bound L-Trp and the active site residues are shown.

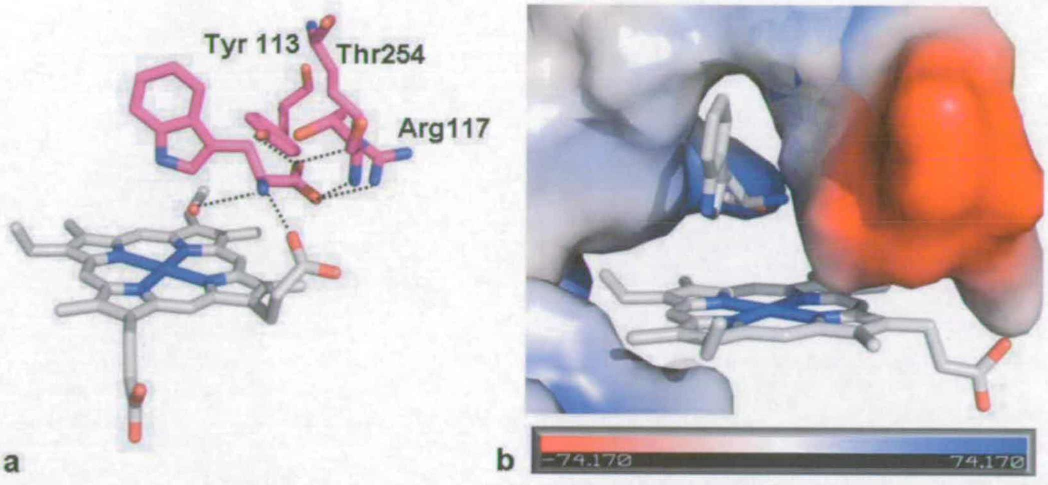

kT/e electrostatic surface potential of TDO in PyMOL

Fig 3.18: Interactions of L-Trp in the active site are shown a) Hydrogen bond network between the carboxylate group of L-Trp and Tyr113, Arg117, Thr254, heme 7-propionate side chain and water molecule in the active site b) The electrostatic surface of the L-Trp pocket. In this figure the darker the blue colour indicates a more positive charge, whilst the darker the red means that the charge in that area is more negative.

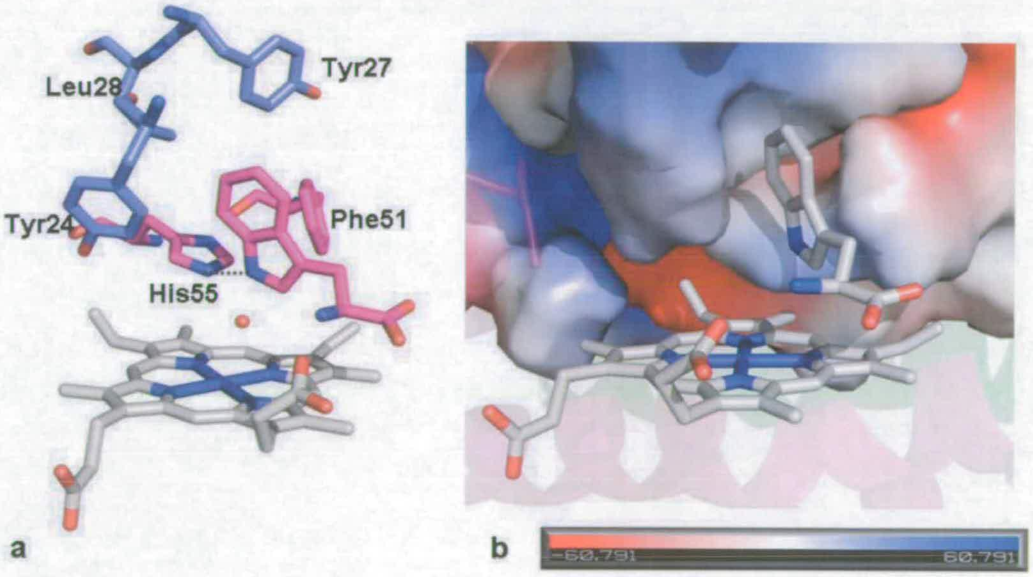

kT/e electrostatic surface potential of TDO in PyMOL

Fig 3.19: Interactions of L-Trp in the active site are shown; a) van der Waals interactions of the indole ring of L-Trp with Try24, Leu28, Tyr27 and Phe51; hydrogen bond between N1nitrogen of the indole ring with His55 b) Hydrophobic wall of the L-Trp pocket. In this figure the darker the blue colour indicates a more positive charge, whilst the darker the red means that the charge in that area is more negative.

A water molecule is present in the active site of this binary complex, hydrogen-bonded to the ammonium ion of L-Trp and the main-chain amide of residue Gly125 (see fig 3.17). The water is 3.5 Å from the ferrous atom in the heme, too far for ligating interactions. The iron atom is still 0.3 Å out of the plane of the heme, on the side of the proximal His240 ligand (fig 3.17).

3.8 6-F-Trp binary complex

The structure of the 6-fluoro-Trp binary complex is essentially identical to that of the L-Trp binary complex, apart from the presence of 6-F-Trp bound in the active site. The electron density surrounding the 6-F-Trp is shown in fig 3.20. The atomic coordinates have been deposited in the Protein Data Bank, accession code 2NW9.

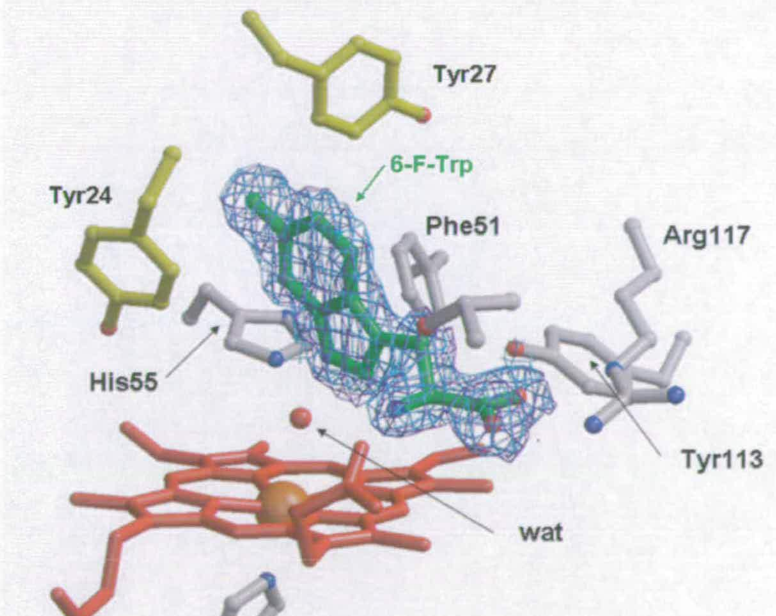

Fig 3.20: In cyan is represented the final $2F_o–F_c$ *electron density at 1.8 Å resolution for 6-F-Trp in the active site, while in purple is the* $F_o–F_c$ *omit density.* $2F_o–F_c$ *map contoured at 1*σ*,* $2F_o–F_c$ *map at 3*σ*. Figure produced with Molscript* [54] *and rendered with Raster3D* [55].

3.9 Induced-fit behaviour of TDO

The structural information described here suggests that TDO is an induced-fit enzyme. Although the active site pocket is well defined in the binary complex, the αJ–αK loop, which helps to form the walls of this pocket, is disordered in the free enzyme, and the αD-αE loop has a somewhat different conformation. Moreover, the Arg117 side chain assumes a different conformation in the free enzyme (fig 3.21a and 3.21b). Upon recognition of the L-Trp substrate, a complex and extensive network of interactions is established, thus stabilizing the active site region. Although this region is exposed to solvent in the free enzyme (fig 3.21c), it is almost completely shielded from the solvent in the binary complex, and only the carboxylate group of the 6-propionate of heme is visible on the surface (fig 3.21d).

Additional evidence for the induced-fit behaviour is observed in the active site of the second TDO monomer in the asymmetric unit. The binding mode of the L-Trp substrate is very different in this monomer. The L-Trp side chain is not positioned as deeply into the pocket, and the hydrogen bond between the ring nitrogen and the side chain of His55 is lost (distance of 3.8 Å, fig 3.22b). Both nitrogen atoms are instead hydrogen-bonded to a water molecule, located 3.5 Å from the heme iron but at a position distinct from that of the water in the active site of the other monomer.

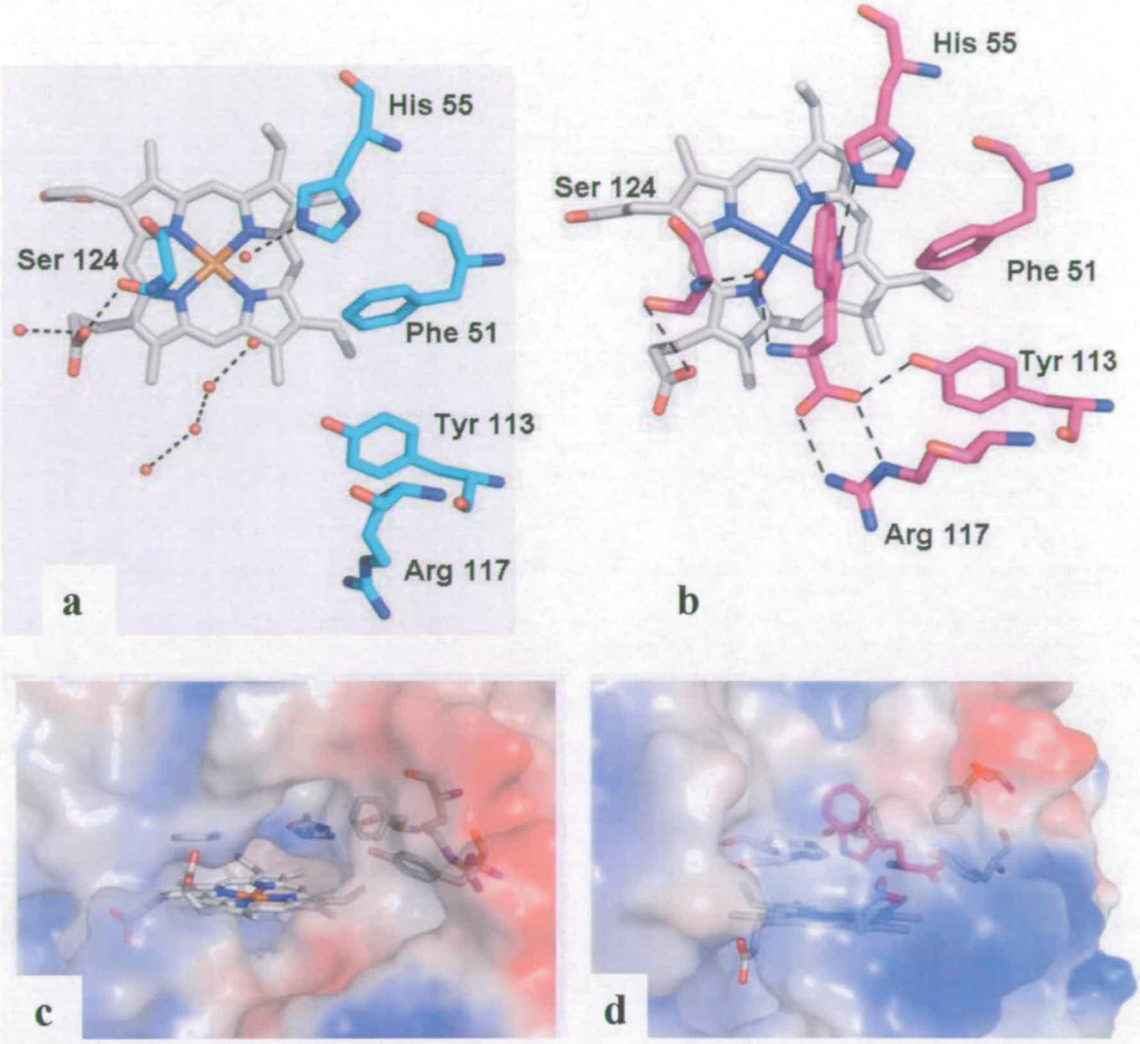

Fig 3.21: TDO is an induced-fit enzyme with significant structural changes on binding of substrate. The active site here is shown in the open and closed conformations; a) detailed view of the open(substrate free) active site (top view); b) comparison of the features of the closed active site when the substrate is bound (top view); the dotted line marks the hydrogen bonds interactions in the open and the closed structures; c) and d) comparison of the surface features of the closed and open conformation structures. Blue areas are positively charged, and red areas are negatively charged.

This conformation may also be stabilized by crystal packing interactions, as the 7-propionate of heme is ion-paired with an Arg residue from another TDO tetramer in the crystal. The main chain atoms of the Trp substrate appear to be disordered, because no clear electron density was observed for them.

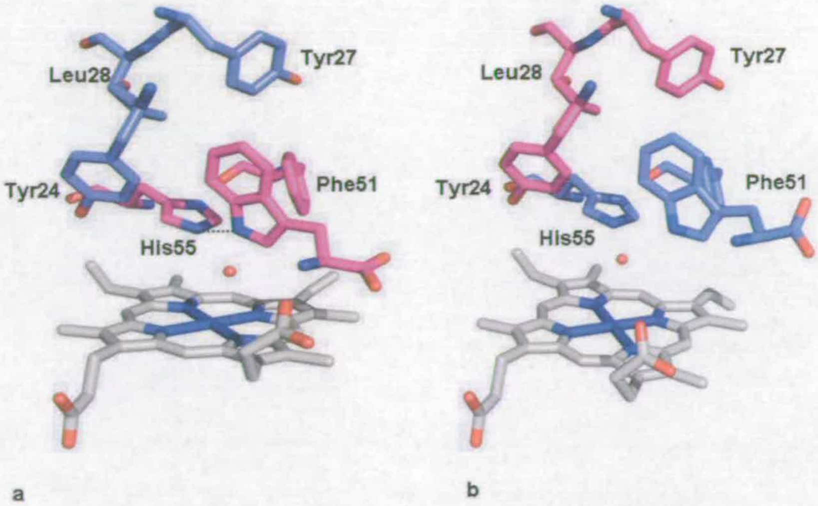

Fig 3.22: Representation of the active site in the two subunits; in monomer a L*-Trp is productively bound to the active site in a stable conformation; the monomer in b has fewer interactions (in particular the H-bond with His55, represented by a dotted line) and has assumed a transient binding geometry.*

Consistent with this finding, the αJ–αK loop is disordered in this molecule, similar to that in the substrate free enzyme.

This complex may represent an initial stage in the formation of the Michaelis complex of TDO. Proper positioning of the L-Trp substrate for catalysis would lead to the recognition of its main chain atoms and the ordering of the αJ–αK loop.

3.10 Comparison of IDO and TDO

With the exception of the smaller N-terminal domain of IDO, the structures of IDO and TDO are very similar. Indeed, in comparing 201 structurally equivalent Cα atoms between TDO and the large domain of IDO the rmsd (root mean square difference) is only 3.1 Å. A comparison between IDO and TDO structure is shown in figures 3.23a and 3.23b. An overlay of the structures is shown in Figure 3.23c.

The "dimeric" arrangement in TDO, which involves the N-terminal region of one monomer comprising part of the substrate-binding site in the adjacent monomer, is not possible in monomeric IDO. However, the two tyrosine residues in TDO that are proposed to be important in this arrangement, Tyr24 and Tyr27, are in equivalent positions to Tyr126 and Cys129 in IDO. In TDO the side chain of Tyr27 occupies a space that is taken by the side chain of Phe164 in IDO.

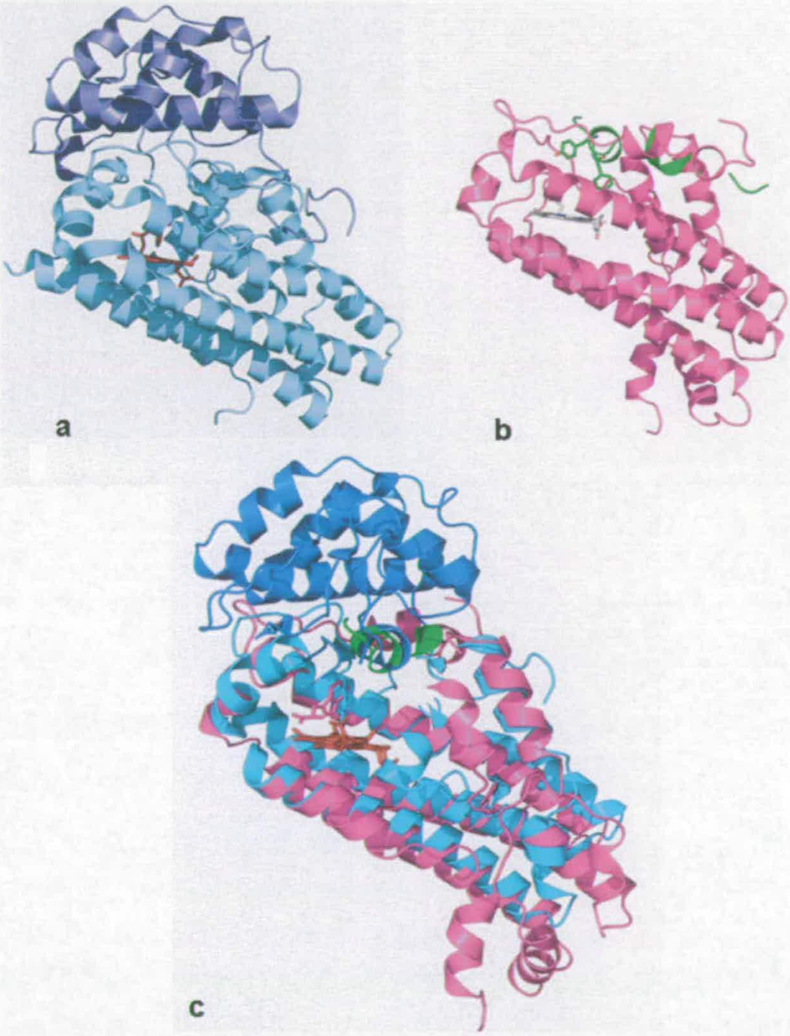

Fig 3.23: A comparison between a) human IDO and b) one monomer of X. campestris TDO; also shown is the N-terminal region of TDO (in green, residues 21-40) of the adjacent monomer which forms part of the active site. The heme groups are shown in sticks c) an overlay of human IDO (same coloring as and b) with one monomer of X. campestris TDO

3.10.1 The Active Site

The active sites of IDO and TDO have several similarities. The substrate binding site of TDO is well characterised due to the presence of L-Trp in the crystal structure and it has been already described in section 3.12.

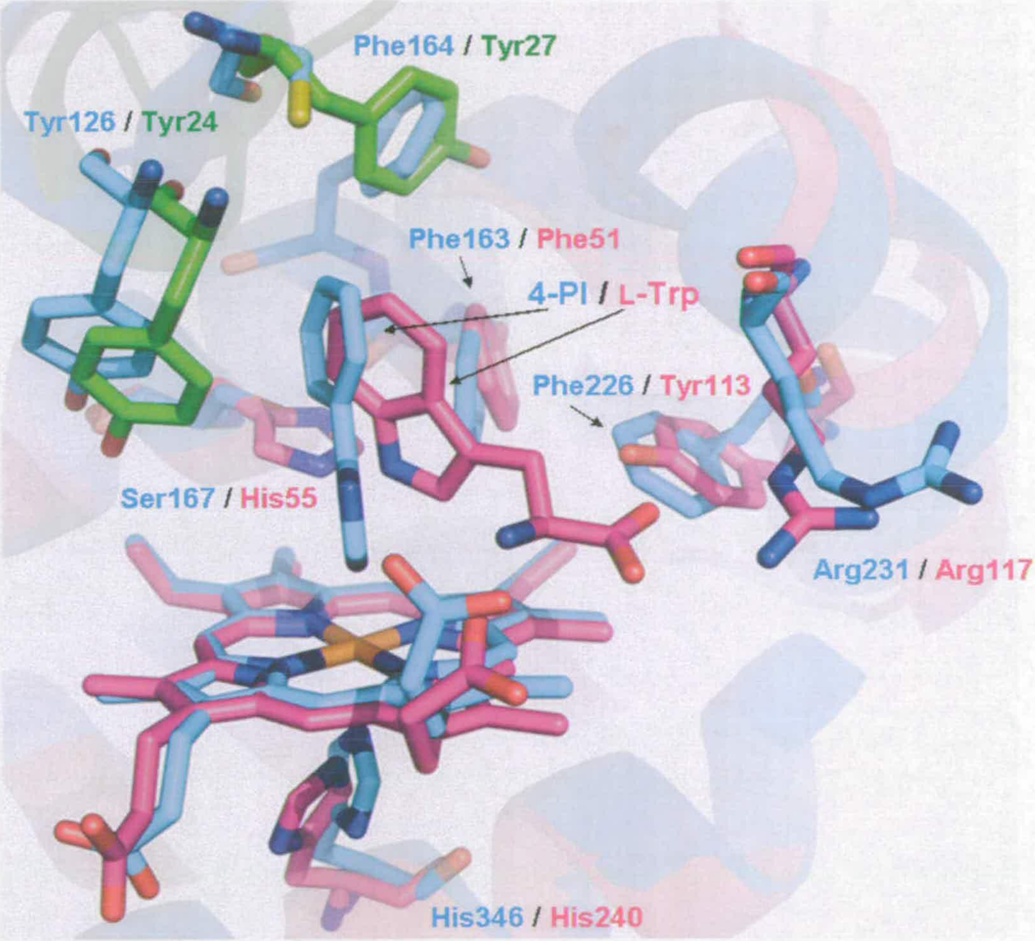

Fig 3.24: An overlay of the active sites of IDO (cyan) and TDO (magenta and green).

In contrast to TDO, the structure of IDO is not available with any substrate bound, but has been solved with the inhibitor 4-PI [52] at the active site (fig. 3.7 and fig 3.24)). This model shows that 4-PI binds to the heme iron as expected, but does not yield any information regarding the mode of substrate binding in IDO. Given the similarity between the active sites of both dioxygenases it is perhaps reasonable to assume a similar substrate-binding mode in IDO. This is supported by comparison of the active sites of IDO and TDO (fig 3.24).

For example, it can be seen that Arg117 in TDO is equivalent to Arg231 in IDO, while Phe51 in TDO is in the same position as Phe163 in IDO and Tyr24 in TDO is equivalent to Tyr126 in IDO. Similarly, the position occupied by Tyr113 in TDO is taken by Phe226 in IDO. However, in addition to these similarities it should be noted that the equivalent region in IDO of the loop comprising residues 250-260 of TDO is disordered in the IDO structure. This region is particularly important in TDO because it includes Thr254 that, as mentioned above, is involved in binding the ammonium and carboxylate moieties of L-Trp. It is interesting to note that in the absence of L-Trp this loop region is also disordered in the TDO structure, and that substrate binding is required to induce its ordering. This may also be the case for IDO, but the possibility exists that there is no equivalent interaction between IDO and L-Trp.

Perhaps the most obvious difference between the active sites of the two enzymes is the presence of His55 in TDO and its equivalent Ser167 in IDO. In TDO the histidine side chain is hydrogen-bonded to the indole nitrogen atom of L-Trp, and the role of His55 would appear to be in regulating substrate binding (paper in preparation). The role of Ser167 in IDO is less clear in the absence of a substrate-bound crystal structure, but it is unlikely that this residue plays any crucial role in IDO [56].

3.11 An allosteric binding site in the tetramer interface?

In the TDO-L-Trp structure was observed the binding of four L-Trp residues at the interface of the tetramer, with well defined electron density. The L-Trp molecule appears to be recognized specifically by the enzyme in this pocket. There have been reports of allosteric activation by the substrate L-Trp [57, 58], and our observations offer a possibility for this effector site. Kinetic studies so far have not shown any allosteric effects with *X. campestris* TDO. This site is not occupied in the 6-F-Trp complex, possibly because of the lower concentration of the substrate in the crystallization solution.

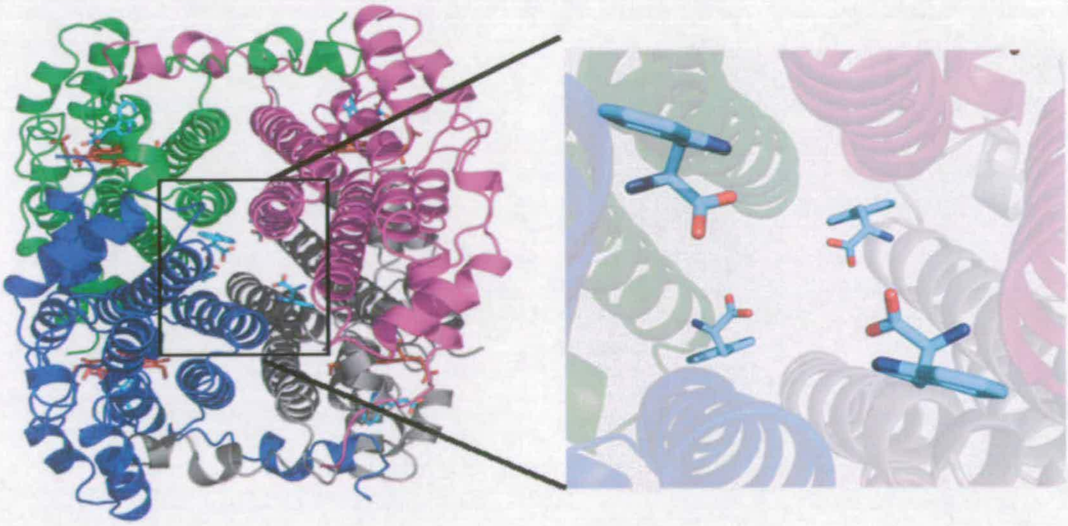

Fig 3.25: The L-Trp binding site in the tetramer interface. Each L-Trp molecule occupies an identical site with respect to the four monomers

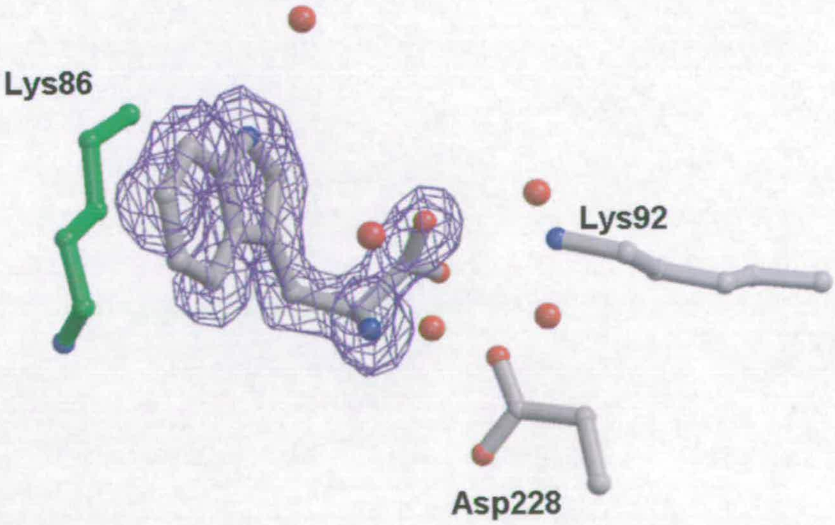

Fig 3.26: Final $2F_0 - F_c$ electron density map at 1.6 Å resolution for L-Trp and the hydrogen bonding residues in the putative allosteric binding site.

3.12 Biochemical studies confirm the structural observations

X. campestris TDO has robust catalytic activity toward L-Trp and 6-F-Trp but is inactive toward D-Trp, tryptamine or indolepropionic acid (Table 3.2), confirming its designation as a TDO. In fact, D-Trp is a weak, competitive inhibitor of the enzyme at high concentrations. Binding data show that D-Trp has much lower affinity for the enzyme than L-Trp, consistent with our structural information, and explaining why D-Trp cannot be oxygenated by TDO (data from Miss Sarah J. Thackray).

			K_d	
Substrate	k_{cat} (s^{-1})	K_m µM	**Ferric heme (mM)**	**Ferrous heme (µM)**
L-Trp	19.5 ±1.2	114 ± 1	3.84 ± 0.14	4.12 ± 0.24
D-Trp	0	16.5 ± 3.3* mM	>50†	NC
6-F-D/L-Trp	37.3 ± 0.6	186 ± 12	2.45 ± 0.42	<1†
5-F- D/L -Trp	2.4 ± 0.1	100 ± 6	1.51 ± 0.08	<1¶
Indol. acid	0	0	>10†	126 ±11

*Table 3.2: Summary of kinetic data on X. campestris TDO; NC, No spectral change detected; *Inhibitory constant,* K_i.*; †Although a spectral change was evident, substrate solubility prevented accurate measurement of* K_d. *Values were estimated based on the maximum substrate concentration attainable.*
¶Binding was too tight to be measured. Values quoted represent the minimum K_d *that can be measured under standard assay conditions. Indol acid: indolepropionic acid*

The biochemical studies also provide direct evidence for the induced-fit behaviour of TDO. Indeed, there is a large increase in the affinity of the enzyme for L-Trp when the heme iron is reduced (K_d (Fe (III) heme) = 3.8 mM, whereas K_d (Fe (II) heme) = 4.1 µM). These parameters were converted to free energy changes (i.e. $\Delta G = -\ln(1/K_d)$, expressed as *RT* units (where *R*, gas constant, *T*, absolute temperature). In fact, the shift in reduction potential almost perfectly correlates with the increase in affinity for L-Trp on reduction, from which the variation of free energy due to heme reduction ($\Delta\Delta G$) was computed as the difference in binding energy between ferric and ferrous forms of the enzyme

($\Delta\Delta G=\Delta G(\text{ferric})-\Delta G(\text{ferrous})$) in the presence and absence of substrate: both gave an estimated $\Delta\Delta G$ of 15 kJ/mol. The electrical potential of the reaction (ΔE) can be then derived from the Nernst equation shown below, where n is the number of electrons involved in the reaction and F is the Faraday constant (23.06 kcal/volt/mol or 94.4 kJ/volt/mol):

$$\Delta G = -nF\Delta E$$

The electrochemistry data show a large, positive shift in reduction potential (+136 mV) in the presence of 15 mM L-Trp [23]. These data show that there is a significant stabilization of the ferrous form when substrate is bound. This stabilization could also play a physiological role in keeping the protein reduced, and therefore active, when L-Trp is present.

Our structural studies have defined the binding mode of the substrate L-Trp to TDO, revealing the structural basis for the stereospecificity of this important enzyme. The induced-fit behaviour of TDO, confirmed by biophysical studies [23], appears crucial for the exclusion of water from the active site and for stabilizing the enzyme in the presence of the substrates. Finally, structural comparisons among these enzymes reveal the striking evolutionary conservation of the heme-dependent dioxygenases.

3.13 Ternary complexes with dioxygen analogs in crystals

The Fe (II) atom of the heme prosthetic group of TDO has high affinity for O_2, NO, and CO, and the binding of diatomic molecules is of critical importance for TDO catalysis. Kinetic study of diatomic ligands binding behaviour to TDO has been investigated by Miss Sarah J. Thackray (unpublished results) only on the ferrous, active form of the enzyme. Indeed, the affinity of NO for ferrous heme is too high to be determined with spectrophotometry techniques. CO reveals a high affinity for TDO ferrous heme, with a K_d of 90 μM. Furthermore, both NO and CO can bind to TDO ferrous heme. In order to obtain the ternary complex of the ferrous active form of the enzyme, the preparation of stable TDO ternary complexes with gaseous diatomic ligands required anaerobic conditions.

We have invested significant effort into obtaining the crystal structure of TDO–CO and TDO-NO complexes in the presence of L-Trp. This is because these data would provide important insights into the structure of the Michaelis complex.

In a first attempt to obtain the ternary complex of TDO with L-Trp and an inactive diatomic ligand in the active site, we used the following procedure. Before mounting in nylon loops and flash-freezing in liquid nitrogen, crystals were immersed in a cryoprotectant solution composed of mother liquor (with L-Trp concentration increased to 50 mM) supplemented with 23% (v/w) glycerol and bubbled initially with N_2 for 15 minutes and then with nitric oxide (NO) or carbon monoxide (CO) for 15 minutes before use. The crystals were exposed to the solution saturated with NO or CO before being flash-frozen in liquid nitrogen.

We did not observe the binding of this dioxygen analogue in the structure. This was confirmed by our structure of the binary complex with 6-F-Trp, which was not exposed to NO but contained the same density for the water molecule. NO probably diffused rapidly from solution during the pre-flash-cooling manipulations in the anaerobic box.

3.13.1 Pressure cells for preparing gas/protein complexes in crystals

In a second attempt to obtain the ternary complex of TDO, we used a Cajon ® Ultra-Torr fitting cell [59, 60] as described in Vernède, X. & Fontecilla-Camps, J. C., 1999 [61]. These experiments were performed in Grenoble at the Laboratoire de Cristallographie et Cristallogenèse des Protéines (LCCP), Institut de Biologie Structurale, under the guidance of Dr Juan-Carlos Fontecilla-Camps and Mr Xavier Vernède. In this cell, it is possible to pressurize a crystal already mounted on a cryoloop (fig 3.27).

Such a procedure shows some advantages compared to the technique used previously. In particular, gases can more easily access the crystal interior due to the smaller volume of solvent surrounding it.

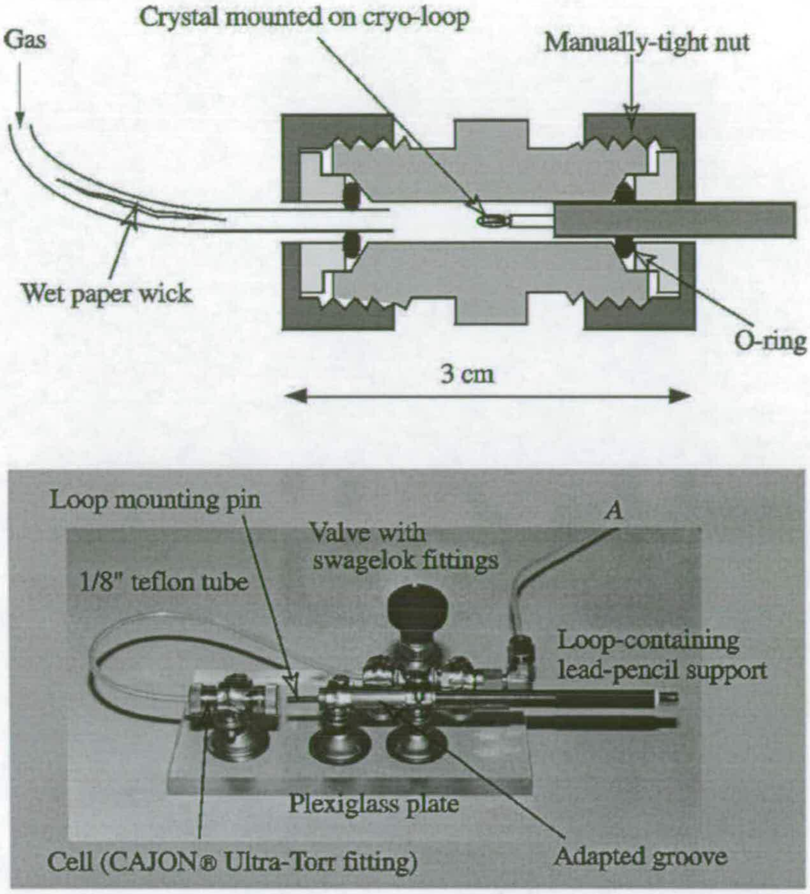

Fig 3.27: Schematic representation of the cell (Cajon® Ultra-Torr fitting) and photograph of the pressure-cell setup. From [61]*. The crystal monted in the cryoloop is held by a lead pencil support. The pressure chamber is connected (A) to a manometer equipped with a three-way valve to allow for pressurization and depressurization.*

Under these conditions the maximum applied pressure was 1.5 bar for both NO (1% v/w) and CO (100% v/w). Pressure chamber crystal soaking experiments were carried out for 5, 10 and 15 minutes for each diatomic gas.

In this setup crystal freezing through rapid flash-cooling in liquid propane was performed. This approach for crystal freezing avoids the use of liquid nitrogen, which may be contaminated by oxygen.

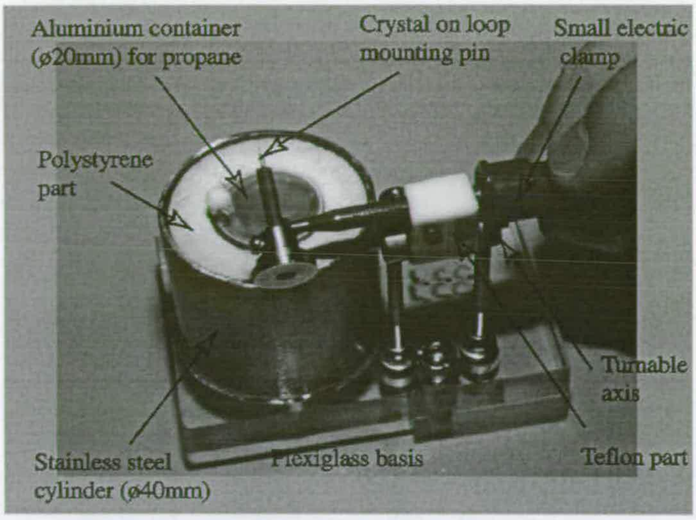

Fig 3.28: The crystal transferring device from [61].

Propane was solidified in a liquid nitrogen bath and introduced to the anaerobic glove box. When the propane was liquefied (~3 minutes) (about 100 K), the loop with the crystal mounted was dipped in the propane container (fig 3.29). The boiling point of propane is 231 K, while its melting point is 83 K. This avoids the formation of the insulating film that occurs during flash-cooling with liquid nitrogen due to its boiling. Liquid propane appears then to be a better freezing agent than liquid nitrogen for protein crystals.

Using this method, the crystals were flash-cooled less than 10 seconds after pressure chamber treatment, decreasing the chances of gas/protein complex dissociation. The device (fig 3.28) containing the crystal mounted on the loop and immersed in liquid propane was then immediately removed from the glove box and the crystal stored under liquid nitrogen.

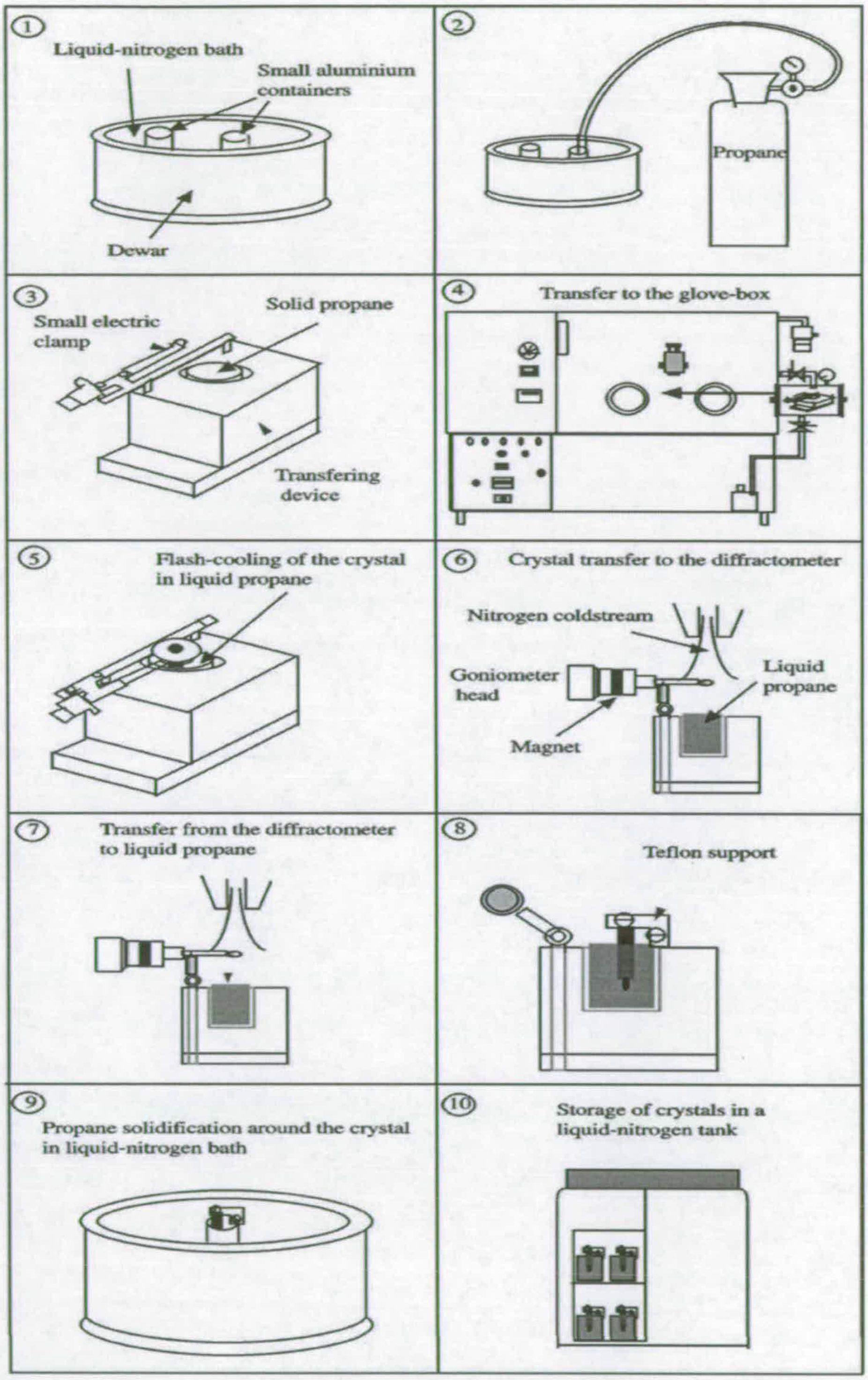

Fig 3.29: Description of the flash-cooling (1-5), transferring (6-7) and storing (8-10) procedure for protein crystals. From [61]

Few data sets of crystals soaked with diatomic ligands were collected, but due to the low quality of the crystals we could not verify the presence of dioxygen analogs in the active site. These experiments are still in progress at IBS Grenoble.

3.14 SO4414: a putative IDO from *Shewanella oneidensis*

To date, more than 50 bacterial TDO sequences have been reported [62]. The large distribution of TDO between different life-forms suggests that the origin of this enzyme is quite ancient.

Bacteria are also believed to use IDO family members for the aerobic metabolism of L-Trp via the kynurenine pathway, although prokaryotic IDO-like proteins bear little sequence similarity to eukaryotic IDO proteins and very little is yet known about them. However it appears that for bacterial IDO, L-Trp is not a true substrate and their actual function is still unknown.

We investigated the structure of the SO4414 protein (sIDO) from *Shewanella oneidensis,* which (fig 3.30) shares a 12% sequence homology with human IDO.

S. oneidensis [63, 64] is a gram-negative bacterium which is used as model organism for electron transfer studies. It can utilize a great variety of electron acceptors for its respiratory process (nitrite, nitrate, thiosulfate, iron (III), manganese (IV), uranium (IV)) and it can grow both aerobically and anaerobically.

```
IDO_(Hs)    -----MAHAM ENSWTISKEY HIDEEVG--F ALPNPQENLP DFYNDWMFIAKHLPDLIESG
sIDO        XKPATYNTEA FDEWIRSRFV ELNSQLEQLY YQQTDRANVQ E-------VGTELKHTLES-

IDO_(Hs)    QLRERVEKLN MLSIDHLTDH KSQRLARLVL GCITMAYVWG KGHGDVRKVL PRNIAVPYCQ
sIDO        EGRELVKAL- ---LDEGNTD EGFDSAFDLL GNVGLYXAAC RRHEITEPT- -RETTSPLLE

IDO_(Hs)    LS-------K KLELPPILVY ADCVLANWKK KDPNKPLTYE NMDVLFSFRD GDCSKGFFLV
sIDO        ASALAXHIGA SIGVTPRFAT AHLTTHNRAH NGIYKRFTDL PDEKLFVDYN ---TKGI---

IDO_(Hs)    SLLVEIAAAS AIKVIPTVFK AMQMQERDTL LKALLEIASC LEKALQVFHQ IHDHVNPKAF
sIDO        -LAYKRASDA LLKIQPLGIS HPISHDLLRV TK------QA LQDVIESNQQ LFNRLDTDRF

IDO_(Hs)    FSVLRIYLSG WKGNPQLSDG LVYEGFWEDP KEFAGGSAGQ SSVFQCFDVL LGIQQTAGGG
sIDO        FYCVRPYY-- ---KPYRVGS VV-------- --YRGANAGD FAGINVIDLT LGL-CFANEA

IDO_(Hs)    HAAQFLQDMR RYMPPAHRNF LCSLESNPSV R-EFVLSKGD AG-------L REAYDACVKA
sIDO        SYSQXLVDKF LYXXPEDQQI LRECXRRPNL XDDFLQAKGC IHQDWYQENL KLFIEVCELH

IDO_(Hs)    LVSLRSYHLQ IVTKYILIPA SQQPKENKTS EDPSKLEAKG TGGTDLMNFL KTVRSTTEKS
sIDO        GQTAIQHHNE LVTKYIAEPS VSXEQQH--- --LAKVTASG PPLHVLLASL ERLRDRRAAV

IDO_(Hs)    L--------- ----LKEG-- -----
sIDO        LRDDIRTRYY DLKKLKDSLR LEAAA
```

Fig 3.30: Amino acids sequence alignment of Shewanella oneidensis putative IDO (sIDO) (in blue) and human (Hs) IDO (in black). The conserved residues are highlighted in magenta.

3.14.1 Expression and purification of SO4414

Cloning and purification of the SO4414 was performed as described in section 3.7 for TDO. *Shewanella oneidensis* SO4414 (Q8E972_SHEON, NESG ID SoR52) was cloned into a pET21d (Novagen) derivative, generating plasmid pSoR52-21.1. The resulting SoR52 ORFs contain 11 (AAALEHHHHHH) nonnative residues at their C termini. *Escherichia coli* BL21 (DE3) pMGK cells were transformed with pSoR52-21.1. Expression either in LB media and MJ9 media containing selenomethionine, were performed as described in section 3.7 [39, 40].

Purification of sIDO was carried out by using an AKTA-Express (GE Heathcare) two-step purification strategy. The His-tagged protein in the supernatant was loaded onto a HisTrap HP column (GE Heathcare), washed, and eluted with lysis buffer containing 250 mM imidazole into a 10-ml sample loop. The loop content was then injected onto a gel-filtration column (Sephadex 75; GE Heathcare), and eluted in

Buffer 2 (10 mM Tris (pH 7.5)/5 mM DTT/100 mM NaCl/0.2% NaN_3) (fig 3.31a). The purified protein resulting from gel-filtration purification was concentrated to 5-10 mg/ml and sample purity (> 95%), and molecular weight were verified by SDS-PAGE (fig 3.31b).

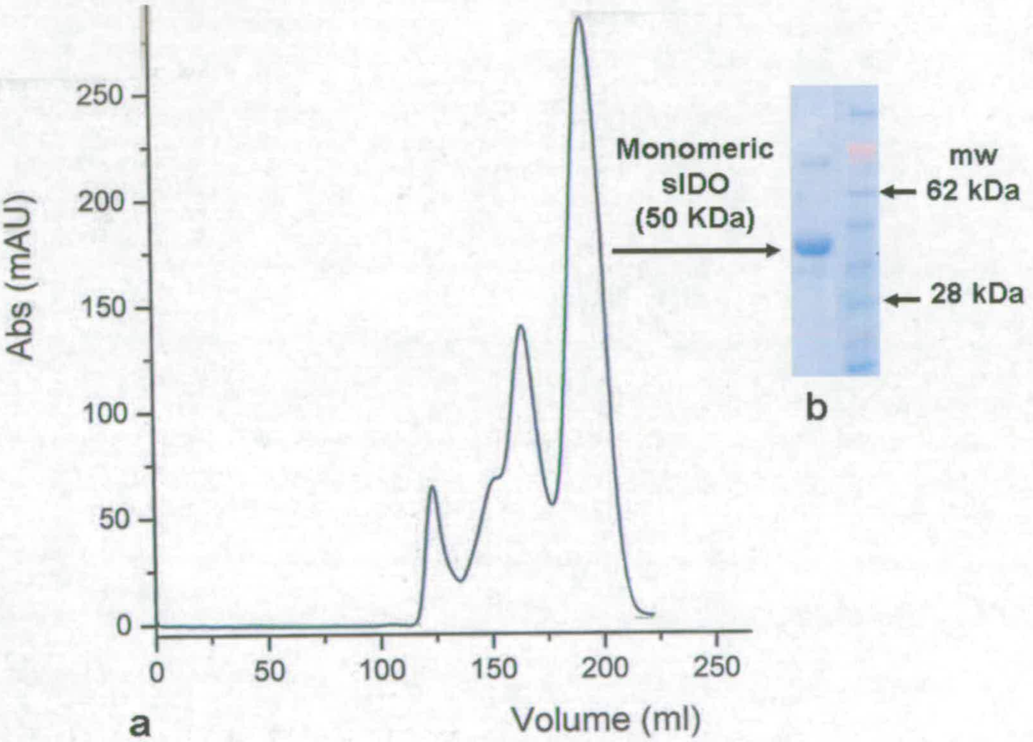

Fig 3.31: (a) Elution profile of 6His-tagged sIDO as monitored by UV adsorption from a 26/60 Superdex-200 column. Elution peak of sIDO is indicated by the arrow and reported on the SDS-PAGE on the right. (b) SDS-PAGE analysis of elution peak.

3.14.2 Protein crystallization

Crystals of the apoenzyme of SO4414 were produced by the hanging-drop vapour-diffusion method at 18°C, and the reservoir solution contained 20 mM Tris (pH 7.5), 18% (wt/vol) PEG 3350, 150 mM lithium sulfate, and 5 mM DTT. Crystals of the holoenzyme of SO4414 were grown anaerobically as described in section 3.8.

Briefly, pure protein was introduced to the anaerobic glove box and chemically reduced with sodium dithionite. The excess of sodium dithionite was then removed using a gel filtration column (Sephadex G-25) and eluted with a buffer containing 10-50 mM L-Trp. The crystals were produced by the sitting-drop vapour-diffusion method, with a reservoir solution of 100 mM Tris (pH 7), 20% (w/v) PEG 3350, and 50 mM magnesium formate and 10-50 mM L-Trp. The enzyme was at 10 mg/ml concentration. Crystals of the apoenzyme were cryoprotected in paratone, while crystals of the holoenzyme were protected in mother liquor supplemented with 25% (v/v) glycerol.

3.14.3 Data collection and processing

X-ray diffraction data were collected on an ADSC CCD at the X4A beam line of Brookhaven National Laboratory for both the apo- and holoenzymes of SO4414. The diffraction images were processed and scaled with the HKL package [45]. The data processing statistics are summarized in Table 3.3.

Crystals of the apo- and holoenzymes of SO4414 belong to space group $P2_12_12$, with cell dimensions a = 138.1 Å, b = 68.0 Å, and c = 91.0 Å, and a = 138.8 Å, b = 68.7 Å, and c = 87.8 Å, respectively. In both, there were two monomers in the asymmetric unit.

3.14.4 Structure determination and refinement

The SO4414 apoenzyme structure was determined by the selenomethionyl single-wavelength anomalous diffraction method [46]. The reflection phases were calculated with Solve/Resolve [48]. The structure of the holoenzyme was determined by the molecular-replacement method, with the programs COMO [49] and AMoRe [50]. The atomic models were built with the program XtalView [65] and TURBO-FRODO [52] and the structure refinement was carried out with CNS [53].

The structure of the SO4414 holoenzyme from *Shewanella oneidensis* [66] was determined at 2.4 Å resolution by molecular replacement based on the structure of the apoenzyme (PDB entry 1ZEE).

Protein	**SO4414 (holoenzyme)**	**SO4414 (apoenzyme)**
Beam line	NSLS X4A	NSLS X4A
PDB entry	2NWB	1ZEE
Space group	$P2_12_12$,	$P2_12_12$,
cell dimensions (Å)	$a = 138.8$, $b = 68.7$, $c = 87.8$ Å	$a = 138.1$, $b = 68.0$, $c = 91.0$
resolution (Å)	29.2-2.4 (2.4-2.49)*	30.0-2.3 (2.3-2.38)*
no. of unique reflections	33304	70105
completeness (%)	100.0 (100.0)*	96.5 (99.6)*
$I/[\sigma(I)]$	16.98 (2.81)*	17.0 (4.46)*
R_{merge} (%)^a	10.4 (63.0)*	6.6 (30.6)*
R_{work} (%)^b	21.7 (23.5)*	23.4 (26.7)*
R_{free} (%)^c	22.5 (24.1)*	27.5 (31.5)*
rmsd from ideal values		
bond lengths (Å)	0.007	0.006
bond angles (deg)	1.1	1.0
Ramachandran analysis		
most favoured (%)	91.6	91.2
additionally allowed (%)	8.4	8.5
no. of waters included in refinement	307	309

Table 3.3: Data collection and refinement statistics * *Values in parentheses represent statistics for the highest resolution shell* ^{a} $R_{merge} = \Sigma_h\Sigma_i|I(h) - I_I(h)|/\ \Sigma_h\Sigma_i I_I(h)$, *where* $I_I(h)$ *and* $I(h)$ *are the ith and mean measurement of reflection h, respectively.* ^{b} $R_{work} = \Sigma_h|F_o - F_c|/\ \Sigma_h F_o$, *where* F_o *and* F_c *are the observed and calculated structure factor amplitudes of reflection h, respectively.* ^{c} R_{free} *is the test reflection data set, 5 % selected randomly for cross validation during crystallographic refinement.*

3.14.5 The structure of sIDO

Structural similarity is observed between human IDO and the SO4414 protein from *S. oneidensis*, with an rms distance of 4.4 Å for 206 equivalent carbon-α atoms, suggesting that SO4414 may also be a dioxygenase. The structure contains an extra domain that is formed by residues at the N terminus, similar to the small domain in human IDO (fig 3.35). Both the active sites are located on the larger subunit scaffold.

3.14.6 The putative active site of sIDO

Although SO4414 crystals were grown in the presence of 10-50 mM L-Trp, we did not observe the binding of L-Trp in its putative active site. Our biochemical efforts so far have not been able to demonstrate IDO (or TDO) activity for this protein, suggesting that SO4414 may prefer a different substrate for oxygenation.

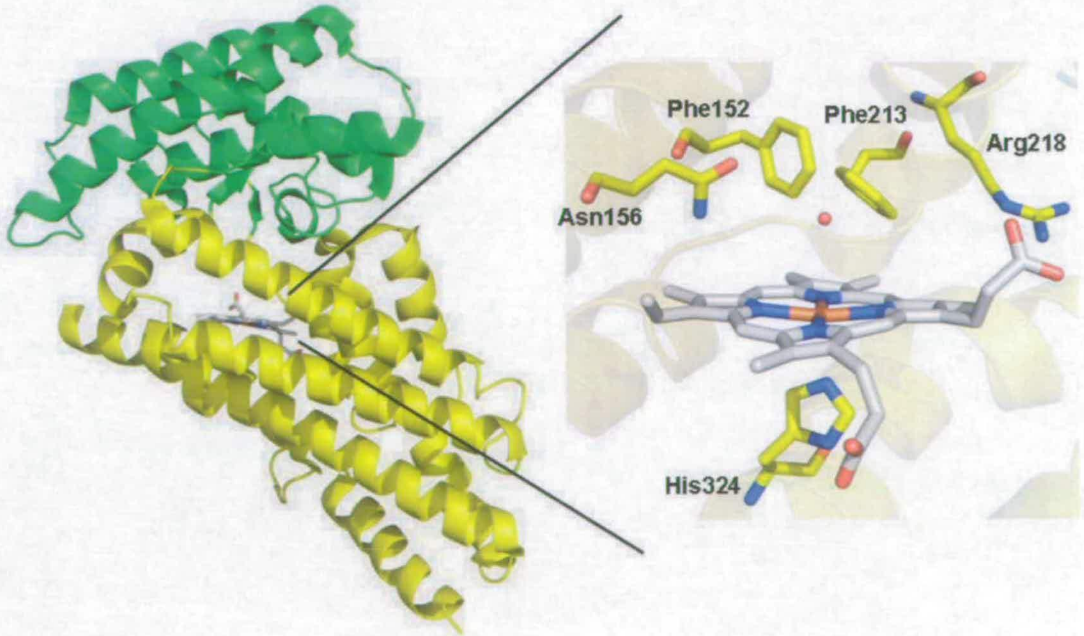

Fig 3.32: a) The location of the putative active site in sIDO; b) a detailed side view of active site residues Asn156, Phe152, Phe213, Arg218 and the fifth heme ligand His324. The water molecule in the active site is hydrogen bonded to Asn156.

The mode of substrate binding in human IDO is not well characterised due to the absence of any substrate in the crystal structure (see section 3.5). However, it is clear (fig 3.33) that human IDO and SO4414 share structurally similar active sites. In particular comparison of the active sites indicates the presence of the same residues around the heme. Arg231, Phe226, and Phe163 in human IDO corresponds respectively to Arg218, Phe213, and Phe152 in SO4414, being essentially superposable.

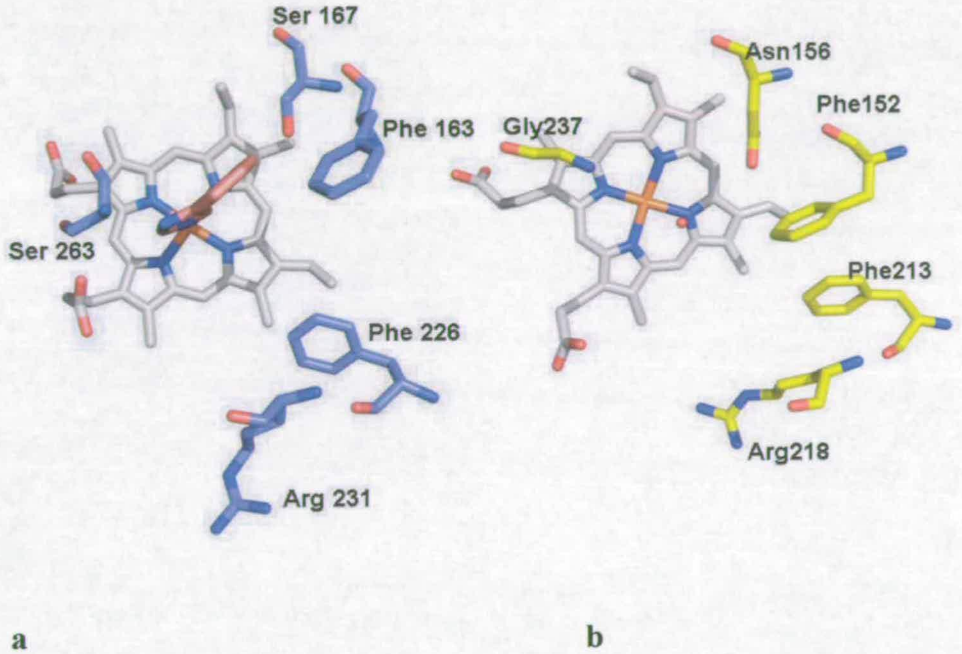

Fig 3.33: Comparison of the active sites of the human IDO (a) (in blue) and SO4414 (b) (in yellow). The two sites are structurally similar and some residues (Arg231/ Arg218, Phe226/ Phe213, Phe163/ Phe152) are identical and in similar orientations

The core of the active site around the heme consists of seven α-helices that are arranged the same in both enzymes (fig 3.35). Furthermore, the key residues possibly involved in substrate binding (illustrated in fig 3.34), are carried by the same α-chains.

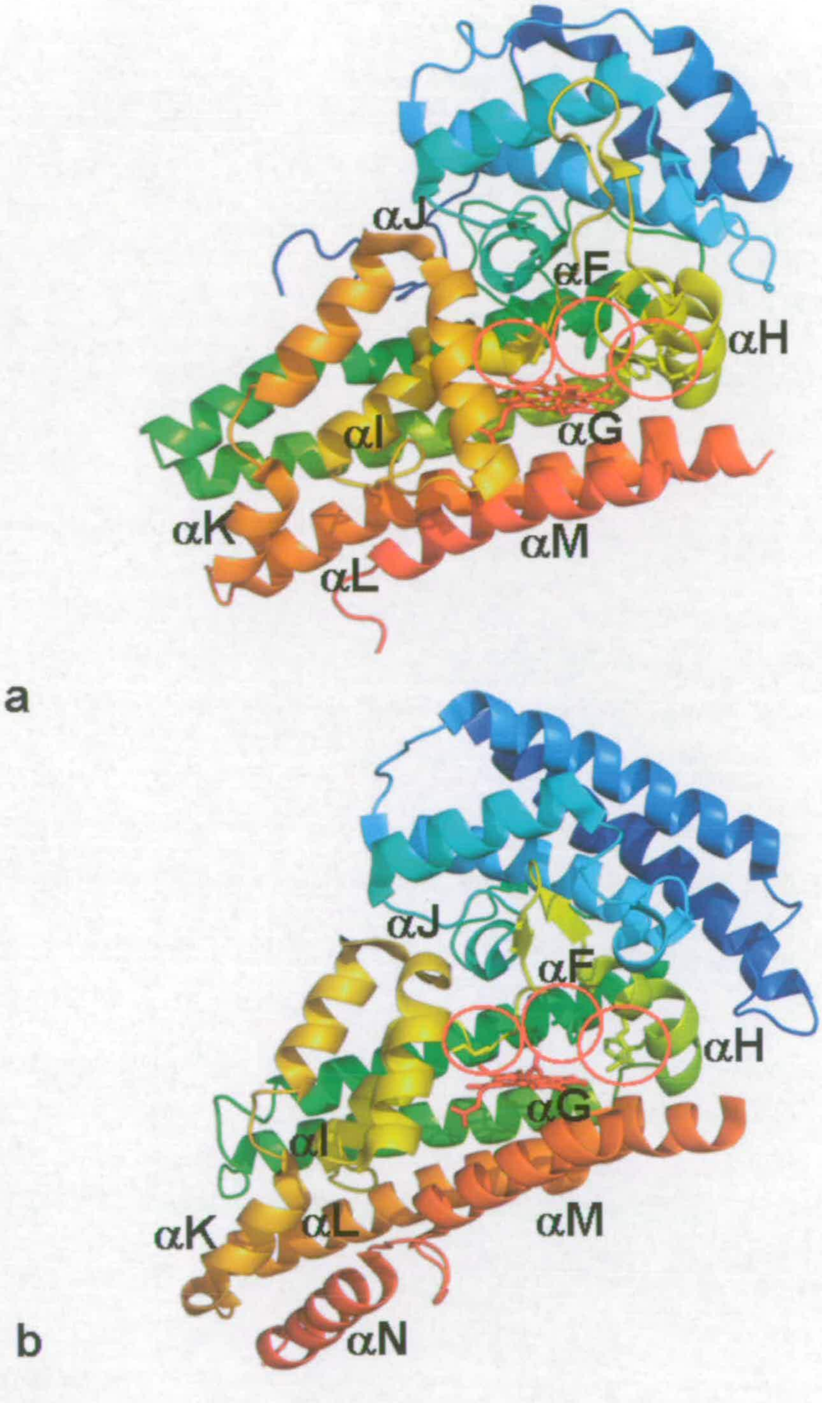

Fig 3.34: a) human IDO b) SO4414, both coloured as chainbow. The two enzymes show limited primary sequence similarity. Nevertheless they have nearly identical folds and their 3D structures are conserved. In the red circles: Phe226 and Arg231 from (a) and Phe231 and Arg218 from (b) all belonging to the α-H chains of the two enzymes. Phe163 and Ser167 from (a) and Phe152 and Asn156 from (b) belong to α-F, and Ser263 from (a) and Gly237 from (b) are both in close proximity of α-I.

3.15 Conclusions

The crystal structures of *X. campestris* TDO presented here show the exact positioning of the substrate in the active site. The role of the heme propionate group and the surrounding residues in ligand binding is fundamental in dictating the strict substrate specificity of TDO. These findings, in conjunction with the high level of overall structural similarity with human IDO, contribute to the understanding of the structure-activity relationships in this important family of dioxygenases. The structural information provided is complemented by biochemical studies and altogether offer significant molecular insight into tryptophan dioxygenation by TDO and IDO.

As yet, very little is known about substrate binding in SO4414. Despite differing sequence, human IDO and SO4414 show to have converged upon a very similar active site design and are therefore likely to share a common mechanism.

3.16 References

1. Yoshida, R. & Hayaishi, O. Indoleamine 2,3-dioxygenase. Methods Enzymol. 142, 188-195 (1987).

2. Takikawa, O. Biochemical and medical aspects of the indoleamine 2,3-dioxygenase-initiated l-tryptophan metabolism. Biochem. Biophys. Res. Commun 338, 12-19 (2005).

3. Sono, M., Roach, M., Coulter, E. & Dawson, J. Heme-Containing Oxygenases. Chem Rev 96, 2841-2887 (1996).

4. Allegri, G., Ragazzi, E., Bertazzo, A., Costa, C. V. L. & Rocchi, R. Tryptophan metabolism along the kynurenine pathway in rats. Advances in Experimental Medicine and Biology 527, 481-496 (2003).

5. Takikawa, O. Biochemical and medical aspects of the indoleamine 2,3-dioxygenase-initiated L-tryptophan metabolism. Biochemical and Biophysical Research Communications 338, 12-19 (2005).

6. Ohashi, H. et al. Changes in quinolinic acid production and its related enzymes following D-galactosamine and lipopolysaccharide-induced hepatic injury. Archives of Biochemistry and Biophysics 428, 154-159 (2004).

7. Saito, K. et al. Mechanism of increases in L-kynurenine and quinolinic acid in renal insufficiency. American Journal of Physiology 279, F565-F572 (2000).

8. Tankiewicz, A., Pawlak, D. & Buczko, W. Enzymes of the kynurenine pathway. Postepy Higieny i Medycyny Doswiadczalnej 55, 715-731 (2001).

9. Aquilina, J. A., Carver, J. A. & Truscott, R. J. W. Oxidation products of 3-hydroxykynurenine bind to lens proteins: relevance for nuclear cataract. Experimental Eye Research 64, 727-735 (1997).

10. http://www.eyes-and-vision.com/cataract-symptoms-treatments.html

11. Mellor, A. Indoleamine 2,3 dioxygenase and regulation of T cell immunity. Biochem Biophys Res Commun 338, 20-24 (2005).

12. Munn, D. et al. Prevention of Allogeneic Fetal Rejection by Tryptophan Catabolism Science 281, 1191-1193 (1998).

13. Grohmann, U., Fallarino, F. & Puccetti, P. Tolerance, DCs and tryptophan: much ado about IDO. Trends Immunol 24, 242-248 (2003).

14. Uyttenhove, C. et al. Evidence for a tumoral immune resistance mechanism based on tryptophan degradation by indoleamine 2,3-dioxygenase. Nat Med 9, 1269-1274 (2003).

15. Schwarcz, R. The kynurenine pathway of tryptophan degradation as a drug target. Curr Opin Pharmacol 4, 12-17 (2004).

16. Muller, A., DuHadaway, J., Donover, P., Sutanto-Ward, E. & Prendergast, G. Inhibition of indoleamine 2,3-dioxygenase, an immunoregulatory target of the cancer suppression gene Bin1, potentiates cancer chemotherapy. Nat Med 11, 312-319 (2005).

17. Platten, M. et al. Treatment of Autoimmune Neuroinflammation with a Synthetic Tryptophan Metabolite Science 310, 850-855 (2005).

18. Wirleitner, B., Neurauter, G., Schroecksnadel, K., Frick, B. & Fuchs, D. Interferon-gamma -induced conversion of tryptophan: Immunologic and neuropsychiatric aspects. Current Medicinal Chemistry 10, 1581-1591 (2003).

19. MacKenzie, C. R., Heseler, K., Mueller, A. & Daeubener, W. Role of indoleamine 2,3-dioxygenase in antimicrobial defense and immunoregulation: tryptophan depletion versus production of toxic kynurenines. Current Drug Metabolism 8, 237-244 (2007).

20. Kotake, Y. & Masayama, I. The intermediary metabolism of tryptophan. XVIII. The mechanism of formation of kynurenine from tryptophan. Z. physiol. Chem. 243, 237-44 (1936).

21. Batabyal, D. & Yeh, S.-R. Human tryptophan dioxygenase: A comparison to indoleamine 2,3-dioxygenase. Journal of the American Chemical Society 129, 15690-15701 (2007).

22. Allegri, G., Ragazzi, E., Bertazzo, A., Biasiolo, M. & Costa, C. V. L. Tryptophan metabolism in rabbits. Advances in Experimental Medicine and Biology 527, 473-479 (2003).

23. Forouhar, F. et al. Molecular insights into substrate recognition and catalysis by tryptophan 2,3-dioxygenase. Proc. Natl. Acad. Sci. USA 104, 473-8 (2007).

24. Zhang, Y. et al. Crystal Structure and Mechanism of Tryptophan 2,3-Dioxygenase, a Heme Enzyme Involved in Tryptophan Catabolism and in Quinolinate Biosynthesis. Biochemistry 46, 145-155 (2007).

25. Ishimura, Y. L-Tryptophan 2,3-dioxygenase (tryptophan pyrrolase) (Pseudomonas fluorescens). Methods in Enzymology 17, 429-434 (1970).

26. Yamamoto, S. & Hayaishi, O. Tryptophan pyrrolase of rabbit intestine. D- and L-tryptophan-cleaving enzyme or enzymes. J. Biol. Chem. 242, 5260-5266 (1967).

27. Yoshida, R., Urade, Y., Tokuda, M. & Hayaishi, O. Induction of indoleamine 2,3-dioxygenase in mouse lung during virus infection. Proc. Natl Acad. Sci. USA 76, 4084-4086 (1979).

28. Allegri, G., Bertazzo, A., Biasiolo, M., Costa, C. & Ragazzi, E. Tryptophan metabolism along the kynurenine pathway in rats. Adv. Exp. Med. Biol 527, 455-463 (2003).

29. Littlejohn, T., Takikawa, O., Truscott, R. & Walker, M. Production of Truncated Enzymically-Active Human Indoleamine 2,3-Dioxygenase (IDO) Using Site-Directed Mutagenesis. J. Biol. Chem. 278, 29525-29531 (2003).

30. Laurentis, W. D. et al. The Second Enzyme in Pyrrolnitrin Biosynthetic Pathway Is Related to the Heme-Dependent Dioxygenase Superfamily. Biochemistry 46, 12393-12404 (2007).

31. Batabyal, D. & Yeh, S.-R. Human Tryptophan Dioxygenase: A Comparison to Indoleamine 2,3-Dioxygenase. J. Am. Chem. Soc. 129, 15690 -15701 (2007).

32. http://www.umassvegetable.org/soil_crop_pest_mgt/disease_mgt

33. http://microbewiki.kenyon.edu/index.php/Xanthomonas.

34. Thieme, F. et al. Insights into Genome Plasticity and Pathogenicity of the Plant Pathogenic Bacterium *Xanthomonas campestris* pv. vesicatoria Revealed by the Complete Genome Sequence. Journal of Bacteriology 187, 7254-7266 (2005).

35. Sugimoto, H. et al. Crystal structure of human indoleamine 2,3-dioxygenase: Catalytic mechanism of O2 incorporation by a heme-containing dioxygenase Proc Natl Acad Sci USA 103, 2611-2616 (2006).

36. Oda, S.-i., Sugimoto, H., Yoshidac, T. & Shiro, Y. Crystallization and preliminary crystallographic studies of human indoleamine 2,3-dioxygenase. Acta Cryst. F62,, 221-223 (2006).

37. Murzin, A., Brenner, S., Hubbard, T. & Chothia, C. A Structural Classification of Protein Database for the Investigation of Sequences and Structures.. J. Mol. Biol. 247, 536-540 (1995).

38. Acton, T. et al. Robotic cloning and protein production platform of the Northeast Structural Genomics Consortium. Methods Enzymol. 394, 210-243 (2005).

39. Littlejohn, T. et al. Expression and purification of recombinant human indoleamine 2,3-dioxygenase. Protein Expr Purif 19, 22-29 (2000).

40. Jansson, M. et al. High-level production of uniformly 15N- and 13C-enriched fusion proteins in Escherichia coli Biomol. NMR 7, 131−141 (1996).

41. Doublie, S. et al. Crystallization and preliminary X-ray analysis of the 9 kDa protein of the mouse signal recognition particle and the selenomethionyl-SRP9. FEBS Lett 384, 219-221 (1996).

42. Bradford, M. A Rapid and Sensitive Method for the Quantitation of Microgram Quantities of Protein Utilizing the Principle of Protein-Dye Binding. Anal. Biochem. 72, 248-254 (1976).

43. Paul, K., Theorell, H. & Akeson, A. The molar light absorption of pyridine ferroprotoporphyrin (pyridine haemochromogen. Ada Chemica Scandinavica 7, 1284-1290 (1953).

44. McPherson, A. (ed.) Crystallization of Biological Macromolecules (Cold Spring Harbor Laboratory Press, New York, 1999).

45. Otwinowski, Z. & Minor, W. Processing of x-ray diffraction data collected in oscillation model. Methods Enzymol. 276, 307-326 (1997).

46. Hendrickson, W. Determination of macromolecular structures from anomalous diffraction of synchrotron radiation. Science 254, 51-58 (1991).

47. Weeks, C. & Miller, R. The design and implementation of SnB v2.0. J. Appl. Cryst. 32, 120-124 (1999).

48. Terwilliger, T. SOLVE and RESOLVE: automated structure solution and density modification. Methods Enzymol. 374, 22-37 (2003).

49. Jogl, G., Tao, X., Xu, Y. & Tong, L. COMO: a program for combined molecular replacement. Acta Cryst. D57, 1127-1134 (2001).

50. Navaza, J. AMoRe: an automated package for molecular replacement. Acta Cryst. A50, 157-163 (1994).

51. Jones, T., Zou, J., Cowan, S. & Kjeldgaard, M. Improved methods for binding protein models in electron density maps and the location of errors in these models. Acta Crystallogr. A47, 110-119 (1991).

52. Roussel, A. & Cambillau, C. (eds.) In Silicon Graphics Geometry Partners Directory 86 (Mountain View, CA, USA: Silicon Graphics, 1991).

53. Brunger, A. T. et al. Crystallography & NMR system: A new software suite for macromolecular structure determination. Acta Crystallogr D Biol Crystallogr D54, 905-921 (1998).

54. Kraulis, P. MOLSCRIPT: a program to produce both detailed and schematic plots of protein structures. J Appl Crystallogr 24, 946-950 (1991).

55. Merritt, E. & Bacon, D. Raster 3D: Photorealistic molecular graphics. Methods Enzymol 277, 505-524 (1997).

56. Chauhan, N. et al. The Role of Serine 167 in Human Indoleamine 2,3-Dioxygenase: A Comparison with Tryptophan 2,3-Dioxygenase. Biochemistry 47 4761-4769 (2008).

57. Terentis, A. et al. A Cooperative Oxygen Binding Hemoglobin from Mycobacterium tuberculosis J Biol Chem 277, 15788-15794 (2002).

58. Unno, M. et al. Crystal Structure of the Dioxygen-bound Heme Oxygenase from Corynebacterium diphtheriae J Biol Chem 279, 21055-21061 (2004).

59. Djinovic Carugo, K., Everitt, P. & Tucker, P. A cell for producing xenon-derivative crystals for cryocrystallographic analysis. J. Appl. Cryst. 31, 812-814 (1998).

60. Soltis, S., Stowell, M., Wiener, M., Philips, G. & Rees, D. Successful flash-cooling of xenon-derivatized myoglobin crystals. J. Appl. Cryst. 30, 190-194 (1997).

61. Vernède, X. & Fontecilla-Camps, J. C. A method to stabilize reduced and/or gas-treated protein crystals by flash-cooling under a controlled atmosphere. J. Appl. Cryst. 32, 505-509 (1999).

62. Zhang, Y. et al. Crystal Structure and Mechanism of Tryptophan 2,3-Dioxygenase, a Heme Enzyme Involved in Tryptophan Catabolism and in Quinolinate Biosynthesis. Biochemistry 46, 145-155 (2007).

63. Daraselia, N. et al. Reannotation of *Shewanella oneidensis* genome. OMICS: A Journal of Integrative Biology 7, 171-175 (2003).

64. Kolker, E. et al. Global profiling of Shewanella oneidensis MR-1: Expression of hypothetical genes and improved functional annotations Proc. Natl. Acad. Sci. USA 102 (6) 2099-2104 (2005).

65. McRee, D. XtalView/Xfit—A Versatile Program for Manipulating Atomic Coordinates and Electron Density J Struct Biol. 125, 156-165 (1999).

66. Daraselia, N. et al. Reannotation of Shewanella oneidensis Genome. OMICS: A Journal of Integrative Biology 7, 171-175 (2003).

Chapter 4

Crystallographic studies on histidine 55 mutant of tryptophan 2,3-dioxygenase from Xanthomonas campestris

Crystallographic studies on histidine 55 mutant of tryptophan 2,3-dioxygenase from *Xanthomonas campestris*

4.1 Introduction

As described in chapter 3, the crystal structures of bacterial TDO [1, 2] and human IDO [3] reveal similarities between the two enzymes and allow the identification of potentially important active-site residues.

The catalytic mechanisms of TDO and IDO have, so far, not been fully elucidated. It has been proposed that their catalytic mechanism involves the base-catalyzed deprotonation of the indole nitrogen of the substrate [4]. However, the structures of TDO and IDO show that while TDO contains a histidine residue in its active site, IDO does not contain any residues in its active site capable of performing base-catalyzed deprotonation. In the TDO active site the histidine 55 hydrogen bonded to L-Trp could be implicated as the active site base. This chapter reports the crystallographic study of a *X. campestris* TDO mutant, where the active-site residue histidine 55 has been substituted by alanine (H55A). The structural data, in conjunction with potentiometric and kinetic studies on the mutant, attempt to resolve the question of whether an active site base is necessary for catalytic activity in TDO and provide information on the molecular mechanism used by TDO to control substrate binding.

4.2 Reaction mechanism of TDO: a model for the Michaelis complex

A model for the Michaelis complex can help to provide insight into the catalytic mechanism of TDO (fig 4.1). The model was built by placing one oxygen atom (O1) of the dioxygen substrate directly over the heme iron, at a distance of 2.1 Å. The distal oxygen atom (O2) is placed such that the O1–O2 bond is parallel to the C2–C3 bond of indole ring, giving a Fe–O1–O2 angle of 135° (Fig 4.1b). This conformation places the

O2 atom within 0.5 Å of the water molecule observed in the crystal structure (PDB entry 2NW8) (Fig 4.1a), suggesting that this water should be ejected from the active site upon dioxygen binding. The active site is therefore completely devoid of solvent molecules in this Michaelis complex. The modeled dioxygen-binding mode reveals the activation mechanism of this substrate for the reaction.

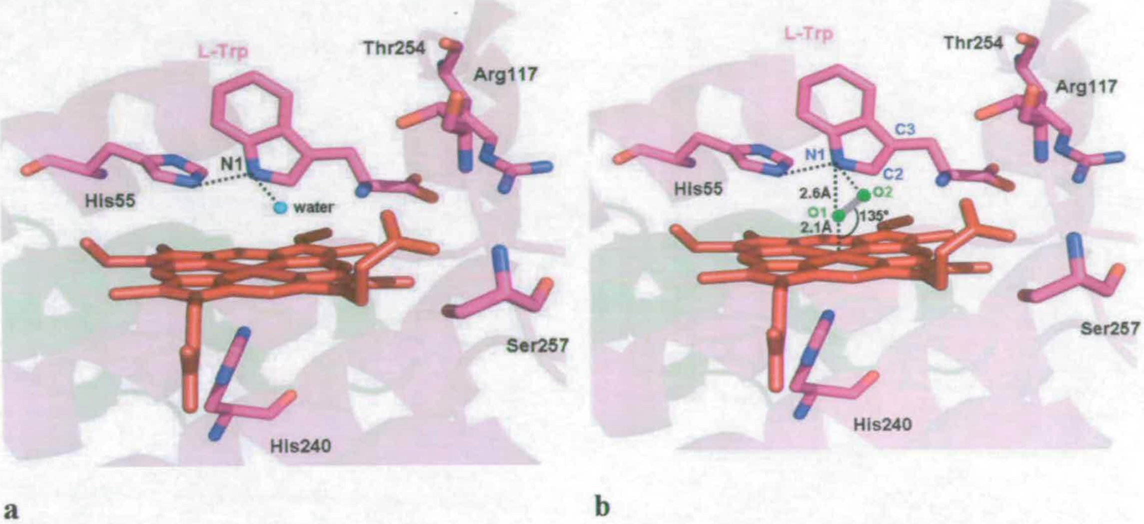

Fig 4.1: Molecular insights into the catalysis by TDO. a) Crystallographic model showing the water in the active site as a small sphere in cyan. b) Model of the Michaelis complex where the oxygen atoms are represented in green.

It has been established that TDO has an ordered catalytic cycle [4]. The protein (with heme in its ferrous form) first binds L-Trp near the sixth coordination position of the heme iron. This event is followed by the binding of dioxygen to the distal coordination of the heme iron. The model for the Michaelis complex (fig 4.1b) of TDO shows that the O1 atom is 2.6 Å from the N1 atom of L-Trp and therefore might act as a base to extract the proton from the N1 atom [4-6] In the model, the distal oxygen atom (O2) interacts with the L-Trp ammonium moiety and the backbone amide nitrogen of Gly125 (not shown in the figure). The Lewis acidity of the hydrogen-bonding donors, coupled with the electron-withdrawing nature of the heme, would increase the electrophilicity of the bound dioxygen and facilitate the nucleophilic attack by the substrate C3 atom.

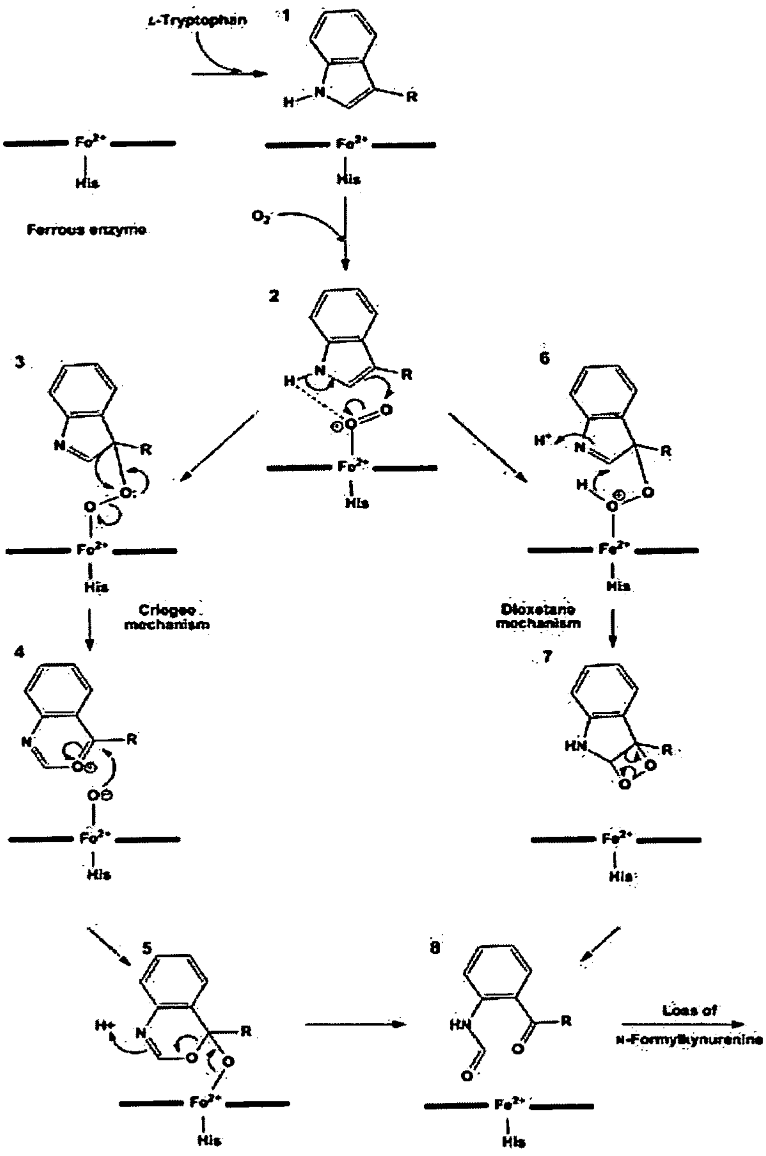

Fig 4.2: Schematic representation of the reaction mechanism of TDO. The figure displays an ionic, base catalyzed mechanism of L-Trp dioxygenation. Firstly substrate binds to the protein (1), followed by dioxygen binding to form the ternary complex (2). The mechanism proceeds by the formation of a hydroperoxide intermediate (3 and 6), which can undergo two different rearrangements to form the product, N-formylkynurenine (8), a Criegee rearrangement (4 and 5) or a dioxetane rearrangement (7). The product (N-formylkynurenine) is then released leaving the protein in the active ferrous state. The reaction scheme is proposed on the basis of the active site architecture and according to the mechanism proposed by Terentis A. et al., 2002 [4].

After the initial attack by the C3 atom, the reaction may proceed via a Criegee rearrangement or a dioxetane intermediate (Fig. 4.2 indicated respectively as 3 and 6 intermediates). However, the Criegee pathway seems to be favoured, based on chemical, thermodynamic, and quantum mechanical considerations [6].

In TDO the N1 atom of L-Trp is hydrogen-bonded to His55. In order to investigate the role of the histidine side chain involved in substrate binding this residue was replaced, alternately, by alanine (H55A) and by serine (H55S) [7]. The mutant enzymes showed slightly higher Michaelis constants (K_m) and lower k_{cat} values for L-Trp oxidation. The k_{cat} values for both the H55A and H55S enzymes were about 10-fold lower than the value for the wild-type enzyme (Table 4.1).

In the wild-type enzyme there is a large increase in the affinity of the enzyme for L-Trp for ferrous vs. ferric enzyme (K_d Fe (III) = 3.8 mM, K_d Fe(II) = 4.2 μM) (table 4.1, data from Miss Sarah J. Thackray, [7]). For both the H55A and the H55S mutants this effect is essentially destroyed, with only a small increase in the affinity of ferrous enzyme for L-Trp relative to ferric (Table 4.1). This trend in K_d is repeated for other substrates (tables 4.2 and 4.3). The presence of His55 decreases the affinity of the oxidised protein for substrate, and its removal increases binding affinity by a factor of>300.

				K_d L-Trp (μM)	
Enzyme	**Substrate**	**k_{cat} (s^{-1})**	**K_m (μM)**	**Ferric heme**	**Ferrous heme**
TDO wt	**L-Trp**	19.5 ± 1.2	114 ± 1	3840 ± 140	4.12 ± 0.24
TDO H55A	**L-Trp**	2.86 ± 0.10	133 ± 7	11.8 ± 0.2	3.7 ± 1.3
TDO H55S	**L-Trp**	2.60 ± 0.01	197 ± 2	18.4 ± 3.0	5.25 ± 1.0

Table 4.1: Summary of kinetic data on X. campestris TDO wild-type (wt) and TDO H55A and H55S with L-Trp. Experiments were performed at 25 °C, in 100mM phosphate buffer, pH 7.5 as described in [7]

				K_d L-Trp (μM)	
Enzyme	**Substrate**	**k_{cat} (s^{-1})**	**K_m (μM)**	**Ferric heme**	**Ferrous heme**
TDO wt	**6F- D/L-Trp**	37.3 ± 0.6	186 ± 12	2450 ± 420	<1.00
TDO H55A	**6F- D/L -Trp**	3.78 ± 0.10	195 ± 1	165 ± 44	73 ± 3
TDO H55S	**6F- D/L -Trp**	3.8 ± 0.04	546 ± 36	86.0 ± 12	6.16 ± 0.9

Table 4.2: Summary of kinetic data on X. campestris TDO wild-type (wt) and TDO H55A and H55S with 6F-D/L-Trp. Experiments were performed at 25 °C, in 100mM phosphate buffer, pH 7.5 as described in [7]

				K_d L-Trp (μM)	
Enzyme	**Substrate**	**k_{cat} (s^{-1})**	**K_m (μM)**	**Ferric heme**	**Ferrous heme**
TDO wt	**5F- D/L-Trp**	2.4 ± 0.1	100 ± 6	1510 ± 80	<1.00
TDO H55A	**5F- D/L -Trp**	0.86 ± 0.14	194 ± 25	66.8 ± 20	9.0 ± 1.2
TDO H55S	**5F- D/L -Trp**	0.80 ± 0.01	183 ± 12	73.4 ± 5.0	<5.0

Table 4.3: Summary of kinetic data on X. campestris TDO wild-type (wt) and TDO H55A and H55S with 5F-D/L-Trp. Experiments were performed at 25 °C, in 100mM phosphate buffer, pH 7.5 as described in [7]*.*

Furthermore, the k_{cat} of TDO is relatively insensitive to pH over the range pH 6.0 to pH 8.0 and the H55A mutant show only a 10-fold decrease in the value of k_{cat}, suggesting that this residue is not essential for catalysis, consistent with the presence of a serine residue in IDO in the equivalent position. On the other hand, the value of K_m shows a marked increase at lower pH, possibly because of the protonation of this residue.

All these data [2, 7] enhance the view that His55 is not acting as a base in the catalytic cycle since its substitution might have been expected to render the enzyme inactive. It must therefore play a different role in catalysis. Effects similar to these are seen in IDO where the equivalent residue to His55 is Ser167 [3]. A possible role of His55 in TDO could be to control the binding affinity of the active site for L-Trp, gating the binding of substrate to wild-type TDO.

4.3 Results

4.3.1 Genetic manipulation, protein expression and purification

Full-length *X. campestris* TDO (NESG (Northeast Structural Genomics Consortium) ID XcR13) was cloned into a pET-21d (Novagen, San Diego, CA) derivative with a C-terminal 6-histidine tag, and overexpressed at 17 °C in *Escherichia coli* BL21 (DE3) pMGK cells. Point mutation H55A was created with the QuikChange II site directed mutagenesis kit (Stratagene, La Jolla, CA). Oligonucleotide primers directing the mutation were designed in an automated fashion by using the Primer Prim'er program, accessible at www-nmr.cabm.rutgers.edu/bioinformatics/Primer_Primer. The mutation and its associated ORF were verified by DNA sequence analysis.

Protein was purified by using nickel-affinity and gel-filtration chromatography as described in section 3.6.2 for the wild-type protein.

Protein and heme concentrations were determined by the Bradford and pyridine hemochrome methods respectively [8, 9]. For wild-type TDO extinction coefficients ε_{404nm} and ε_{431nm} of 180.5 (± 0.1) $mM^{-1}cm^{-1}$ and 113.0 (± 0.1) $mM^{-1}cm^{-1}$ per protomer were calculated for the ferric and ferrous enzymes respectively [2]. For the H55A mutant ε_{431nm} of 120.0 (± 0.1) $mM^{-1}cm^{-1}$and ε_{431nm} of 130.4 (± 0.3) $mM^{-1}cm^{-1}$ per protomer were calculated for the ferric and ferrous enzyme respectively.

4.3.2 Protein crystallization and data collection

Crystallisation of H55A TDO was carried out by hanging drop vapour diffusion at 18 °C in Linbro plates. Crystals were obtained with well solutions comprising 9-10% (w/v) PEG 1000, 80 mM MES buffer pH 6.3, 20 mM bicine buffer pH 9.0, 40 mM $MnCl_2$, 400 mM $MgCl_2$, 8 mM NaCN and 20 mM L-Trp. Hanging drops (4 μl volume) were prepared by adding 2 μl of 8 mg ml^{-1} protein (in 50 mM TrisHCl buffer pH 8.0, 5 mM in EDTA) to 2 μl of well solution. Red tetragonal shaped crystals appeared after approximately one week, reaching full size after two weeks.

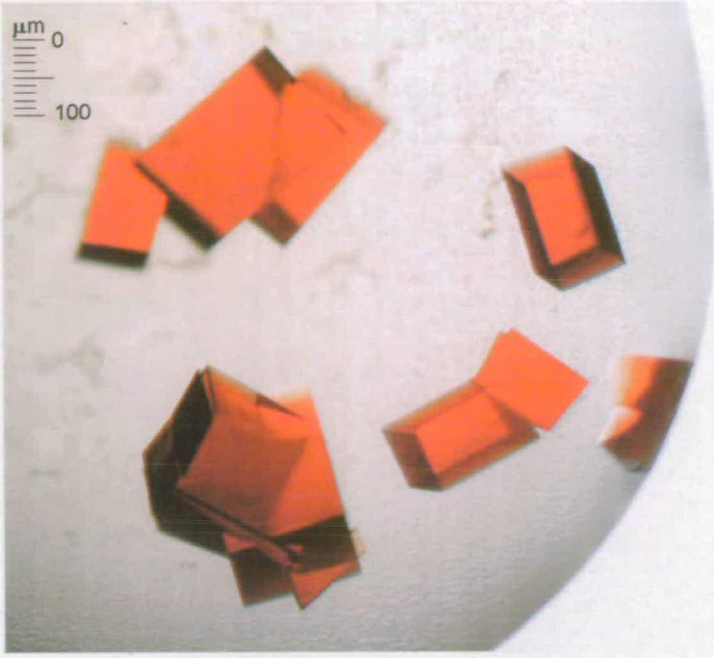

Fig 4.3: Crystals of TDO H55A mutant grown in 10% (w/v) PEG 1000, 80 mM MES buffer pH 6.3, 20 mM bicine buffer pH 9.0, 40 mM $MnCl_2$, 400 mM $MgCl_2$, 8 mM NaCN and 20 mM L-Trp

Crystals were immersed in mineral oil prior to being mounted in nylon loops and flash cooled in liquid nitrogen. A data set was collected to 2.15 Å at station 10.1 ($\lambda = 1.381$ Å) at SRS Daresbury using a Mar Research MAR225 CCD detector. Crystals belonged to space group $P2_1$ with unit cell parameters $a = 78.2$ Å, $b = 117.6$ Å, $c = 139.3$ Å and $\beta = 95.7°$. All data processing was carried out using the CCP4 package [10]. The wild-type TDO apo-enzyme structure (PDB ID 1YW0), stripped of water was used as the initial model. Electron density fitting was carried out using the program Turbofrodo [11] and structure refinement was carried out using Refmac [12].

Protein	TDO(H55A)
Beam line	SRS 10.1
Ligand	L-Trp
PDB entry	3BK9
Space group	$P\,2_1$
cell dimensions	$a = 78.2$, $b = 117.6$, $c = 139.3$ (Å) and $\beta = 95.7°$
resolution (Å)	59.66-2.15 (2.27 – 2.15)*
total no. of reflections	312593
no. of unique reflections	131764
completeness (%)	96.9 (91.7)*
$I/[\sigma(I)]$	9.5 (2.5)*
R_{merge} (%)^a	10.0 (47.4)*
R_{work} (%)^b	20.05
R_{free} (%)^c	28.46
rmsd from ideal values	
bond lengths (Å)	0.022
bond angles (deg)	2.004
Ramachandran analysis	
most favoured (%)	91.9
additionally allowed (%)	8.1
no. of waters included in refinement	1026

*Table 4.4: Data collection and refinement statistics * Values in parentheses represent statistics for the highest resolution shell* ^{a} $R_{merge} = \Sigma_h\Sigma_i|I(h) - I_i(h)|/\Sigma_h\Sigma_i I_i(h)$*, where* $I_i(h)$ *and* $I(h)$ *are the ith and mean measurement of reflection h, respectively.* ^{b} $R_{work} = \Sigma_h|F_o - F_c|/\Sigma_h F_o$*, where* F_o *and* F_c *are the observed and calculated structure factor amplitudes of reflection h, respectively.* ^{c} R_{free} *is the test reflection data set, 5 % selected randomly for cross validation during crystallographic refinement.*

4.4 Crystal structure of H55A TDO

It was possible to obtain crystals of the ferric H55A mutant enzyme in a binary complex with the substrate due to the much greater affinity of L-Trp for the oxidised mutant enzyme compared to wild-type TDO (table 4.1).

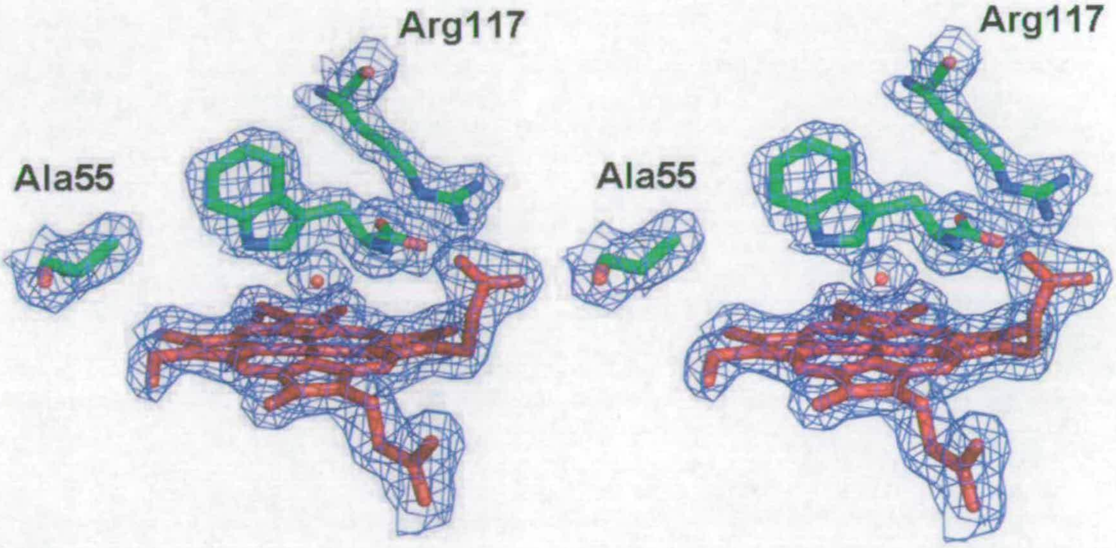

Fig 4.4: Stereoview of electron density around the heme, Ala55, Arg117 and the substrate at the active site of H55A TDO (monomer B) in complex with L-Trp. The electron density map was calculated using Fourier coefficients 2 $F_o - F_c$, where F_o and F_c are the observed and calculated structure factors, respectively, the latter based on the final model. The contour level is 1σ, where σ is the rms electron density.

A data set to 2.15 Å resolution was used to refine the structure to a final *R*-factor of 20.1% (R_{free} = 28.5 %), and the data collection and refinement statistics are summarised in table 4.4. The structure of TDO is an intimately associated tetramer and this is shown in figure 4.5. As already described for wild-type TDO (section 3.7), the N-terminus of each monomer (up to residue Leu40) penetrates into the active site of an adjacent subunit, and is involved in substrate binding. The final model of the TDO H55A mutant enzyme consists of two TDO tetramers (1 and 2), one of which (tetramer 1) is better defined than the other in the electron density map.

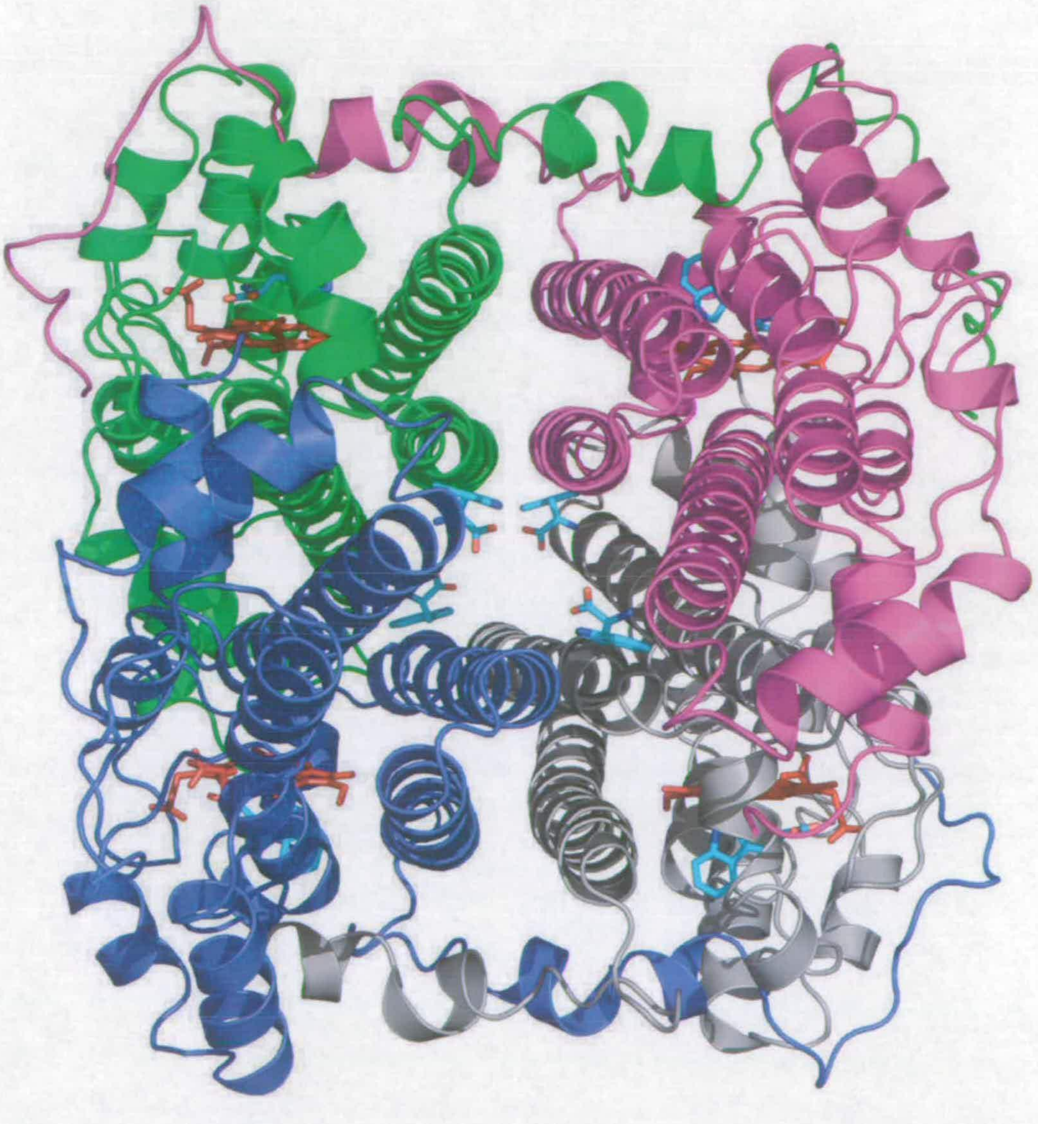

Fig 4.5: Tetramer structure of H55A mutant TDO. The heme groups are shown in red and L-Trp in cyan. One 'dimer' is shown in magenta and green and the other in grey and blue. The interfacial L-Trp molecules can be seen in the centre of the tetramer.

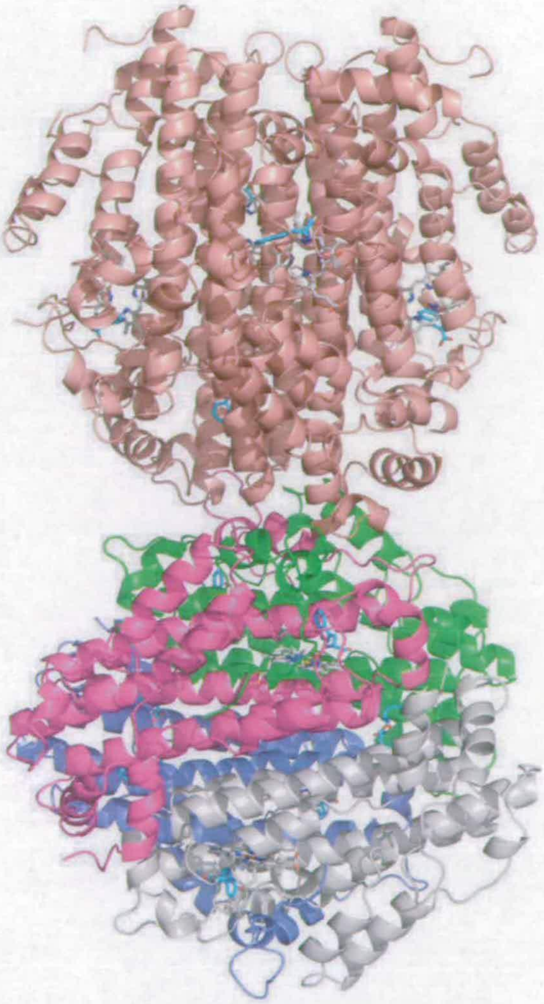

Fig 4.6: Two tetramers making up the asymmetric unit of TDO H55A crystal. Monomers of tetramer 1 are shown in magenta, green blue and gray. Tetramer 2 is more weakly defined in the model and it is shown entirely in light pink. Hemes are represented in sticks and colored in gray. L-tryptophan bound in the active site and in the interface of the monomers are represented in sticks and colored in cyan.

Each of the eight monomers in the model is slightly different in terms of which N- and C-terminal residues are ordered. In this respect the most complete monomer is chain B which consists of residues Leu7-Asn286, while the least well-defined monomer is chain F, consisting of residues Thr23-Gly283 (with a gap of 11 residues between Tyr187 and Asp199). As in the structure of wild-type TDO, approximately 15 residues at the C-terminus of the protein could not be located in the electron density map, and so are omitted from the model. However, the N-terminal region of the H55A mutant enzyme is better defined than in wild-type TDO and is distinguishable in the electron density for tetramer 1 from Leu7 upwards (12 residues more than wild-type TDO), in chains A, B and C (figure 4.7).

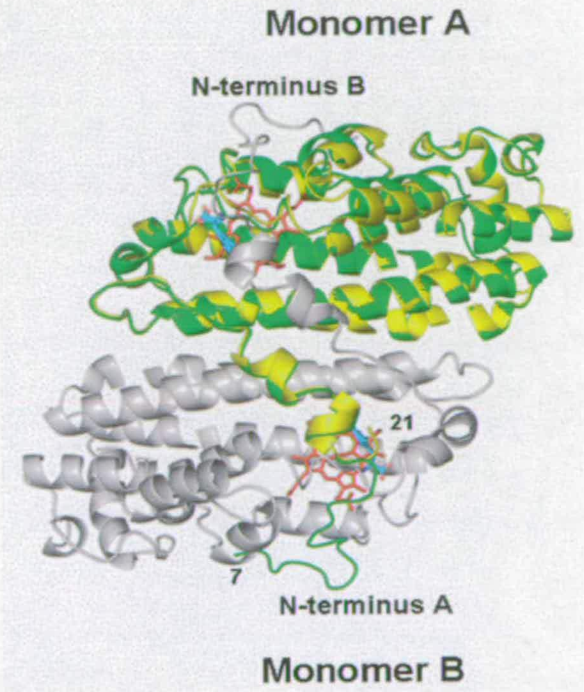

Fig 4.7: Dimers of TDO wild-type and H55A mutant. In yellow is shown the model of monomer A of TDO wild-type (PDB entry 2NW8) overlaid with the model of the corresponding monomer of TDO H55A mutant (in green) (PDB entry 3BK9). The hemes and the substrate are represented as sticks and colored respectively red and cyan. Residues 7-21 are visible only in the TDO H55A model.

Each monomer also binds one heme group and one substrate molecule. Further to this, a second L-Trp molecule is observed at the inter-subunit interface close to each of chains A, B, C, D and E. In addition the model contains 1026 water molecules. The atomic coordinates have been deposited in the Protein Data Bank, accession code 3BK9.

The increased definition of the N-terminal region in some monomers of the H55A mutant enzyme structure is of interest given that these residues (7-21) interact with the loop region which is involved in substrate binding (residues 250–260). It is notable that in the wild-type TDO model the active site tryptophan has temperature factors slightly above the average for the whole protein (23.6 Å^2 vs 21.7 Å^2).

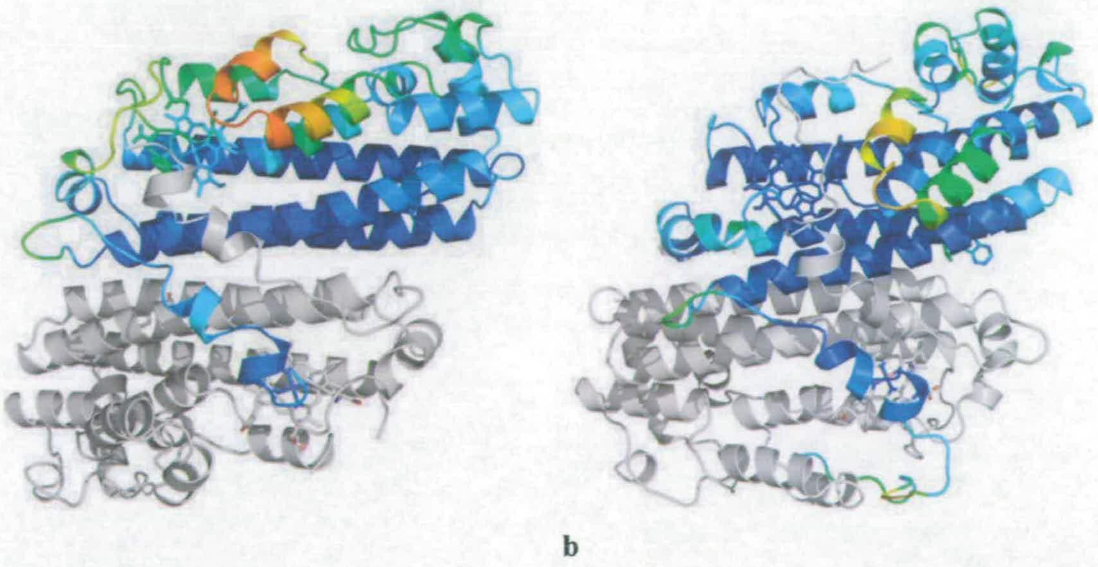

Fig 4.8: Monomers A and B of TDO wild-type (a) and TDO H55A (b) where respectively monomer A and monomer B have been colored as a rainbow gradient according to temperature factor or B-factor on relative scale -- highest B-factors red, lowest blue. The B-factor is measure of how much an atom oscillates around the position specified in the model. TDO H55A model (b) appears to have less motion than wild-type TDO (a).

In addition, the loop region has an average B-factor of 28.4 Å^2. In the model of the H55A enzyme there is a correlation between the substrate temperature factors, those of the substrate binding loop region, and the level of disorder at the N-terminus of each monomer. In this way, when the substrate B-factors are low, then so are those of the loop region and the N-terminus is more ordered.

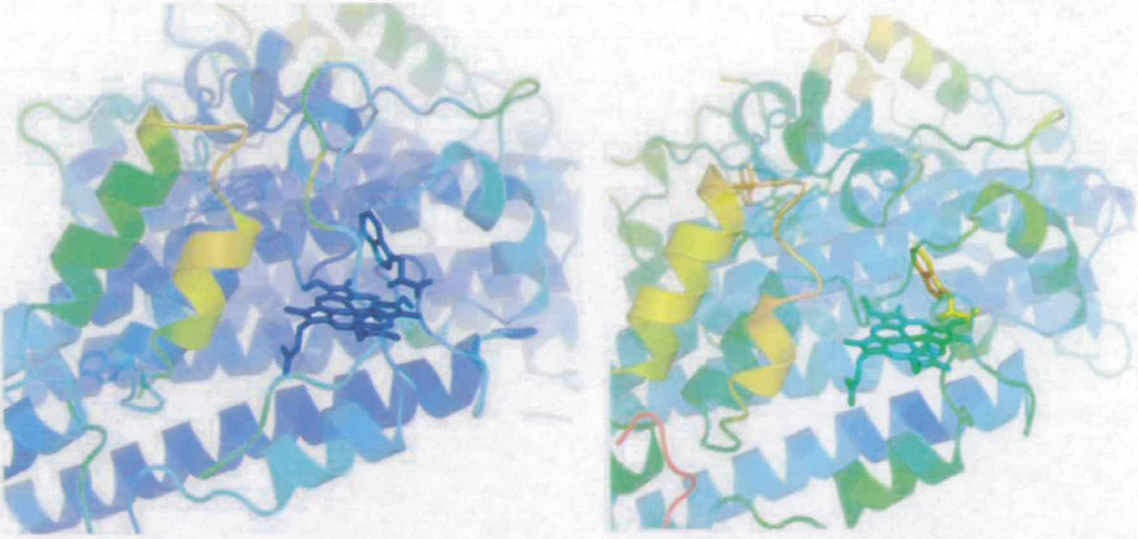

Fig 4.9: TDO H55A active sites of monomer B (a) and monomer F (b) coloured according to their temperature factor. Monomer B is more defined in the electron density and appears to have less motion than to monomer F.

The average rmsd fit of all backbone atoms between all monomers of the H55A TDO model and the structure of the wild-type enzyme (PDB entry 2NW8, in [2]) is 0.6-0.8 Å, indicating no major differences between the two protein structures, except the substitution of His55 by alanine. The quality of the final electron density map around the active site of chain A of tetramer 1 is shown in Figure 4.4.

4.5 Binding mode of L-Trp to H55A TDO

The binding orientation of L-Trp at active site of the H55A mutant enzyme is slightly different from that observed in the wild-type TDO structure. Overlays of the active sites of wild-type TDO and the H55A enzyme are shown in Figures 4.10 and 4.11.

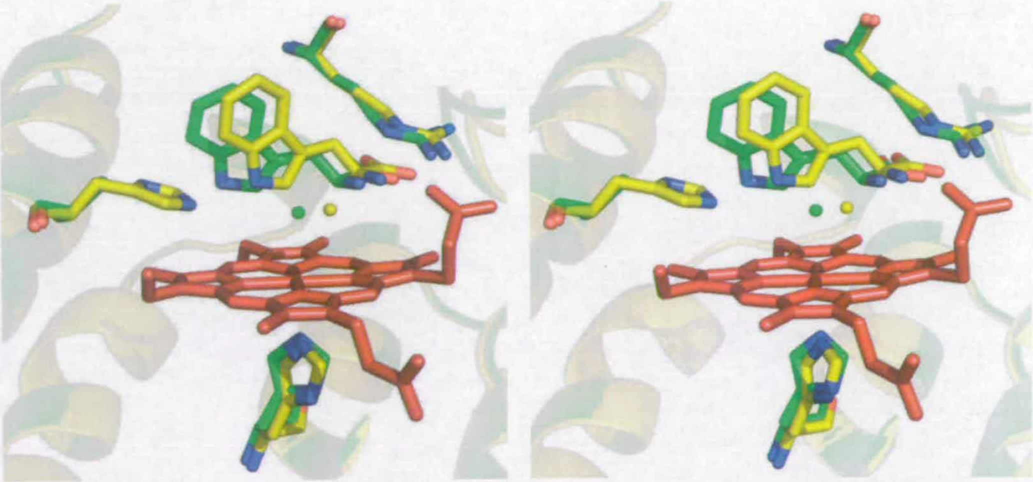

Fig 4.10: Stereoview of an overlay of the active site region of wild-type TDO (yellow) and H55A TDO (green) viewed from the side. The L-Trp from the H55A enzyme (in green) is rotated toward alanine 55 and the heme, relative to the position of the substrate in wild-type TDO (yellow). The H-bond between histidine 55 and the substrate is lost as a result of the substitution by alanine. The position of the water molecule in H55A TDO (wat552) is slightly different than in wild-type enzyme (wat1) due to the altered substrate binding.

The bound L-Trp belonging to the H55A mutant (in green) is rotated by approximately 15° towards alanine 55 relative to the position of L-Trp in the wild-type enzyme (in yellow). Due to the substitution of histidine 55 by alanine, the hydrogen bonding interaction between residue 55 and the substrate indole nitrogen atom is lost. The positions of the side chains of other active-site residues are unperturbed by both the substitution and the change in substrate orientation. In particular, substrate carboxylate interactions with Tyr113, Arg117 and the heme 7-propionate moiety are maintained (Figure 4.12).

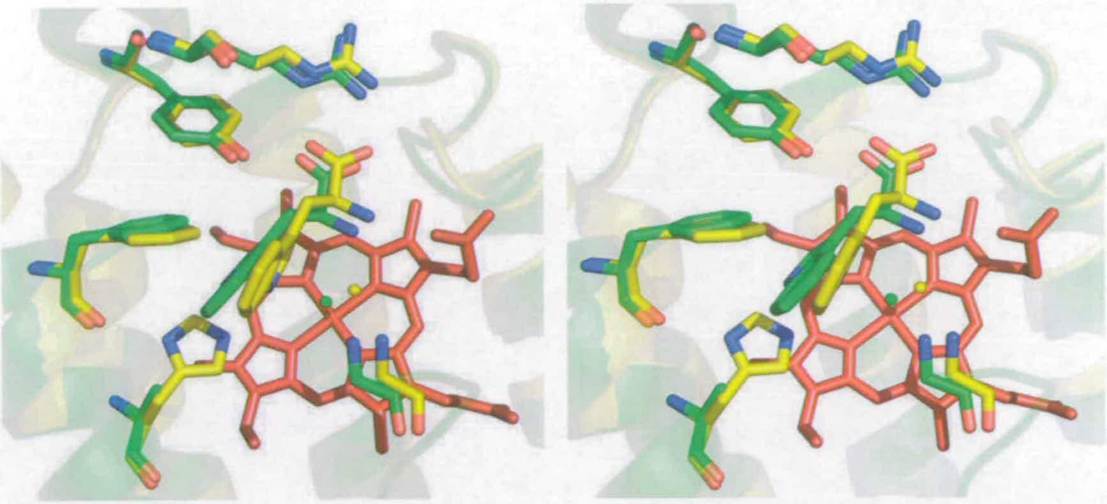

Fig 4.11: Stereoview of an overlay of the active site region of wild-type TDO (yellow) and H55A TDO (green) viewed from above.

Furthermore, the van der Waals interactions between the substrate indole ring and residues Phe51, Tyr24 and Tyr27 and Leu28 (these latter three belonging to the N-terminal region of an adjacent subunit as mentioned above) are conserved in the mutant enzyme.

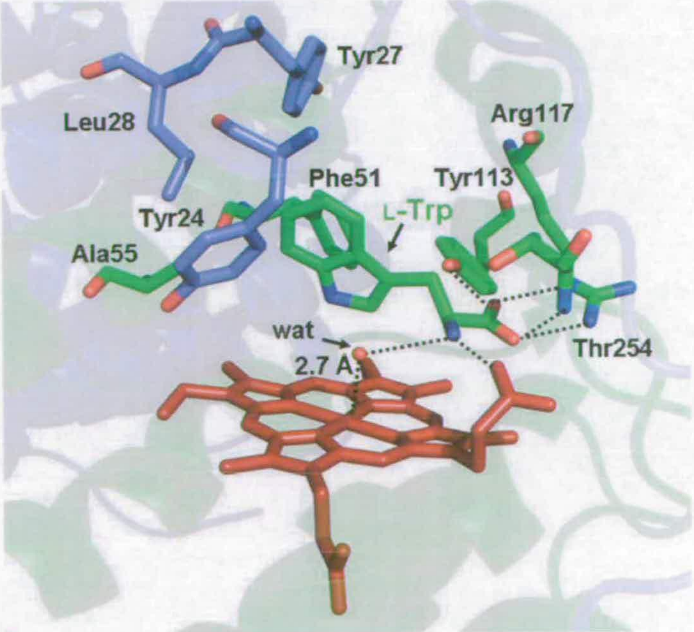

Fig 4.12: The active site of X. campestris TDO H55A mutant. Here the interactions between the bound L-Trp and the active site residues are shown.

A water molecule is found in the active site of both wild-type TDO and the H55A mutant enzyme. This water is H-bonded to the ammonium group of L-Trp (3.0 Å in H55A) and the main-chain amide of glycine 125 (2.8 Å). As a result of the alteration in the position of L-Trp this water is found to be 2.7 Å from the heme Fe in the H55A mutant, compared to a distance of 3.3 Å in wild-type TDO. This is shown in figure 4.12.

In wild-type TDO His55 hydrogen bonds to a water molecule in the substrate free ferrous state (C.G. Mowat, unpublished results) which is displaced upon binding of substrate. In the substrate free active site of the H55A crystal structure there is no equivalent water molecule, thus allowing greater access to the binding cavity compared to wild-type TDO.

An interesting finding in the structure of the substrate-bound ferrous wild-type TDO was the existence of a second L-Trp binding site in the tetrameric interface, and it is possible that this represents an allosteric site (section 3.11). In the structure of the H55A mutant enzyme tetramer 1 this site contains four L-Trp molecules (per tetramer) interacting with Arg85, Lys92 and Asp228 from one monomer and Lys86 from another (fig 4.5). However, in tetramer 2 there is only interpretable L-Trp density in one of the four interfacial binding sites.

The decrease in the value of k_{cat} for L-Trp oxidation in the H55A mutant (see table 4.1) may be explained by the orientation of L-Trp in the active site. The new position of L-Trp in the active site of TDO H55A (figures 4.10 and 4.11) is accompanied by a slight increase in the substrate K_m value, implying a small decrease in the stability of the enzyme ternary complex. The rotation has resulted in the tryptophan indole ring being further from the dioxygen binding site, thus decreasing the overlap of the molecular orbitals involved in catalysis. The transition state for the reaction will therefore be less stable, resulting in greater activation energy for catalysis. This will decrease the rate of turnover for the H55A mutant compared to wild-type TDO.

4.6 Electrochemical studies (Miss Sarah J. Thackray)

Electrochemical data for wild-type TDO [2] and the H55A mutant [7] show that there is a much smaller shift in the reduction potential upon binding of substrate ($\Delta E_{mid\ H55A}$= 23 mV) for the H55A enzyme compared to wild-type TDO ($\Delta E_{mid\ WT}$ = 136 mV). The shift in reduction potential of 23 mV almost perfectly correlates with the increase in affinity for L-Trp for ferrous H55A enzyme vs the ferric form (K_d (Fe (II)) = 3.7 μM vs. K_d (Fe (III)) = 11.8 μM), both giving an estimated $\Delta\Delta G$ of 3.5 kJ mol^{-1}. In fact, the difference in these $\Delta\Delta G$ values calculated for wild-type TDO and the H55A mutant enzyme is approximately 11.5 kJ mol^{-1}, within the range of energies for a single hydrogen bond. It is possible that the lower affinity of oxidised wild-type TDO for substrate may be attributed to subtle changes in the structure of the active site (in terms of the hydrogen-bonding pattern) between the oxidised and reduced enzymes.

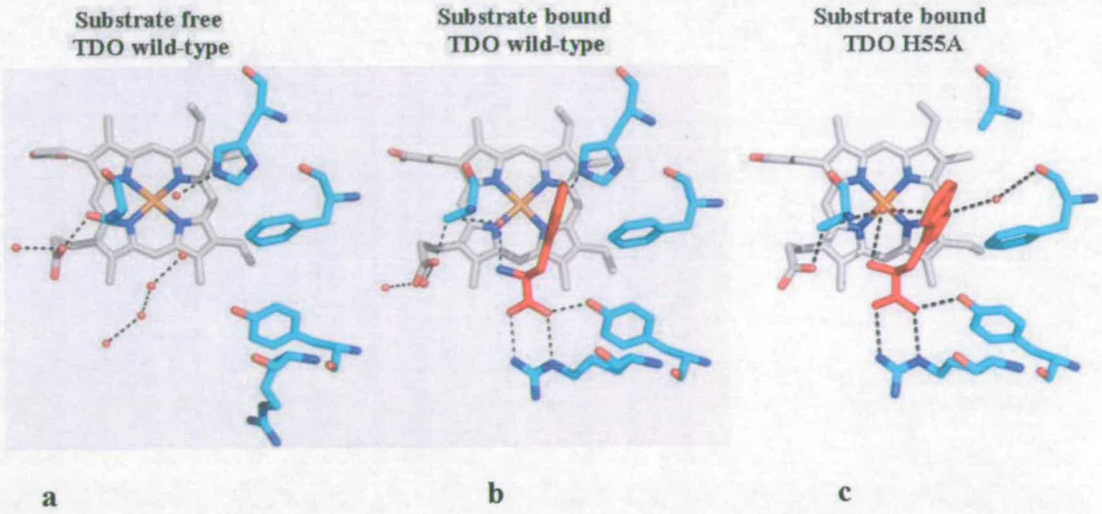

Fig 4.13: Top views of X. campestris TDO. a) Ferric substrate free wild-type, b) ferrous substrate bound wild-type, and c) ferric substrate bound H55A mutant.
In the substrate bound structures, the hydrogen-bonding network is disrupted by the entrance of the L-Trp. A water molecule is still visible in the active site (b and c), but in a different position, and out of range of hydrogen bonding interaction with the nitrogen atom of the histidine (b). A new water molecule appears in the H55A active site, hydrogen bonding with the main chain of Phe51 (c).

Binding of L-Trp accompanies expulsion of solvent from the active site and results in the formation of a hydrogen-bond between histidine 55 and the pyrrole nitrogen of the indole ring.

In ferric wild-type TDO there is a tightly bound water molecule occupying the vacant heme iron coordination site (fig 4.13a). This water would be held in place by a combination of interactions with active site residues (including His55) and other solvent molecules. Upon reduction of the enzyme there is likely to be a restructuring of the active site solvent content. The implication of this rearrangement is that L-Trp is unable to effectively displace the waters when the enzyme is in the ferric form (hence the high L-Trp K_d (mM)) but is able to do so in the ferrous form as reflected in the low L-Trp K_d value (μM) (see table 4.1). The substitution of histidine 55 by alanine is therefore proposed to destabilise the bound waters and make the ferric active site more like that of the ferrous enzyme. In the H55A mutant enzyme the carbon atom of alanine side chain is unable to form the same hydrogen-bonds that histidine 55 can in wild-type TDO. Consequently there may be less rearrangement of the active site hydrogen-bonding interactions necessary to allow L-Trp binding, and the K_d for substrate binding to ferric enzyme is correspondingly small. All other interactions binding L-Trp in the active site are analogous to wild-type TDO. Consequently, the absence of significant oxidation-state-dependent changes in the active site in H55A TDO results in decreased specificity of binding to the oxidised or reduced enzyme.

4.7 Conclusions

Kinetic and electrochemical data, together with the crystal structure, indicate that His55 does not assume the role of active site base, but reveal a role for His55 in controlling substrate binding at the active site, greatly decreasing the affinity of the oxidised enzyme for substrate and regulating the binding of dioxygen, thus allowing precise control of the mechanism of turnover. This prevents unproductive coupling to the ferrous enzyme that would lead to the production of superoxide and the dead-end ferric complex. Substrate must bind first before dioxygen binding takes place.

4.8 References

1. Zhang, Y. et al. Crystal Structure and Mechanism of Tryptophan 2,3-Dioxygenase, a Heme Enzyme Involved in Tryptophan Catabolism and in Quinolinate Biosynthesis. Biochemistry 46, 145-155 (2007).

2. Forouhar, F. et al. Molecular insights into substrate recognition and catalysis by tryptophan 2,3-dioxygenase. Proc. Natl. Acad. Sci. USA 104, 473-8 (2007).

3. Sugimoto, H. et al. Crystal structure of human indoleamine 2,3-dioxygenase: Catalytic mechanism of O_2 incorporation by a heme-containing dioxygenase Proc. Natl Acad. Sci. USA 103, 2611-2616 (2006).

4. Terentis, A. C. et al. The Heme Environment of Recombinant Human Indoleamine 2,3-Dioxygenase. J Biol Chem 277, 15788-15794 (2002).

5. Littlejohn, T., Takikawa, O., Truscott, R. & Walker, M. Production of Truncated Enzymically-Active Human Indoleamine 2,3-Dioxygenase (IDO) Using Site-Directed Mutagenesis. J. Biol. Chem. 278, 29525-29531 (2003).

6. Sono, M., Roach, M. P., Coulter, E. D. & Dawson, J. H. Heme-containing oxygenases. Chem. Rev. 96, 2841-2887 (1996).

7. Thackray, S. J. et al. Histidine 55 of tryptophan 2,3-dioxygenase is not an active site base but regulates catalysis by controlling substrate binding. Submitted (2008).

8. Bradford, M. A Rapid and Sensitive Method for the Quantitation of Microgram Quantities of Protein Utilizing the Principle of Protein-Dye Binding. Anal. Biochem. 72, 248-254 (1976).

9. Berry, E. & Trumpower, B. Simultaneous Determination of Hemes *a, b,* and *c* from Pyridine. Hemochrome Spectra. Anal. Biochem. 161, 1-15 (1987).

10. CCP4. The CCP4 suite: programs for protein crystallography. Acta Crystallogr. D50, 760-763 (1994).

11. Roussel, A. & Cambillau, C. (eds.) In Silicon Graphics Geometry Partners Directory 86 (Mountain View, CA, USA: Silicon Graphics, 1991).

12. Murshudov, G., Vagin, A. A. & Dodson, E. Refinement of macromolecular structures by the maximum-likelihood method. Acta Cryst. D53, 240-255 (1997).

Chapter 5

Structural characterisation of the N42C:K324C mutant of flavocytochrome b_2

Structural characterisation of the N42C:K324C mutant of flavocytochrome b_2

5.1 Introduction

Flavocytochrome b_2 from *Saccharomyces cerevisiae* is a flavohemoprotein localized in the yeast mitochondrial intermembrane space, and catalyzes the oxidation of L-lactate to pyruvate. This reaction is coupled to cytochrome c reduction (fig 5.1).

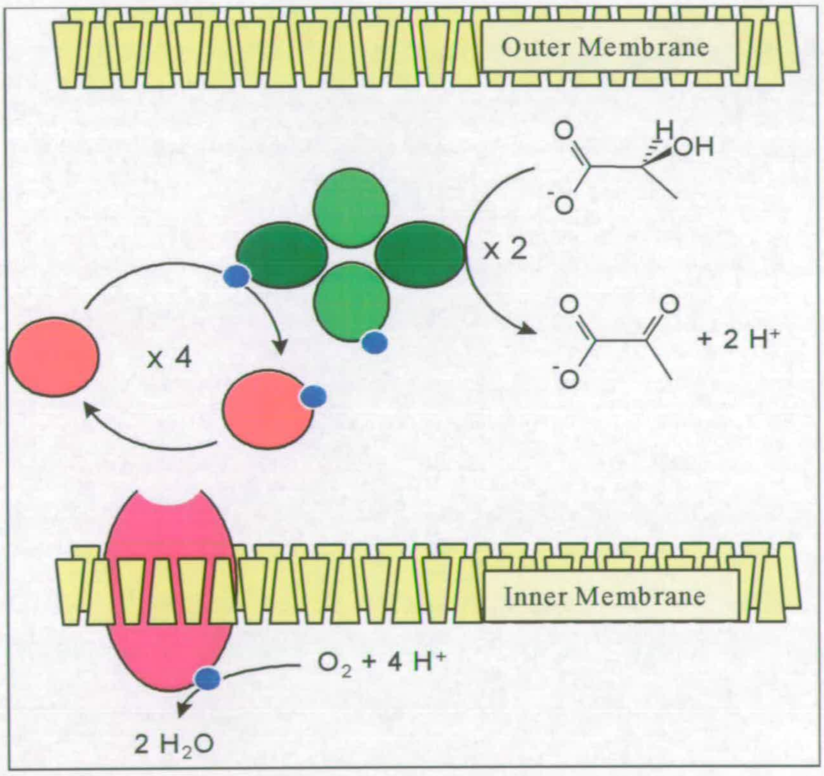

Fig 5.1: Schematic illustration of the biological role of flavocytochrome b_2 (represented in green as a tetramer). Flavocytochrome b_2 is localized in the intermembrane space. The oxidation of L-lactate results in the reduction of cytochrome c (represented in red). Electrons involved in the reaction are shown in blue and are passed from flavocytochrome b_2, via cytochrome c and cytochrome c oxidase (in dark magenta),) to finally reduce water.

The crystal structure of the native enzyme has been solved to 2.4 Å resolution in 1990 [1, 2].

The enzyme is a homotetramer (fig 1.23). Each subunit of the tetrameramer is formed by two functionally distinct domains, each one carrying a prosthetic group. The N-terminal moiety of the protein (residues 1-88) (Fig 5.2 in purple) carries the heme. The C-terminus (residues 106-486) (fig 5.2 in yellow) binds the flavin (FMN) and contains the L-lactate binding site. The two domains are connected by a flexible loop (residues 89-105) (fig 5.2 in blue).

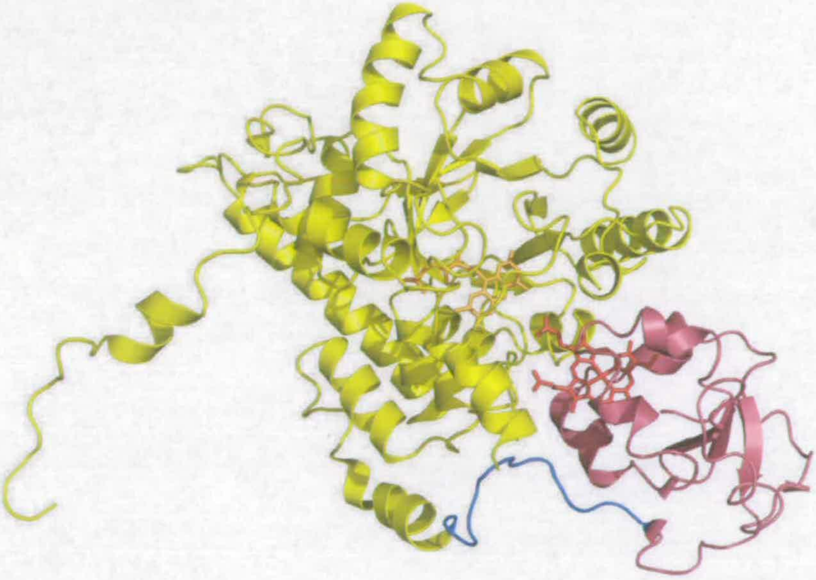

Fig 5.2: An individual subunit of flavocytochrome b_2[2]. The heme domain is represented in dark magenta, the hinge domain is shown in blue, and the flavin domain is shown in yellow. The heme and the FMN are represented as sticks and coloured respectively in dark red and orange.

5.2 The inter-domain hinge region of flavocytochrome b_2

The catalytic cycle of flavocytochrome b_2 has been extensively studied [3-7] and consists of five steps as described in section 1.5.5.

Although the enzyme is tetrameric (fig 1.23), each subunit acts independently [8]. After the oxidation of L-lactate to pyruvate, the two electrons gained from the reaction are transferred from the flavin to the heme domain, through sequential electron-transfer reactions. Then the electrons are transferred to the acceptor, cytochrome *c* (fig 5.1).

The mechanism of such electron transfer is deeply connected with the folding of flavocytochrome b_2 into two distinct domains.

Domain mobility plays a crucial role in catalysis by many enzymes [9]. An example of protein flexibility is the so called “hinge mechanism”. The hinge mechanism allows rigid body movements in proteins which do not display extensive inter-domain contacts. Indeed, hinge bending is a very common motion in proteins and an important mechanism at the basis of functional changes in enzyme conformations [10-14]. Hinge motions have been reported to contribute to ligand binding [15, 16], mediate allosteric effects [17] and modulate the function of enzymes [18].

Hinge regions are generally characterized by a high percentage of short-side chain and uncharged residues, such as glycine, alanine and proline. The characteristics of these residues seem to contribute to the hinge bending [19].

In flavocytochrome b_2, the folding of the flavin and heme domains is globular and quite rigid, allowing only a limited internal motion [2]. The flavin and heme domains are linked together through a flexible loop (fig 5.2, in blue) that constitutes the hinge region. The hinge region has been proposed to confer domain mobility, allowing movement of the heme domain with respect to the flavin domain [20].

Inter-domain mobility of flavocytochrome b_2 has been confirmed both by crystallographic [2] and NMR spectroscopic [21] observations. The crystal structure [2] showed two distinct monomeric subunits in the tetramer. In one of these, no pyruvate is bound at the active site, and the cytochrome domain is well-resolved. In contrast, in the second subunit pyruvate is present, but the electron density for the heme domain is not visible. The reason why the heme domain is not defined when pyruvate is bound at the active site is probably the mobility of the heme domain with respect to the flavin domain. This flexibility was even more clear in solution, where NMR spectroscopic data [21] revealed that the heme domain is more mobile than expected for a large tetrameric protein such a flavocytochrome b_2.

5.3 The role of domain mobility in flavocytochrome b_2

In order to investigate the domain mobility of flavocytochrome b_2, White *et al.* [20] constructed a hybrid enzyme, where the hinge region of the *Saccharomyces cerevisiae* enzyme was replaced with the shorter and more acidic hinge region of flavocytochrome b_2 from *Hansenula anomala* (hinge-swap-b_2). Inter-domain electron transfer was shown to be severely affected in the hybrid enzyme. Kinetic experiments have shown that the major effect in hinge-swap-b_2 was a significant decrease in the rate of flavin to heme reduction [20].

Further experiments demonstrate the importance of maintaining the structural integrity of the hinge for optimal inter-domain electron transfer. Three mutant enzymes with truncated hinge regions (named HΔ3, HΔ6 and HΔ9 respectively with three, six and nine amino acids deleted) were constructed and characterized [22]. In addition, two other mutants with elongated hinge domains (named H*I*3 and H*I*6, with insertion between residues 100 and 101 of respectively three and six residues) were engineered [23]. All the altered hinge regions are illustrated in fig 5.3, in comparison with the wild-type hinge region.

Wild-type	^{89} P P E L V C P P Y A P G E T K ^{103}
H*I*3	P P E L V C P P Y A P G A P G E T K
H*I*6	P P E L V C P P Y A P G A P G A P G E T K
HΔ3	P P E L V C P P Y - - - E T K
HΔ6	P P E L V C - - - - - - E T K
HΔ9	P P E - - - - - - - - - E T K

Figure 5.3: The amino acid sequence for the inter-domain hinge is shown, from Pro89 to Lys103 of the wild-type flavocytochrome b_2. The HI3 and HI6 enzymes have the typical tripeptide motif Ala-Pro-Gly inserted in the primary structure (insertions are indicated in magenta). The gaps in the sequence represent the amino acid residues deleted from the hinge sequence in the HΔ3, HΔ6 and HΔ9 enzymes.

Kinetic characterization of all the mutants shown in fig 5.3 was conducted using both ferricyanide and the natural reaction partner cytochrome *c* as electron acceptors. With ferricyanide, the steady-state k_{cat} values for L-lactate oxidation were decreased only with the HΔ3 and HΔ6 mutant enzymes [22]. In contrast, with cytochrome *c* as the electron acceptor, the steady-state k_{cat} values were dramatically decreased for all the mutants (table 5.1). Such a difference in the k_{cat} values can be explained since it is known that cytochrome *c* can only accept electrons from the heme of flavocytochrome b_2 [24], while ferricyanide receives the electrons both from the FMN and the heme-domains [25].

Enzyme	**k_{cat} (s^{-1})**	**L-lactate K_m (mM)**
Wild-type [a]	207 ± 10	0.24 ± 0.04
H*I*3 [b]	28.3 ± 0.7	> 0.10
H*I*6 [b]	12.7 ± 0.3	> 0.10
HΔ3 [c]	39 ± 1	0.25 ± 0.03
HΔ6 [d]	33.5 ± 1.4	0.09 ± 0.01
HΔ9 [d]	7.9 ± 0.4	0.02 ± 0.01

Table 5.1: Steady-state kinetic parameters using cytochrome c as electron acceptor for wild-type flavocytochrome b_2 and hinge-modified mutants. All the measurements were carried out at 25 °C, in 10 mM TrisHCl, pH 7.5, I 0.10. More details about the conditions are described in the quoted references: [a] [26], [b] [22], [c] [27], [d] [23].

Pre-steady-state kinetic analysis [22, 23, 26, 27] demonstrates that by altering the length of the hinge domain there is a little effect on L-lactate oxidation, while the inter-domain electron transfer is severely affected. The integrity of the hinge was proved to be important for controlling the mobility of the flavin and the heme domain with respect to each other, maybe helping to position the FMN and the heme at the optimal distance for efficient electron transfer. The rate limitation at the inter-domain electron transfer step in the hinge mutants, was confirmed by the pre-steady-state heme reduction experiments [22, 23, 26, 27].

5.4 An inter-domain disulfide bridge in flavocytochrome b_2

To investigate the heme domain mobility relative to the FMN-domain in flavocytochrome b_2 a more recent approach (Bell, PhD thesis, 1997, [37]) involved the restriction of inter-domain movement by the introduction of a covalent bond between the FMN-binding and heme domains.

5.4.1 Disulfide bond engineering as a tool to study conformational changes

The amino acid cysteine can oxidatively pair up with another and produce a disulfide bond. Disulfide bonds play important roles in the folding of many proteins [28, 29] and they can represent a structural motif for increasing stability in many proteins. Disruption of S-S bonds leads to lowering the thermal stability of the tertiary structure [30]. The geometry of a disulfide bond is shown in fig 5.4.

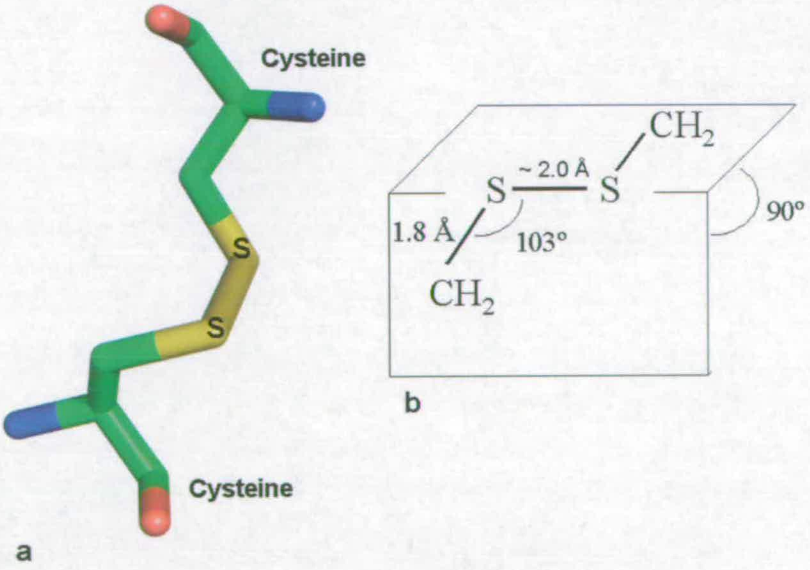

Fig 5.4: a) Cysteines pair up (colour code: carbon in green, oxygen in red, nitrogen in blue, sulfur in yellow) b) disulfide bond geometry: the optimal sulfur-sulfur distance is about 2.0 Å, with the angle between the carbon and the sulfur of about 103°. The dihedral angle between the C-S-S-C - atoms, is usually close to ± 90°.

Disulfide bonds form between the thiol groups (-SH) of two cysteine residues through an oxidation reaction that involves two electrons (fig 5.5).

$$\text{R-SH} + \text{R'-SH} \rightleftharpoons \text{R-S-S-R'} + 2\text{H}^+ + 2\text{e}^-$$

Fig 5.5: The general redox scheme describes the overall reactions that create (oxidize) or destroy (reduce) disulfide bonds

Disulfide bonds occur naturally *in vivo*. Under oxidative conditions a bond between the two sulfur atoms of cysteines positioned at a suitable distance will form spontaneously. The ultimate electron acceptor for thiol oxidation is normally O_2, while in the case of anaerobic conditions an electron acceptor such as fumarate or nitrate reductase can be used [31].

In vitro, development of site-direct mutagenesis allows the replacement of naturally occurring cysteine residues by other amino acids preventing the formation of an S-S bond. It is also possible to engineer strategically placed non-native disulfide bonds within a given protein. This has been a powerful tool for analyzing protein conformational changes [32-34]. In the past, many attempts at disulfide bond engineering yielded low success rates, mainly due to a lack of methods for determining the optimal site for introduction of a disulfide bond within a protein. Lately, computational approaches to predict protein folding and protein folding studies have increased the chance of success of these strategies [35].

5.4.2 Disulfide link between the two domains of flavocytochrome *b_2*

In flavocytochrome b_2, by creating a disulfide bond the two domains can be locked together and their mobility decreased. Consequently the electron transfer rate may be affected. Such a method has been previously applied in the case of fumarate reductase from *Shewanella frigidimarina* [36], where the introduction of an inter-domain cross-link between the FAD- and clamp-domains of the enzyme, successfully restricted the relative mobility of the two domains.

In a previous attempt, site direct mutagenesis was used to introduce a disulfide link between the two domains of *Saccharomyces cerevisiae* flavocytochrome b_2 [37]. Alanine 67, located in b_2-heme domain, was substituted by a cysteine (A67C) (fig 5.6). This engineered cysteine was expected to form a disulfide bridge with the naturally occurring Cys233 of the flavin-binding domain. Although Ellman assays and kinetic assays [37] suggested the formation of such a disulfide bridge between the two domains, this was never proven because no crystal structure for this mutant enzyme was available.

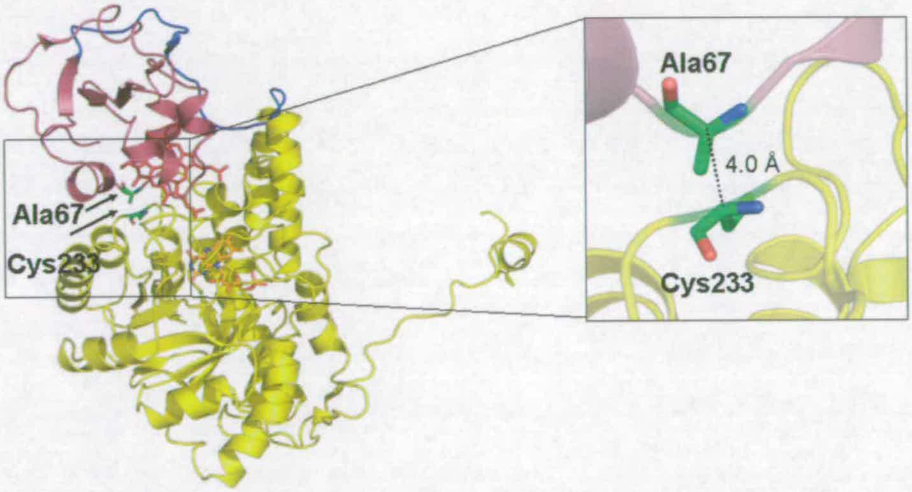

Fig 5.6: A single monomer of flavocytochrome b_2. The domains are coloured as for fig 5.2. The target residue for cysteine modification (Ala67) is indicated in green, as is the naturalyl occurring Cys233[37], while the distance between their α-carbon atoms is shown as a dotted line (insert).

Subsequentially, site-directed mutagenesis has been used to construct the N42C:K324C double mutant *Saccharomyces cerevisiae* flavocytochrome b_2 [38]. The α-carbon atoms of the residues at position 42 of the heme-binding domain and position 324 of the flavin-binding domain are 5.9 Å from one another. From the three-dimensional model of the native enzyme [2] was clear that the introduced cysteine residues can readly adopt a S-S distance of 2.0 Å, an ideal distance to form a disulfide bridge. Figure 5.7 highlights the location of residues 42 and 324 at the interface of the flavin and cytochrome domains.

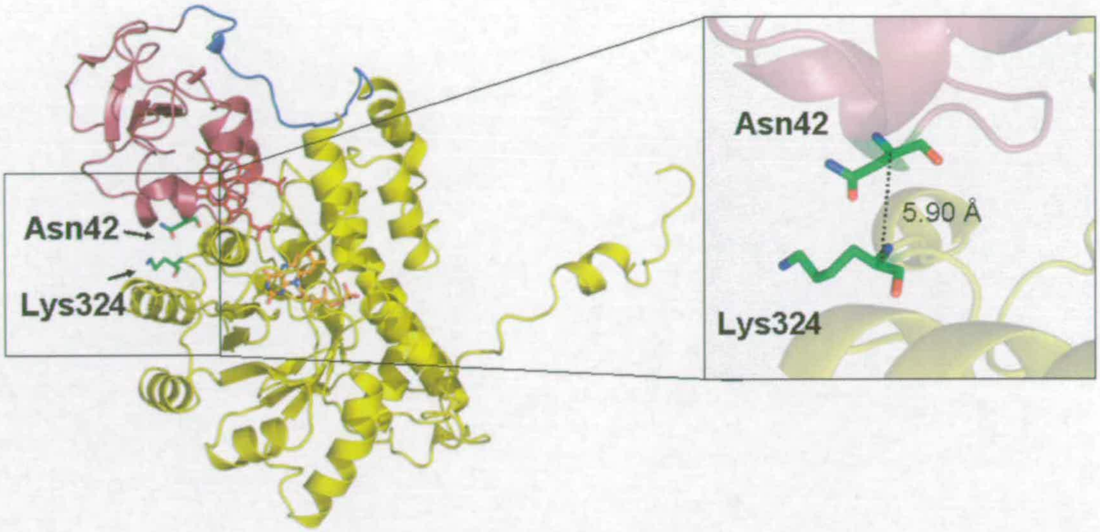

Fig 5.7: A single monomer of flavocytochrome b_2. The domains are coloured as for fig 5.2. The target residues for cysteine modification (Asn42 and Lys324) are indicated in green [37] *and the distance between their a-carbon atom as a dotted line in the insert on the right.*

5.5 Kinetic characterization of the flavocytochrome *b*$_2$ N42C:K324C mutant

The kinetic behaviour of the flavocytochrome b_2 N42C:K324C mutant has been reported by Drewette (2006) [38]. Steady-state kinetic experiments were conducted both using the physiological electron acceptor cytochrome *c* and the artificial electron acceptor ferricyanide $[Fe\ (CN)_6]^{-3}$. Assays were carried out in both the closed (disulfide bridge formed) and open (disulfide bridge reduced by the addition of DTT) conformations of the enzyme. The resulting k_{cat} and K_m values were compared with those for the wild-type enzyme [39] and are summarised in table 5.2.

	Electron acceptor: $[Fe(CN)_6]^{-3}$		
Enzyme	**k_{cat} (s^{-1})**	**Km (mM)**	**10^5 x k_{cat}/K_m (M^{-1} s^{-1})**
Wild-type *	400 ± 10	0.49 ± 0.05	8.2
Open	76 ± 4	1.8 ± 0.3	0.43
Closed	5.1 ± 1.6	0.72 ± 0.24	0.07
	Electron acceptor: cytochrome c		
Enzyme	**k_{cat} (s^{-1})**	**Km (mM)**	**10^5 x k_{cat}/K_m (M^{-1} s^{-1})**
Wild-type *	207 ± 10	0.24 ± 0.04	8.6
Open	13 ± 1	1.2 ± 0.2	0.11
Closed	0.84 ± 0.14	0.33 ± 0.09	0.03

Table 5.2: Steady-state kinetics results for Saccharomyces cerevisiae flavocytochrome b_2 N42C:K324C mutant with L-lactate as substrate. All measurements were carried out at 25 °C, in 10 mM TrisHCl, pH 7.5, I 0.10. Electron acceptor concentrations were 5 mM for $[Fe(CN)_6]^{-3}$ and 100 μM for cytochrome c [38]*.*
** Wild-type values were reported in Miles et al. (1992)* [39].

From the steady-state kinetic analysis shown in table 5.2, it appears that although the mutant enzyme retains activity, the rate of FMN reduction by L-lactate is affected by the disulfide bridge formation.

In the open form (where the disulfide bond is not formed) the k_{cat} value with $[Fe(CN)_6]^{3-}$ as electron acceptor shows only a 5-fold decrease compared to the wild-type enzyme. However, with cytochrome *c* as the electron acceptor a more pronounced decrease in k_{cat} (some 16-fold) is observed. A decreased k_{cat} value with cytochrome *c* as electron acceptor has been previously reported for flavocytochrome b_2 with other point mutations (F39A and P44A) [40]. Interestingly, both these mutations lie in close proximity to the substituted asparagine residue in the N42C:K324C mutant enzyme. This may indicate a disruption of one of the electron-transfer steps, either FMN to heme or heme to cytochrome *c*.

The closed form of the enzyme (where the disulfide bridge is formed) reveals a 15-fold decrease in k_{cat} compared to the open mutant enzyme, with both the electron acceptors. In addition, the catalytic efficiency (indicated by the k_{cat}/K_m ratio) of the closed form is lower than the open form. With $[Fe(CN)_6]^{3-}$ as electron acceptor the k_{cat}/K_m ratio is approximately 16 % of that of the open form of the mutant enzyme, while when cytochrome *c* is used as the electron acceptor, the catalytic efficiency is 27 % of that of the open form.

This result is important for the understanding of electron flow through flavocytochrome b_2. As mentioned in section 5.3, ferricyanide can receive electrons from both the FMN and heme of flavocytochrome b_2, while cytochrome *c* accepts electrons only from the heme. The fact that in the closed form of the enzyme both electron acceptors show a 15-fold decrease in k_{cat} indicates that is the rate of FMN reduction by L-lactate that is primarily affected by disulfide bridge formation.

Pre-steady-state kinetic analyses were consistent with the steady-state data. FMN reduction was confirmed to be rate limited by the formation of the disulfide bridge [38].

In this chapter the crystal structure of the double mutant flavocytochrome b_2 N42C:K324C, obtained at 3.0 Å resolution is described. This confirms the formation of the disulfite bond and validates the kinetic assays. In addition, steady-state kinetic control experiments, conducted on single mutants N42C and K324C are reported.

5.6 Results

5.6.1 Mutagenesis and expression

Flavocytochrome b_2 mutants (N42C, K324C, and N42C:K324C) were created by Dr. Katy J. Drewette and by Dr. Caroline S. Miles, at the Institute of Structural and Molecular Biology, University of Edinburgh, as described in Drewette (2006) [38]. Site-directed mutagenesis was performed by the Kunkel method of nonphenotypic selection [41]. *E. coli* stain AR120 was used for production of cultures containing the expression vector pKD209 for N42C, pKD212 for K324C and pKD213 for N42C:K324C flavocytochrome b_2 mutants. Cultures were grown aerobically in LB media containing 50μg/ml carbenicillin to mid-exponential phase (O.D. ~ 0.6) at 37 °C for 24 hours and then cells were harvested.

Mutant enzyme	Code
asparagine 42 → cysteine	N42C
lysine 324 → cysteine	K324C
asparagine 42 , lysine 324 → cysteine , cysteine	N42C:K324C

Table 5.3:Summary of the mutants studied in sections 5.7, 5.8, and 5.9

5.6.2 Purification

N24C, K324C and N42C:K324C mutant flavocytochromes b_2 expressed in *E. coli* were isolated from cells using a previously reported procedure [38, 42].

Flavocytochrome b_2 single mutants (N42C, K324C) were purified according to the following procedure.

The cell pellet was resuspended in buffer 1 (100 mM phosphate buffer pH 7.0, 1 mM EDTA, and 10 mM L-lactate) and then sonicated on ice. Cell debris was removed by centrifugation. The proteins contained in the soluble fraction were precipitated by addition of ammonium sulfate, (70% saturation). Precipitated proteins (including flavocytochrome b_2) were resuspended in 100 mM phosphate buffer pH 7.0, 10 mM L-lactate and dialyzed overnight against the same buffer.

The suspension was loaded into a DE-52 column (Amersham) previously equilibrated with buffer 1. The flow through from DE-52 was then applied to a hydroxapatite column equilibrated with buffer 1. The bound flavocytochrome b_2 was extensively washed with the equilibration buffer until A_{280} was found to be zero. The protein was then eluted with a step gradient of $(NH_4)_2SO_4$ added (up to 10% saturation in 2% increments). Flavocytochrome b_2 eluted between 8% and 10% saturation $(NH_4)_2SO_4$. The purity of each 5 ml fraction was determined by UV/vis spectrophotometry. Only the fractions whose spectral ratio (A_{423nm}/A_{269nm}) had a value ≥ 2 were pooled together and precipitated with 70% saturation $(NH_4)_2SO_4$.

The red pellet containing flavocytochrome b_2 was resuspended in TrisHCl 10 mM pH 7.5 I 0.10.

The buffer was then exchanged using a Sephadex G-25 desalting column (Sigma) which was equilibrated in 10 mM TrisHCl pH 7.5 I 0.10.

For the flavocytochrome b_2 double mutant (N42C:K324C) the same purification procedure was followed, with the difference that all the buffers were supplemented with 5 mM DTT. Furthermore, in the last step of purification the N42C:K324C mutant enzyme was purified through a Superdex 200 column equilibrated with TrisHCl 10 mM pH 7.5 *I* 0.10. The double mutant N42C:K324C eluted at a volume corresponding to ~240 kDa molecular weight.

Purified enzyme samples were stored either as precipitates from a 70% saturated $(NH_4)_2SO_4$ solution (short-term storage), as concentrated solutions at -80 °C, or as flash-frozen enzyme aliquots in liquid nitrogen (long-term storage).

5.6.3 Aggregation of the N42C:K324C mutant enzyme

Previous attempts to purify N42C:K324C flavocytochrome b_2 enzym, did not take in account the tendency of this double cysteine mutant to form intermolecular disulfide bridges and aggregate in the absence of DTT (fig 5.8). This happened during the last chromatographic step of gel filtration when the DTT was removed from the buffer.

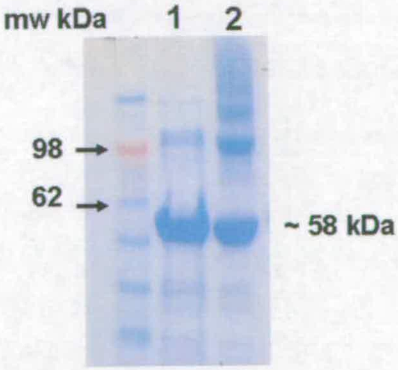

Fig 5.8: SDS PAGE showing the purification results for the flavocytochrome b_2 N42C:K324C mutant. Samples were prepared by adding SDS-PAGE buffer and heating at 100 °C. Sample in lane 1 was augmented with 10 mM DTT. The 58 kDa bands indicated the presence of the monomers (mw ~ 58 kDa). DTT chemically reduces covalent bonds and allows the protein in lane 1 to run as a monomer. However, close examination shows at least other 3 visible bands at higher molecular weigh in lane 2, where DTT is not present. The bands at higher molecular weight in lane 2 are protein aggregates, formed due to inter-subunit covalent bonds, and also appear in the purification profile from gel filtration (see fig 5.8).

It was demonstrated using an analytical gel filtration column that there were different profiles of elution from the Superdex 200 purification step between the wild-type flavocytochrome b_2, the N42C:K324C mutant in the presence of 10 mM DTT and the N42C:K324C mutant in the absence of DTT.

As is shown in fig 5.9a, wild-type flavocytochrome b_2 (molecular weight ~ 58 kDa) elutes with a main peak corresponding to the molecular weight of a tetramer, around 240 kDa.

In contrast, the elution profile of the N42C:K324C mutant show that the engineered cysteine residues can form inter-subunit disulfide-bridges, together with the desired bond between the cytochrome and flavin-binding domains (fig5.9b). In fact, the peaks eluting at higher molecular weight than 240 kDa are likely to be caused by the tetramers aggregating together. Due to the localization of the engineered cysteines at the surface, they may possibly have formed inter-subunit covalent bonds rather than just only the intended inter-domain disulfide bridge. Aggregation of surface cysteine mutants has been previously reported (e.g. [43]).

When DTT was added to the equilibration and elution buffer of the analytic gel filtration, the N42C:K324C mutant displayed an elution profile similar to that of the wild-type enzyme (fig 5.9c).

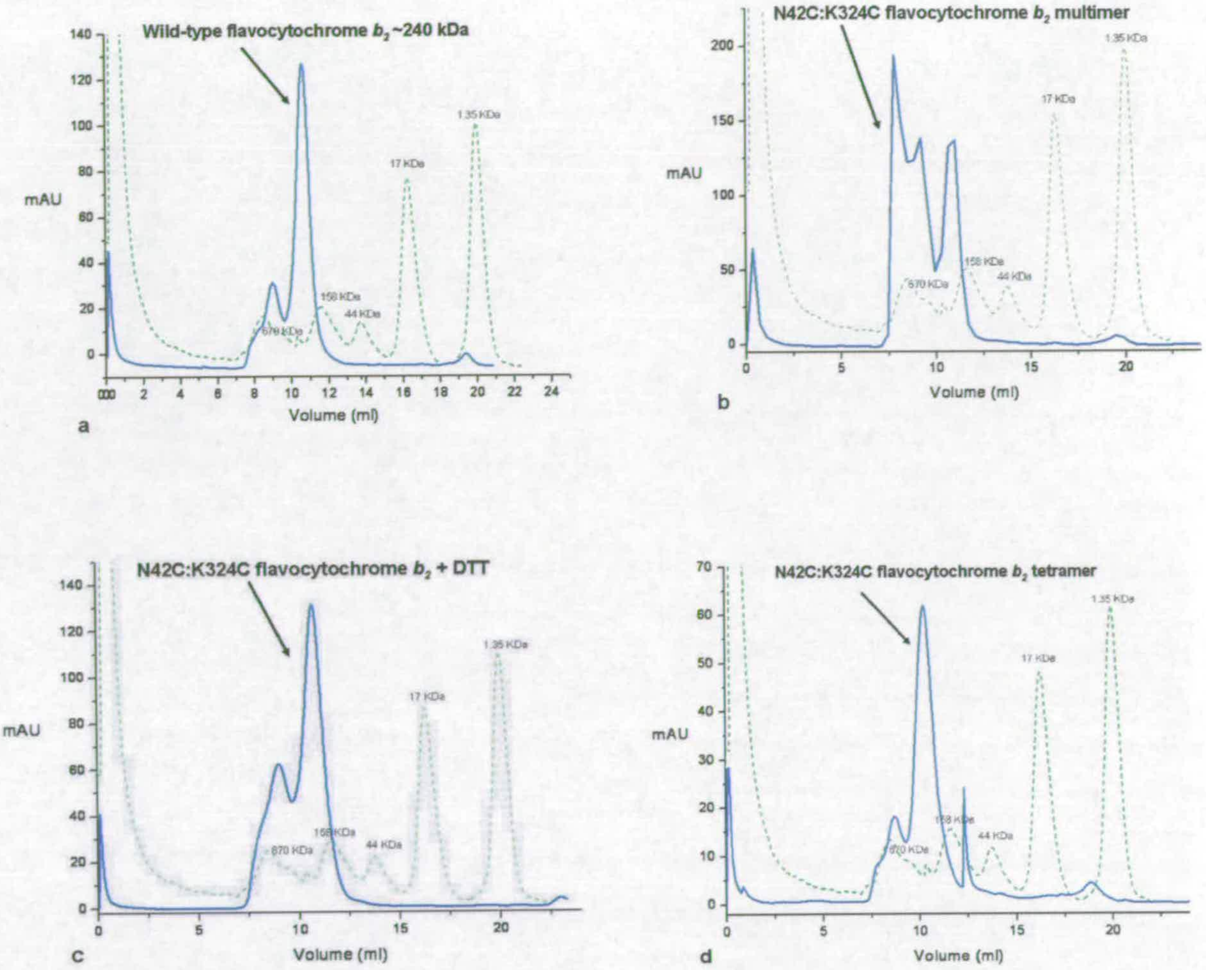

Figure 5.9: Elution profiles (shown in blue) from Superdex 200 gel filtration column of flavocytochrome b_2 samples (a) wild-type enzyme,running buffer TrisHCl 10 mM pH 7.5 I 0.10 (b) N42C:K324C, running buffer TrisHCl 10 mM pH 7.5 I 0.10, and 10 mM DTT. (c) N42C:K324C mutant enzyme + DTT, (d) previously gel filtrated tetrameric N42C:K324C mutant. For both the running buffer was TrisHCl 10 mM pH 7.5 I 0.10. The elution profile of the molecular weight standards (in green) is also shown.

In order to exclude the possibility that the gel-filtered mutant enzyme re-aggregate over time in oxidising conditions, the tetrameric protein was isolated and then incubated for 30 minutes at 4 °C before being run again through the Superdex 200 column. The resulting elution profile (fig5.9d) is similar to that of the wild-type enzyme, indicating that once in the tetrameric state the N42C:K324C mutant will not re-aggregate as a multimer.

Appropriate molecular weight standards were passed through the column to calibrate it. Extrapolation from a plot of Log M_r *vs* V_v/V_e (fig 5.10) allowed the determination of the molecular weight of the sample peaks.

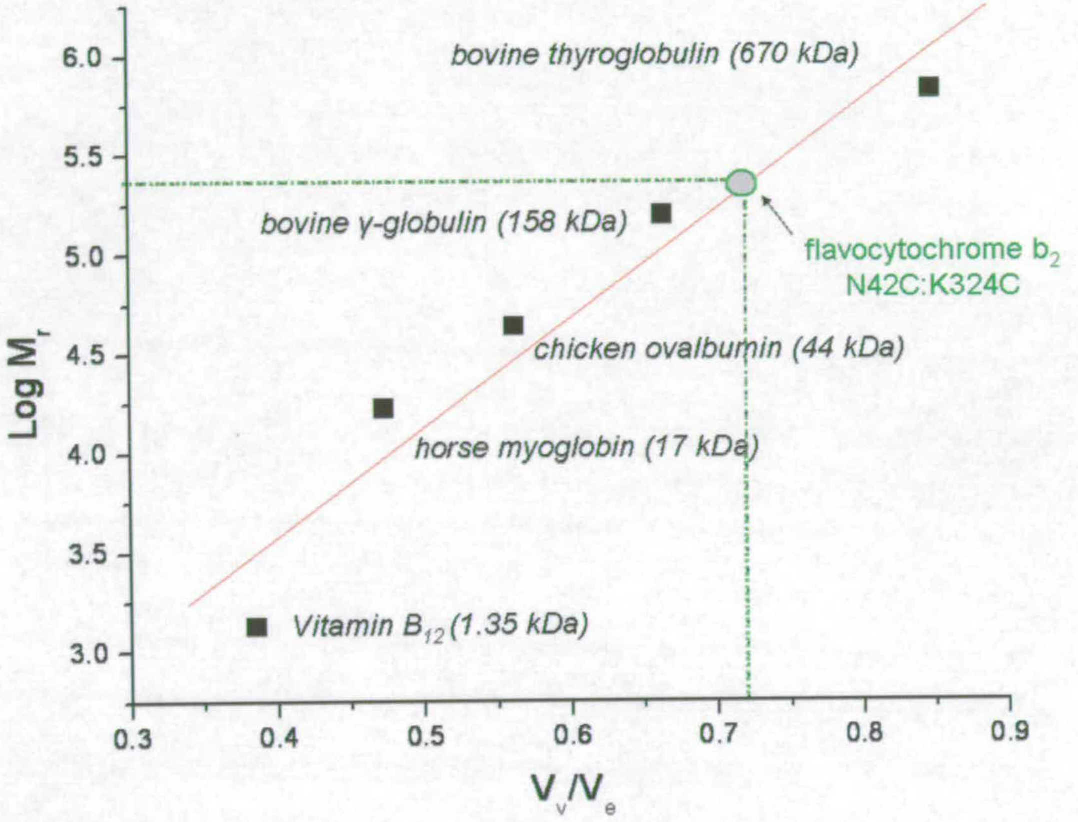

Figure 5.10: Molecular mass determination of flavocytochrome b_2 N42C:K324C by gel filtration. Plot of Log Mr vs void volume (V_v)/elution volume (V_e) of the standard molecular weights. The points were fitted to a linear gradient, ($y=mx + c$, where $m = 5.5 \pm 0.8$, $c = 1.4 \pm 0.5$). The corresponding V_v/V_e for the N42C:K324C tetramer is highlighted by the green-grey circle.

Only fractions eluting from the gel filtration at the molecular weight of 240 kDa were pooled together and concentrated to 20 mg ml^{-1} (fig 5.11).

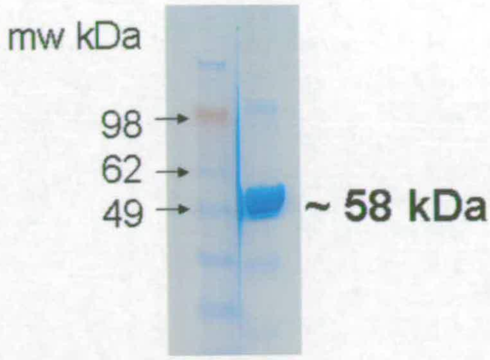

Fig 5.11: SDS-PAGE of the flavocytochrome b_2 N42C:K324C gel filtered sample used for crystallographic experiments.

5.6.4 Protein concentration determination

Protein concentration was determined spectrophotometrically. The extinction coefficients for flavocytochrome b_2 in both its oxidised and reduced forms are shown in table 5.4.

Oxidation State	**Soret Maximum / nm**	**ε (M^{-1} cm^{-1})**
Oxidised	413	129500
Reduced	423	183000

Table 5.4: Extinction coefficients for oxidased and reduced flavocytochrome b_2

5.6.5 Crystallization of flavocytochrome b_2 N42C:K324C mutant

Crystals of b_2 N42C:K324C were grown by the hanging-drop vapour diffusion method. 2µl of protein (at 20 mg/ml in 10 mM TrisHCl pH 7.5 *I* 0.10) were mixed with 2µl of well solution (0.1 M sodium citrate pH 5.0, 10% PEG 4000, 0.2 M sodium bromide, 5% glycerol, and 50 mM sodium pyruvate) at 18°C in the dark. Red crystals appear after 3 days (fig 5.12).

Before flash-cooling in liquid nitrogen, crystals were cryoprotected in 0.1 M sodium citrate pH 5.0, 10% PEG 4000, 0.2 M sodium bromide, 23% glycerol, and 50 mM pyruvate.

5.6.6 Data collection and processing

The best dataset was collected to 3.0 Å resolution at ESRF (Grenoble, France) on beamline BM14 using a Mar research CCD detector (wavelength $\lambda = 0.9537$ Å). Crystals were found to belong to space group $P2_1$ with cell dimensions $a = 64.226$ Å, $b = 179.895$ Å, $c = 96.369$ Å and $\beta = 90.68°$. Data processing was carried out using MOSFLM [44]. The structure was solved by molecular replacement using MOLREP [45] and the wild-type flavocytochrome b_2 structure (PDB entry 1FCB) stripped of water, was used as a starting model. Electron density fitting was carried out using the program TURBO-FRODO [46], and structure refinement was carried out using Refmac[47].

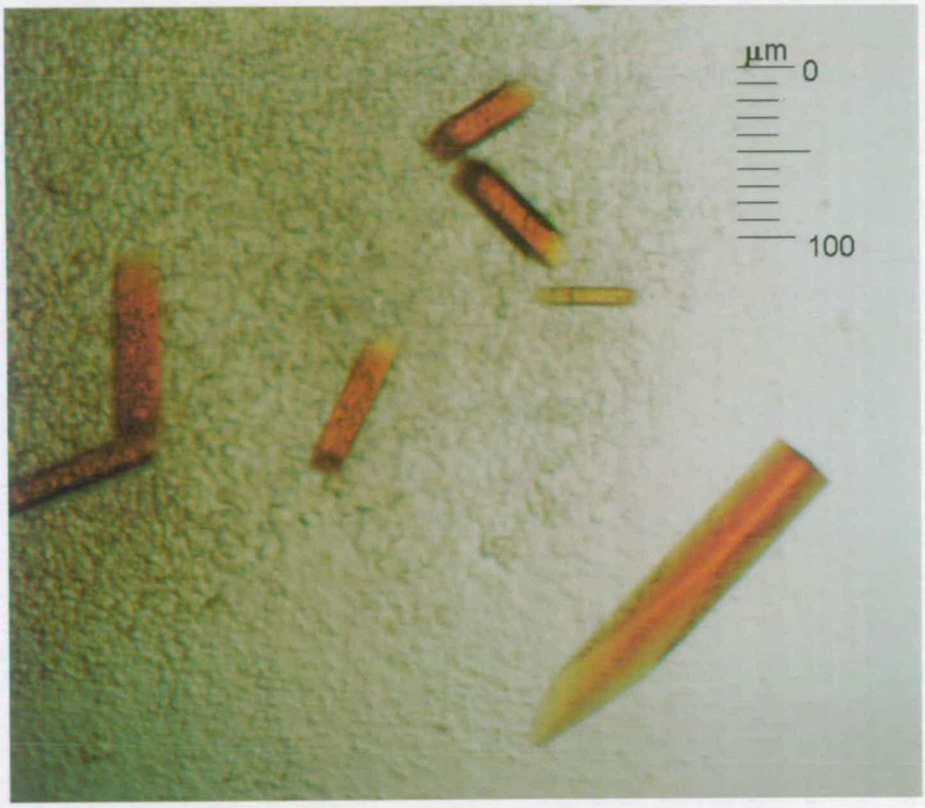

Fig 5.12: Crystals of flavocytochrome b_2 N42C:K324C mutant grown in 0.1 M sodium citrate pH 5.0, PEG 4000 10%, 0.2 M sodium bromide, 5% glycerol and 50 mM sodium pyruvate

5.7 The crystal structure of N42C:K324C flavocytochrome b_2

A dataset to 3.0 Å resolution was used to refine the structure of N42C:K324C flavocytochrome b_2 to a final R-factor of 18.03 % ($R_{\mathrm{free}} = 25.62$ %; table 5.5).

Space group	***P* 2₁**
cell dimensions (Å)	$a = 64.226$, $b = 179.895$, $c = 96.369$, $\beta = 90.68$ °
resolution (Å)	26.87-3.00
total no. of reflections	160404 (22292)[a]
no. of unique reflections	42925 (6178)[a]
completeness (%)	98.3 (97.5)[a]
$I/[\sigma(I)]$	11.5 (3.0)[a]
R_{merge} (%)[b]	10.2 (35.3)[a]
R_{cryst} (%)[c, d]	18.03
R_{free} (%)[c]	25.62
rmsd from ideal values	
bond lengths (Å)	0.048
bond angles (deg)	4.162
Ramachandran analysis	
most favoured (%)	92.4
additionally allowed (%)	5.3
no. of waters included in refinement	213

Table 5.5: Data collection and refinement statistics.
[a] Values in parentheses represent statistics for the highest resolution shell, 3.16 – 3.00 Å. [b] $R_{merge} = \Sigma_h\Sigma_i|I(h) - I_i(h)|/\Sigma_h\Sigma_i I_i(h)$, where $I_i(h)$ and $I(h)$ are the ith and mean measurement of reflection h, respectively. [c] $R_{cryst} = \Sigma_h|F_o - F_c|/\Sigma_h F_o$, where F_o and F_c are the observed and calculated structure factor amplitudes of reflection h, respectively. R_{free} is the test reflection data set, 5 % selected randomly for cross validation during crystallographic refinement. [d] Medium NCS restraints were used during refinement, with each subunit (A – D) being defined as a group.

Initial refinement was done without waters, but adding these improved the R-factors and the quality of the map in certain areas. Each added water was checked and ejected if unreasonable.

The final model consists of four protein molecules (subunits A-D) each including residues Glu1 to Ala511, one b_2-heme and one FMN. In addition the model contains 213 water molecules. The arrangement of the subunits to form the tetrameric enzyme in the asymmetric unit is shown in fig 5.13. In all subunits residues 300-317 are not visible in the electron density because of disorder, similar to that found in other structures of this enzyme [2].

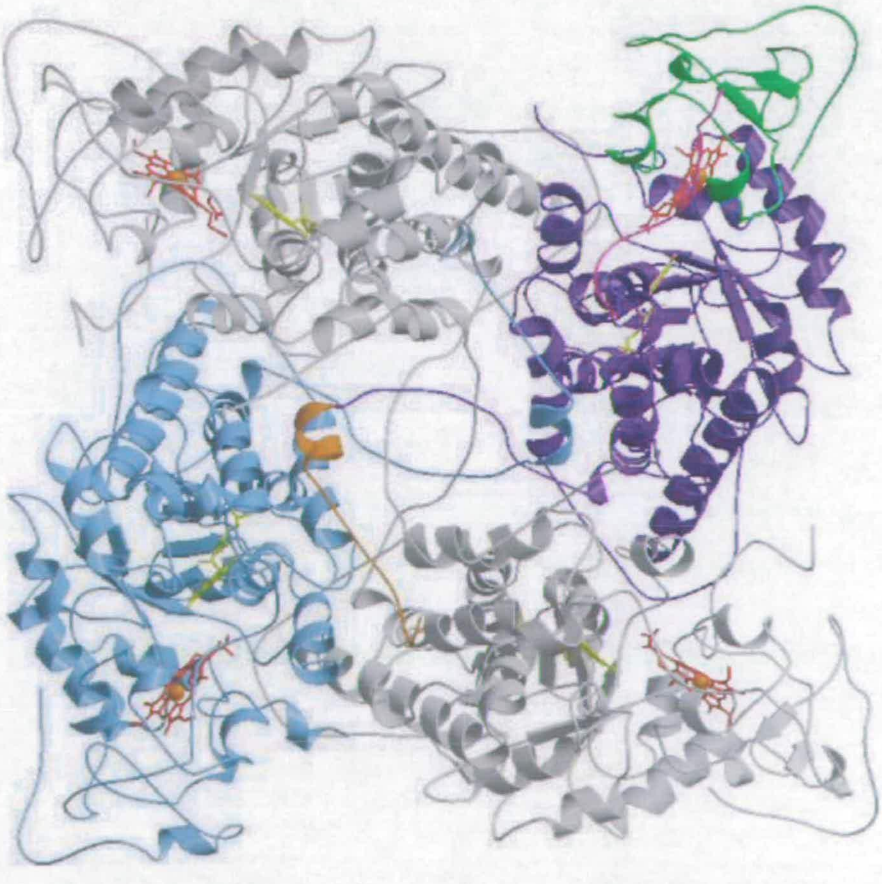

Figure 5.13: The asymmetric unit content of N42C:K324C flavocytochrome b_2. Subunit A is shown with the cytochrome domain in green and the flavin domain in purple. Subunit C is shown in cyan. Subunits B and D are shown in grey. In all subunits FMN is yellow and heme is red. Figure produced using Molscript [48] and Raster3D [49].

The presence of the amino-acid substitutions (N42C and K324C) is evident from the electron density map (fig 5.14a). From the electron density it is also confirmed that in each subunit a disulfide bond has been formed between Cys42 and Cys324 (fig 5.14a and 5.14b). The major effect of this inter-domain disulfide bond formation is the presence of an ordered heme domain in each of the four subunits. There are several other structures of holo-flavocytochrome b_2 deposited in the PDB, all from crystals which belong to space group $P3_221$ [2, 5, 50]. In all cases the model consists of two subunits, at least one of which has a disordered cytochrome domain (see section 5.2).

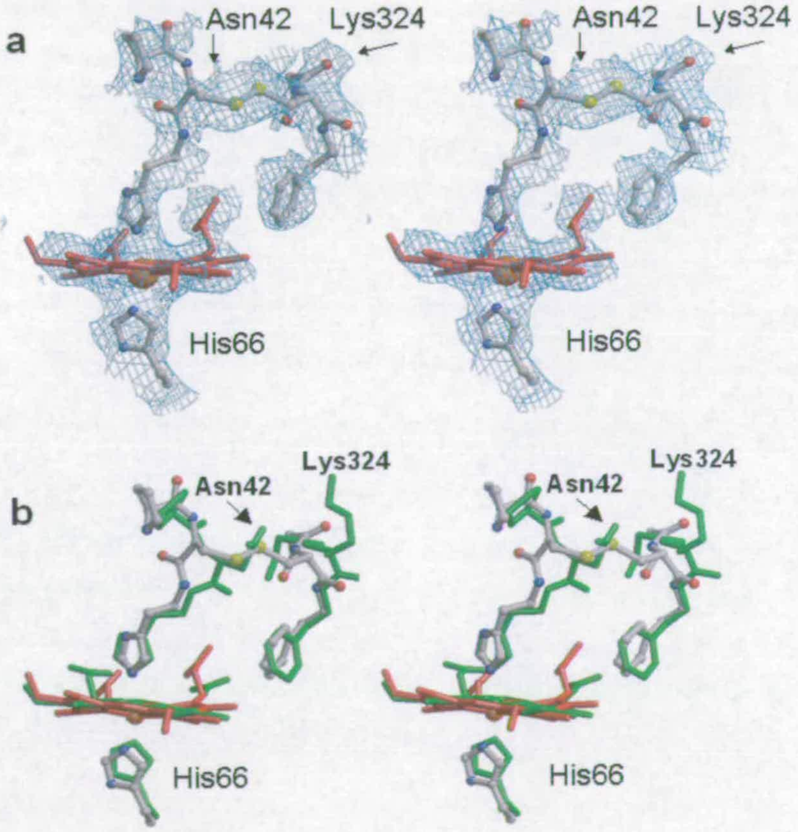

Figure 5.14: (a) Stereo view of the $2F_o - F_c$, electron density map surrounding the heme (in red) and residues 41-43 and 323-325 of subunit A of N42C:K324C flavocytochrome b_2. The disulfide bond is clearly visible in the electron density map. The contour level is 1σ, where σ is the rms electron density. (b) Stereo view of the same region overlaid with that in subunit A of the wild-type enzyme (in green, PDB entry 1FCB). Figure produced with Molscript [48] and Raster3D [49].

Although the conditions used to grow crystals of flavocytochrome b_2 N42C:K324C were almost identical to those used to grow crystals of other forms of the protein [2, 5, 50], flavocytochrome b_2 N42C:K324C, crystallized in the $P2_1$ space group. This represents evidence of the structural changes imposed by the formation of the four disulfide bonds in the tetrameric enzyme. However, the presence of the disulfide bond has little effect on the overall structure of the protein, with the average rmsd fit for α-carbon atoms of each subunit with those of subunit A of the wild-type enzyme structure (PDB entry 1FCB) being 0.95 Å (fig 5.14).

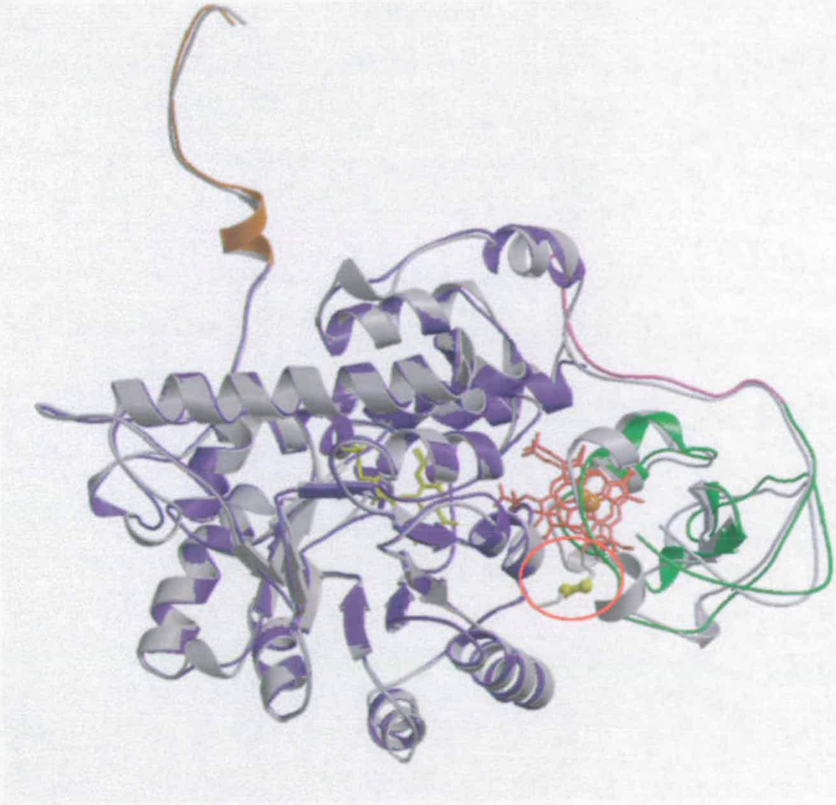

Figure 5.15: The overlay of subunit A of the N42C:K324C double mutant enzyme (green and purple) with subunit A of the wild-type enzyme (in grey). It can be observed that there is only a little change in the position of the cytochrome domain as the result of the disulfide bridge formation. Heme and FMN are shown as sticks and coloured respectively in red and yellow. The disulfide bridge is highlighted in the red circle. Figure produced with Molscript [48] and Raster3D [49].

The formation of a disulfide bond results in the locking of the cytochrome domain to the flavin domain, and the major effect of 'fixing' the two domains is the presence of an ordered heme domain in each of the four subunits of the tetramer. However, the disulfide bridge does not prevent mobility within the heme domain itself. B-factors of the cytochrome domain are considerably higher than the average over the whole protein (70-100 Å^2 compared to a mean B-value of ~49 Å^2 over the whole model).

As already described in section 5.2, in the structure of wild-type enzyme [2] pyruvate is visible at the active site of only one of the two subunits (where the heme domain is disordered). In the structure of N42C:K324C flavocytochrome b_2, although the crystallization condition contains 50 mM pyruvate, electron density for the substrate is absent in the model. This suggests that cross-linking the heme and flavin domains could restrict the access of the substrate to the active site.

In the N42C:K324C flavocytochrome b_2 there are water molecules present at the active site. The number of water molecules varies from 1 to 3 between the four subunits. In subunit A (fig 5.16) there are three water molecules (wat25, wat146 and wat194). Wat25 is hydrogen bonded to the flavin (3.1 Å from N5 of the FMN) and also to His373 and to Tyr143 (respectively 3.2 Å and 3.7 Å apart). Wat146 is 3.3 Å from Wat25, and is also hydrogen bonding to one of the heme propionate groups at a distance of 2.7 Å. The third water, wat194, is 3.1 Å from wat146. The heme propionate double hydrogen bond Tyr143 (being 2.5 Å and 3.9 Å apart), and around 4.2 Å from where pyruvate would be bound if it was present in the same position as observed in the wild-type enzyme structure.

The 3.0 Å resolution of the flavocytochrome b_2 N42C:K324C model is limiting for any further speculation. However this structure has certainly confirmed the presence of a disulfide bond between the heme and flavin-binding domains.

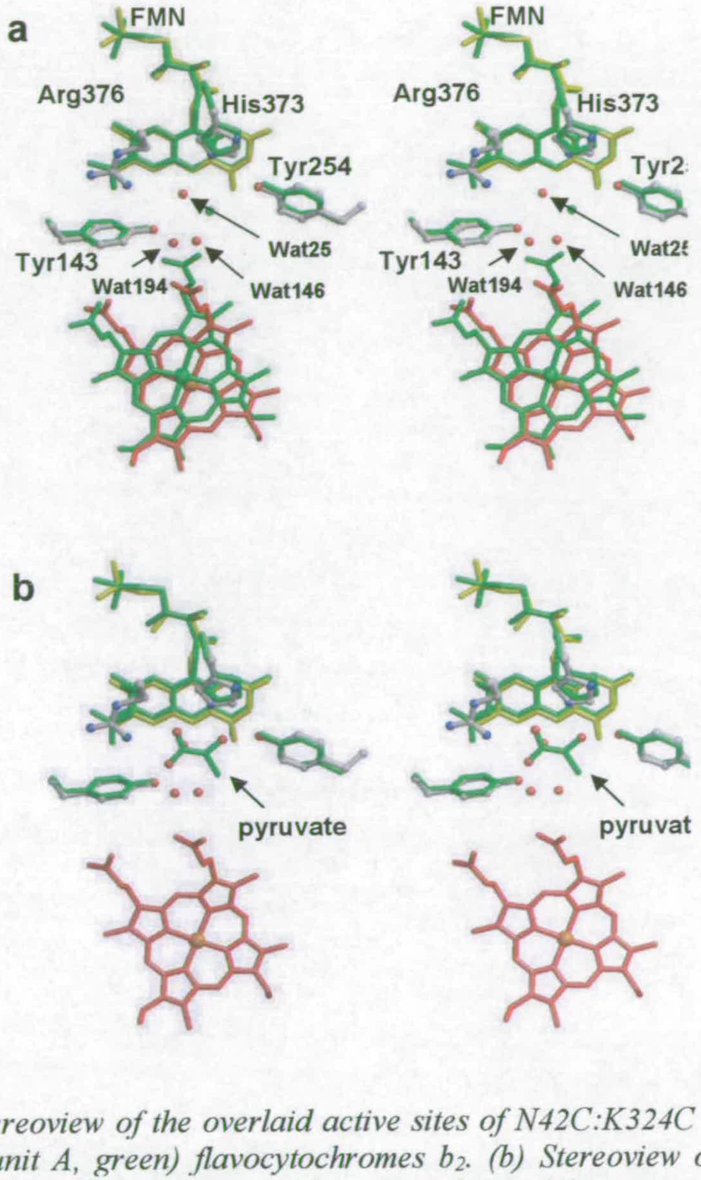

Figure 5.16: (a) Stereoview of the overlaid active sites of N42C:K324C (subunit A) and wild-type (subunit A, green) flavocytochromes b_2. (b) Stereoview of the same region in the N42C:K324C enzyme overlaid (carbon alpha of the protein chain) with that in subunit B of the wild-type enzyme (green). The positions of the water molecules in the double mutant enzyme are indicated by the arrows, as is the pyruvate in subunit B of the wild-type enzyme. The propionate of the heme groups is near to the substrate binding site. Figure produced with Molscript [48] *and Raster3D* [49].

5.8 Steady-state kinetic analysis of single mutants N42C and K324C

Steady-state kinetic analysis is a technique that allows observation of enzyme under turnover conditions, in terms of its consumption of substrate or generation of products.

Steady-state kinetic analysis was conducted on the single mutants N42C and K324C as control experiments, in order to verify the effect on catalysis of the individual single mutations and validate the kinetic results of the double mutant flavocytochrome b_2 N42C:K324C [38].

Steady-state kinetic analyses were carried out in 10 mM TrisHCl, pH 7.5, *I* 0.10 at 25°C. The flavocytochrome b_2 mutants (N42C, K324C) used were thawed on ice directly prior to use, and incubated on ice throughout the whole experiment.

The concentration of the enzyme was determined before use (see section 5.7.4) and a suitable concentration of enzyme to obtain a good trace was added to each assay. Assays were carried out using both ferricyanide ($K_3[Fe(CN)_6]$, Fisons) and cytochrome *c* (horse heart, type VI, Sigma) as electron acceptors. The data obtained for steady-state kinetic analysis with L-lactate as substrate are shown in table 5.6, in comparison with the wild-type and the double-mutant N42C:K324C (both in the open and closed conformation). L-lactate solution was made as a standard by the addition of buffer (10 mM TrisHCl, pH 7.5, I 0.10) to the calculated amount of lithium salt of L-lactic acid.

Ferricyanide reduction (Fe(III) to Fe(II)) was followed by monitoring the decrease in absorbance at 420 nm ($\varepsilon_{\text{ox-red}} = 1010\ M^{-1}cm^{-1}$). Saturating concentrations of between 1 and 5 mM ferricyanide were satisfactory depending on the mutant form, however, this resulted in the need to use 2 mm or 5 mm path length cuvettes and either smaller or larger assay volumes depending on the cuvette path length.

Cytochrome *c* was used freshly prepared in 10 mM TrisHCl, pH 7.5, *I* 0.10 and diluted to a suitable concentration. A saturating cytochrome *c* concentration of 100 μM was used. Cytochrome *c* reduction by flavocytochrome b_2 mutants was monitored at 550 nm ($\varepsilon_{\text{ox-red}} = 22640\ M^{-1}\ cm^{-1}$) [51].

All steady-state kinetic data were fitted to a normal Michaelis–Menten model using non-linear least squares analysis in the program Microcal Origin to obtain values for k_{cat} and K_m.

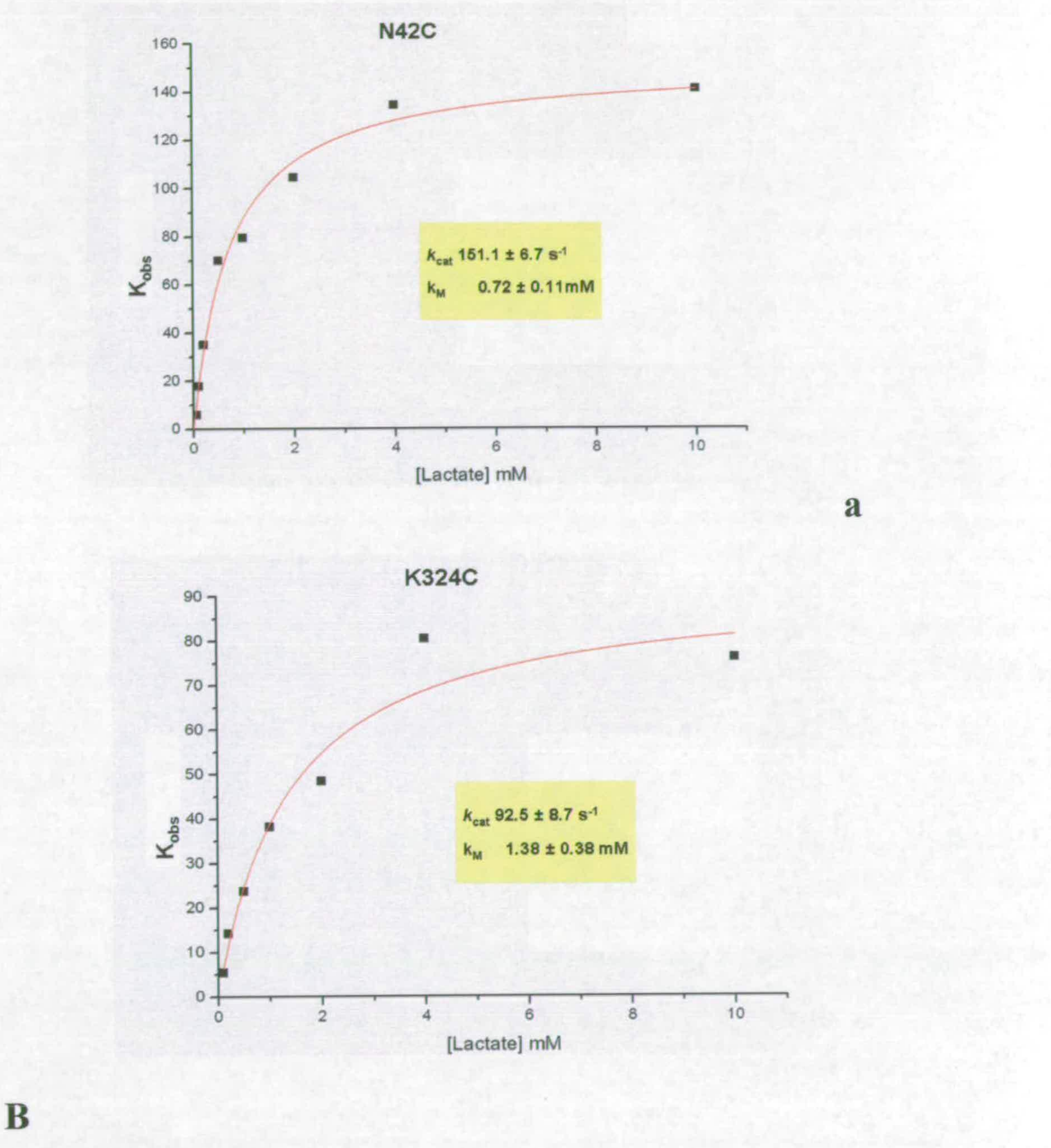

Fig 5.17: Michaelis plots for L-lactate dependence of flavocytochrome b_2 a) N42C, b) K324C, both obtained using ferricyanide as the electron acceptor. K_{obs} is the first order rate constants, which has units of 1/time (s^{-1}). Conditions were 100 mM TrisHCl buffer pH 7.0, 25 °C, I 0.10

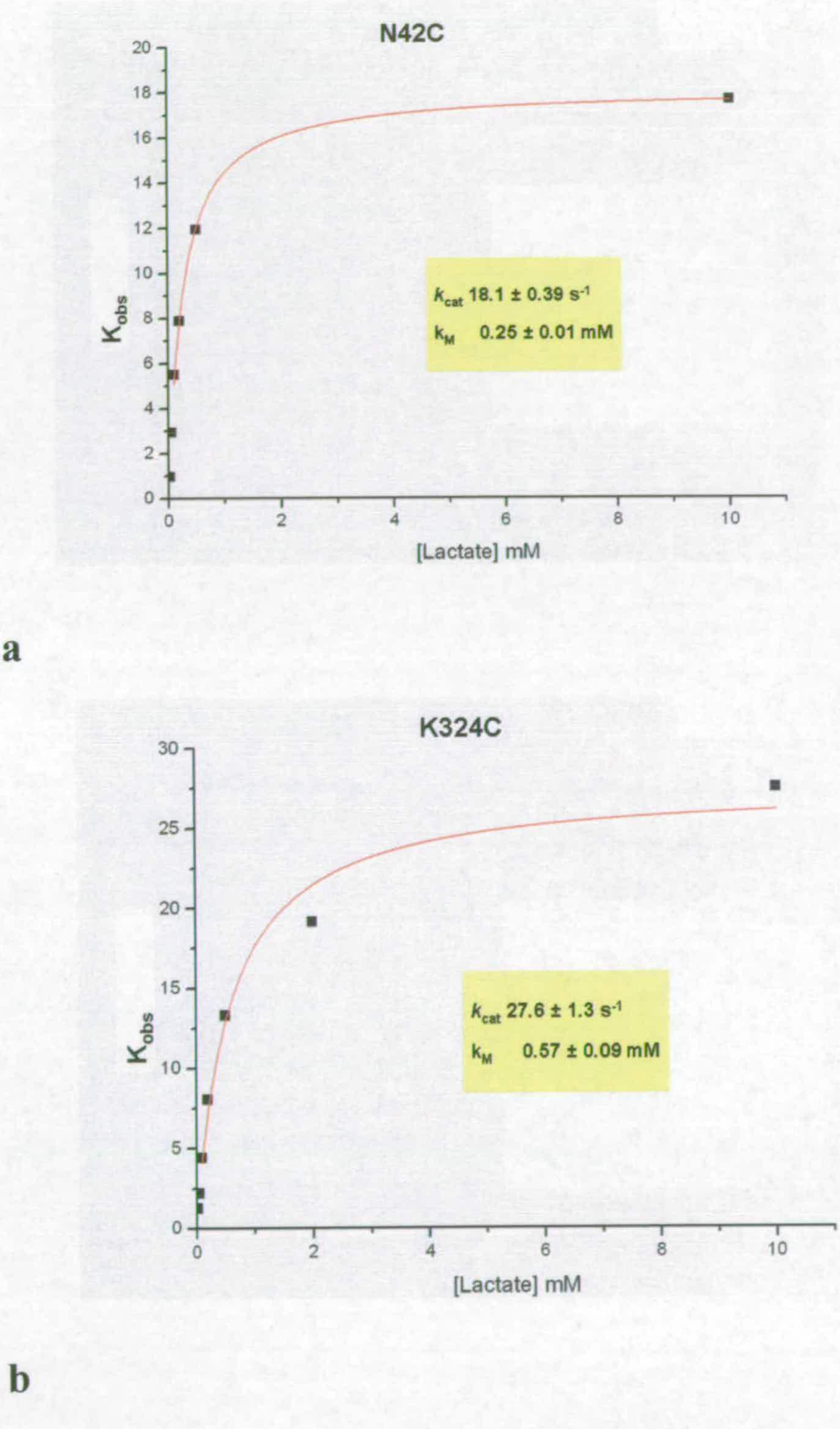

Fig 5.18: Michaelis plots for L-lactate dependence of flavocytochrome b_2 a) N42C, b) K324C, both obtained using cytochrome c as the electron acceptor. . K_{obs} is the first order rate constants, which has units of 1/time (s^{-1}). Conditions were 100 mM TrisHCl buffer pH 7.0, 25 °C, I 0.10

Electron acceptor: $[Fe(CN)_6]^{3-}$			
Enzyme	**$k_{cat}(s^{-1})$**	**K_m (mM)**	**10^3 x k_{cat}/K_m ($M^{-1}s^{-1}$)**
Wild-type	400 ± 10	0.49 ± 0.05	8.20
N42C;K324C open	76 ± 4	1.8 ± 0.3	0.43
N42C:K324C closed	5.1 ± 1.6	0.72 ± 0.24	0.07
N42C	151.1 ± 6.7	0.72 ± 0.11	0.20
K324C	92.5 ± 8.7	1.38 ± 0.38	0.67
Electron acceptor: cytochrome *c*			
Enzyme	**$k_{cat}(s^{-1})$**	**K_m (mM)**	**10^3 x k_{cat}/K_m ($M^{-1}s^{-1}$)**
Wild-type	207 ± 10	0.24 ± 0.04	8.60
N42C:K324C open	13 ± 1	1.2 ± 0.2	0.11
N42C:K324C closed	0.84 ± 0.14	0.33 ± 0.09	0.03
N42C	18.1 ± 0.39	0.25 ± 0.01	0.72
K324C	27.6 ± 1.3	0.57 ± 0.09	0.48

Table 5.6: Steady-state kinetic parameters for flavocytochrome b_2 wild-type (from [39], N42C:K324C mutant (open and closed conformations) (from [38]) , and N42C and K324C mutants

With both ferricyanide and cytochrome *c* as electron acceptors the single mutants behave in a similar way to the N42C:K324C open form of the enzyme. These results confirm that is only the cross-linked formation that deeply affects the enzyme's activity. When the disulfide bridge is formed, there is a decrease of 15-fold or more in the k_{cat} values and a significant decrease of the catalytic efficiency (k_{cat}/K_m), compared to the N42C:K324C open form and to the two single mutants.

From these data it is possible to conclude that the disulfide bridge, preventing the mobility of the heme domain, decrease the substrate accessibility to the active site.

5.9 Conclusions

Steady-state and pre-steady-state kinetic analyses from Drewette (2006) [38] indicate that the rate of flavin reduction by L-lactate is influenced by the formation of the disulfide-bridge. Inter-domain mobility does not seem to play a direct role in cytochrome *c* reduction. However, cross-linking the b_2-heme and flavin-binding domains clearly effects the efficiency of this reaction.

The crystal structure of the flavocytochrome b_2 N42C:K324C mutant, solved at 3.0Å resolution, confirms the presence of the disulfide bridge. From a crystallographic point of view, the major effect of locking these two domains together was the observation of clear electron density for the cytochrome domain in each of the four subunits. Notably, although the crystals were grown in the presence of 50 mM pyruvate, in the final structure the substrate electron density was not distinguishable at the active site.

From the above data, including the crystallographic observations, it appears that in the wild-type enzyme the b_2-heme domain must move away from the flavin-domain in order to allow the substrate to access the active site. The engineered disulfide-bridge between the b_2-heme and flavin-binding domains prevents mobility of the cytochrome domain and blocks the pathway taken by the substrate to the active site.

When the disulfide bond is cleaved by DTT addition, or in the single N42C and K324C mutations, the enzyme behaves again in its native manner, confirming that flexibility in the hinge region is required for efficient substrate access.

5.10 References

1. Xia, Z.-X. et al. Three-Dimensional Structure of Flavocytochrome b_2 from Baker's Yeast at 3.0 Å Resolution Proc. Natl. Acad. Sci. USA 84, 2629-2633 (1987).

2. Xia, Z. & Mathews, F. Molecular structure of flavocytochrome b_2 at 2.4 Å resolution. J Mol Biol. 212, 837-63 (1990).

3. Short, D., Walkinshaw, M., Taylor, P., Reid, G. & Chapman, S. Location of a cytochrome *c* binding site on the surface of flavocytochrome b_2. J.Biol.Inorg.Chem. 3, 246-252 (1998).

4. Mowat, C. & Chapman, S. (eds.) Flavocytochrome b_2. Subcellular Biochemistry (Kluwer Academic/Plenum Publishers, 2000).

5. Mowat, C. et al. Changing the heme ligation in flavocytochrome b_2: Substitution of His66 by Cys J.Biol.Inorg.Chem. 5, 584-592 (2000).

6. Cunane, L. et al. Crystallographic study of the recombinant flavin-binding domain of Baker's yeast flavocytochrome b_2: Comparisons with the wild-type enzyme. Biochemistry 41, 4264-4272 (2002).

7. Daff, S., Ingledew, W., Reid, G. & Chapman, S. New insights into the catalytic cycle of flavocytochrome b2 Biochemistry 35, 6345-6350 (1996).

8. Capeillère-Blandin, C., Bray, R., Iwatsubo, M. & Labeyrie, F. Flavocytochrome b_2: kinetic studies by absorbance and electron-paramagnetic-resonance spectroscopy of electron distribution among prosthetic groups. Eur J Biochem. 54, 549-566 (1975).

9. Teague, S. J. Implications of protein flexibility for drug discovery. Nature Reviews Drug Discovery 2, 527-541 (2003).

10. Xiang, J., Sun, J. & Sampson, N. The importance of hinge sequence for loop function and catalytic activity in the reaction catalyzed by triosephosphate isomerase. J. Mol. Biol. 307, 1103-1112 (2001).

11. Falcon, C. & Matthews, K. Glycine insertion in the hinge region of lactose repressor protein alters DNA binding. J. Biol. Chem. 274, 30849-30857 (1999)).

12. Hirano, M. & Hirano, T. Hinge-mediated dimerization of SMC protein is essential for its dynamic interaction with DNA. EMBO 21, 5733-5744) (2002).

13. McCammon, J., Gelin, B., Karplus, M. & Wolynes, P. Hinge-bending mode in lysozyme. Nature Reviews Drug Discovery 262, 325-326 (1976).

14. Sinha, N., Kumar, S. & Nussinov, R. Inter-domain interactions in hinge-bending transitions. Structure 9 1165-1181 (2001).

15. Bahar, I., Atilgan, A., Demirel, M. & Erman, B. Vibrational dynamics of folded proteins: significance of slow and fast motions in relation to function and stability. Phys. Rev. Lett. 80, 2733-2736 (1998).

16. Towler, P. et al. ACE2 X-ray structures reveal a large hinge-bending motion important for inhibitor binding and catalysis. J. Biol. Chem. 279, 17996-18007 (2004).

17. Xu, C., Tobi, D. & Bahar, I. Allosteric changes in protein structure computed by a simple mechanical model: hemoglobin T <-> R2 transition. J. Mol. Biol. 333, 153-168 (2003).

18. Gutteridge, A., Thornton, J. & Bartlett, G. Using a neural network and spatial clustering to predict the location of active sites in enzymes. Biochemistry 37, 11940-11948 (2003).

19. Argos, P. An investigation of oligopeptides linking domains in protein tertiary structures and possible candidates for general gene fusion. J Mol Biol. 211, 943-58 (1990).

20. White, P., Manson, F., Brunt, C., Chapman, S. & Reid, G. The importance of the interdomain hinge in intramolecular electron transfer in flavocytochrome b_2. J. Biochem. 291, 89-94 (1993).

21. Labeyrie, F., Beloeil, J. & Thomas, M. Evidence by NMR for mobility of the cytochrome domain within flavocytochrome b_2. Biochim Biophys Acta. 2, 134-141 (1988).

22. Sharp, R., Chapman, S. & Reid, G. Deletions in the Interdomain Hinge Region of Flavocytochrome b_2 - Effects on Intraprotein Electron-Transfer. Biochemistry 35, 891-899 (1996).

23. Sharp, R., Chapman, S. & Reid, G. Modulation of flavocytochrome b_2 intraprotein electron transfer via an interdomain hinge region. Biochem J. 316, 507-513 (1996).

24. Ogura, Y. & Nakamura, T. Kinetic Studies on the Oxidation and Reduction of the Protoheme Moiety of Yeast L(+)-Lactate Dehydrogenase. J. Biochem. Tokyo 60 77-86 (1966).

25. Tegoni, M., Janot, J. & Labeyrie, F. Inhibition of L-lactate: cytochrome-c reductase (flavocytochrome b_2) by product binding to the semiquinone transient. Loss of reactivity towards monoelectronic acceptors. Eur J Biochem. 190, 329-342 (1990).

26. Pompon, D. Flavocytochrome b_2 from baker's yeast. Computer-simulation studies of a new scheme for intramolecular electron transfer. Eur J Biochem. 106, 151-159 (1980).

27. Sharp, R., White, P., Chapman, S. & Reid, G. Role of the interdomain hinge of flavocytochrome b_2 in intra- and inter-protein electron transfer. Biochemistry 33, 5115-5120 (1994).

28. Shirley, B. A. (ed.) Protein Stability and Folding: Theory and Practice (Humana Press, 1995).

29. Wedemeyer, W. J., Welker, E., Narayan, M. & Scheraga, H. A. Disulfide Bonds and Protein Folding. Biochemistry 39 4207 -4216 (2000).

30. Burova, T., Choiset, Y., Tran, V. & Haertle, T. Role of. free Cys121 in stabilization of bovine b-lactoglobulin. B. Protein. Eng. 11, 1065-1073 (1998).

31. Bader, M., Muse, W., Ballou, D., Gassner, C. & Bardwell, J. Oxidative protein folding is driven by the electron transport system. Cell. Biol 98, 217-227 (1999).

32. Wells, J. A. & Powers, D. B. In vivo formation and stability of engineered disulfide bonds in subtilisin. J. Biol. Chem. 261, 6564-6570 (1986).

33. Storch, E., Daggett, V. & Atkins, W. Engineering out motion: introduction of a de novo disulfide bond and a salt bridge designed to close a dynamic cleft on the surface of cytochrome b_5. Biochemistry 38, 5054-5064 (1999).

34. Tiebel, B., Aung-Hilbrich, L., Schnappinger, D. & Hillen, W. Conformational changes necessary for gene regulation by Tet repressor assayed by reversible disulfide bond formation. EMBO J. 17, 5112-5119 (1998).

35. Clarke, J. & Schreiber, G. Folding and binding - new technologies and new perspectives. Current Opinion in Structural Biology 13, 71-74 (2003).

36. Rothery, E. et al. Probing domain mobility in a flavocytochrome. Biochemistry 43, 4983-4989 (2004).

37. Bell, C. in School of Chemistry (PhD thesis, University of Edinburgh, Edinburgh, 1997).

38. Drewette, K. J. in School of Chemistry (University of Edinburgh, Edinburgh, 2006). An Engineered Inter-domain Disulfide Bridge in Flavocytochrome b_2: Insights into the Role of Domain Mobility

39. Miles, C. et al. Tyr-143 facilitates interdomain electron transfer in flavocytochrome b_2. Biochem. J. 285, 187-190 (1992).

40. Lê, K. D., Mayer, M. & Lederer, F. Epitope mapping for the monoclonal antibody that inhibits intramolecular electron transfer in flavocytochrome b_2. Biochem J. 373, 115-123 (2003).

41. Kunkel, T. Rapid and efficient site-specific mutagenesis without phenotypic selection. Proc. Natl. Acad. Sci. USA 82, 488-492 (1985).

42. Black, M., White, S., Reid, G. & Chapman, S. High-level expression of fully active yeast flavocytochrome b_2 in Escherichia coli. Biochem J. 258, 255-259 (1989).

43. Sigman, J. A. et al. Involvement of surface cysteines in activity and multimer formation of thimet oligopeptidase. Protein Eng. 16, 623-628 (2003).

44. Leslie, A. G. W. CCP4 Newslett. Protein Crystallogr. 32, 7-8 (1996).

45. Vagin, A. & Teplyakov, A. An approach to multi-copy search in molecular replacement. Acta Cryst. 56, 1622-1624 (2000).

46. Roussel, A. & Cambillau, C. (eds.) In Silicon Graphics Geometry Partners Directory 86 (Mountain View, CA, USA: Silicon Graphics, 1991).

47. Murshudov, G., Vagin, A. & Dodson, E. Refinement of Macromolecular Structures by the Maximum-Likelihood Method. Acta Cryst 53, 240-255 (1997).

48. Kraulis, P. MOLSCRIPT: a program to produce both detailed and schematic plots of protein structures. J Appl Crystallogr 24, 946-950 (1991).

49. Merritt, E. & Bacon, D. Raster3D: Photorealistic molecular graphics. Methods Enzymol 277, 505-524 (1997).

50. Tegoni, M. & Cambillau, C. Structural studies on recombinant and point mutants of flavocytochrome b_2. Biochimie. 76, 501-514 (1994).

51. Hazzard, J., Cusanovich, M., Tainer, J., Getzoff, E. & Tollin, G. Kinetic studies of reduction of a 1:1 cytochrome *c*-flavodoxin complex by free flavin semiquinones and rubredoxin. Biochemistry 25, 3318-3328 (1986).

Chapter 6

Crystallographic studies on rat neuronal nitric oxide synthase heme domain mutant G586S

Dédié à Lilian

Crystallographic studies on rat neuronal nitric oxide synthase heme domain mutant G586S

6.1 Introduction

As was already mentioned in section 1.5.4.1, the cytochrome P450 superfamily includes a wide variety of different enzymes.

In a broad sense nitric oxide synthases (NOSs) could be considered as part of the cytochromes P450 family. Both cytochromes P450s and NOSs are mono-oxygenases, they share the same spectroscopic properties, they both have a *b*-type heme in the active site (which is cysteine thiolate-ligated), they exhibit similar catalytic intermediates, and, notably, mammalian NOS oxygenase domain (NOS_{oxy}) and P450s receive electrons from the same redox partner [1].

The reason why NOSs are not included in the P450s group is that apart from the above mentioned general characteristics, NOSs and P450s have little in common.

1) NOSs are obligatory dimers while most of the P450s are monomers.

2) The polypeptide chain of mammalian NOSs includes both a P450-like oxygenase domain and a cytochrome P450-like reductase domain.

3) The activity of NOS depends on the presence of a cofactor (tetrahydrobiopterin (H_4B)) that acts both as a dimerization factor and as an auxiliary proton donor [2]. Interestingly, H_4B is not required in cytochrome P450 catalysis [3].

Furthermore, substrate specificity is very different, because NOS catalysis is only limited to arginine, N^{ω}-hydroxy-L-arginine (NOHA) and few other substrate analogs[4], while P450s display a wider range of substrates [5].

6.2 Nitric oxide synthase

NOS catalyzes the hydroxylation of L-arginine (L-Arg) producing NO and citrulline in two reaction cycles [6]. In both cycles a molecule of oxygen is consumed [7]. Both steps require electrons (two electrons in the first and one electron in the second step) that are provided by the reductase domain via the two flavin cofactors (FAD that accepts two electrons directly from NADPH, and transfers one electron at a time to the heme *via* the FMN).

The enzyme consists of a C-terminal flavin-binding domain, containing binding sites for the redox cofactors NADPH, FMN, and FAD (fig 6.1a), and an N-terminal *b*-heme domain, that contains the active site (fig 6.1b). The two domains are connected by a 20-25 amino acid functional loop that binds calmodulin (CaM) [8]. In mammalian neuronal NOS (nNOS) there is an additional N-terminal domain, located upstream from the heme domain that is the PDZ domain [9].

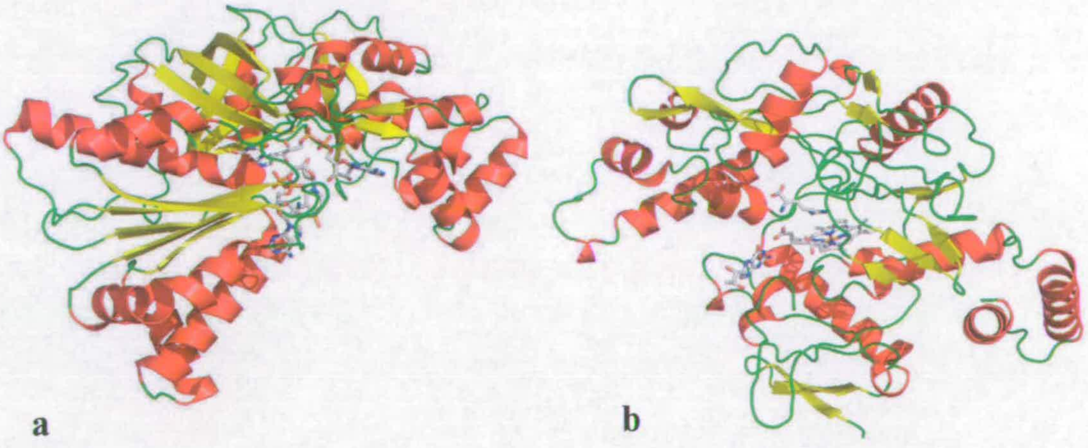

Fig 6.1: Crystal structure models of nNOS. a) Reductase domain (PDB entry 1F20) [10]*, b) oxygenase domain (PDB entry 1OM4)* [11]*. Helices are represented in red, loops in green and β-sheets in yellow. NADPH, FMN, FAD, heme,* H_4B *and L-Arg are represented as stick (colour code: grey, carbon, blue, nitrogen, orange, oxygen).*

Details of the structure of the reductase domain can be found in Zhang, J., *et al.* [10]. The x-ray crystal structure of substrate-bound NOS shows that both the substrate and H_4B are bound at the heme site with a substantial network of hydrogen bonds [11, 12].

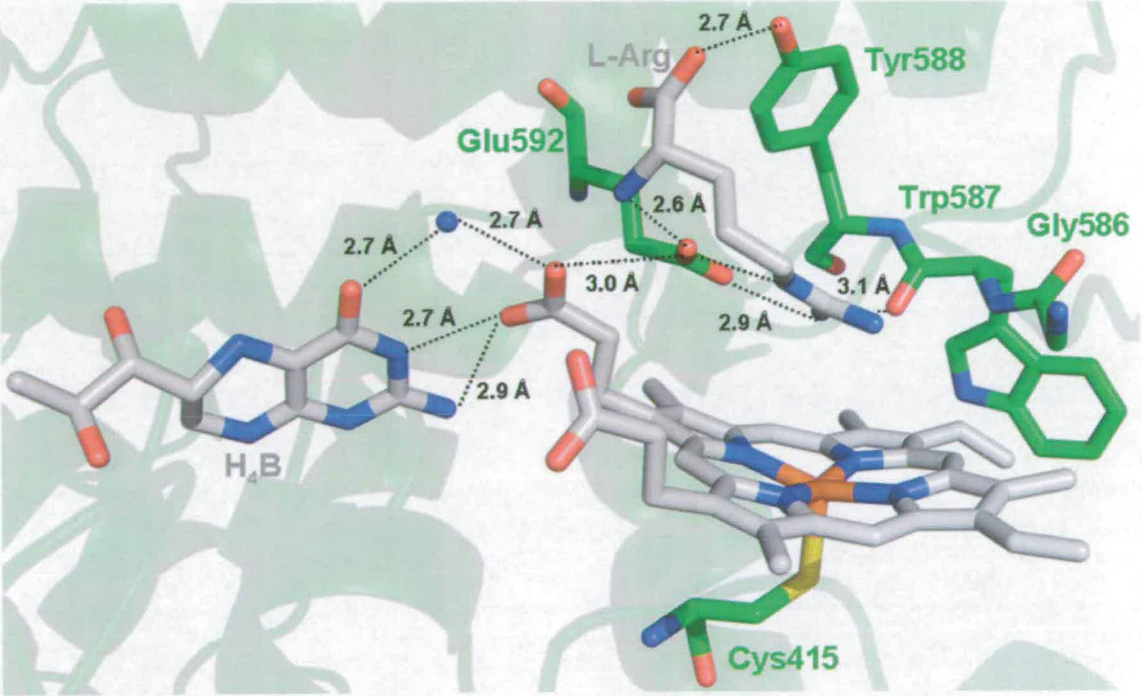

Fig 6.2: The active site of rat nNOS. Here are shown some of the residues involved in interactions between the bound L-Arg, the cofactor H_4B, the heme (color code: carbon in grey, nitrogen in blue, oxygen in red), and the active site residues (color code: carbon in green, nitrogen in blue, oxygen in red, and sulfur in yellow) (PDB entry 1OM4)

6.2 P450 and NOS reactions

The catalytic mechanism of NOS has been proposed based on the better-known mechanism of cytochrome P450 [13-15]. In this section the P450 and NOS catalytic cycles are described in parallel,highlighting similarities and differences. However, it should be noted that the NOS reaction consists of two reaction cycles, while the P450 reaction involves only one.

1) *Substrate binding and first electron delivery*

- The initial step in P450 catalysis is the binding of substrate at the active site. This event corresponds to the expulsion of a water molecule bound to the heme and as a consequence induces a positive shift in the heme reduction potential. P450 is at this point more easily reduced to its ferrous form by electrons derived from its redox partner NAD(P)H. Such a mechanism prevents P450s from entering into an uncoupled cycle when substrate-free. Only the ferrous forms are capable of binding molecular oxygen, forming the oxy-ferrous compound (Fe^{2+}-O_2).
- NOS does not depend entirely on substrate binding for the shift in the reduction potential of the heme, which is already partially high spin, in particular in the presence of H_4B [16]. Nevertheless, the reduction potential of the heme increases when the substrate binds to the active site. As already mentioned in section 6.1, NOS does not require an external redox partner, but it receives the electron from its reductase domain via the flavin cofactors.

2) *Oxygen binding*

- Both P450 and NOS bind O_2 after heme reduction.

3) *Second electron delivery*

- At this stage, the oxy-ferrous complex is reduced by a second electron. In P450s reaction, the second electron is delivered by NAD(P)H-bound protein, producing the peroxy-ferric species (Fe^{3+}-OO^{2-}).
- In contrast, the reaction of NOS at this stage involves the donation of one electron from H_4B [17, 18]. The involvement of H_4B in NOS reflects the most important difference in its catalytic cycle compared to P450.

4) *Protonation and oxy-ferryl species formation*

- The reaction in P450 continues with two protonations, the first of which produces a hydroperoxy-ferric intermediate (Fe^{3+}-OOH^{-}), that accepts the second proton and, by losing a water molecule, produces the highly reactive cationic oxy-ferryl species (Fe^{4+}=O).
- At this stage, H_4B in NOS has been suggested to be involved in the proton transfer, together with a heme propionate and a conserved glutamic acid side chain (Glu363) [19]. Although in NOS there is no evidence for the production of the hydroperoxy-ferric intermediate (Fe^{3+}-OOH^{-}) after the second electron delivery, a similar superoxy-ferrous species has been observed [20]. This putative hydroperoxy-ferric intermediate is thought to be the reactive species in NOS, but it has never been directly observed. Indeed, the peroxy-ferric complex could be the active species.

5) *Product formation*

- As the P450 reaction proceeds, the oxy-ferryl (Fe^{4+}=O) compound creates a substrate radical by abstraction of a hydrogen atom. The heme (at this point in a hydroxy-ferric form) and the substrate radical rebind through the central oxygen, forming a hydroxylated product that dissociates successively from the heme, which remains in its ferric form [21-23].
- In NOS the putative double protonation of the peroxy-ferric complex weakens its oxygen-oxygen bond, and this eventually breaks to broduce a water molecule. The process lead to the formation of the oxy-ferryl (Fe^{4+}=O) compound, which can attack the arginine nitrogen (or the hydroxylated nitrogen of N-hydroxy-L-arginine in the second cycle) to form NOHA in the first cycle and NO and citrulline in the second cycle. The heme is oxidised prior to the release of NO, because the affinity of NO for ferrous heme is much higher than for ferric heme.

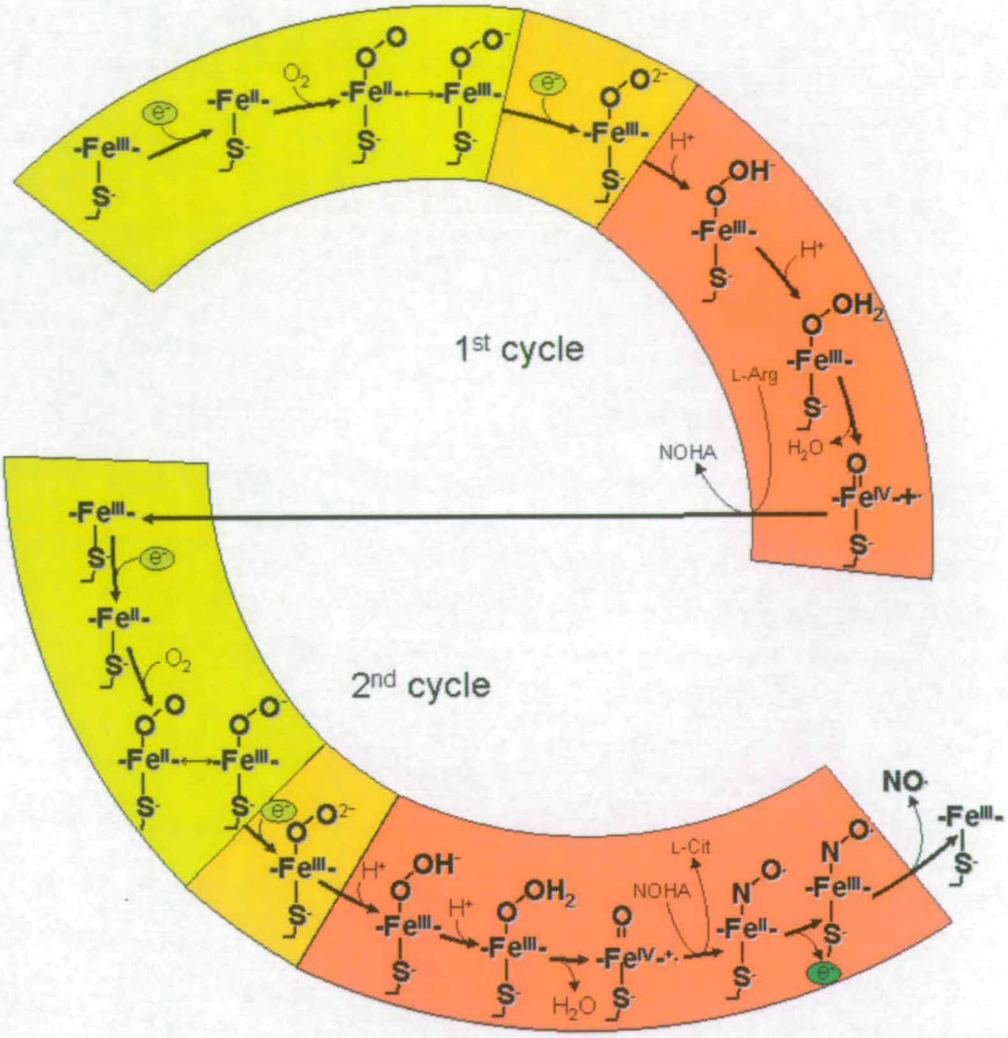

Fig 6.3: Overall of NOS reaction scheme (from [24]). The reaction of NOS described in the text is here divided by colour code. In yellow are illustrated steps 1 (substrate binding and first electron delivery) and step 2 (oxygen binding). In orange is shown step 3 (second electron delivery), and in red, steps 4 and 5 (protonation, oxy-ferryl species formation and product productions). The electron transfers are shown in green, reductions being light green and oxidation darker green.

The structures of three transient intermediates in the hydroxylation reaction of camphor (cam) by P450cam have been recently solved by crystallographic techniques, in combination with data collection using sequentially short and long wavelength x-rays [25].

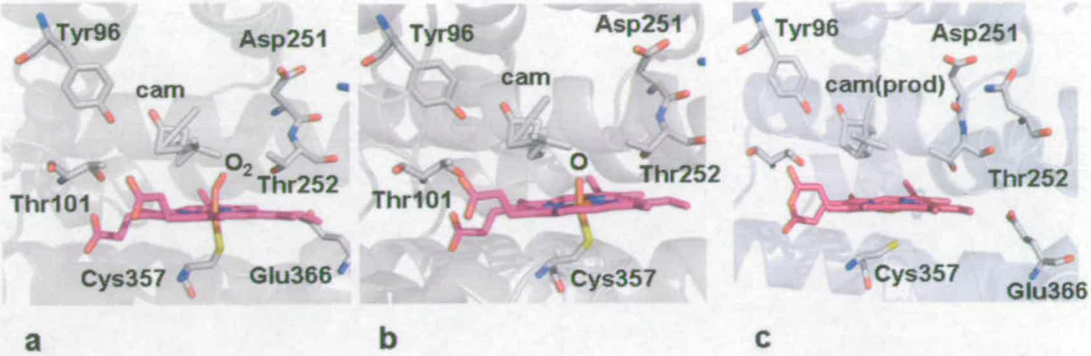

Fig 6.4: Crystal structures of three transient intermediates in the reaction ofP450cam ***from Pseudomonas putida*** *(a, b, and c). The O_2 complex was obtained by exposure to a high pressure of O_2 just before flash cooling. The first dataset (a) was collected with short-wavelength x-rays to minimize reduction of the heme. The result is the structure of the* ***oxygen bound complex of P450cam (PDB entry 1DZ8).*** *The second data set (b) was collected after illuminating the same crystal used for (a) for 3 hours with long-wavelength x-rays to produce hydrated electrons, and consequently driving the reaction toward the reduced, activated oxygen intermediate. The result is oxo-complex of P450cam* ***(PDB entry 1DZ9).*** *The third dataset (c) was collected after thawing and refreezing the same crystal. This final data correspond to the product complex (PDB entry 1DZ6).*
Cam represents the substrate, while cam(prod) is the final product of the reaction [25].

The process of redox partner recognition and the reaction mechanism of P450s have been crucial and interesting problems for P450 investigations. Although the structures of several members of the P450 family have been solved [21, 26, 27], the question of how P450s interact with their redox partners and the precise nature of the reaction mechanism still remains to be answered [28].

Conclusions about the reaction mechanism of NOS are even more difficult to draw. The intermediate species formed in the catalytic site have been identified only up to the formation of the oxy-ferrous species [20]. The events taking place after that are not clear, and this is due in particular to the lack of accumulation of the intermediates formed during the subsequent steps of the reaction cycle.

6.3 Neuronal NOS_{oxy} G586S mutant

More information on the nature of the transient species formed during the NOS reaction could contribute to a better understanding of the mechanism. In the past, several approaches have been used in order to identify the intermediates generated upon oxygen activation in the NOS catalytic site. The catalytic reaction has been analysed at very low temperature in an attempt to trap and isolate the intermediates [20, 29]. Furthermore, H_4B analogues have been used to characterize the reaction activated by the second electron transfer [30, 31].

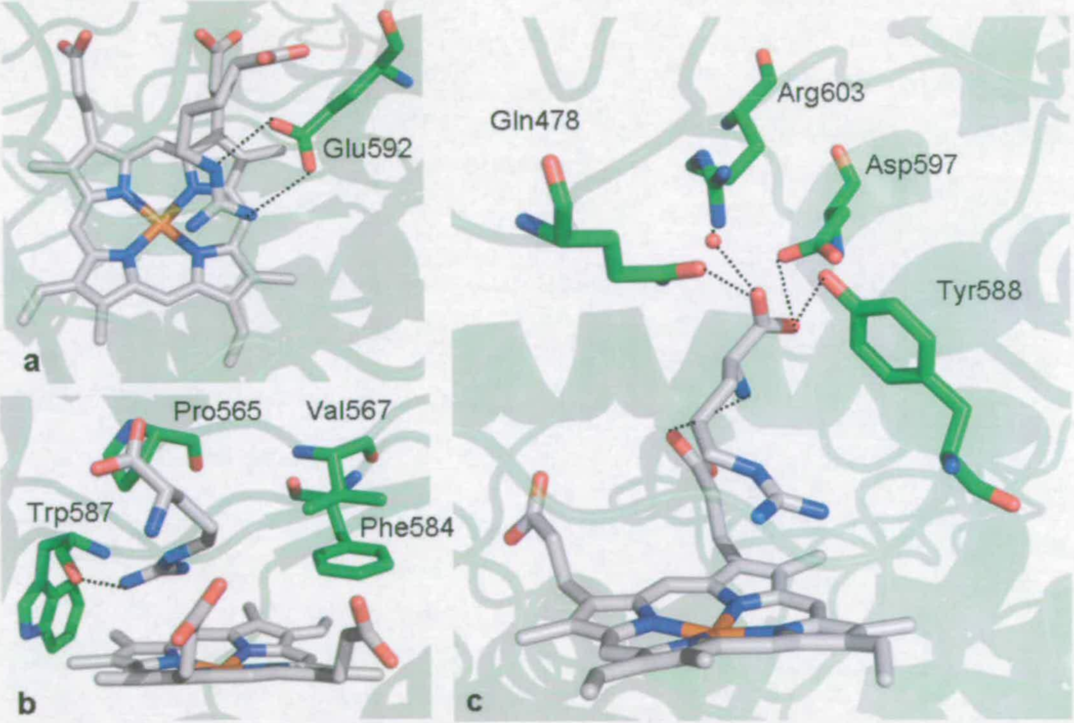

Fig 6.4: *The active site of rat nNOS. All the interactions between the active site residues and the substrate L-Arg are shown (PDB entry 1OM4).*

As already described in section 6.3, NOS and P450 reactions are similar. However, from analysis of the active site residues of NOS [11] it is clear that the amino acid residues localized at the distal side of the heme reveal a hydrophobic character fig 6.4b). This observation is in contrast with the cytochrome P450 active site, where hydrophilic residues are predominant, and play a key role during the activation of oxygen.

In NOS, the introduction by site-direct mutagenesis of a hydrophilic amino acid residue, close to the substrate binding site, could stabilize the transient species of the reaction, by forming hydrogen-bonding interactions with them.

Indeed, the mutant of rat neuronal NOS_{oxy} where glycine 586 was replaced by a serine residue ($nNOS_{oxy}$ G586S) showed the capability to stabilize an intermediate of the reaction that is formed after the oxyferrous compound [24].

In Papale D., 2008 [24] it was observed that the G586S mutation has altered the UV-Vis spectroscopic spectrophotometric characteristics of the mutant in comparison with the wild type enzyme. The spectroscopic, electrochemical and catalytic behaviour of the mutant was tested thoroughly under a variety of conditions and analyzed in comparison with the wild type [24]. As part of this project structural studies were conducted on the $nNOS_{oxy}$ G586S mutant.

In this chapter the crystal structure of the $nNOS_{oxy}$ G586S mutant is described, solved in complex with L-Arg to 2.6 Å resolution. The crystal structure confirms the presence of the serine mutation and reveals the interactions between the Ser586 and the substrate.

6.4 Results

6.4.1 Genetic manipulation

The neuronal NOS heme domain G586S construct was created by Dr. Caroline S. Miles, at the Institute of Structural and Molecular Biology, University of Edinburgh. The NOS G586S heme domain mutant was generated by site-directed mutagenesis using the Kunkel method [32]. The *E.coli* strain BL21 was used for the expression of G586S mutant construct using plasmid pCRNNR [33]. An N-terminal 6-His tag was added to the plasmid in order to purify the enzyme taking advantage of its affinity for nickel.

6.4.2 Purification

The G586S mutant of the nNOS heme domain was expressed and purified as described in Ost, T. and S. Daff, 2005 [30].

For crystallographic studies the purification protocol was modified, following the procedure described in [11] in order to obtain a higher degree of purity of the preparation.

Cell lysate containing $nNOS_{oxy}$ G586S mutant was loaded into a HisTrap HP column (GE Healthcare), equilibrated with 50 mM sodium phosphate buffer at pH 7.8 containing 10% glycerol, 1 mM dithiothreitol (DTT), 20 μM H_4B, 0.1 mM L-arginine, 0.3 M NaCl, and 20 mM imidazole. The protein was eluted from the HisTrap HP column using a 100-150 mM imidazole step gradient using 5 bed volumes of 50 mM sodium phosphate buffer at pH 7.8 containing 10% glycerol, 1 mM DTT, 20 μM H_4B, 0.1 mM L-Arg, 0.3 M NaCl, and 500 mM imidazole.

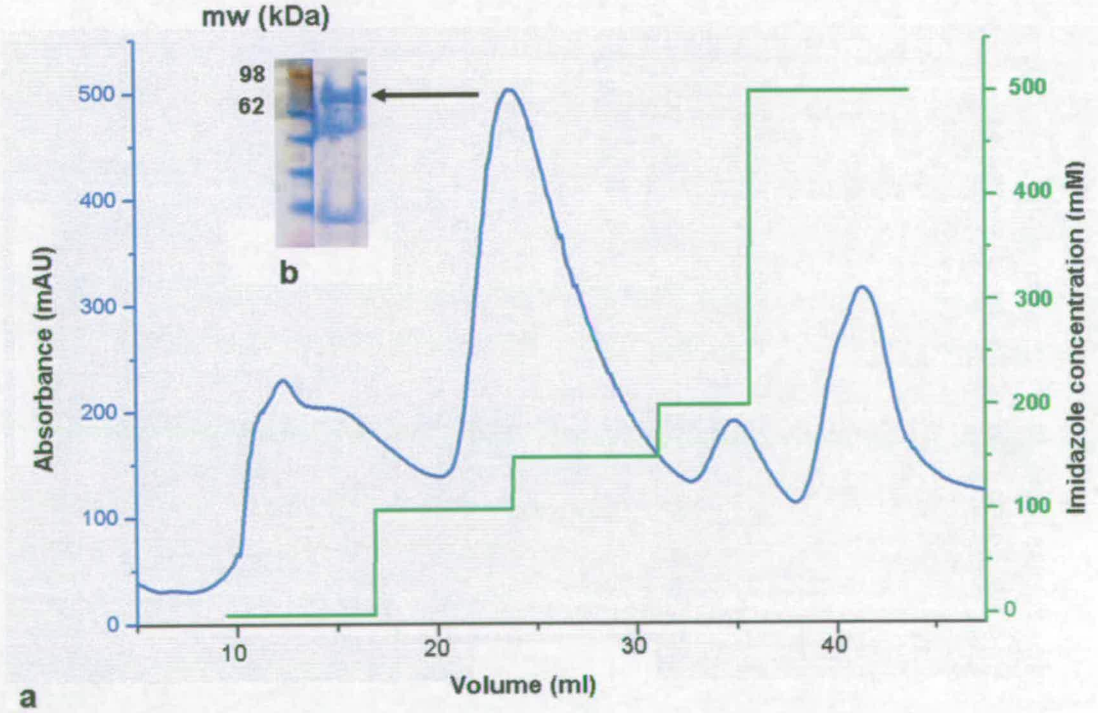

Fig 6.5: a) A_{280} trace (blue) from HisTrap HP purification and elution gradient trace (green). The corresponding fractions of the peak were analysed by SDS-PAGE (b).

The colored elution peak fractions were pooled together and dialyzed overnight at 4°C against buffer 1 (HEPES 50 mM pH 7.5, 10% glycerol, 1 mM DTT, 20 μM H_4B, 0.1 mM L-Arg and 0.25 mM PMSF).

A HITrapQ FF anion-exchange column was equilibrated with five bed-column volumes of the buffer 1. Post-dialysis fractions from HisTrap HP were loaded onto the HITrapQ FF column. The column was washed with 2 bed-column volumes of buffer 1 containing 100 mM NaCl. The protein was then eluted with a 100– 300 mM NaCl gradient using 10 bed-column volumes.

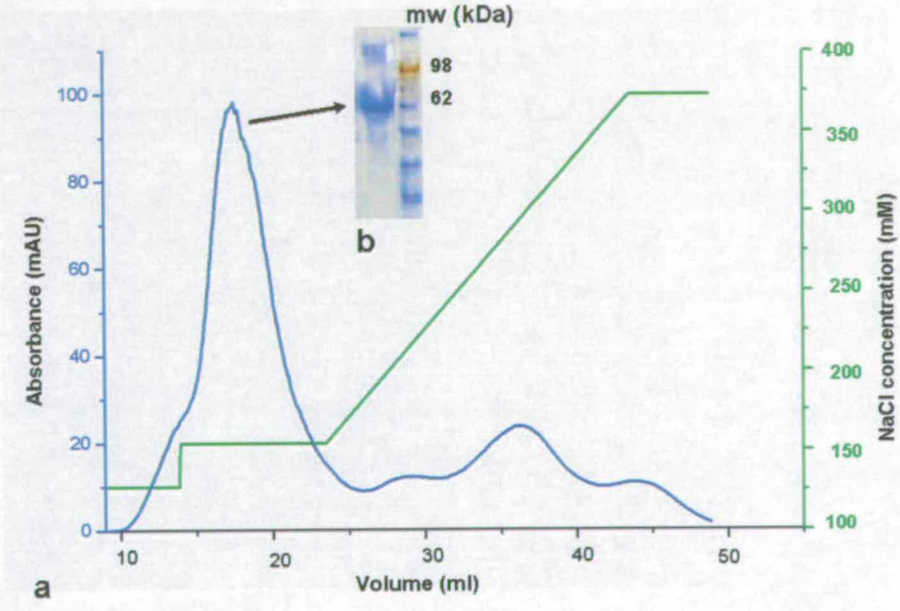

Fig 6.6: a) The elution profile from ion exchange chromatography using a HITrapQ FF column. A_{280} trace is represented in blue and elution gradient trace in green. The target enzyme peak can be seen on the elution profile and the corresponding fractions were analysed by SDS-PAGE (b)

The G586S mutant nNOS heme domain used for crystallographic studies was produced by a limited trypsin digestion of the protein after the Ni- and Q-Trap column steps.

Neuronal NOS PDZ domain is composed of a 6-stranded anti-parallel β-barrel and 2 α-helices [34] (fig 6.7a). Due to its high mobility, no structure of nNOS has been solved using protein including the PDZ domain sequence.

The trypsin digestion was carried out by incubating the partially purified protein on ice for 8 h with a nNOS:trypsin (weight) ratio of 100:1 under continuous stirring.
The results of partial trypsin proteolysis were analyzed by SDS-PAGE and undigested enzyme was used as a comparison (fig 6.7b). As expected, the difference in molecular weight between the digested and undigested enzyme was 15 kDa. Such a molecular weight corresponds to the removed PDZ domain.

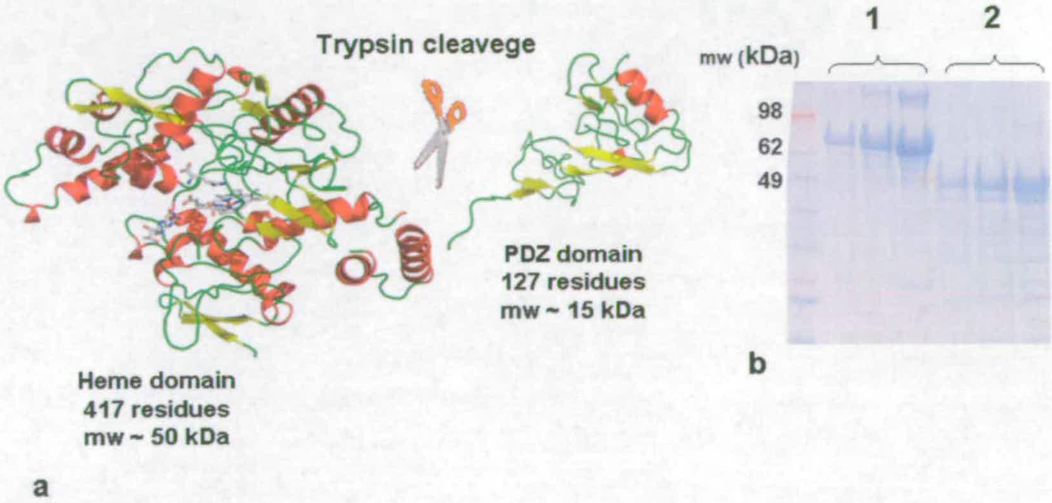

Fig 6.7: a) Illustration of the trypsin digestion of $nNOS_{oxy}$, where the PDZ domain is cleaved from the heme domain; b) comparative analysis by SDS-PAGE of the trypsin digestion product (2) with the undigested protein (1).

The digested protein was then further purified through a Superdex 200 column equilibrated with 50 mM TrisHCl, pH 7.8, containing 10% glycerol, 10 mM DTT, 20 μM H_4B, 0.1 mM L-Arg, and 200 mM NaCl (fig 6.8). The protein eluted at a volume corresponding to ~ 50 kDa molecular weight.

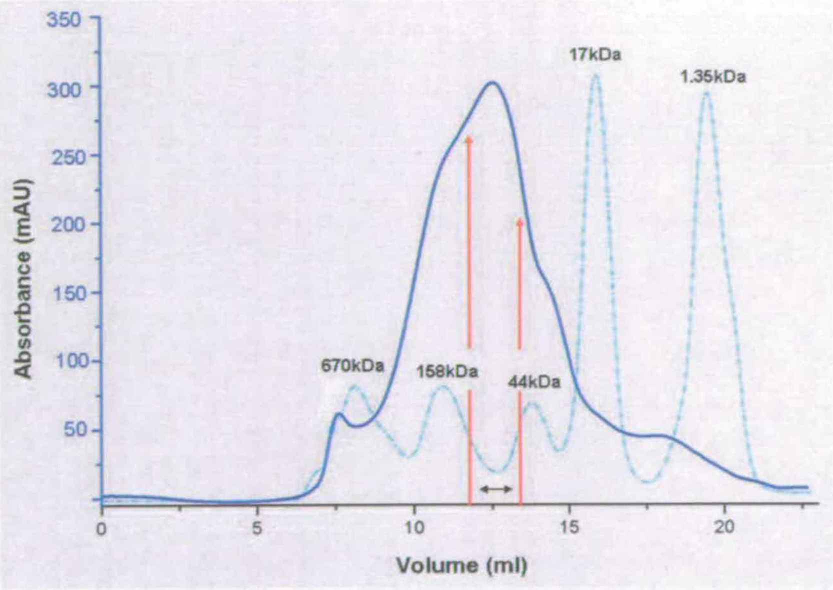

Fig 6.8: The elution profile from gel-filtration chromatography using a Superdex-200 10/30 column for nNOS$_{oxy}$ *G586S mutant (blue) overlaid with the elution profile of the molecular weight markers (cyan). The elution peak appears to be broad and asymmetric, due to the heterogeneity of the sample after trypsin digestion. However, only the fraction of the elution peak in between the two red arrows were pooled together and concentrated.*

The nNOS heme domain produced from trypsin digestion retains the 6-His tag.

Protein concentration was determined spectrophotometrically exploiting the absorbance difference between the ferrous and the ferrous CO-bound forms (extinction coefficient $\Delta\varepsilon_{444\text{-}467} = 55,000\ M^{-1}cm^{-1}$) [30].

6.4.3 Crystallization

A critical reason that finally increased the crystallization rate of nNOS$_{oxy}$, compared to the initial attempts, has been the improvement of the purification protocol and the exclusive use highly homogenous sample for crystallization experiments. Furthermore, the crystallization experiments were entirely performed in the anaerobic box (although the protein was not reduced) including the flash-cooling step. Finally, it was noted that all the crystals flash-cooled using liquid propane as a freezing agent instead of liquid nitrogen yielded a higher quality of the diffraction.

Crystals of G586S mutant of nNOS heme domain were produced by the hanging-drop or sitting-drop vapour diffusion methods at 18°C, by mixing 2 μl of 7-9 mg/ml protein (in 50 mM TrisHCl, pH 7.8, 10% glycerol, 10 mM DTT, 20 μM H_4B, 0.1 mM L-Arg, and 200 mM NaCl) with 2 μl of reservoir solution (0.1 M pH 5.8/6.0 MES, 22-24% PEG 3350, 0.2 M ammonium acetate, 25 mM L-Arg, 35 μM sodium dodecyl sulfate (SDS), 5 mM glutathione (GSH), 2% isopropanol).

Small crystals appear after 24 h (rod shape) and reached maximum size in 1 week (fig 6.9).

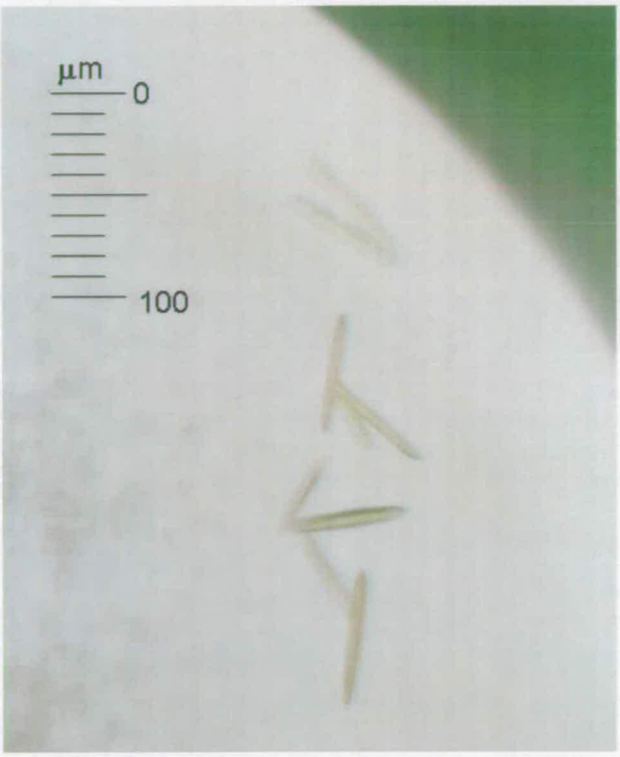

Fig 6.9: Crystals of the G586S NOS_{oxy} grown in a 4 μl volume sitting drop

6.4.4 Freezing procedure

Crystals of the His-tagged G586S nNOS heme domain were washed with reservoir solution and then exposed to increasing amounts of cryoprotectant in a step-wise fashion. The final cryoprotectant solution consisted of 25% (w/v) PEG 3350, 0.1 M MES, pH 5.8/6.0, 0.1 M ammonium acetate, 10% (v/v) glycerol, 10% (w/v) trehalose, 5% (w/v) sucrose, 5% (w/v) mannitol and 1 mM L-Arg [35]. Crystals were flash-cooled in liquid propane as described in section 3.20 for TDO crystals [36].

6.4.5 Data collection

The best dataset was collected to 2.59 Å resolution at 100 K at the ERSF (Grenoble, France) on beam line BM14 (wavelength λ = 0.9737 Å) using a Mar Research CCD detector.

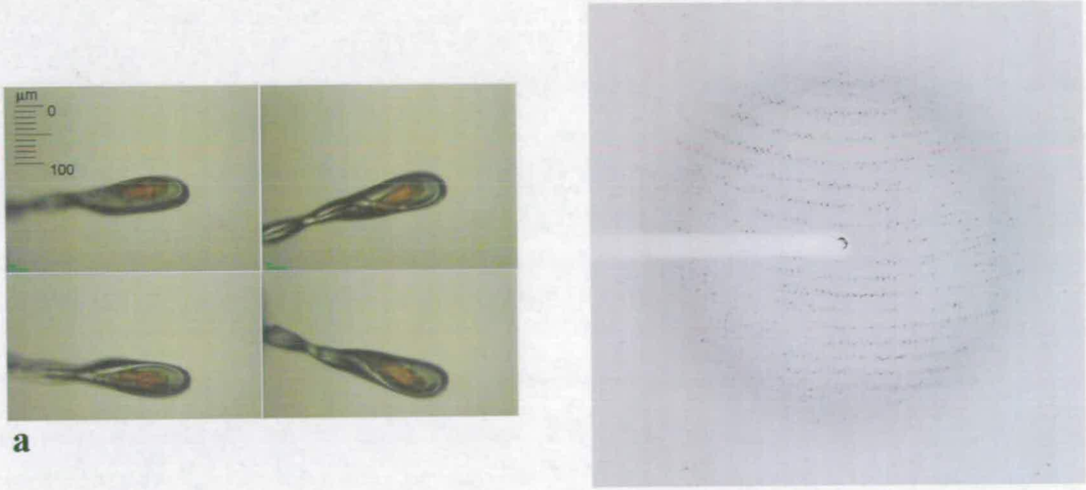

a

b

Fig 6.10: a) Crystal snapshots on beam line BM14, ESRF. b) Diffraction pattern of NOS G586S mutant crystal. Oscillation range 1.0°, Exposure time 30.0 s; detector distance 269.4 mm; resolution at corner 2.5 Å; resolution at edge 3.54 Å.

Crystal were found to belong to space group $P2_12_12_1$ with cell dimensions a = 51.9630 b = 110.8470 c = 164.6270 $\alpha=\beta=\gamma=$ 90.

Data processing was carried out using MOSFLM [37] and SCALA [38]. The structure was solved by molecular replacement using PHASER [39] and the wild-type nNOS_{oxy} structure (PDB entry 1OM4), stripped of water, was used as a starting model. Electron density fitting was carried out using the programs TURBO-FRODO [40] and COOT [41] and structure refinement was carried out using PHENIX [42].

6.5 The crystal structure of G586S nNOS

A dataset to 2.59 Å resolution was used to refine the structure of G586S nNOS heme domain to a final R-factor of 19.8% (R_{free} = 25.3 %; table 6.1).

The final model consists of two protein molecules each comprising residues 299-716 and one *b*-heme. In addition each subunit contains one H_4B molecule bound in the cofactor binding pocket (fig 6.11) and one L-Arg bound in the active site.

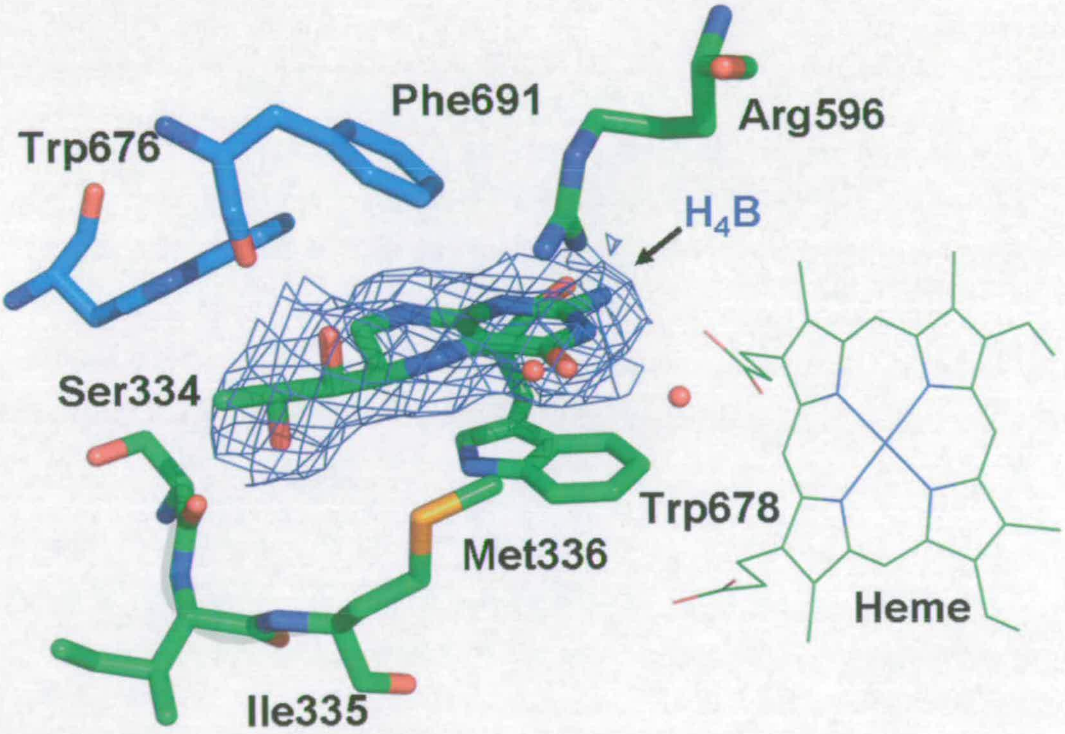

Fig 6.11: the $2F_0 - F_c$ electron density map around the H_4B. The map is contoured at 1 σ. In this figure are also shown some relevant residues binding the cofactor. Residues in green belong to the same monomer, while residues in blue belong to the other monomer of the dimer.

Protein	nNOSoxy (G586S)
Ligand	L-Arg
PDB entry	To become available
Space group	$P2_12_12_1$
cell dimensions	$a = 51.9630$ $b = 110.8470$ $c = 164.6270$ $\alpha=\beta=\gamma= 90$
resolution (Å)	35.00-2.60 (2.69-2.60)*
total no. of reflections	408362
no. of unique reflections	27819
completeness (%)	92.7 (70.8)*
$I/[\sigma(I)]$	13.9 (2.7)*
R_{merge} (%)[a]	10.0 (24.0)*
R_{work} (%)[b]	19.87
R_{free} (%)[c]	25.39
rmsd from ideal values	
bond lengths (Å)	0.006
bond angles (deg)	1.047
Ramachandran analysis	
most favoured (%)	88.0
additionally allowed (%)	11.6
no. of waters included in refinement	196

Table 6.1: Data collection and refinement statistics * *Values in parentheses represent statistics for the highest resolution shell* [a] $R_{merge} = \Sigma_h\Sigma_i|I(h) - I_I(h)|/ \Sigma_h\Sigma_i I_I(h)$, *where* $I_I(h)$ *and* $I(h)$ *are the ith and mean measurement of reflection h, respectively.* [b] $R_{work} = \Sigma_h|F_o - F_c|/ \Sigma_h F_o$, *where* F_o *and* F_c *are the observed and calculated structure factor amplitudes of reflection h, respectively.* [c] R_{free} *is the test reflection data set, 5 % selected randomly for cross validation during crystallographic refinement.*

The presence of the amino acid substitution (G586S) is apparent from the electron density around residue 586 (fig 6.12).

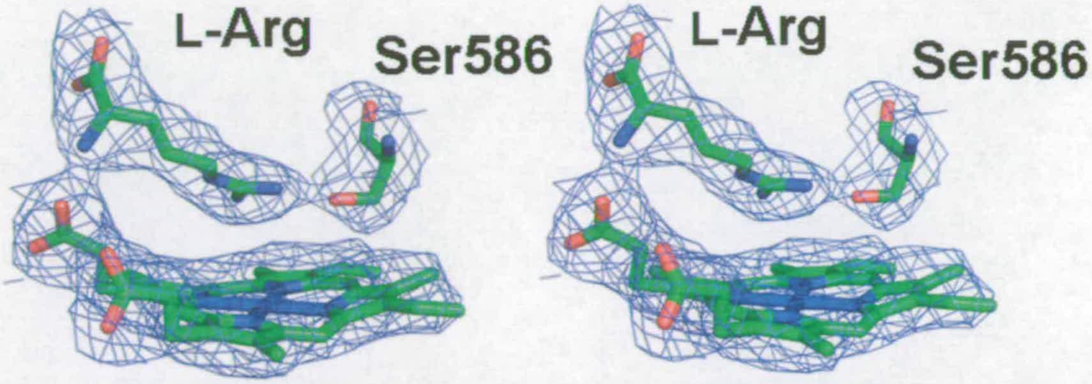

Fig 6.12: Stereoview of electron density around the heme, serine 586, and L-Arg at the active site of G586S nNOS (monomer A). The electron density map was calculated using Fourier coefficients 2 $F_o - F_c$, where F_o and F_c are the observed and calculated structure factors, respectively, the latter based on the final model. The contour level is 1.0 σ, where σ is the rms electron density

The substitution in the active site has little effect on the overall structure of the protein. The rms (root-mean-square) deviation of the backbone α-carbon the atoms of each monomer with those of each monomer of the wild-type enzyme structure (PDB entry 1OM4) is only 0.3 Å. An overlay of the monomer of G586S mutant with the wild-type is shown in fig 6.13.

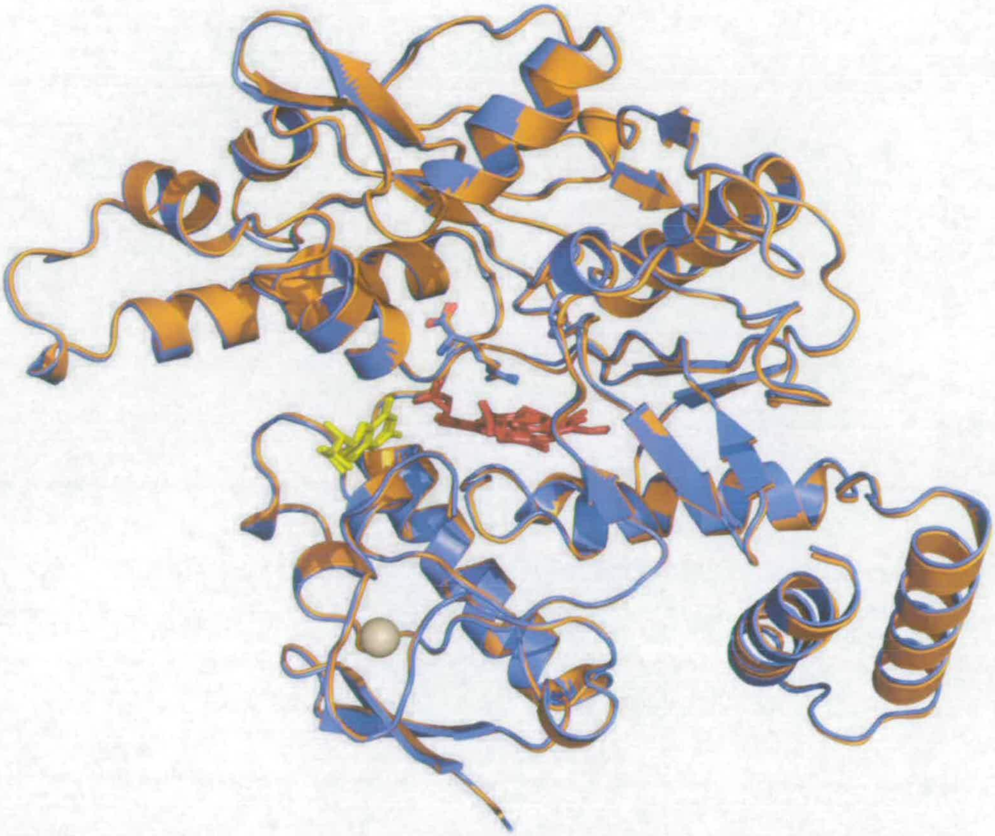

Fig 6.13: Overlay of nNOS$_{oxy}$ wild-type (orange, PDB entry 1OM4) and G586S mutant (blue). The hemes and the H$_4$B are represented as sticks and coloured respectively dark red and yellow. The Zn atom at the dimer interface is represented as a sphere. The substrates bound at the active site are coloured according to the chain colour.

The binding orientation of L-Arg at the active site of the G586S mutant enzyme is very similar to that observed in the wild-type nNOS$_{oxy}$ model. Figures 6.14 and 6.15 show the active sites of the wild-type and the G586S mutant structures with L-Arg bound. The occupancy of L-Arg in the mutant is 100% with an average B-factor of 34 Å^2. B-factors are consistent with 100 % L-Arg occupancy because the contacting atoms between L-Arg and the protein have similar B-factor values. No restraints on B-factors were applied.

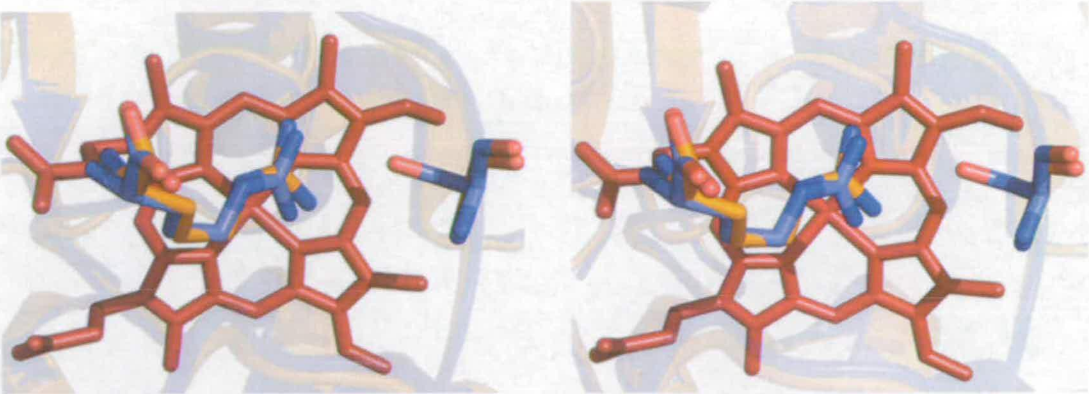

Fig 6.14: Stereoview of an overlay of the active site region of wild-type nNOS (orange) and G586S mutant (blue) viewed from the top. L-*Arg from the G586S enzyme (in blue) and* L-*Arg from the wild-type display the same position in the active site.*

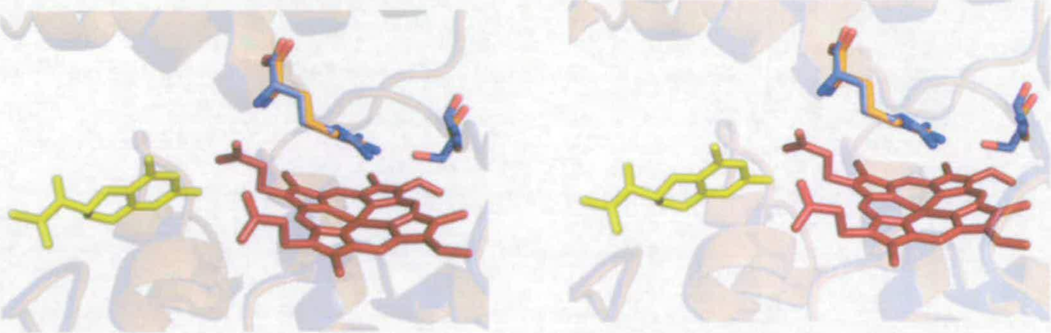

Fig 6.15: Stereoview of an overlay of the active site region of wild-type nNOS (orange) and G586S nNOS TDO (blue) viewed from the side.

From the kinetic characterization of the $nNOS_{oxy}$ G586S mutant it was possible to observe the formation of a novel reaction intermediate in the presence of H_4B and substrate, subsequent to the formation of the oxy-ferrous compound [24]. If this observation is due to the introduction of a new interaction in the active site, it is likely that this would be a hydrogen bond between Ser586 and the substrate.

As shown in fig 6.16, L-Arg maintains the same interactions with the G586S enzyme that it has with the wild-type enzyme. However, the distance between the guanidinium nitrogen of L-Arg and the side chain oxygen of Ser586 is 2.9 Å, in line with the formation of a hydrogen bond.

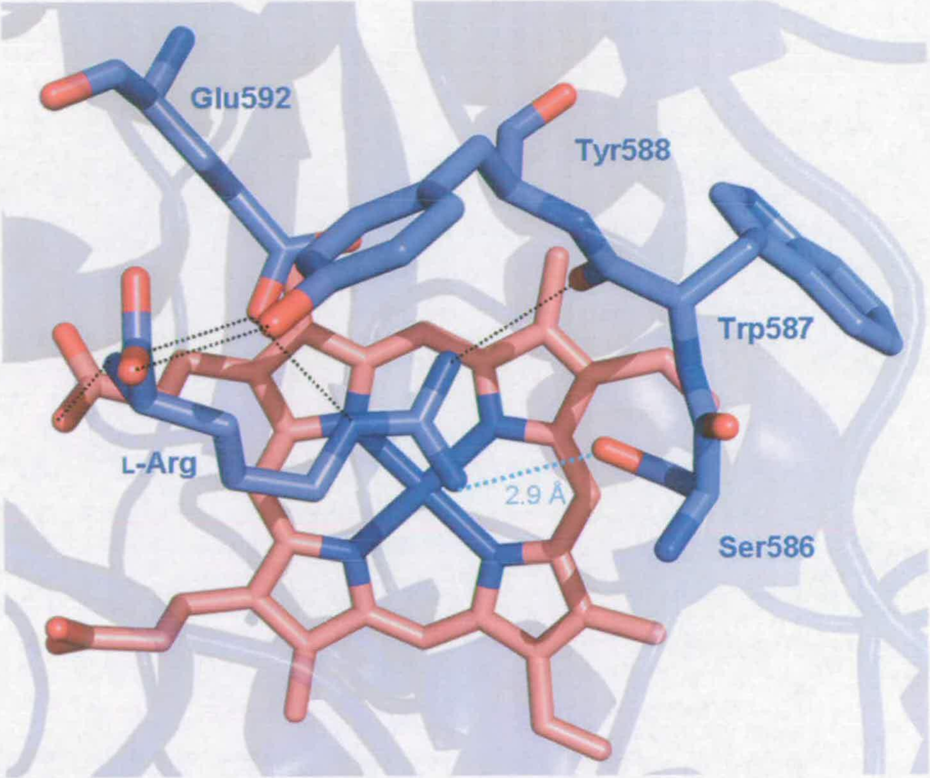

Fig 6.18: The active site of the nNOS$_{oxy}$ G586S mutant, showing some of the interactions between the bound L*-Arg and the active site residues, that are the same as observed in the wild-type enzyme structure. The new hydrogen bond between* L*-Arg and Ser586 is represented in cyan as a dotted line.*

The affinities of NOS$_{oxy}$ wild-type for L-Arg and NOHA are very similar (table 6.2), while the G586S mutant displays increased affinities for both substrates.

	NOS G586S K$_d$ (μM)	**NOS wild-type K$_d$ (μM)**
L-Arg	0.10 ± 0.05	1.0 ± 0.1
NOHA	0.5 ± 0.1	0.9 ± 0.1

Table 6.2: Dissociation constants of ferric wild type and G586S nNOS$_{oxy}$ for L*-Arg and NOHA.*

Interestingly, in the G586S enzyme the affinity for L-Arg is a factor of 10 greater then in wild-type, while the affinity for NOHA is only doubled in the G586S enzyme (data from Papale D., 2008 [24]).

This comparison suggests a new capability for L-Arg of forming a supplementary hydrogen bond induced by the presence of Ser586.

NOHA, on the other hand, has a slightly greater volume due to the additional hydroxyl group, which can clash with the oxygen of Ser586. This may negatively affect its binding in the catalytic site.

A model of the active site, built by overlaying NOHA with the L-Arg in the crystal structure, can help to visualize and explain substrate specificities and affinities.

Such a model has been built only for only illustrative purposes, and is obviously not taking into account the residue motion that can occur upon NOHA binding. The crystal structure of $nNOS_{oxy}$ G586S in complex with NOHA would certainly provide more information on the NOHA binding affinity.

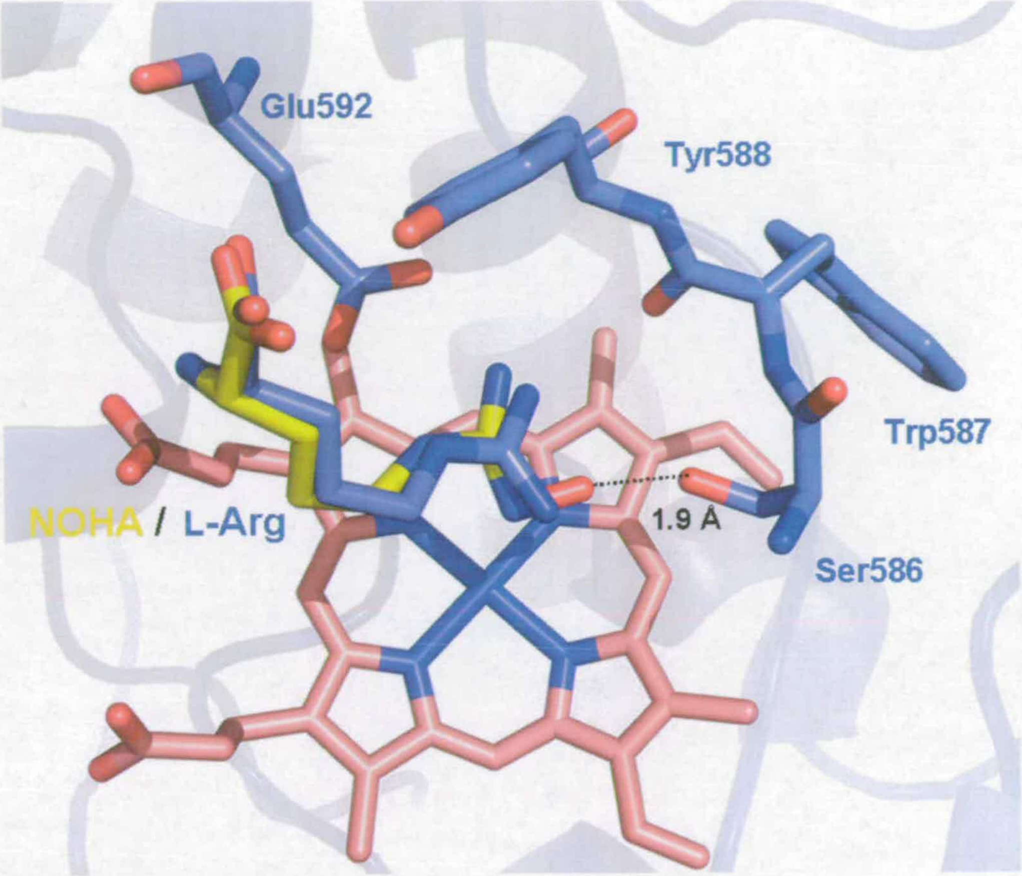

Fig 6.19: Model of nNOS$_{oxy}$ in complex with NOHA created by placing the NOHA over the bound L-Arg. It is possible to observe that in this model the additional hydroxyl group of NOHA clashes with the oxygen of Ser586

6.6 Ternary complexes with dioxygen analogs in crystals

Diatomic molecules such as NO and CO bind to the nNOS$_{oxy}$ heme [11]. Structural characterization of their binding has been important as a source of information about the binding manner of oxygen in the very unstable oxy-heme complexes [11]. In addition, NO binding to the heme is important, as part of the catalytic cycle [43]. Although not physiologically relevant, the CO binding mode to the heme provides information on the normal functioning of NOS, because its binding mode at the heme is more similar to that assumed by oxygen [11].

Affinities of both NO and CO in the wild type and G586S mutant enzyme have been measured under different conditions [24]. NO binding to wild-type enzyme has been reported only with ferric heme, because the affinity of NO for ferrous heme is too high to be determined using standard techniques [24]. CO shows a high affinity only for ferrous heme, while the binding affinity for ferric heme is too low to be interesting.

	No substrate	**L-Arg**	**NOHA**
G586S K_d (μM)	1.8 ± 0.1	3.2 ± 0.2	2.2 ± 0.2
wt K_d (μM)	2.5 ± 0.2	6.9 ± 0.4	20.3 ± 1.8

Table 6.3: Dissociation constants of ferric wild type and G586S nNOS for nitric oxide in the absence and presence of substrates (L-Arg and NOHA). From Papale D., 2008 [24].

	No substrate	**L-Arg**	**NOHA**
G586S K_d (μM)	11.5 ± 1.5	2.9 ± 0.3	2.6 ± 0.2
wt K_d (μM)	10.4 ± 1.0	21.4 ± 2.3	30.8 ± 1.9

Table 6.4: Dissociation constants of ferrous wild type and G586S nNOS for carbon monoxide in the absence and presence of substrates (L-Arg and NOHA). From Papale D., 2008 [24].

The G586S mutation does not cause a significant change in the values of the binding constants for each diatomic molecule in the absence of substrate, but there are differences between the wild-type and mutant enzymes concerning their binding affinities when the enzyme is complexed with the substrates (table 6.3 and 6.4).

Indeed, the substitution increases the affinity for the diatomic ligand by a factor ranging from 2-fold (difference for NO binding to L-Arg-bound enzymes), to 12-fold (CO binding to NOHA-bound enzymes).

Such a difference is probably due to the newly formed hydrogen-bond in the active site of the enzyme. The different values can be explained by the slightly different positions of the substrates in the ternary complex. In the G586S mutant, substrates can possibly assume a position closer to the heme and form a tighter hydrogen bond with the heme sixth ligand.

In an attempt to obtain the structure of the ternary complex of nNOS$_{oxy}$ G586S with substrate and a diatomic ligand (nNOS$_{oxy}$-L-Arg-NO or nNOS$_{oxy}$-L-Arg-CO), crystals were brought inside an anaerobic glove box. Crystals were reduced during the cryoprotection procedure, using a cryoprotectant solution because was used a freezing solution (see section 6.4.4) containing 10 mM DTT. After reduction, crystals were mounted in a pressure chamber (see fig 3.27) and exposed to high pressures of each diatomic gas. Soaking proceeded for 5, 10 or 15 minutes, as described in section 3.13 for TDO, before flash-cooling in liquid propane [36].

Although several datasets for crystals soaked with diatomic ligands were collected, we did not observe the binding of these dioxygen analogs in the structures. This was mainly due to the poor diffraction quality of the crystals exposed to the high-pressure chamber.

6.7 Conclusions

The detection of a novel reaction intermediate during the G586S nNOS$_{oxy}$ catalytic reaction, subsequent to the generation of the oxy-ferrous compound, has been previously reported (Papale D., 2008) [24]. The 2.6 Å resolution crystal structure of G586S nNOS$_{oxy}$ confirms the presence of the mutation and reveals new active site geometries due to the formation of a hydrogen bond between the side chain of the introduced serine 586 and the bound L-Arg.

6.8 References

1. Masters, B. The journey from NADPH-cytochrome P450 oxidoreductase to nitric oxide synthase. Biochem. Biophys. Res. Commun 338, 507-519 (2005).

2. Werner, E., Werner-Felmayer, G. & Mayer, B. Tetrahydrobiopterin, cytokines, and nitric oxide synthesis. Proc Soc Exp Biol Med 219, 171-182 (1998).

3. Garcin, E. et al. Structural basis for isozyme-specific regulation of electron transfer in nitric-oxide synthase. J. Biol. Chem. 279 37918-37927 (2004).

4. Mansuy, D. & Boucher, J.-L. Alternative nitric oxide-producing substrates for NO synthases. Free Radic. Biol. Med. 37, 1105-1121 (2004).

5. Meunier, B., deVisser, S. P. & Shaik, S. Mechanism of oxidation reactions catalyzed by cytochromes P450 enzymes. Chem. Rev. 104, 3947-3980 (2004).

6. Griffith, O. W. & Stuehr, D. J. Nitric oxide synthases: properties and catalytic mechanism. Annu Rev Physiol 57, 707-736 (1995).

7. White, R. & Coon, M. Oxygen activation by cytochrome P-450. Annu. Rev. Biochem. 49, 315-356 (1980).

8. Craig, D. H., Chapman, S. K. & Daff, S. Calmodulin Activates Electron Transfer through Neuronal Nitric-oxide Synthase Reductase Domain by Releasing an NADPH-dependent Conformational Lock. J. Biol. Chem. 277, 33987-33994 (2002).

9. Kone, B. Protein-protein interactions controlling nitric oxide synthases. Acta Physiol Scand. 168, 27-31 (2000).

10. Zhang, J. et al. Crystal structure of the FAD/NADPH-binding domain of rat Neuronal nitric-oxide synthase comparison with NADPH-cytochrome P450 oxidoreductase J. Biol. Chem. 276, 37506-37513 (2001).

11. Li, H., Igarashi, J., Jamal, J., Yang, W. & Poulos, T. L. Structural studies of constitutive nitric oxide synthases with diatomic ligands bound. J Biol Inorg Chem. 11, 753-68 (2006).

12. Matter, H. et al. Structural Analysis of Isoform-Specific Inhibitors Targeting the Tetrahydrobiopterin Binding Site of Human Nitric Oxide Synthases. J.Med.Chem. 48, 4783-4792 (2005).

13. Sono, M., Roach, M. P., Coulter, E. D. & Dawson, J. H. Heme-containing oxygenases. Chem. Rev. 96, 2841-2887 (1996).

14. Meunier, B., Visser, S. d. & Shaik, S. Mechanism of oxidation reactions catalyzed by cytochrome P450 enzymes. Chem. Rev. 104, 3947-3980 (2004).

15. Denisov, I., Makris, T., Sligar, S. & Schlichting, I. Structure and chemistry of cytochrome P450. Chem. Rev. 105, 2253-2277 (2005).

16. Presta, A., Weber-Main, A., Stankovich, M. & Stuehr, D. Comparative effects of substrates and pterin cofactor on the heme midpoint potential in inducible and neuronal nitric oxide synthases. J. Am. Chem. Soc. 120, 9460-9465 (1998).

17. Bec, N., Gorren, A., Voelker, C., Mayer, B. & Lange, R. Reaction of neuronal nitric-oxide synthase with oxygen at low temperature. Evidence for reductive activation of the oxy-ferrous complex by tetrahydrobiopterin. J. Biol. Chem. 273, 13502-13508 (1998).

18. Wei, C.-C., Wang, Z.-Q., Hemann, C., Hille, R. & Stuehr, D. A tetrahydrobiopterin radical forms and then becomes reduced during N ω-hydroxyarginine oxidation by nitric-oxide synthase. J. Biol. Chem. 278 46668-46673 (2003).

19. Sørlie, M. et al. Single-turnover of nitric-oxide synthase in the presence of 4-amino-tetrahydrobiopterin. Proposed role for tetrahydrobiopterin as a proton donor. J. Biol. Chem. 278, 48602-48610 (2003).

20. Davydov, R. et al. EPR and ENDOR characterization of intermediates in the cryoreduced oxy-nitric oxide synthase heme domain with bound l-arginine or NG-hydroxyarginine. Biochemistry 41, 10375-10381 (2002).

21. Li, H. & Poulos, T. L. The structure of the cytochrome p450BM-3 hemedomain complexed with the fatty acid substrate, palmitoleic acid. Nat. Struct. Biol. 4(2), 140-146 (1997).

22. Raag, R. & Poulos, T. L. Crystal structure of the carbon monoxide-substrate-cytochrome P-450CAM ternary complex. Biochemistry 28, 7586-7592 (1989).

23. Schlichting, I., Jung, C. & Schulze, H. Crystal structure of cytochrome P450cam complexed with the (1S)-camphor enantiomer. FEBS Lett. 415, 253-257 (1997).

24. Papale, D. in PhD thesis, School of Chemistry (University of Edinburgh, Edinburgh, 2008). Oxygen activation during neuronal NOS reaction.

25. Schlichting, I. et al. The catalytic pathway of cytochrome p450cam at atomic resolution. Science 5458, 1615-1622 (2000).

26. Poulos, T. L., Finzel, B. C., Gunsalus, I. C., Wagner, G. C. & Kraut, J. The 2.6-.ANG. crystal structure of Pseudomonas putida cytochrome P-450. J. Biol. Chem. 260, 16122-16130 (1985).

27. Ravichandran, K. G., Boddupalli, S. S., Hasermann, C. A., Peterson, J. A. & Deisenhofer, J. Crystal structure of hemoprotein domain of P450BM-3, a prototype for microsomal P450's. Science 261(5122), 731-736 (1993).

28. Bach, R. & Dmitrenko, O. The "somersault" mechanism for the P-450 hydroxylation of hydrocarbons. The intervention of transient inverted metastable hydroperoxides. J. Am. Chem. Soc. 128, 1474-1488 (2006).

29. Hurshman, A. R., Krebs, C., Edmondson, D. E., Huynh, B. H. & Marletta, M. A. Formation of a pterin radical in the reaction of the heme domain of inducible nitric oxide synthase with oxygen. Biochemistry 38, 15689-15696 (1999).

30. Ost, T. W. & Daff, S. Thermodynamic and kinetic analysis of the nitrosyl, carbonyl, and dioxy heme complexes of neuronal nitric-oxide synthase. The roles of substrate and tetrahydrobiopterin in oxygen activation. J Biol Chem. 280, 965-973 (2005).

31. Wei, C. C. et al. Structure of tetrahydrobiopterin tunes its electron transfer to the heme-dioxy intermediate in nitric oxide synthase. Biochemistry 42, 1969-1977 (2003).

32. Kunkel, T. Rapid and efficient site-specific mutagenesis without phenotypic selection. Proc. Natl. Acad. Sci. USA 82, 488-492 (1985).

33. Newton, D. C., Montgomery, H. J. & Guillemette, J. G. Archives of Biochemistry and Biophysics 359, 249-257 (1998).

34. Tochio, H., Zhang, Q., Mandal, P., Li, M. & Zhang, M. Solution structure of the extended neuronal nitric oxide synthase PDZ domain complexed with an associated peptide. Nature Structural Biology 6, 417 - 421 (1999).

35. Li, H. et al. The Novel Binding Mode of N-Alkyl-N'-hydroxyguanidine to meuronal nitric oxide synthase provides mechanistic Insights into NO biosynthesis Biochemistry 41, 13868-13875 (2002).

36. Vernède, X. & Fontecilla-Camps, J. C. A method to stabilize reduced and/or gas-treated protein crystals by flash-cooling under a controlled atmosphere. J. Appl. Crystallogr. 32, 505-509 (1999).

37. Leslie, A. G. W. CCP4 Newslett. Protein Crystallogr. 32, 7-8 (1996).

38. Kabsch, W. Evaluation of Single-Crystal X-ray Diffraction Data from Position Sensitive Detectors. J. Appl. Crystallography. 21, 916-924 (1988).

39. McCoy, A. et al. Phaser crystallographic software. J. Appl. Cryst. 40, 658-674 (2007).

40. Roussel, A. & Cambillau, C. (eds.) In Silicon Graphics Geometry Partners Directory 86 (Mountain View, CA, USA: Silicon Graphics, 1991).

41. Emsley, P. & Cowtan, K. Coot: model-building tools for molecular graphics. Acta Crystallographica D60, 2126-2132 (2004).

42. Adams, P. D. et al. PHENIX: building new software for automated crystallographic structure determination. Acta Cryst. D58, 1948-1954 (2002).

43. Abu-Soud, H. M. et al. Nitric Oxide Binding to the Heme of Neuronal Nitric-oxide Synthase Links Its Activity to Changes in Oxygen Tension. J. Biol. Chem. 270, 22997-23006 (1995).

Chapter 7

Summary

Summary

- The crystal structure of TDO from *X. campestris* in complex with its natural substrate has been solved to 1.6 Å resolution, showing the exact positioning of the substrate in the active site and explaining the substrate specificity of TDO. The structural information, integrated with biochemical studies, allow the identification of potentially important active-site residues.

- Significant effort has been invested in order to obtain the crystal structure of the ternary complexes of TDO with L-Trp and or NO. This data would have provided important insights into the structure of the Michaelis complex. As such, it would be interesting to continue the structural work in this direction, to investigate the effects of diatomic ligands binding into the active site.

- Another important point that still remains obscure is the presence of the allosteric binding site of tryptophan. Again, the combination of kinetic and structural information on mutant forms of the enzyme, where the residues interacting with the second tryptophan are mutated, will clarify if there is any functional role of such putative allosteric binding site.

- We have also determined at 2.4 Å resolution the structure of the SO4414 protein (sIDO) from *Shewanella oneidensis*. Anyway, very little is yet known about substrate binding in SO4414. Future work will be addressed on attempts to crystallize SO4414 in complex with a substrate or an inhibitor.

- The question behind chapter 3- why is there such a strict substrate specificity in TDO compared with IDO and which is the mechanism of catalysis? was then only partially answered. Although we have sufficient elements to explain the substrate specificity of TDO, on the other side the catalytic mechanisms of TDO and IDO have, so far, not been completely understood. For TDO it has been proposed that its reaction mechanism involves the base-catalyzed deprotonation of the indole nitrogen of the substrate.

- Indeed, compared with IDO structure, the most obvious difference between the active sites of the two enzymes is the presence of His55 in TDO and its equivalent Ser167 in IDO. In order to answer the question – is the active site histidine 55 hydrogen bonded to L-Trp implicated as the active site base in TDO?- a crystallographic study of a *X. campestris* TDO mutant, where the active-site residue histidine 55 has been substituted by alanine has been conducted. The structural data, in conjunction with potentiometric and kinetic studies on the mutant have provided information on the mechanism used by TDO to control substrate binding. Our data indicate that His55 does not assume the role of active site base, but instead reveal a role for His55 in controlling substrate binding at the active site, significantly decreasing the affinity of the oxidised enzyme for substrate and regulating the binding of dioxygen.

- The crystal structure of the flavocytochrome b_2 N42C:K324C mutant, solved at 3.0Å resolution, confirms the presence of the disulfide bridge. The major effect of locking these two domains together was the observation of an ordered cytochrome domain in each of the four monomers of the enzyme. Interestingly, despite the crystallising conditions containing 50 mM pyruvate, the presence of the substrate was not observed at the active site in our crystal structure.

- The question posed on chapter 5 was - why is there inter-domain mobility in flavocytochrome b_2 and is it important for catalysis? From our data it appears that the role of inter-domain mobility is to allow the b_2-heme domain to move away from the flavin-binding domain in order for substrate to effectively access the active site. Cross-linking the b_2-heme and flavin-binding domains prevents mobility about the cytochrome domain and essentially disrupts the usual pathway taken by the substrate to the active site. On reduction of the disulfide bond by DTT, or in the single N42C and K324C mutations the enzyme is again able to behave in its native manner, indicating its requirement for dynamic flexibility about the hinge region.

- The 2.6 Å resolution crystal structure of G586S nNOS$_{oxy}$ confirms the presence of the mutation and reveals the formation of a new hydrogen bond between the side chain of the introduced serine 586 and the bound L-Arg.

  Future efforts should be certainly addressed to obtain the crystal structure of nNOS$_{oxy}$ G586S in complex with N$^{\omega}$-hydroxy-L-Arg in order to understand the reason of the different binding affinity for the two substrates.

  Another future goal will be the structural characterization of nNOS$_{oxy}$ in ternary complex with a substrate and diatomic ligands, such as NO or CO. This has already represented an important source of information about the binding manner of oxygen in the very unstable oxy-heme complexes. In particular, the CO binding mode to the heme will provide information on the normal functioning of NOS, because its binding mode at the heme is more similar to that assumed by oxygen.

Molecular insights into substrate recognition and catalysis by tryptophan 2,3-dioxygenase

Farhad Forouhar*, J. L. Ross Anderson†, Christopher G. Mowat†, Sergey M. Vorobiev*, Arif Hussain*, Mariam Abashidze*, Chiara Bruckmann†, Sarah J. Thackray†, Jayaraman Seetharaman*, Todd Tucker*, Rong Xiao‡, Li-Chung Ma‡, Li Zhao‡, Thomas B. Acton‡, Gaetano T. Montelione‡, Stephen K. Chapman†, and Liang Tong*§

*Department of Biological Sciences, Northeast Structural Genomics Consortium, Columbia University, New York, NY 10027; †School of Chemistry, University of Edinburgh, West Mains Road, Edinburgh EH9 3JJ, United Kingdom; and ‡Center for Advanced Biotechnology and Medicine and Northeast Structural Genomics Consortium, Rutgers University, Piscataway, NJ 08854

Communicated by Wayne A. Hendrickson, Columbia University, New York, NY, November 13, 2006 (received for review September 25, 2006)

Tryptophan 2,3-dioxygenase (TDO) and indoleamine 2,3-dioxygenase (IDO) constitute an important, yet relatively poorly understood, family of heme-containing enzymes. Here, we report extensive structural and biochemical studies of the *Xanthomonas campestris* TDO and a related protein SO4414 from *Shewanella oneidensis*, including the structure at 1.6-Å resolution of the catalytically active, ferrous form of TDO in a binary complex with the substrate L-Trp. The carboxylate and ammonium moieties of tryptophan are recognized by electrostatic and hydrogen-bonding interactions with the enzyme and a propionate group of the heme, thus defining the L-stereospecificity. A second, possibly allosteric, L-Trp-binding site is present at the tetramer interface. The sixth coordination site of the heme-iron is vacant, providing a dioxygen-binding site that would also involve interactions with the ammonium moiety of L-Trp and the amide nitrogen of a glycine residue. The indole ring is positioned correctly for oxygenation at the C2 and C3 atoms. The active site is fully formed only in the binary complex, and biochemical experiments confirm this induced-fit behavior of the enzyme. The active site is completely devoid of water during catalysis, which is supported by our electrochemical studies showing significant stabilization of the enzyme upon substrate binding.

cancer | heme enzymes | immunomodulation | indoleamine 2,3-dioxygenase

Tryptophan 2,3-dioxygenase (TDO) and indoleamine 2,3-dioxygenase (IDO) catalyze the oxidative cleavage of the L-tryptophan (L-Trp) pyrrole ring, the first and rate-limiting step in L-Trp catabolism through the kynurenine pathway (1–3). In addition, IDO has been implicated in a diverse range of physiological and pathological conditions, including suppression of T cell proliferation, maternal tolerance to allogenic fetus, and immune escape of cancers (4–8), and is an attractive target for drug discovery against cancer and autoimmune and other diseases (2, 9–12).

Despite catalyzing identical biochemical reactions (Fig. 1*a*), the sequence similarity between TDO and IDO is extremely low. An alignment of their sequences is only possible based on their structures, which suggests a sequence identity of 10% between them (Fig. 1*b*). In comparison, *Xanthomonas campestris* TDO shares 34% sequence identity with human TDO (Fig. 1*b*), demonstrating the remarkable evolutionary conservation of this enzyme. TDO is a homotetrameric enzyme and is highly specific for L-Trp and related derivatives such as 6-fluoro-Trp as the substrate. In comparison, IDO is monomeric, and shows activity toward a larger collection of substrates, including L-Trp, D-tryptophan (D-Trp), serotonin, and tryptamine (3), although the K_m for D-Trp is ≈100-fold higher than that for L-Trp (13). The structure of human IDO in the catalytically inactive, ferric [Fe(III)]-heme state in complex with the 4-phenylimidazole inhibitor has recently been reported (14). Although this structure gave information about important active site residues, the inhibitor is coordinated to the heme iron and does not provide any information regarding Trp or oxygen binding.

To provide direct insight into substrate recognition and catalysis by these enzymes, we report here the crystal structures at up to 1.6-Å resolution of the active, reduced (Fe(II)) TDO from *X. campestris* in a binary complex with the substrate L-Trp or 6-fluoro-Trp. Our structures reveal for the first time the structural basis for the stereospecificity of this important enzyme. Our structural information is confirmed by biochemical studies and offers significant molecular insight into tryptophan dioxygenation by TDO and IDO.

Results

Structure Determination. Crystals of the reduced (Fe(II)) TDO from *X. campestris* in a binary complex with the substrate L-Trp or 6-fluoro-Trp were obtained after extensive efforts and by using anaerobic conditions, because the oxidized (Fe(III)) enzyme has much lower affinity for L-Trp (see below). The structures at up to 1.6-Å resolution of these binary complexes [Table 1; and see supporting information (SI) Table 3] as well as that of the free enzyme were determined by molecular replacement based on the structure of the apo enzyme, in the absence of heme, which we had determined by the selenomethionyl single-wavelength anomalous diffraction method (PDB entry 1YW0) (15).

The structure of the SO4414 protein from *Shewanella oneidensis* (16) was determined at 2.4-Å resolution by molecular replacement based on our structure of the apo enzyme (PDB entry 1ZEE).

Structure of TDO. The structure of *X. campestris* TDO monomer contains 12 helices (named αA through αL) and no β-strands (Figs. 1*b* and 2*a*). TDO is an intimately associated tetramer (Fig. 2*b*), and ≈4,500 Å^2 of the surface area of each monomer is buried in the tetramer. Helices αB and αC are located in the extensive, mostly hydrophobic interface between two of the monomers. The N-terminal segments (residues 21–40, including helix αA) of the two monomers are swapped in this dimer (Fig.

Author contributions: F.F., J.L.R.A., and C.G.M. contributed equally to this work; F.F., J.L.R.A., C.G.M., G.T.M., S.K.C., and L.T. designed research; F.F., J.L.R.A., C.G.M., S.M.V., A.H., M.A., C.B., S.J.T., J.S., T.T., R.X., L.-C.M., L.Z., and T.B.A. performed research; F.F., J.L.R.A., C.G.M., S.M.V., A.H., M.A., C.B., S.J.T., J.S., R.X., L.-C.M., T.B.A., G.T.M., S.K.C., and L.T. analyzed data; and F.F., J.L.R.A., C.G.M., T.B.A., G.T.M., S.K.C., and L.T. wrote the paper.

The authors declare no conflict of interest.

Abbreviations: D-Trp, D-tryptophan; IDO, indoleamine 2,3-dioxygenase; L-Trp, L-tryptophan; TDO, tryptophan 2,3-dioxygenase.

Data deposition: The atomic coordinates have been deposited in the Protein Data Bank, www.pdb.org (PDB ID codes 1YW0, 2NW7, 2NW8, 2NW9, 1ZEE, and 2NWB).

§To whom correspondence should be addressed. E-mail: ltong@columbia.edu.

This article contains supporting information online at www.pnas.org/cgi/content/full/0610007104/DC1.

www.pnas.org/cgi/doi/10.1073/pnas.0610007104

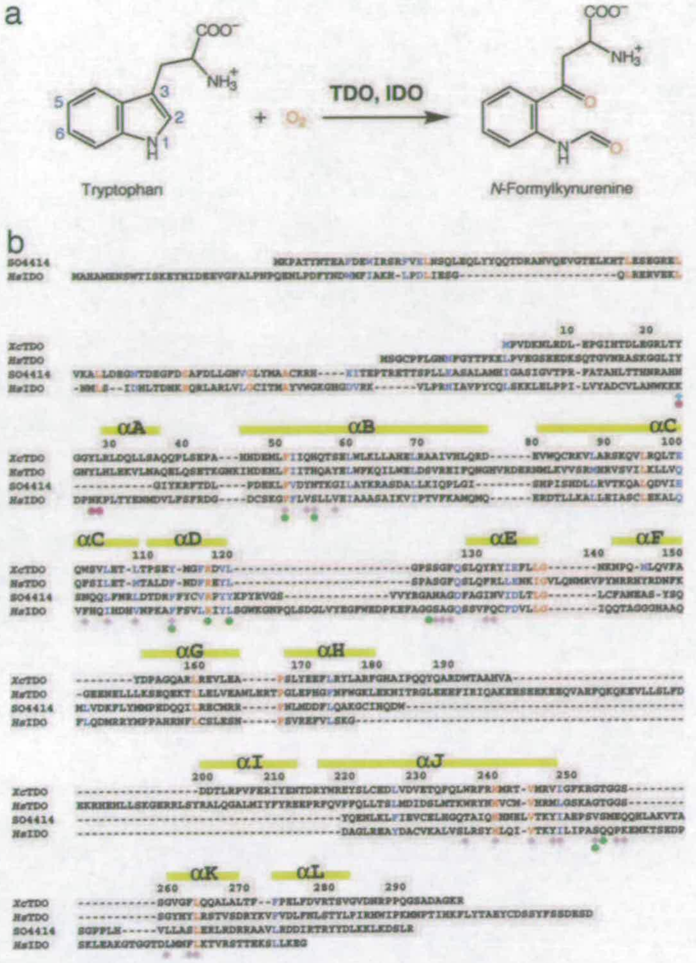

Fig. 1. Primary structures of TDO and IDO. (*a*) The biochemical reaction catalyzed by TDO and IDO. (*b*) Amino acid sequence alignment of *X. campestris* TDO (*Xc*TDO), human TDO (*Hs*TDO), *S. oneidensis* SO4414 (SO4414), and human IDO (*Hs*IDO). The filled circles indicate residues involved in binding L-Trp, and the diamonds indicate residues involved in binding heme. The symbols for residues before helix αA are given different colors, to indicate that they are from another monomer of the tetramer.

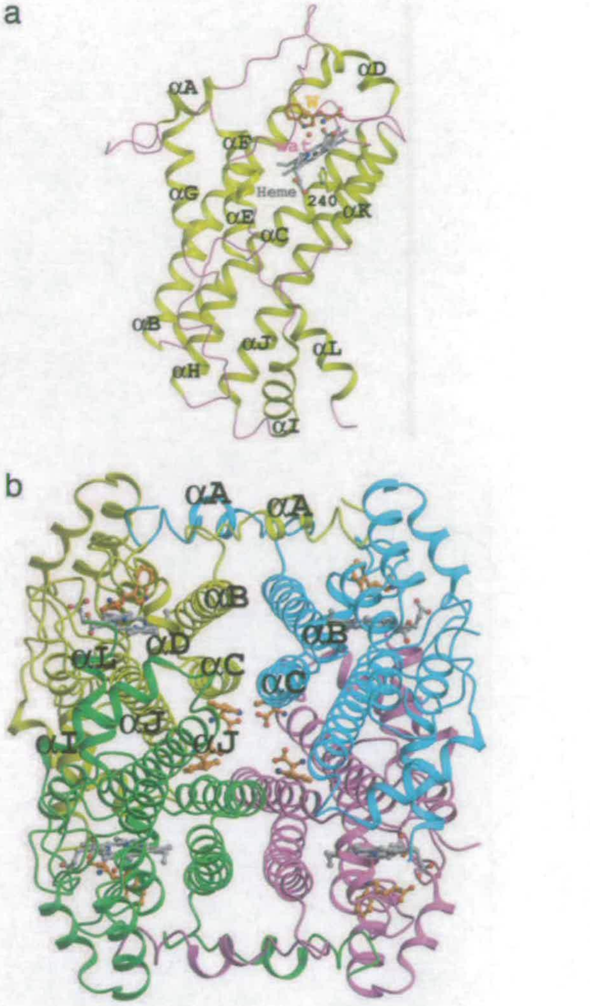

Fig. 2. The structure of TDO. (*a*) Schematic representation of the structure of the monomer of *X. campestris* TDO. The α-helices are shown in yellow and labeled. Heme is shown in gray, and L-Trp is shown in orange (labeled W). The water molecule is shown as a red sphere (labeled wat). (*b*) Schematic representation of the tetramer of *X. campestris* TDO. The four monomers are colored in yellow, cyan, violet, and green. Helices in the tetramer interface are labeled. The Trp molecules in the tetramer interface are also shown. Produced with Molscript (35) and rendered with Raster3D (36).

2*b*), which is important for the catalysis by TDO because several residues in this segment are part of the binding site for the Trp residue in the active site (see below).

Binding Mode of the L-Trp Substrate to TDO. Our structure of the binary complex defines the molecular mechanism for the recognition of the L-Trp substrate by TDO. Clear electron density was observed for heme and L-Trp in the active site based on the crystallographic analysis at 1.6-Å resolution (Fig. 3*a*). The L-Trp substrate is located in a pocket over the distal face of the heme, having interactions with residues in helices αB and αD, and the αD–αE and αJ–αK loops (Figs. 1*b* and 3*b*). The carboxylate group of Trp is recognized by bidentate ion-pair interactions with the side chain of Arg 117 (in helix αD). The carboxylate group is also hydrogen-bonded to the side chain hydroxyl of Tyr113 (helix αD) and the main chain amide of Thr 254 (αJ-αK loop). The ammonium ion of L-Trp is recognized by the 7-propionate side chain of the heme group (Fig. 3*b*), and it is also hydrogen-bonded to the side chain hydroxyl of Thr 254. The indole ring is located ≈3.5 Å above and perpendicular to the heme and is held in place by van der Waals interactions with the side chains of Phe 51 (helix αB) and several other hydrophobic residues, including Tyr 24, Tyr 27, and Leu 28 from the N-terminal segment of another monomer of the tetramer (Fig. 3*b*). In addition, the N1 nitrogen of the indole ring is hydrogen-bonded to the side chain of His 55 (helix αB) (Fig. 3*b*).

A water molecule is present in the active site of this binary complex (Fig. 3*a*), hydrogen-bonded to the ammonium ion of L-Trp and the main-chain amide of residue Gly 125 (Fig. 3*b*). The water is 3.5 Å from the ferrous atom in the heme, too far for ligating interactions. The iron atom is still 0.3 Å out of the plane of the heme, on the side of the proximal His 240 ligand (SI Fig. 5).

The crystal was exposed to a solution saturated with nitric oxide (NO) before being flash-frozen, but we did not observe the binding of this dioxygen analog in the structure. This is confirmed by our structure of the binary complex with 6-fluoro-Trp, which was not exposed to NO but contained the same density for the water molecule (SI Fig. 6). The structure of the 6-fluoro-Trp binary complex is essentially identical to that of the L-Trp binary complex (SI Fig. 6). NO probably dissociated from the heme during the cryofreezing manipulations in the anaerobic box.

Induced-Fit Behavior of TDO. Our structural information suggests that TDO is an induced-fit enzyme. Although the active site

Table 1. Summary of crystallographic information

Protein	TDO (holoenzyme)	TDO (holoenzyme)	TDO (holoenzyme)	TDO (apoenzyme)	SO4414 (holoenzyme)	SO4414 (apoenzyme)
Ligand	L-Trp	6-fluoro-Trp	None	None	None	None
Maximum resolution, Å	1.6	1.8	2.7	2.7	2.4	2.3
R_{merge}, %*	6.9 (52.7)	8.6 (60.9)	13.0 (32.3)	16.6 (74.0)	10.4 (63.0)	6.6 (30.6)
Beam line	ESRF BM14	ESRF BM14	NSLS X4A	APS 21BM	NSLS X4A	NSLS X4A
Completeness, %	87 (65)	87 (61)	72 (54)	82 (68)	83 (60)	87 (71)
R factor, %†	17.1 (18.9)	16.6 (17.9)	25.7 (25.7)	25.0 (32.1)	21.7 (23.5)	23.4 (26.7)
Free R factor, %	18.9 (22.0)	18.4 (21.1)	26.3 (26.2)	29.4 (35.1)	22.5 (24.1)	27.5 (31.5)
rms deviation in bond lengths, Å	0.005	0.005	0.008	0.011	0.007	0.006
rms deviation in bond angles, °	1.0	1.0	1.2	1.6	1.1	1.0
Most-favored region, %	92	91	89	86	92	91

*$R_{merge} = \Sigma_h \Sigma_i |I_{hi} - \langle I_h \rangle| / \Sigma_h \Sigma_i I_{hi}$. The numbers in parentheses are for the highest-resolution shell.

†$R = \Sigma_h |F_h^o - F_h^c| / \Sigma_h F_h^o$.

pocket is well defined in the binary complex (Fig. 3*b*), the αJ–αK loop, which helps to form the walls of this pocket, is disordered in the free enzyme, and the αD-αE loop has a somewhat different conformation (Fig. 3*c*; and see SI Fig. 7). Moreover, the Arg 117 side chain assumes a different conformation in the free enzyme (Fig. 3*c*). Upon recognition of the L-Trp substrate, a complex and extensive network of interactions is established (Fig. 3*b*), thus stabilizing the active site region. Although this region is exposed to the solvent in the free enzyme, it is completely shielded from the solvent in the binary complex, and only the carboxylate group of the 6-propionate of heme is visible on the surface.

Additional evidence for the induced-fit behavior is observed in the active site of the second TDO monomer in the asymmetric unit. The binding mode of the L-Trp substrate is very different in this monomer (Fig. 3*d*; and see SI Fig. 7). The Trp side chain is not positioned as deeply into the pocket, and the hydrogen bond between the ring nitrogen and the side chain of His 55 is lost (distance of 3.8 Å). Both nitrogen atoms are instead hydrogen-bonded to a water molecule, located 3.5 Å from the heme iron but at a position distinct from that of the water in the active site of the other monomer (Fig. 3*d*). This conformation may also be stabilized by crystal packing interactions, as the 7-propionate of heme is ion-paired with an Arg residue from another TDO tetramer in the crystal. The main chain atoms of the Trp substrate appear to be disordered, because no clear electron density was observed for them (Fig. 3*e*). Consistent with this finding, the αJ–αK loop is disordered in this molecule, similar to that in the free enzyme (Fig. 3*d*). This complex may represent an initial stage in the formation of the Michaelis complex of TDO. Proper positioning of the L-Trp substrate for catalysis would lead to the recognition of its main chain atoms and the ordering of the αJ–αK loop.

Implications for Substrate Binding by IDO. Our structure of the binary complex of TDO also has significant implications for substrate recognition by the IDOs. The rms distance for 201 structurally equivalent Cα atoms between TDO and the large domain of human IDO (PDB entry 2D0T) (14) is 3.1 Å (SI Fig. 8), calculated with the program Dali (17). Despite sharing only 10% overall sequence identity, key active-site residues are similar in TDO and IDO (Fig. 1*b*; and see SI Table 4), and L-Trp may have the same binding mode to the active site of IDO (SI Fig. 9). Ionic interactions that are important for recognizing the L-Trp ammonium ion and carboxylate group are conserved in IDO (Arg 231 and 7-propionate), explaining why L-Trp is a much better substrate than D-Trp for IDO. At the same time, hydrogen-bonding interactions to these atoms may be absent in IDO, because Tyr 113 of TDO is replaced by Phe 226 in IDO (SI Fig. 9), and the Thr 254 residue may not have an equivalent in IDO because the αJ–αK loop, disordered in the IDO structure (SI Fig. 9) (14), has highly divergent sequences in IDO compared with TDO (Fig. 1*b*). Therefore, IDO may have weaker interactions with tryptophan, which may be the reason why it cannot completely distinguish among the indoleamine substrates.

The structure comparison explains why 1-methyltryptophan is a micromolar inhibitor of IDO (18) but is essentially inactive against TDO (10). The N1 atom is directly hydrogen-bonded to the His 55 side chain in TDO (Fig. 3*b*), and its methylation will cause steric clash with this residue. In comparison, His 55 is replaced by Ser 167 in IDO (SI Table 4), which creates a small pocket that can accommodate the 1-methyl group (SI Fig. 9).

Structural similarity is also observed with the SO4414 protein from *S. oneidensis* (SI Fig. 8) (16), with an rms distance of 4.4 Å for 206 equivalent Cα atoms, suggesting that SO4414 may also be a dioxygenase. Moreover, the structure contains an extra domain that is formed by residues at the N terminus, similar to the small domain in human IDO (SI Fig. 8). In contrast to human IDO, SO4414 is a tetramer but with a different organization compared with that of TDO (SI Fig. 10). Our biochemical efforts so far have not been able to demonstrate IDO (or TDO) activity for this protein, suggesting that SO4414 may prefer a different substrate for oxygenation.

A Model for the Michaelis Complex. To help provide further insight into the catalysis by these enzymes, we built a model for the Michaelis complex, by placing one oxygen atom (O1) of the dioxygen substrate directly over the heme iron, at a distance of 2.1 Å (Fig. 4*a*). The distal oxygen atom (O2) was placed such that the O1–O2 bond is parallel to the C2–C3 bond of indole ring, giving a Fe–O1–O2 angle of 135°. This conformation places the O2 atom within 0.5 Å of the water molecule observed in our structure (Fig. 4*a*), suggesting that this water should be ejected from the active site upon dioxygen binding. The active site is therefore completely devoid of solvent molecules in this Michaelis complex.

The modeled dioxygen-binding mode reveals the activation mechanism of this substrate for the reaction. It has been established that TDO has an ordered catalytic cycle in which the protein first binds L-Trp to the ferrous form, and then binding of dioxygen is facilitated, and nucleophilic attack from the substrate C3 is initiated (3, 13, 19). In the model, the distal oxygen atom interacts with the L-Trp ammonium moiety and the backbone amide nitrogen of Gly 125 (Fig. 4*a*). The Lewis acidity

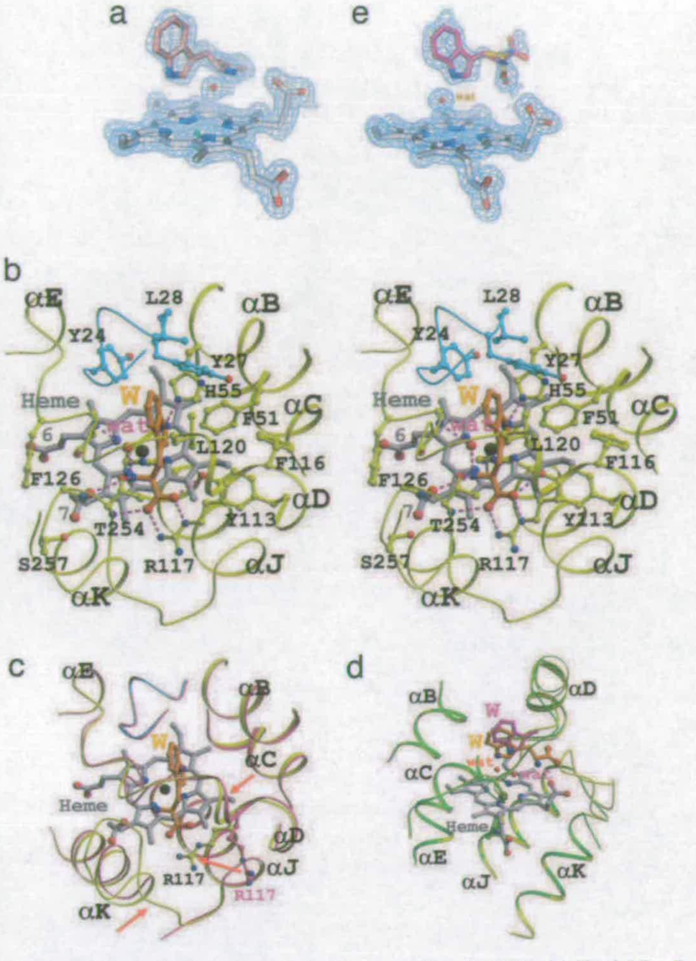

Fig. 3. Molecular basis for substrate recognition by TDO. (*a*) Final $2F_o - F_c$ electron density at 1.6-Å resolution for heme, L-Trp, and a water in the active site. Contoured at 1σ. (*b*) Stereo drawing showing the active site of *X. campestris* TDO in the binary complex with L-Trp. The segment in cyan is from another monomer of the tetramer. Hydrogen-bonding interactions are indicated with dashed lines in magenta. (*c*) Overlay of the structures of the free enzyme (in orchid) and the binary complex (yellow and cyan) in the active-site region. Regions of conformational differences are indicated with the red arrows. (*d*) Overlay of the active-site region of the second monomer (in green) and that of the first monomer (in yellow). Only the side-chain atoms of Trp are shown in the second monomer (in magenta). (*e*) Final $2F_o - F_c$ electron density at 1.6-Å resolution for heme, L-Trp, and a water in the active site of the second TDO molecule in the crystal. Contoured at 1σ. Two conformations for the main chain atoms are shown, but neither fit the density well. For the stereo version of *c* and *d*, please see SI Fig. 7. Produced with Molscript (35) and rendered with Raster3D (36).

of the hydrogen-bonding donors, coupled with the electron-withdrawing nature of the heme, would increase the electrophilicity of the bound dioxygen and render it more susceptible to nucleophilic attack by the substrate C3 atom. The increased hydrophobicity of the active site upon the exclusion of water would also aid the stabilization of an oxyferrous species. Studies with heme oxygenase suggest that the hydrogen-bonding interactions to the dioxygen substrate may also help to prevent its heterolysis (20), and the exclusion of water probably removes a hydrogen-bond competitor to the dioxygen. After the initial attack by the C3 atom, the reaction may proceed via a Criegee rearrangement or a dioxetane intermediate (SI Fig. 11). In the model, the O1–O2 atoms are in a trans configuration relative to the C2–C3 atoms of L-Trp (Fig. 4*a*), which may favor the Criegee rearrangement pathway (SI Fig. 11) (19). The Criegee pathway is also favored based on chemical, thermodynamic, and quantum mechanical considerations (3).

Our model for the Michaelis complex shows that the O1 atom is 2.6 Å from the N1 atom of L-Trp and therefore can act as the general base to extract the proton from the N1 atom (SI Fig. 11) (19). The N1 atom is hydrogen-bonded to His 55 in TDO. However, our biochemical studies show that the k_{cat} of TDO is relatively insensitive to pH over the range examined (pH 6 to pH 8) (Fig. 4*b*), and the H55A mutant had only a 10-fold decrease in the k_{cat} (Table 2), suggesting that this residue is not essential for catalysis, consistent with its replacement with a Ser residue in IDO. On the other hand, the K_m shows a marked increase at lower pH (Fig. 4*b*), probably because of the protonation of this residue.

An Allosteric Binding Site in the Tetramer Interface. We also observed the binding of four L-Trp residues to an allosteric site in the interface of the tetramer (Fig. 2*b*), with well defined electron density (SI Fig. 12). The L-Trp residue appears to be recognized specifically by the enzyme in this pocket (SI Fig. 12). There have been reports of allosteric activation by the substrate L-Trp (21, 22), and our observations offer a possibility for this effector site. Unfortunately, our kinetic studies so far have not shown any allosteric effects with *X. campestris* TDO. This site is not occupied in the 6-fluoro-Trp complex, possibly because of the lower concentration of this compound in the crystallization solution.

Biochemical Studies Confirm the Structural Observations. *X. campestris* TDO has robust catalytic activity toward L-Trp and 6-fluoro-Trp but is inactive toward D-Trp, tryptamine or indolepropionic acid (Table 2), confirming its designation as a TDO. In fact, D-Trp is a weak, competitive inhibitor of the enzyme at high concentrations (Table 2). Our binding data show that D-Trp has much lower affinity for the enzyme than L-Trp (Table 2), consistent with our structural information and explaining why D-Trp cannot be oxygenated by TDO.

The biochemical studies also provide direct evidence for the induced-fit behavior of TDO. There is a large increase in the affinity of the enzyme for L-Trp when the heme iron is reduced (K_d [ferric Fe(III) heme] = 3.8 mM, whereas K_d [ferrous Fe(II) heme] = 4.1 μM) (Table 2). The electrochemistry data show a large, positive shift in reduction potential (+136 mV) in the presence of 15 mM L-Trp (Fig. 4*c*). In fact, the shift in reduction potential almost perfectly correlates with the increase in affinity for L-Trp on reduction, both giving an estimated ΔΔG of 15 kJ/mol. These data show that there is a significant stabilization of the ferrous form when substrate is bound. This stabilization could also play a physiological role to keep the protein reduced, and therefore active, when L-Trp is present.

Our structural studies have defined the binding mode of the substrate L-Trp to TDO, revealing the structural basis for the stereospecificity of this important enzyme. The induced-fit behavior of TDO, confirmed by our biophysical studies, appears crucial for the exclusion of water from the active site and for stabilizing the enzyme in the presence of the substrates. Finally, structural comparisons among these enzymes reveal the striking evolutionary conservation of the heme-dependent dioxygenases.

Materials and Methods

The experimental protocols are summarized here. More detailed information can be found in *SI Materials and Methods*.

Protein Expression and Purification. Full-length *X. campestris* TDO (NESG ID XcR13) and *S. oneidensis* SO4414 (NESG ID SoR52) were cloned into a pET-21d (Novagen, San Diego, CA) derivative, with a C-terminal hexahistidine tag, and overexpressed at 17°C in *Escherichia coli* BL21(DE3) pMGK cells. Hemin (7 μM

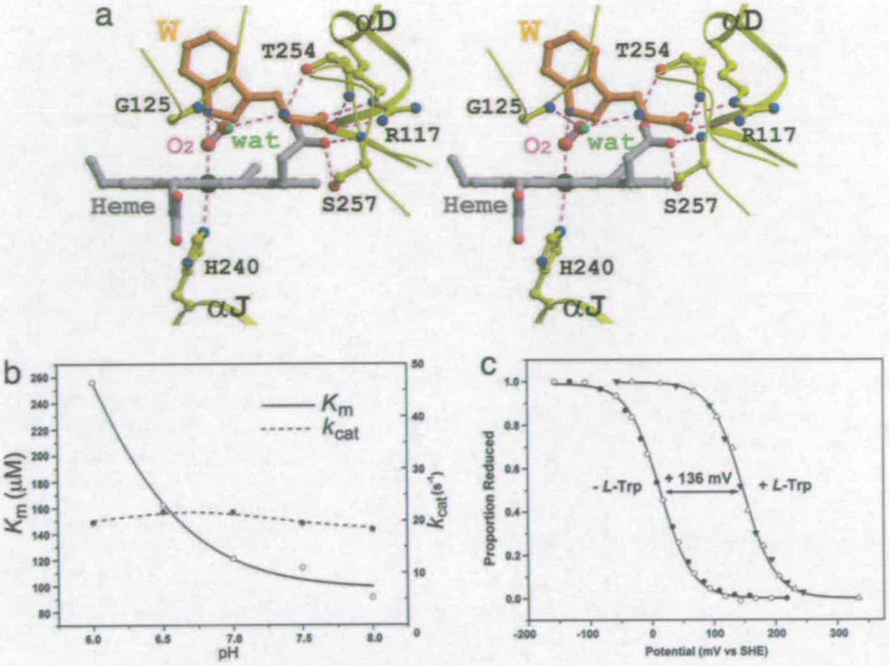

Fig. 4. Molecular insights into the catalysis by TDO. (*a*) Model of the Michaelis complex. The water molecule is shown as a small sphere in green. Produced with Molscript (35) and rendered with Raster3D (36). (*b*) The pH dependence of the k_{cat} and K_m values of *X. campestris* TDO. (*c*) The presence of L-Trp causes a large, positive shift in the reduction potential of TDO. SHE, standard hydrogen electrode.

final concentration) was included in the media for preparation of the holoenzyme samples (23). The protein was purified by using nickel-affinity and gel-filtration chromatography.

Point mutations were created with the QuikChange II site-directed mutagenesis kit (Stratagene, La Jolla, CA). The mutations and their associated ORFs were verified by DNA sequence analysis.

Protein Crystallization. To obtain the structure of TDO in the ferrous state, the protein was reduced by the addition of sodium dithionite, and all steps were performed in an anaerobic glove box (Belle Technology, Dorset, U.K.), with the O_2 concentration maintained <2 ppm. Excess sodium dithionite was removed by gel filtration (Sephadex G25 column) before crystallization. Crystals of TDO were grown by the sitting-drop vapor diffusion method with a well solution comprising 100 mM Mes (pH 6.3), 10–12% (wt/vol) PEG 4000, 60 mM $MnCl_2$, 10 mM sodium dithionite, and 2 mM L-Trp. Before mounting in nylon loops and flash-freezing in liquid nitrogen, crystals were immersed in a cryoprotectant solution composed of mother liquor (with L-Trp concentration increased to 50 mM) supplemented with 23% (vol/vol) glycerol and bubbled with nitric oxide for 15 min before use.

Data Collection and Processing. X-ray diffraction data were collected at the X4A beam line of National Synchrotron Light Source (Brookhaven National Laboratory, Upton, NY), the 21BM beam line at Advanced Photon Source (Argonne National Laboratory, Argonne, IL), and the BM14 beam line at the

Table 2. Summary of kinetic data on *X. campestris* TDO

				K_d	
Enzyme	Substrate	k_{cat} (s^{-1})	K_m, μM	Ferric heme, mM	Ferrous heme, μM
Wild type					
	L-Trp	19.5 ± 1.2	114 ± 1	3.84 ± 0.14	4.12 ± 0.24
	D-Trp	0	16.5 mM ± 3.3*	>50†	NC
	6-F-D/L-Trp	37.3 ± 0.6	186 ± 12	2.45 ± 0.42	<1†
	5-F-D/L-Trp	2.40 ± 0.10	100 ± 6	1.51 ± 0.08	<1‡
	Indolepropionic acid	0	0	>10†	126 ± 11
	O_2§	35.4 ± 0.9	119 ± 2	0	NA
H55A mutant	L-Trp	2.86 ± 0.10	133 ± 7	ND	3.7 ± 1.3

NA, K_d for O_2 cannot be measured in the absence of substrate because of oxidation or in the presence of substrate because of turnover; NC, No spectral change detected; ND, not done.

*Inhibitory constant, K_i.

†Although a spectral change was evident, substrate solubility prevented accurate measurement of K_d. Values were estimated based on the maximum substrate concentration attainable.

‡Binding was too tight to be measured. Values quoted represent the minimum K_d that can be measured under standard assay conditions.

§The peak positions of the oxyferrous complex (O_2-TDO) are at 420 nm, 548 nm, and 578 nm.

European Synchrotron Radiation Facility (Grenoble, France). The diffraction images were processed and scaled with the HKL package (24). The data-processing statistics are summarized in Table 1, and more complete information can be found in SI Table 3.

Structure Determination and Refinement. The structures of the apo enzymes of TDO and SO4414 were determined by the selenomethionyl single-wavelength anomalous diffraction method (15). The selenium sites were located with SnB (25), and the reflection phases were calculated with Solve/Resolve (26). The structures of the holoenzymes and the ternary complex were determined by the molecular-replacement method, with the programs COMO (27) and AMoRe (28). The atomic models were built with the program XtalView (29) and TURBO-FRODO (30), and the structure refinement was carried out with CNS (31).

Electronic Spectroscopy, Steady-State Assays, and Dissociation Constant Measurements. Electronic absorption spectra were recorded by using a Cary 50-Probe UV-Visible spectrophotometer at 25°C. Assays for the steady-state turnover (at pH 7.5) of L-Trp and derivatives were performed as described (32, 33), except that substrate concentrations of 0–15 mM were used. The kinetic data were fitted to the Michaelis–Menten equation. The pH dependence of the steady-state kinetics was determined in the same manner, by using phosphate (pH 6.0–8.0) and Tris (pH 8.0–9.0) buffers. The electronic absorption spectra of the steady state were recorded by using a stopped-flow spectrophotometer (SX.17MV; Applied-Photophysics, Surrey, U.K.) in conjunction with a diode array detector, housed in an anaerobic glove box ([O_2], <5 ppm; Belle Technology).

OTTLE Electrochemistry. Anaerobic potentiometric titrations were carried out as described (34) at 25°C by using a modified quartz EPR OTTLE cell. Titrations were performed in both the absence and presence of L-Trp (15 mM), and the heme reduction potentials were determined by fitting the data to the Nernst equation for a single-electron process by using Origin software (MicroCal, Northampton, MA). Reduction potentials are quoted versus the standard hydrogen electrode.

We thank Randy Abramowitz and John Schwanof at the National Synchrotron Light Source (Brookhaven National Laboratory, Upton, NY) and Hassan Belrhali at the European Synchrotron Radiation Facility (Grenoble, France) for setting up the beam lines and G. DeTitta of Hauptman Woodward Research Institute (Buffalo, NY) for crystallization screening. This research was supported by Grants P50 GM62413 and U54 GM074958 from the Protein Structure Initiative of the National Institutes of Health.

1. Yoshida R, Hayaishi O (1987) *Methods Enzymol* 142:188–195.
2. Takikawa O (2005) *Biochem Biophys Res Commun* 338:12–19.
3. Sono M, Roach MP, Coulter ED, Dawson JH (1996) *Chem Rev* 96:2841–2887.
4. Mellor A (2005) *Biochem Biophys Res Commun* 338:20–24.
5. Munn DH, Zhou M, Attwood JT, Bondarev I, Conway SJ, Marshall B, Brown C, Mellor AL (1998) *Science* 281:1191–1193.
6. Mellor AL, Munn DH (2004) *Nat Rev Immunol* 4:762–774.
7. Grohmann U, Fallarino F, Puccetti P (2003) *Trends Immunol* 24:242–248.
8. Uyttenhove C, Pilotte L, Theate I, Stroobant V, Colau D, Parmentier N, Boon T, van den Eynde BJ (2003) *Nat Med* 9:1269–1274.
9. Schwarcz R (2004) *Curr Opin Pharmacol* 4:12–17.
10. Muller AJ, DuHadaway JB, Donover PS, Sutanto-Ward E, Prendergast GC (2005) *Nat Med* 11:312–319.
11. Miller CL, Llenos IC, Dulay JR, Weis S (2006) *Brain Res* 1073–1074, 25–37.
12. Platten M, Ho PP, Youssef S, Fontoura P, Garren H, Hur EM, Gupta R, Lee LY, Kidd BA, Robinson WH, *et al.* (2005) *Science* 310:850–855.
13. Littlejohn TK, Takikawa O, Truscott RJW, Walker MJ (2003) *J Biol Chem* 278:29525–29531.
14. Sugimoto H, Oda S-I, Otsuki T, Hino T, Yoshida T, Shiro Y (2006) *Proc Natl Acad Sci USA* 103:2611–2616.
15. Hendrickson WA (1991) *Science* 254:51–58.
16. Daraselia N, Dernovoy D, Tian Y, Borodovsky M, Tatusov R, Tatusova T (2003) *OMICS* 7:171–175.
17. Holm L, Sander C (1993) *J Mol Biol* 233:123–138.
18. Cady SG, Sono M (1991) *Arch Biochem Biophys* 291:326–333.
19. Terentis AC, Thomas SR, Takikawa O, Littlejohn TK, Truscott RJW, Armstrong RS, Yeh S-R, Stocker R (2002) *J Biol Chem* 277:15788–15794.
20. Unno M, Matsui T, Chu GC, Couture M, Yoshida T, Rousseau DL, Olson JS, Ikeda-Saito M (2004) *J Biol Chem* 279:21055–21061.
21. Ishimura Y, Makino R, Iizuka T (1980) *Adv Enzyme Regul* 18:291–302.
22. Sono M (1989) *Biochem* 28:5400–5407.
23. Littlejohn TK, Takikawa O, Skylas D, Jamie JF, Walker MJ, Truscott RJW (2000) *Protein Expr Purif* 19:22–29.
24. Otwinowski Z, Minor W (1997) *Methods Enzymol* 276:307–326.
25. Weeks CM, Miller R (1999) *J Appl Crystallogr* 32:120–124.
26. Terwilliger TC (2003) *Methods Enzymol* 374:22–37.
27. Jogl G, Tao X, Xu Y, Tong L (2001) *Acta Crystallogr D* 57:1127–1134.
28. Navaza J (1994) *Acta Crystallogr A* 50:157–163.
29. McRee DE (1999) *J Struct Biol* 125:156–165.
30. Roussel A, Cambillau C (1991) *TURBO-FRODO. Silicon Graphics Geometry Partners Directory* 86 (Silicon Graphics, Mountain View, CA).
31. Brunger AT, Adams PD, Clore GM, DeLano WL, Gros P, Grosse-Kunstleve RW, Jiang J-S, Kuszewski J, Nilges M, Pannu NS, *et al.* (1998) *Acta Crystallogr D* 54:905–921.
32. Ishimura Y (1970) *Methods Enzymol* 17A:429–434.
33. Papadopoulou ND, Mewies M, McLean KJ, Seward HE, Svistunenko DA, Munro AW, Raven EL (2005) *Biochem* 44:14318–14328.
34. Ost TW, Clark JP, Anderson JLR, Yellowlees LJ, Daff S, Chapman SK (2004) *J Biol Chem* 279:48876–48882.
35. Kraulis PJ (1991) *J Appl Crystallogr* 24:946–950.
36. Merritt EA, Bacon DJ (1997) *Methods Enzymol* 277:505–524.

Biochemistry **2008,** *47,* 10677–10684

Histidine 55 of Tryptophan 2,3-Dioxygenase Is Not an Active Site Base but Regulates Catalysis by Controlling Substrate Binding[‡]

Sarah J. Thackray,[§] Chiara Bruckmann,[§] J. L. Ross Anderson,[§] Laura P. Campbell,[§] Rong Xiao,[∥] Li Zhao,[∥]
Christopher G. Mowat,[§] Farhad Forouhar,[⊥] Liang Tong,[⊥] and Stephen K. Chapman[*,§]

EaStCHEM, School of Chemistry, University of Edinburgh, West Mains Road, Edinburgh EH9 3JJ, U.K., Department of Biological Sciences, Northeast Structural Genomics Consortium, Columbia University, New York, New York 10027, and Center for Advance Biotechnology and Medicine, Rutgers University, Piscataway, New Jersey 08854

Received June 27, 2008; Revised Manuscript Received August 6, 2008

ABSTRACT: Tryptophan 2,3-dioxygenase (TDO) from *Xanthomonas campestris* is a highly specific heme-containing enzyme from a small family of homologous enzymes, which includes indoleamine 2,3-dioxygenase (IDO). The structure of wild type (WT TDO) in the catalytically active, ferrous (Fe^{2+}) form and in complex with its substrate L-tryptophan (L-Trp) was recently reported [Forouhar et al. (2007) *Proc. Natl. Acad. Sci. U.S.A. 104*, 473–478] and revealed that histidine 55 hydrogen bonds to L-Trp, precisely positioning it in the active site and implicating it as a possible active site base. In this study the substitution of the active site residue histidine 55 by alanine and serine (H55A and H55S) provides insight into the molecular mechanism used by the enzyme to control substrate binding. We report the crystal structure of the H55A and H55S mutant forms at 2.15 and 1.90 Å resolution, respectively, in binary complexes with L-Trp. These structural data, in conjunction with potentiometric and kinetic studies on both mutants, reveal that histidine 55 is not essential for turnover but greatly disfavors the mechanistically unproductive binding of L-Trp to the oxidized enzyme allowing control of catalysis. This is demonstrated by the difference in the K_d values for L-Trp binding to the two oxidation states of wild-type TDO (3.8 mM oxidized, 4.1 μM reduced), H55A TDO (11.8 μM oxidized, 3.7 μM reduced), and H55S TDO (18.4 μM oxidized, 5.3 μM reduced).

Oxidative cleavage of the L-tryptophan (L-Trp)[1] pyrrole ring and the insertion of molecular oxygen to produce *N*-formylkynurenine is the first and rate-limiting step in the kynurenine pathway and is catalyzed by tryptophan 2,3-dioxygenase (TDO) and indoleamine 2,3-dioxygenase (IDO) (*2, 3*). The kynurenine pathway processes 95% of L-Trp utilized by humans, leading ultimately to the formation of nicotinamide adenine dinucleotide (NAD^+), an essential coenzyme (*4*). Kynurenine pathway metabolites have been implicated in a number of diseases ranging from neurological disorders, such as cerebral malaria and multiple sclerosis, to cataract formation (*5, 6*). Recent findings have implicated tryptophan catabolism via the kynurenine pathway in immune tolerance, including immune suppression in maternal fetal tolerance and the immune escape of cancers (*7–10*). These properties make elucidation of the precise catalytic mechanism of these enzymes extremely important.

TDO and IDO belong to a little-characterized family of dioxygenases that occurs in both prokaryotes and eukaryotes (*11*). These enzymes have homologous 3-D structures but dissimilar primary structures, with sequence identity often less than 10% between family members (*12*). First identified in 1936 (*13*), TDO is mainly found in the liver of mammals but has also been recently identified in mammalian mucous membranes, epididymis, and brain (*14, 15*). The enzyme discussed here is a prokaryotic TDO from *Xanthomonas campestris* (the causative agent of black rot in cabbages), which shares 34% sequence identity with human TDO. The enzyme is a homotetramer that displays high substrate specificity, catalyzing the oxidation of L-Trp, 5-F-Trp, and 6-F-Trp (*1*). In contrast, IDO is found throughout the body in mammals, except for in the liver, and no prokaryotic IDO protein has yet been identified. IDO is monomeric and catalyzes the dioxygenation of L-Trp, D-Trp, serotonin, tryptamine, and 5-OH-Trp, displaying less substrate specificity than TDO (*11, 16*). The crystal structures of WT *X. campestris* TDO (*1, 17*) and human IDO (*12*) have been published recently, revealing similarities between the two enzymes and allowing the identification of potentially important active site residues.

The catalytic mechanisms employed by TDO and IDO have, as yet, not been elucidated, but two proposed mechanisms for tryptophan dioxygenation are shown in Figure 1.

[‡] The atomic coordinates for H55A and H55S mutant enzymes of TDO have been deposited in the Protein Data Bank, entries 3BK9 and 3E08, respectively.

[*] To whom correspondence should be addressed. E-mail: S.K.Chapman@ed.ac.uk. Tel: +44 131 650 4760. Fax: +44 131 650 6453.

[§] University of Edinburgh.

[∥] Rutgers University.

[⊥] Columbia University.

[1] Abbreviations: TDO, tryptophan 2,3-dioxygenase; IDO, indoleamine 2,3-dioxygenase; L-Trp, L-tryptophan; 5-F-Trp, 5-fluoro-DL-tryptophan; 6-F-Trp, 6-fluoro-DL-tryptophan; WT, wild type; H55A, histidine 55 → alanine; H55S, histidine 55 → serine; SHE, standard hydrogen electrode; OTTLE, optically transparent thin-layer electrochemistry.

10.1021/bi801202a CCC: $40.75

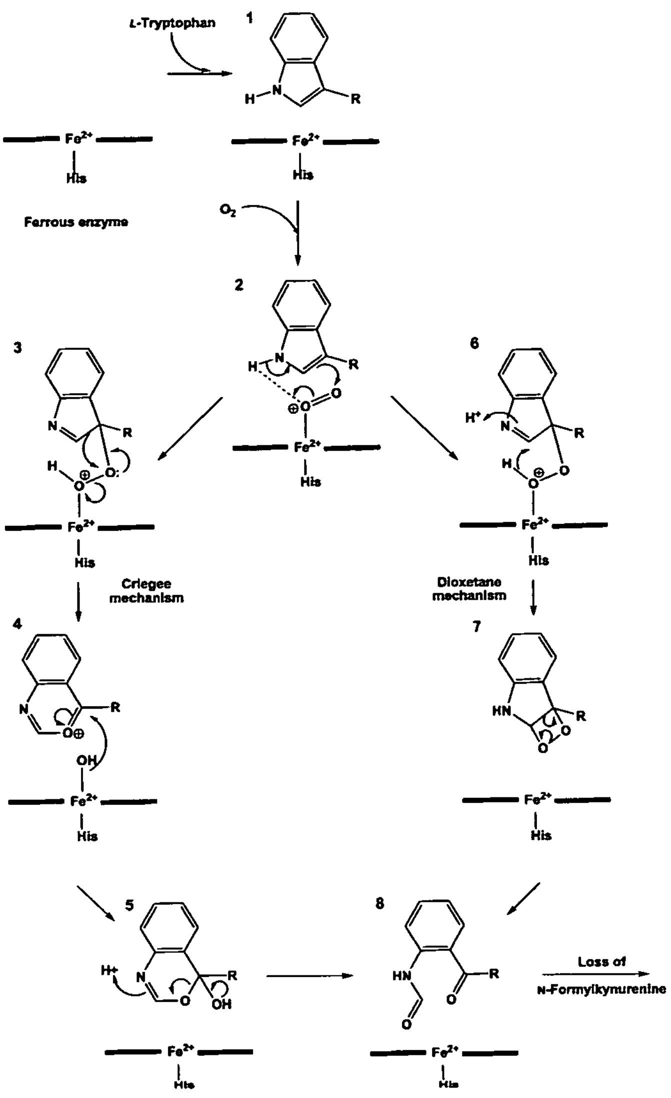

FIGURE 1: Catalytic mechanism proposed for L-tryptophan dioxygenation by TDO. The figure displays an ionic, base-catalyzed mechanism of L-Trp dioxygenation. The first substrate binds to the protein (1), followed by dioxygen binding to form the ternary complex (2). The mechanism proceeds by the formation of a hydroperoxide intermediate (3 and 6), which can undergo two different rearrangements to form the product, *N*-formylkynurenine (8), a Criegee rearrangement (4 and 5), or a dioxetane rearrangement (7). The product is then released leaving the protein in the active ferrous state.

It is proposed that the catalytic mechanism involves the base-catalyzed deprotonation of the indole nitrogen of the substrate. However, the structures of TDO and IDO show that while TDO contains a histidine residue in its active site, IDO does not contain any residues in its active site capable of performing base-catalyzed deprotonation. Instead, it has been proposed that proton abstraction is facilitated by a bound dioxygen molecule (Figure 2).

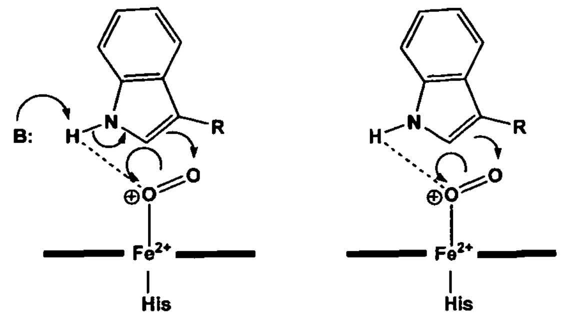

FIGURE 2: Proposed catalytic intermediates involved in proton abstraction of the indole nitrogen of L-tryptophan. The ternary enzyme−substrate−dioxygen complex can either undergo (a) a base-catalyzed proton abstraction or (b) proton abstraction by the bound dioxygen.

In the TDO active site histidine 55 hydrogen bonds to L-Trp and is implicated as the active site base. In this study we attempt to resolve the question of whether an active site base is necessary for catalytic activity in TDO. To accomplish this, histidine is replaced by alanine or serine (H55A and H55S mutants of TDO). These substitutions were chosen due to the inability of alanine to act as an active site base and the presence in IDO of a serine residue in the analogous position to histidine 55. We report the crystal structure of the H55A mutant to 2.15 Å resolution and the crystal structure of the H55S mutant to 1.90 Å resolution and relate these to electrochemical and kinetic data for the mutant enzymes.

EXPERIMENTAL PROCEDURES

Genetic Manipulation, Protein Expression, and Purification. Full-length *X. campestris* TDO (NESG (Northeast Structural Genomics Consortium) ID XcR13) was cloned into a pET-21d (Novagen, San Diego, CA) derivative with a C-terminal hexahistidine tag and overexpressed at 17 °C in *Escherichia coli* BL21(DE3) pMGK cells. Point mutations H55A and H55S were created by employing the QuikChange II site-directed mutagenesis kit (Stratagene, La Jolla, CA). Oligonucleotide primers directing mutations were designed in an automated fashion by using the Primer Prim'er program, accessible at www-nmr.cabm.rutgers.edu/bioinformatics/Primer_Primer/. The mutations and their associated ORF were verified by DNA sequence analysis (*1*).

WT TDO and its mutant forms were purified using nickel-affinity and gel-filtration chromatography. Protein and heme concentrations were determined by the Bradford and pyridine hemochrome methods, respectively (*18, 19*). For WT TDO extinction coefficients ε_{404nm} and ε_{431nm} of 180.5 (±0.1) mM^{-1} cm^{-1} and 113.0 (±0.1) mM^{-1} cm^{-1} per protomer were calculated for the ferric and ferrous enzymes, respectively (*1*). For the H55A mutant enzyme extinction coefficients ε_{405nm} and ε_{431nm} were 130.4 (±0.3) mM^{-1} cm^{-1} and 120.0 (±0.1) mM^{-1} cm^{-1} per protomer. For the H55S mutant extinction coefficients ε_{405nm} and ε_{431nm} were 132.0 (±0.3) mM^{-1} cm^{-1} and 116.0 (±0.2) mM^{-1} cm^{-1} per protomer.

Protein Crystallization and Data Collection. Crystallization of H55A and H55S TDO was carried out by hanging drop vapor diffusion at 18 °C in Linbro plates. Crystals were obtained with well solutions comprising 9−10% (w/v) PEG 1000, 80 mM MES buffer, pH 6.3, 20 mM bicine buffer, pH 9.0, 40 mM $MnCl_2$, 400 mM $MgCl_2$, 8−15 mM NaCN, and 20 mM L-Trp. Hanging drops (4 μL volume) were prepared by adding 2 μL of 8 mg mL^{-1} protein (in 50 mM Tris-HCl buffer, pH 8.0, 5 mM in EDTA) to 2 μL of well solution. Red tetragonal shaped crystals appeared after approximately 1 week, reaching full size after 2 weeks. Crystals were immersed in mineral oil prior to being mounted in nylon loops and flash cooled in liquid nitrogen. For crystals of both H55A and H55S enzymes, data sets were collected to a resolution of 2.15 and 1.90 Å, respectively, at station

10.1 at SRS Daresbury ($\lambda = 1.381$ Å for H55A TDO, $\lambda = 1.045$ Å for H55S). In both cases crystals belonged to space group $P2_1$ with unit cell parameters $a = 78.2$ Å, $b = 117.6$ Å, $c = 139.3$ Å, and $\beta = 95.7$ ° (H55A) and $a = 77.9$ Å, $b = 117.8$ Å, $c = 139.1$ Å, and $\beta = 95.7$ ° (H55S).

Data processing was carried out using the CCP4 package (*20*) and PHENIX (*21*). The wild-type TDO apoenzyme structure (PDB ID 1YW0), stripped of water, was used as the initial model. Electron density fitting was carried out using PHENIX and Turbofrodo (*22*), and structure refinement was carried out using PHENIX and Refmac (*23*).

Steady-State Kinetic Analysis and Binding Constant Assays. UV−visible spectra were recorded at 25 °C using a Cary 50-Probe UV−visible spectrophotometer. Steady-state turnover assays (at pH 7.5) for oxidation of L-Trp and fluorinated derivatives were performed as described by Ishimura (*24*), except that substrate concentrations of up to 15 mM L-Trp were used. The rate of formation of *N*-formylkynurenine was monitored by measuring the change in absorbance at 321 nm (ϵ_{321}(*N*-formylkynurenine) = 3750 $M^{-1}\ cm^{-1}$). Kinetic data were fitted to the Hill equation using Origin software (MicroCal, Northampton, MA). Dissociation constants (K_d) for binding to ferric and ferrous WT TDO and mutant enzymes were determined by established procedures in a Belle Technology anaerobic glovebox with [O_2] maintained below 5 ppm. The electronic absorption spectra at the steady state were recorded by using a stopped-flow spectrophotometer (SX.17MV; Applied-Photophysics, Surrey, U.K.) in conjunction with a diode array detector, housed in an anaerobic glovebox. The oxygen binding affinity (K_m) was measured by standard methods by adding varying concentrations of O_2 ($\leq$1 mM) to the L-Trp saturated (25 mM) assay and by calculating the steady-state parameters as described above. Oxygen concentration was determined spectrophotometrically by titrating aliquots of oxygenated buffer into a solution of electrochemically reduced methyl viologen. The subsequent change in absorbance at 540 nm (ϵ_{540}(methyl viologen) = 13000 $M^{-1}\ cm^{-1}$) due to reduction of molecular oxygen was used to calculate [O_2] (*1*).

OTTLE Electrochemistry. Anaerobic potentiometric titrations on WT TDO and mutant enzymes were carried out as previously described (*1, 25*) at 25 °C using a modified quartz EPR OTTLE cell, with the exception that 100 mM Tris-HCl buffer, pH 7.5, and 300 mM KCl (with or without 10% glycerol) buffer was used. A range of mediators were added (2-hydroxy-1,4-naphthoquinone (−145 mV vs SHE), 5-hydroxy-1,4-naphthoquinone (−3 mV), phenazine ethosulfate (+55 mV), phenazine methosulfate (+82 mV), and 1,2-naphthoquinone (+135 mV)) to ensure efficient reduction and reoxidation of the protein. Titrations were performed in both the absence and presence of substrate for WT TDO (15 mM L-Trp), the H55A mutant (5 mM L-Trp), and the H55S mutant (10 mM L-Trp). Heme reduction potentials were determined by fitting the data to a Nernst equation for a single-electron process using Origin software. Reduction potentials are quoted versus the standard hydrogen electrode.

RESULTS AND DISCUSSION

Crystal Structures of H55A and H55S TDO. It was possible to obtain crystals of the ferric H55A and H55S mutant enzymes in binary complex with the substrate due to the much greater affinity of L-Trp for the oxidized mutant enzymes compared to WT TDO (see below and Table 3). For H55A TDO a data set to 2.15 Å resolution was used to refine the structure to a final *R*-factor of 20.5% (R_{free} = 28.5%), while for H55S TDO data to a resolution of 1.90 Å were used to refine the structure to a final *R*-factor of 17.8% (R_{free} = 21.6%). Data collection and refinement statistics are summarized in Table 1.

Table 1: H55A and H55S Data Collection and Refinement Statistics

	H55A	H55S
resolution (Å)	59.66−2.15	17.56−1.90
total no. of reflections	312593	362159
no. of unique reflections	131764	189203
completeness (%)	96.9	93.6
$I/[\sigma(I)]$	9.5	7.3
R_{merge} (%)[a]	10.0	7.8
R_{merge} in outer shell (2.27−2.15 Å) (%)	47.4	48.0
R_{cryst} (%)[b]	20.5	17.8
R_{free} (%)[b]	28.5	21.6
rmsd from ideal values		
bond lengths (Å)	0.022	0.007
bond angles (deg)	2.004	0.952
Ramachandran analysis		
most favored (%)	91.9	92.2
additionally allowed (%)	8.1	7.8
average *B*-factor (overall) (Å^2)	23.2	23.2
average *B*-factor (substrate) (Å^2)	25.7	24.1

[a] $R_{merge} = \sum_h \sum_i |I(h) - I_i(h)| / \sum_h \sum_i I_i(h)$, where $I_i(h)$ and $I(h)$ are the *i*th and mean measurement of reflection *h*, respectively. [b] $R_{cryst} = \sum_h |F_o - F_c| / \sum_h F_o$, where F_o and F_c are the observed and calculated structure factor amplitudes of reflection *h*, respectively. R_{free} is the test reflection data set, 5% selected randomly for cross-validation during crystallographic refinement.

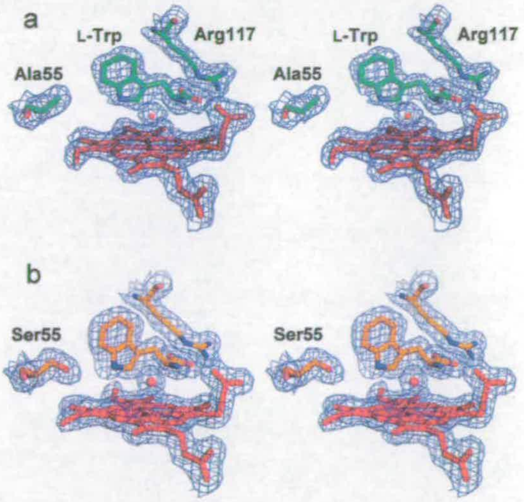

FIGURE 3: Stereoview of electron density around the heme, bound L-Trp, arginine 117, and residue 55 at the active site of (a) H55A TDO and (b) H55S TDO. The electron density map was calculated using Fourier coefficients $2F_o - F_c$, where F_o and F_c are the observed and calculated structure factors, respectively, the latter based on the final model. The contour level is 1σ, where σ is the rms electron density. This figure was generated using PYMOL (*30*).

For each of the H55A and H55S mutant enzymes the final model consists of two TDO tetramers (1 and 2), one of which (tetramer 1) is better defined than the other in the electron density map. The quality of the final electron density map around the active site of chain A of tetramer 1 of both mutant enzymes is shown in Figure 3.

In both mutant enzymes each monomer also binds one heme group and one substrate molecule. Further to this, a

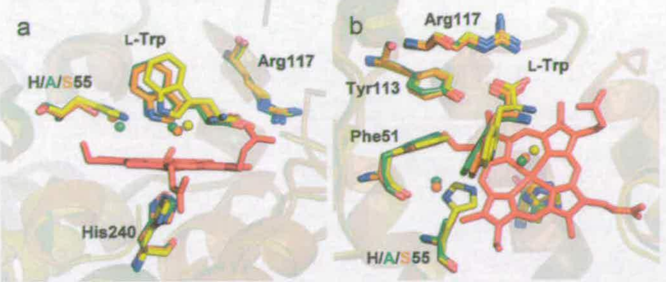

FIGURE 4: An overlay of the active site region of WT TDO (yellow), H55A TDO (green), and H55S TDO (orange) viewed from the side (a) and from above (b). The L-Trp from the H55A and H55S enzymes (in green and orange, respectively) are rotated toward alanine/serine 55 and the heme, relative to the position of the substrate in WT TDO (yellow). The H-bond between histidine 55 and the substrate is lost as a result of the substitution by alanine/serine. The position of the water molecule (water A; see Figure 5) above the heme group in H55A and H55S TDOs is slightly different than in WT enzyme due to the altered substrate binding. This figure was generated using PYMOL (*30*).

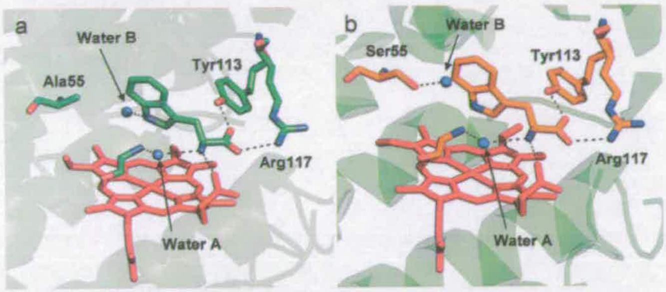

FIGURE 5: The active site of (a) H55A TDO and (b) H55S TDO. Hydrogen-bonding interactions are indicated by dashed lines. The subtly different positions of water B in the mutant enzymes can be seen. This figure was generated using PYMOL (*30*).

second L-Trp molecule is observed at the intersubunit interface close to each of chains A, B, C, D, and E in the H55A TDO structure, and in the H55S model there is one interfacial L-Trp per monomer. In addition, the H55A and H55S models contain 1026 and 1955 water molecules, respectively. The atomic coordinates have been deposited in the Protein Data Bank, accession codes 3BK9 (H55A) and 3E08 (H55S).

Binding Mode of L-Trp to H55A and H55S Mutants. The binding orientation of L-Trp at the active site of the H55A mutant enzyme is slightly different from that observed in the WT TDO structure. An overlay of the active sites of WT TDO and the H55A and H55S enzymes (based on α-C overlay) is shown in Figure 4. The bound L-Trp substrates belonging to the H55A and H55S mutant enzymes (in green and orange, respectively) are shifted toward the side chain of residue 55 relative to the position of L-Trp in the wild-type enzyme (in yellow). Due to the substitution of histidine 55 by alanine or serine the hydrogen-bonding interaction between residue 55 and the substrate indole nitrogen atom is lost. The remaining interactions between the substrate and active site residues that are observed in the wild-type enzyme are maintained in both mutant enzymes (Figure 5).

The active sites of WT TDO and both of the H55A and H55S mutant enzymes contain a water molecule above the distal face of the heme (water A in Figure 5). In all three enzymes this water is H-bonded to the ammonium group of L-Trp and the main-chain amide nitrogen of glycine 125 but is too far (≥2.7 Å) from the heme iron to be a ligand. Further to this, an additional water molecule is found in the active site of the H55A and H55S mutant enzymes (water B in Figure 5) in a position which would be sterically inhibited by the histidine 55 side chain in WT TDO. In the H55A mutant enzyme water B is H-bonded to the substrate indole nitrogen (Figure 5a), but in the H55S model water B is instead H-bonded to the side-chain hydroxyl group of serine 55 (Figure 5b), too far away (~3.4 Å) from L-Trp to maintain a hydrogen-bonding interaction.

In WT TDO the histidine 55 imidazole moiety H-bonds to a water molecule in the substrate-free ferrous state, which is displaced upon binding of substrate. The removal of the histidine side chain in either mutant enzyme would almost certainly result in the absence of a water molecule in such a position.

Steady-State Kinetics and Substrate/Substrate Analogue Binding. It has been previously reported that WT TDO shows catalytic activity toward L-Trp, 6-F-Trp, and 5-F-Trp. We have also observed activity toward 5-methyl-DL-tryptophan and 6-methyl-DL-tryptophan. H55A and H55S mutant enzymes show catalytic activity toward L-Trp, 6-F-Trp, 5-F-Trp, 5-methyl-DL-tryptophan, and 6-methyl-DL-tryptophan but no activity with any other compounds investigated. Kinetic parameters are shown in Table 2, and there is about a 7-fold decrease in k_{cat} values, compared to WT TDO, for both mutant enzymes. As previously reported, there is no inhibition of WT TDO catalytic activity on addition of 1-Me-DL-tryptophan, and the same result is obtained for the mutant enzymes (*1*). This contrasts with findings on IDO, where 1-Me-DL-tryptophan is a known inhibitor of L-Trp dioxygenation activity (*11*). Catalytic activity is observed only by the ferrous enzyme for both WT TDO and its mutant forms, in contrast to recent findings that show catalytic activity by ferric human TDO.

The substitution of histidine 55 may have been expected to render the enzyme inactive if a base is required in the catalytic cycle, but the possibility that a water molecule could be bound, in the vacant space made by the substitution of histidine 55, must be considered. This water molecule could, possibly, act as an active site base dependent on its pK_a in the active site. A water molecule is found near this position in both of the mutant enzymes, but it is not optimally aligned for the deprotonation of L-Trp. It is also located 3.3 Å away from the indole nitrogen atom, outside the range of a normal H-bonding interactions, and we propose that it plays no role in the catalytic cycle (Figure 1). These data, and the relative insensitivity of the WT TDO k_{cat} to pH (Supporting Information Table 1), support the idea that histidine 55 or a solvent molecule is not required to deprotonate the indole nitrogen atom. In IDO where the active site is devoid of solvent, the equivalent residue to histidine 55 is serine 167, which is incapable of acting as a catalytic base. Turnover still occurs, and like TDO k_{cat} is observed to be insensitive to pH (*26*).

The decrease in k_{cat} for L-Trp oxidation in both the H55A and H55S mutants may be explained by the movement of L-Trp in the active site. It can be seen from the crystal structures that for both mutants L-Trp has rotated toward the substituted amino acid (and away from the iron atom) relative to the position of L-Trp in WT TDO. The L-Trp indole ring has also shifted toward the heme (shown in Figure 4). These movements are accompanied by a slight increase in the

Table 2: Kinetic Parameters for *X. campestris* TDO Wild Type and Mutants

	WT TDO			H55A			H55S		
	k_{cat} (s^{-1})	K_m (μM)	k_{cat}/K_m	k_{cat} (s^{-1})	K_m (μM)	k_{cat}/K_m	k_{cat} (s^{-1})	K_m (μM)	k_{cat}/K_m
L-Trp[a]	19.5 ± 1.2	114 ± 1	1.711 (100)	2.86 ± 0.10	133 ± 7	0.215 (100)	2.6 ± 0.01	197 ± 2	0.132 (100)
6-F-D/L-Trp[a]	37.3 ± 0.6	186 ± 12	2.005 (117)	3.78 ± 0.10	195 ± 1	0.194 (90)	3.80 ± 0.04	546 ± 36	0.070 (53)
5-F-D/L-Trp[a]	2.40 ± 0.10	100 ± 6	0.240 (14)	0.68 ± 0.14	194 ± 25	0.035 (16)	0.80 ± 0.01	183 ± 12	0.044 (33)
6-Me-D/L-Trp[a]	41.0 ± 1.2	975 ± 48	0.421 (25)	1.65 ± 0.03	386 ± 4	0.0443 (21)	4.66 ± 0.18	1980 ± 170	0.024 (18)
5-Me-D/L-Trp[a]	3.59 ± 0.05	357 ± 12	0.101 (6)	0.40 ± 0.01	395 ± 20	0.010 (5)	1.45 ± 0.01	1302 ± 21	0.011 (8)

[a] Experiments were performed at 25 °C in 100 mM phosphate buffer, pH 7.5, by varying the concentration of the substrate. It should be noted that these rates are determined under normal atomospheric conditions; therefore, the rates determined are "apparent" for k_{cat} as oxygen is not present at a saturating level. The peak positions of the oxyferrous complex (O_2−TDO) are at 420, 548, and 578 nm, and V_{max}, K_m, and K_i are calculated using L-Trp.

Table 3: Substrate Binding to Oxidized and Reduced *X. campestris* TDO Wild Type and Mutants[a]

	TDO WT (K_d)		H55A (K_d)		H55S (K_d)	
substrate	Fe^{3+} (mM)	Fe^{2+} (μM)	Fe^{3+} (μM)	Fe^{2+} (μM)	Fe^{3+} (μM)	Fe^{2+} (μM)
L-Trp	3.84 ± 0.14	4.1 ± 0.2	11.8 ± 0.2	3.7 ± 1.3	18.4 ± 3.0	5.3 ± 1.0
6-F-D/L-Trp	1.51 ± 0.08	<1.00[b]	165 ± 44	73 ± 3	86 ± 12	6.2 ± 0.9
5-F-D/L-Trp	2.45 ± 0.42	<1.00[b]	67 ± 20	9.0 ± 1.7	73 ± 5	<5.00[b]

[a] Experiments were performed at 25 °C in 100 mM phosphate buffer, pH 7.5. Absorbance changes upon substrate binding are small (~5−10% of initial peak absorbance) but easily quantifiable due to tight substrate binding. [b] Binding was too tight to be measured. Values quoted represent the minimum K_d that can be measured under standard assay conditions.

substrate K_m values, implying a small decrease in the stability of the Michaelis complex. The rotation has resulted in the displacement of the tryptophan indole ring from the dioxygen binding site, thus decreasing overlap of the molecular orbitals involved in catalysis. The transition state for the reaction will be less stable, thus increasing the activation energy for catalysis. This will decrease the turnover rates for both mutants compared to WT TDO.

In WT TDO there is a large increase in the affinity of the enzyme for L-Trp for ferrous vs ferric enzyme ($K_d(Fe^{3+})$ = 3.8 mM, $K_d(Fe^{2+})$ = 4.1 μM) (Table 3). This is in contrast to recent findings for human TDO, where there was found to be little discrimination of binding between the ferric and the ferrous enzymes (27). For both mutant proteins this effect is essentially destroyed, with only a small increase shown in the affinity of the ferrous enzyme for L-Trp relative to ferric (Table 3). This trend in K_d is repeated for other substrates. These findings suggest that one role of histidine 55 is to disfavor substrate binding to the oxidized protein, and its removal increases binding affinity by a factor > 300. It can therefore be hypothesized that histidine 55 is responsible for controlling the binding affinity of the active site for L-Trp, effectively gating the binding of substrate to WT TDO. In this way histidine 55 greatly disfavors the mechanistically unproductive binding of L-Trp to the oxidized enzyme, promoting the productive binding of L-Trp to the reduced enzyme.

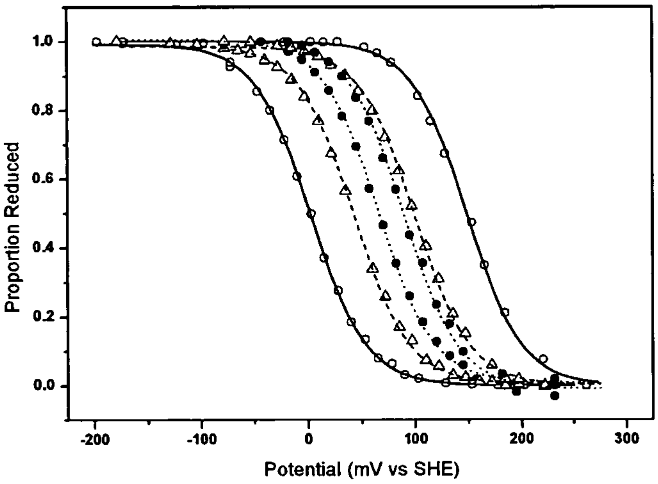

FIGURE 6: OTTLE potentiometric curves for wild-type TDO (open circles), H55A mutant (closed circles), and H55S mutant (open triangles) with (right-hand plots) and without (left-hand plots) L-Trp substrate present (±L-Trp). Each curve is produced from both reduction and oxidation of the layer of interest.

Table 4: Electrochemical Midpoint Potentials

	potential (mV vs SHE)		
	no L-Trp	+L-Trp	change
TDO WT	8 ± 5	144 ± 6	+136
H55A	64 ± 3	87 ± 2	+23
H55S	44 ± 2	101 ± 2	+57
rlTDO[a]	100	160	+60
rhIDO[b]	−30 ± 4	16 ± 3	+46

[a] See ref 29. [b] See ref 26.

Electrochemical Studies. Electrochemical data for WT TDO and the H55A mutant are shown in Figure 6, and the measured midpoint potentials are displayed in Table 4. There is a much smaller shift in the reduction potential upon binding of substrate ($\Delta E_{mid\,H55A}$ = +23 mV) ($\Delta E_{mid\,H55S}$ = +57 mV) for the mutant enzymes compared to WT TDO ($\Delta E_{mid\,WT}$ = +136 mV). The shift in reduction potential of 23 mV for the H55A mutant enzyme almost perfectly correlates with the increase in affinity for L-Trp for the ferrous vs the ferric form (K_d (Fe(II)) = 3.7 μM vs K_d (Fe(III)) = 11.8 μM), both giving an estimated $\Delta\Delta G$ of 3.5 kJ mol^{-1}. In fact, the difference in these $\Delta\Delta G$ values calculated for WT TDO and the H55A mutant enzyme is approximately 11.5 kJ mol^{-1}, within the range of energies for a single hydrogen bond. The data are less clear for H55S, with a 57 mV shift in the reduction potential on L-Trp binding. The increase in affinity for L-Trp to the ferrous H55S vs the ferric give an estimated $\Delta\Delta G$ of 5.5 kJ mol^{-1}. It is possible that the lower affinity of oxidized WT TDO for substrate may be attributed to subtle changes in the structure of the active site (in terms of the hydrogen-bonding pattern) between the oxidized and reduced enzymes. Binding of L-Trp

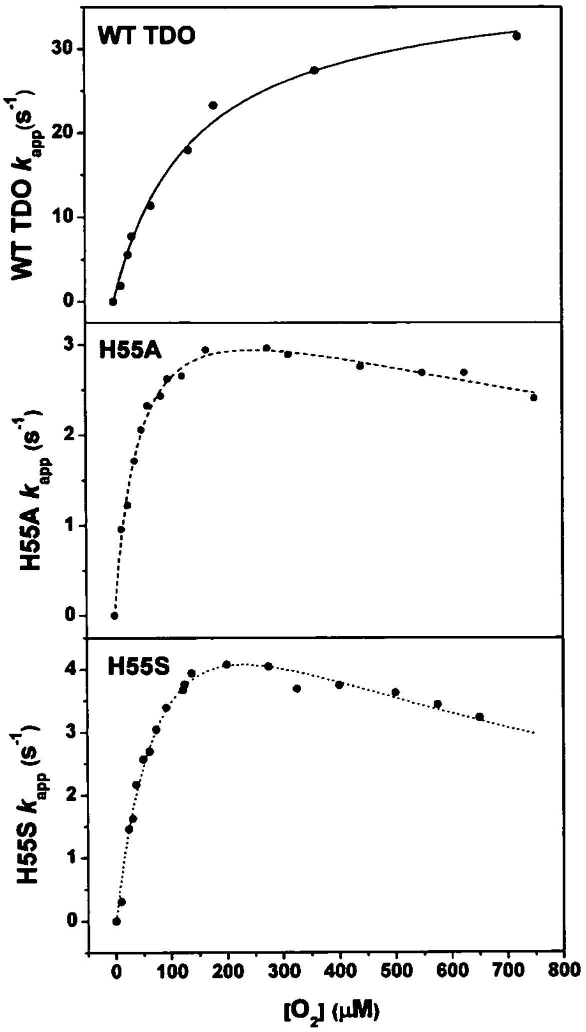

FIGURE 7: Plot of the observed steady-state turnover rate (k_{app}) versus O_2 concentration for wild-type TDO (top) and H55A (middle) and H55S (bottom) mutant forms. The maximum turnover rate (k_{max}), the Michaelis constant (K_m), and the inhibition constant (K_i (for oxygen)) are reported.

accompanies expulsion of solvent from the active site and results in the formation of a hydrogen bond between histidine 55 and the pyrrole nitrogen of the indole L-Trp moiety.

In the H55A mutant enzyme the alanine side chain is unable to form the same hydrogen bonds that histidine 55 can in WT TDO. Consequently, there may be less rearrangement of the active site hydrogen-bonding interactions necessary to allow L-Trp binding, and the K_d for substrate binding to ferric enzyme is correspondingly low. All other amino acid interactions binding L-Trp to the active site are analogous to WT TDO. Consequently, the absence of significant oxidation-state-dependent changes in the active site in H55A TDO results in decreased specificity of binding to the oxidized or reduced enzyme.

The case is similar for the H55S mutant enzyme as the serine side chain is unable to form the same hydrogen bonds that histidine 55 can in WT TDO. It is possible that the serine could form a bonding interaction with a nearby solvent molecule (water 250), but the data suggest that less rearrangement of active site hydrogen-bonding interactions is necessary to allow L-Trp binding than for WT TDO.

Stability of the Michaelis Complex. Figure 7 shows how the observed rate constant for turnover (k_{app}) is dependent on dioxygen concentration, [O_2], under saturating L-Trp concentrations (25 mM). In phosphate buffer (pH 7.5) at 25 °C, $K_m(O_2)$ is approximately 120 μM and k_{app} for WT TDO is only 60% of maximum; however, in the case of the H55A and H55S mutant enzymes, k_{app} is nearly maximal (Table 2). These data seem contrary to the Michaelis model (based on steady-state kinetics) that predicts a lower O_2 binding affinity for the mutant forms.

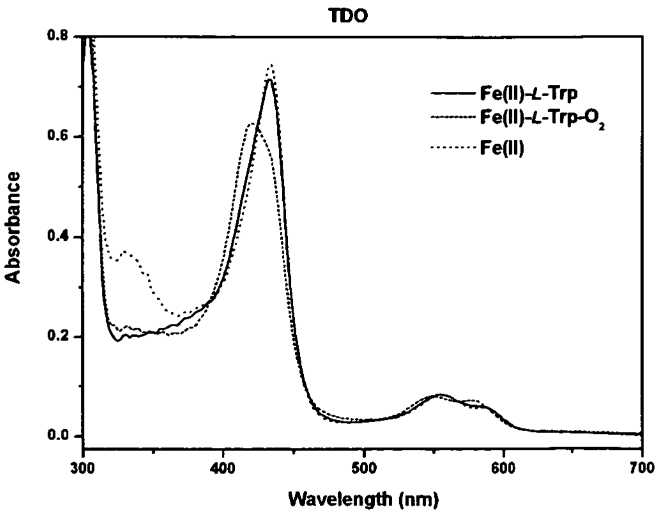

FIGURE 8: Production of the wild-type TDO oxyferrous ternary complex. The peak positions of the oxyferrous ternary complex are at 420, 548, and 578 nm. This decays back to ferrous enzyme and product (*N*-formylkynurenine, peak position 321 nm).

WT TDO has an ordered catalytic cycle in which the reduced enzyme–substrate complex must be formed prior to O_2 binding for turnover to occur (*11, 28*). No ferrous–oxy complex is observed, and addition of oxygen to ferrous WT TDO or the mutant forms in the absence of substrate leads to direct decay to the ferric state. This is also the case for human TDO (*27*), suggesting that instability of the ferrous–oxy species may be common in TDO species. The similar L-Trp binding affinity of the reduced mutant enzymes compared to WT TDO (3.7 and 5.2 μM versus 4.1 μM) and similar K_m values for substrates (Table 2) show that all enzymes can bind substrate and then dioxygen in productive ternary complex formation. Structural data indicate that movement of the indole moiety of L-Trp in the active site is responsible for the decrease in k_{cat} for H55A and H55S. The increased L-Trp binding affinity to the oxidized H55A and H55S enzymes, compared to WT TDO, will lead to a higher probability of nonproductive oxidized enzyme–substrate complex formation, possibly decreasing k_{cat}, but this effect would be small compared to the effect of the destabilized transition state.

Formation and decay of the oxyferrous ternary species generated (Figure 8) for WT TDO show that the (Fe^{2+}–L-Trp) complex displaying a Soret peak at 432 nm binds O_2, producing (Fe^{2+}–L-Trp–O_2), with a corresponding shift in the Soret peak to 419 nm. This then decays to *N*-formylkynurenine (shown by an increase in absorbance at 321 nm) and ferrous enzyme (displaying a Soret peak at 432 nm). This is also observed with 6-F-Trp as the substrate, but for 5-F-Trp some uncoupling is seen, leading to production of the inactive ferric enzyme and the superoxide anion (O_2^-) and release of the substrate. These trends are repeated for H55A and H55S, with uncoupling observed only with 5-F-Trp as substrate. However, the initial

Table 5: Oxygen Dependence of Steady-State Turnover of L-Tryptophan by *X. campestris* TDO Wild Type and Mutants

	TDO WT	H55A	H55S
k_{max} (s^{-1})	35.4 ± 0.9	3.86 ± 0.26	7.88 ± 0.60
K_m (μM)	119 ± 2	45.7 ± 5.6	99 ± 16
K_i (μM)		1380 ± 140	480 ± 50

rates of formation of the ternary complexes are slower, with a rate constant of approximately 50 s^{-1} compared to 100 s^{-1} for WT TDO. Oxyferrous decay parallels this with rate constants of 0.4 s^{-1} and 2 s^{-1} for the mutant enzymes and WT TDO, respectively. This indicates that both mutations do not destabilize the ternary complex significantly, but as the rate of decay is decreased compared to WT TDO, this correlates with a higher activation energy for catalysis due to the movement of the tryptophan indole ring destabilizing the catalytic transition state.

Substrate inhibition is observed at high oxygen concentrations for both mutant forms (Table 5), while none is observed for WT TDO. This unexpected result may be plausibly explained by the lower rate of decay and subsequent slower expulsion of product from the active site by the mutant enzymes. As the active site cavity is larger due to the removal of histidine and its replacement by alanine or serine in the mutant forms, the product, *N*-formylkynurenine, may be less readily expelled at high oxygen concentrations and dioxygen may be able to bind before the product has left. This would trap the product in the active site, causing inhibition of catalytic activity.

CONCLUSIONS

In this study we have investigated whether a putative active site base, histidine 55, is necessary for catalytic activity in TDO. The data we have presented show that in the mutant enzymes H55A and H55S turnover still occurs. This indicates clearly that histidine 55 is not an essential base. Instead, a different role for histidine 55 in controlling substrate binding at the active site has been revealed. On the basis of structural, kinetic, and electrochemical data we have proposed that the role of histidine 55 is to prevent the formation of the nonproductive ferric enzyme−substrate complex. This is most likely achieved by histidine 55 controlling the water content of the substrate-free active site.

SUPPORTING INFORMATION AVAILABLE

A table presenting data on the pH dependence of L-Trp dioxygenation by wild-type TDO and the H55A and H55S mutant forms of the enzyme. This material is available free of charge via the Internet at http://pubs.acs.org.

REFERENCES

1. Forouhar, F., Anderson, J. L. R., Mowat, C. G., Vorobiev, S. M., Hussain, A., Abashidze, M., Bruckmann, C., Thackray, S. J., Seetharaman, J., Tucker, T., Xiao, R., Ma, L.-C., Zhao, L., Acton, T. B., Montelione, G. T., Chapman, S. K., and Tong, L. (2007) Molecular insights into substrate recognition and catalysis by tryptophan 2,3-dioxygenase. *Proc. Natl. Acad. Sci. U.S.A. 104*, 473–478.
2. Takikawa, O. (2005) Biochemical and medical aspects of the indoleamine 2,3-dioxygenase-initiated L-tryptophan metabolism. *Biochem. Biophys. Res. Commun. 338*, 12–19.
3. Yamamoto, S., and Hayaishi, O. (1967) Tryptophan pyrrolase of rabbit intestine. D- and L-tryptophan-cleaving enzyme or enzymes. *J. Biol. Chem. 242*, 5260–5266.
4. Botting, N. P. (1995) Chemistry and neurochemistry of the kynurenine pathway of tryptophan metabolism. *Chem. Soc. Rev. 24*, 401–412.
5. Takikawa, O., Truscott, R. J. W., Fukao, M., and Miwa, S. (2003) Age-related nuclear cataract and indoleamine 2,3-dioxygenase-initiated tryptophan metabolism in the human lens. *Adv. Exp. Med. Biol. 527*, 277–285.
6. Sanni, L. A., Thomas, S. R., Tattam, B. N., Moore, D. E., Chaudhri, G., Stocker, R., and Hunt, N. H. (1998) Dramatic changes in oxidative tryptophan metabolism along the kynurenine pathway in experimental cerebral and noncerebral malaria. *Am. J. Pathol. 152*, 611–619.
7. Mellor, A. L., and Munn, D. H. (2001) Extinguishing maternal immune responses during pregnancy: implications for immunosuppression. *Semin. Immunol. 13*, 213–218.
8. Grohmann, U., Fallarino, F., and Puccetti, P. (2003) Tolerance, DCs and tryptophan: much ado about IDO. *Trends Immunol. 24*, 242–248.
9. Munn, D. H., and Mellor, A. L. (2007) Indoleamine 2,3-dioxygenase and tumor-induced tolerance. *J. Clin. Invest. 117*, 1147–1154.
10. Mellor, A. L., and Munn, D. H. (2004) IDO expression by dendritic cells: tolerance and tryptophan catabolism. *Nat. Rev. Immunol. 4*, 762–774.
11. Sono, M., Roach, M. P., Coulter, E. D., and Dawson, J. H. (1996) Heme-containing oxygenases. *Chem. Rev. 96*, 2841–2887.
12. Sugimoto, H., Oda, S., Otsuki, T., Hino, T., Yoshida, T., and Shiro, Y. (2006) Crystal structure of human indoleamine 2,3-dioxygenase: catalytic mechanism of O_2 incorporation by a heme-containing dioxygenase. *Proc. Natl. Acad. Sci. U.S.A. 103*, 2611–2616.
13. Kotake, Y., and Masayama, I. (1936) The intermediary metabolism of tryptophan. XVIII. The mechanism of formation of kynurenine from tryptophan. *Z. Physiol. Chem. 243*, 237–244.
14. Miller, C. L., Llenos, I. C., Dulay, J. R., Barillo, M. M., Yolken, R. H., and Weis, S. (2004) Expression of the kynurenine pathway enzyme tryptophan 2,3-dioxygenase is increased in the frontal cortex of individuals with schizophrenia. *Neurobiol. Dis. 15*, 618–629.
15. Ishiguro, I., Naito, J., Saito, K., and Nagamura, Y. (1993) Skin L-tryptophan-2,3-dioxygenase and rat hair growth. *FEBS Lett. 329*, 178–182.
16. Littlejohn, T. K., Takikawa, O., Truscott, R. J. W., and Walker, M. J. (2003) Asp274 and His346 are essential for heme binding and catalytic function of human indoleamine 2,3-dioxygenase. *J. Biol. Chem. 278*, 29525–29531.
17. Zhang, Y., Kang, S. A., Mukherjee, T., Bale, S., Crane, B. R., Begley, T. P., and Ealick, S. E. (2007) Crystal structure and mechanism of tryptophan 2,3-dioxygenase, a heme enzyme involved in tryptophan catabolism and in quinolinate biosynthesis. *Biochemistry 46*, 145–155.
18. Bradford, M. M. (1976) A rapid and sensitive method for the quantitation of microgram quantities of protein utilizing the principle of protein-dye binding. *Anal. Biochem. 72*, 248–254.
19. Berry, E. A., and Trumpower, B. L. (1987) Simultaneous determination of hemes *a*, *b*, and *c* from pyridine hemochrome spectra. *Anal. Biochem. 161*, 1–15.
20. Collaborative Computational Project, Number 4. (1994) The CCP4 suite: programs for protein crystallography. *Acta Crystallogr. D50*, 760–763.
21. Adams, P. D., Grosse-Kunstleve, R. W., Hung, L.-W., Ioerger, T. R., McCoy, A. J., Moriarty, N. W., Read, R. J., Sacchettini, J. C., Sauter, N. K., and Terwilliger, T. C. (2002) PHENIX: building new software for automated crystallographic structure determination. *Acta Crystallogr. D58*, 1948–1954.
22. Roussel, A., and Cambillau, C. (1991) TURBO-FRODO, in *Silicon Graphics Geometry Partners Directory 86*, Silicon Graphics, Mountain View, CA.
23. Murshudov, G. N., Vagin, A. A., and Dodson, E. J. (1997) Refinement of macromolecular structures by the maximum-likelihood method. *Acta Crystallogr. D53*, 240–255.
24. Ishimura, Y. (1970) L-Tryptophan 2,3-dioxygenase (tryptophan pyrrolase) (*Pseudomonas fluorescens*). *Methods Enzymol. 17*, 429–434.
25. Ost, T. W. B., Clark, J. P., Anderson, J. L. R., Yellowlees, L. J., Daff, S., and Chapman, S. K. (2004) 4-Cyanopyridine, a versatile spectroscopic probe for cytochrome P450 BM3. *J. Biol. Chem. 279*, 48876–48882.
26. Papadopoulou, N. D., Mewies, M., McLean, K. J., Seward, H. E., Svistunenko, D. A., Munro, A. W., and Raven, E. L. (2005) Redox

and spectroscopic properties of human indoleamine 2,3-dioxygenase and a His303Ala variant: Implications for catalysis. *Biochemistry 44*, 14318–14328.

27. Basran, J., Rafice, S. A., Chauhan, N., Efimov, I., Cheesman, M. R., Ghamsari, L., and Raven, E. L. (2008) A kinetic, spectroscopic, and redox study of human tryptophan 2,3-dioxygenase. *Biochemistry 47*, 4752–4760.

28. Ishimura, Y., Nozaki, M., Hayaishi, O., Nakamura, T., Tamura, M., and Yamazaki, I. (1970) The oxygenated form of L-tryptophan 2,3-dioxygenase as reaction intermediate. *J. Biol. Chem. 245*, 3593–3602.

29. Makino, R., Sakaguchi, K., Iizuka, T., and Ishimura, Y. (1980) L-Tryptophan 2,3-dioxygenase; structure, function and interaction with substrate. *Dev. Biochem. 16*, 179–187.

30. DeLano, W. L. (2002) The PyMOL molecular graphics system, DeLano Scientific, Palo Alto, CA.

BI801202A